Developing Entangled Two-Photon Absorption for Unique Control of Exciting Organic Chromophores: An Experimental and Theoretical Approach

by

Ryan Kristopher Burdick

A dissertation submitted in partial fulfillment
of the requirements for the degree of
Doctor of Philosophy
(Chemistry)
in The University of Michigan
2021

Doctoral Committee:

Professor Theodore Goodson III, Chair
Professor Mackillo Kira
Professor Nicolai Lehnert
Professor Paul Zimmerman

“It does not do to dwell on dreams and forget to live.”

– Albus Dumbledore

Ryan Kristopher Burdick
burdickr@umich.edu
ORCID: 0000-0002-3249-7993

DEDICATION

To those who are on a journey, and they don’t know where it will lead them.
Don’t forget to enjoy the ride.

ACKNOWLEDGEMENTS

My gratitude goes first and foremost to my parents, who have supported my pursuit of learning no matter where it took me. To think that a simple decision of where I wanted to go to high school could be what ultimately led me to where I am today was well beyond the imagination of myself at the time. For my parents to support my decision and to do whatever they had to do to make sure I got there, I am forever thankful.

It is also fair to say that I would not be here on this journey through chemistry if it weren't for the many wonderful chemistry teachers I have had along the way. From my high school chemistry teacher planting the seed and making me want to major in chemistry in college, to my sophomore organic chemistry professor showing me a passion for chemistry that convinced me to pursue research over law school, I wouldn't have made it this far without them. Thank you, Mrs. Nagurney and Dr. Fennie.

To my friends from Scranton who always remained close to me even when I set off to Michigan, you have become a family to me. I didn't realize until I got here just how much Scranton was my home. And while you have made me homesick over the years, you have also given me the strength and courage to keep pushing forward. You have no idea how much that has meant to me.

To my many mentors and friends at Michigan, who have taught me everything I know about spectroscopy. Your knowledge and creative ideas have inspired me every step of the way. I especially want to thank Prof. Ted Goodson for taking me under his wing (and always taking the time to chat about football), Dr. Oleg Varnavski who always seems to have the right answer no matter how stumped I may be, and the members of the Goodson group, past and present, who helped make Michigan a home away from home.

To Rachel, who has been there for me through every up and down, your wisdom, comfort, humor, and care has always been here supporting me, no matter where you may have been. There are no words to describe how important you have been to me these past 4 years. I owe so much of my determination and success to you. I would not have made it this far without you.

And of course, a very special thank you to Minerva and Matilda.

Table of Contents

List of Figures

List of Tables

ABSTRACT

By controlling quantum interactions of molecules and light, new technology in quantum information science promises to outperform classical-based technology in both function and efficiency. In particular, chemists stand to gain much advantage from quantum sensing techniques, allowing them to measure new spectroscopic signals that classical techniques cannot do, control photochemical reactions in new ways, and even measure nonlinear interactions with a simple push of a button. Much of the current work in using entangled photons for spectroscopy has focused on the unique physics of the photons. There is still much to be learned about how the molecule's structure influences quantum spectroscopic signals and leaves its signature. In this dissertation, the unique ways that organic chromophores interact with entangled photons from spontaneous parametric down-conversion (SPDC) has been analyzed in detail. In Chapter 3, I calculate entangled two-photon absorption (ETPA) cross-sections for a few diatomic molecules to show how the varying dipole properties of the molecules affect the ETPA cross-section oscillation vs the entanglement time, T_e. With these cross-section calculations, I show that virtual states in the molecule can constructively interfere to enhance the ETPA cross-section and increase the period between cross-section minima, allowing for better temporal resolution of the ETPA "on" and "off" signals. In Chapter 4, new theory shows that the excited state linewidth from ETPA excitation is extremely narrow compared to classical TPA excitation. This newly derived linewidth provides excellent agreement between calculated ETPA cross-sections of large organic chromophores with experimentally measured cross-sections. I show that the reason for the ETPA linewidth being so narrow is due to the large arrival time uncertainty of the entangled photon pair, which makes the first photons' absorption time in the molecule largely uncertain and effectively narrows the excited state linewidth. In Chapter 5, I used Type-II SPDC to prove, for the first time, that two halogenated anesthetic ethers, sevoflurane and isoflurane, have the ability to target and interact with quantum particles by showing that they interact with 800 nm entangled photons but not 800 nm classical photons. Conversely, I also show that the structurally similar but much less potent anesthetic, diethyl ether, is not sensitive to the entangled photons. This work motivates further studies into

potential quantum mechanisms of anesthetic-induced unconsciousness and the use of entangled photons as a unique probing tool of this mechanism. In Chapter 6, I build an ETPA experimental setup that uses CW laser pumping of Type-I SPDC, which is shown to significantly improve the accuracy, signal-to-noise ratio (SNR), and limit of detection of ETPA while also making the experiment more compact and cost-effective. I also show how to quantify the degree of frequency entanglement using the Schmidt decomposition of the joint frequency spectrum and propose how the Schmidt modes can be tuned to control photochemical reactions. Theoretical work regarding the frequency entanglement of Type-I SPDC photons has shown the great potential for chemists to manipulate the excitation pathway of molecules by tuning the frequency correlations of the photons and not having to change the structure of the molecule itself. Contrary to prior belief in the literature, I show experimentally in Chapter 7 that ETPA with Type-I SPDC increases linearly with increasing T_e, allowing one to increase the ETPA cross-section by an order of magnitude by increasing T_e from a few fs to ~10 ps. This enhancement is due to the entanglement area, A_e, decreasing as the frequency bandwidth decreases, which is how T_e is increased. This spatial-spectral coupling has previously been overlooked in the context of ETPA, causing previous theoretical models to underestimate the ETPA cross-section at ps T_e by 3-4 orders of magnitude. Using ps T_e Type-I SPDC, ps-scale excited state dynamics can be studied using ETPA, and photochemical reactions with intermediate steps, such as isomerizations or solvent reorganization, can be controlled. The experimental techniques and theoretical work here has provided a much needed improvement to make ETPA a more quantitatively robust analytical technique that is useful and accessible to the researchers who can benefit most from its applications: chemists, biologists, and anyone who studies the quantum principles underlying all aspects of chemistry.

CHAPTER 1

Introduction and Background Information

1.1 Scope

Quantum information science (QIS) is a multidisciplinary field that aims to utilize the unique features of quantum mechanics to develop technology and scientific research methods that can outperform classical mechanics-based technology and methods.[1, 2] There are a variety of ways that quantum technology and methods can outperform their classical counterparts, including completing tasks much faster, requiring less resources such as memory and cost to complete tasks, and even completing tasks that would be impossible for classical technology and methods to do. QIS can be broken down into three main pillars: computing, communication, and sensing. While each of these pillars has different end goals, they all rely upon a few important concepts that are unique to quantum mechanics. To set the context of this dissertation, the big picture goal of this work will be explained, followed by introductory information about the unique aspects of quantum mechanics that are important for understanding this work.

The focus of this dissertation lies within the pillar of quantum sensing. Quantum sensing is the multidisciplinary field of using quantum measurement devices to detect or extract information from samples that would be extremely difficult, if not impossible, for classical measurement devices to do.[3, 4] While classical sensing technology today can perform measurements on quantum systems, the measurement device itself may not be a quantum system. By using a quantum measurement system, the quantum state of the sample can interfere with the quantum state of the sensing device, allowing for new signals to be measured that would go unseen by a classical measurement system. Some well-known examples today include the superconducting quantum interference device (SQUID) to measure extremely small magnetic fields[5], scanning tunneling microscope for atomic level images[6], and avalanche photodiode for single photon detection.

In the field of optical sensing, lasers are the most common device used to measure properties of molecular samples. By measuring the properties of the laser's light field before and after interacting with a sample, information about the sample can be extracted. Most laser spectroscopy techniques today can be modeled with classical wave mechanics, making these techniques classical-based. The goal of quantum optical sensing is to use a light source that is a purely quantum system and measure how the properties of this quantum light field change before and after interacting with the sample. The most common quantum light source, which is used extensively throughout the work in this dissertation, is entangled photons produced by spontaneous parametric down-conversion (SPDC). Using entangled SPDC photon pairs, the technique of entangled two-photon absorption (ETPA) has been examined and developed both experimentally and theoretically in this work.

Research on ETPA began with theoretical studies in the 1990s.[7-10] These earlier works, which are highlighted in more detail in the following sections, focused on the unique physics that quantum entangled photons bring to interactions with molecules. Simple molecular systems, such as H_2, were used as toy models as a first step toward understanding how the physics of two-photon absorption changes from using classical photons to entangled photons. Experimental work on ETPA began soon after, with ETPA observed in atomic systems and organic chromophores.[11, 12] These works proved many predictions that the theoretical literature suggested some years prior. With theoreticians predicting unique advantages that ETPA may provide for chemists, and experimentalists demonstrating the ability to measure and manipulate ETPA signals, the next step is developing ETPA specifically to make it useful and accessible to chemists, whether they have laser spectroscopy and quantum optics experience or not. This next step is where the work in this dissertation lies.

This work begins with two theoretical studies into the molecular properties that influence the ETPA cross-section, i.e. the ability for a molecule to absorb entangled photon pairs. Since the early theoretical reports focused on the unique physics of the photons, questions remained about what the molecules bring to the table during the ETPA interaction. The first work (chapter 3) analyzed how the two-photon pathway taken by the entangled photons is influenced by the strength of the dipole moments of a molecule. Because of the computationally intensive nature of the calculations, diatomic molecules were used as a model. The second work (chapter 4) extends the

calculations of ETPA cross-sections to larger organic chromophores that are used experimentally. This work considered another molecular property that influences ETPA: the excited state lineshape. With the first two works uncovering how molecules influence ETPA, the next two works, both experimental, focused on what kinds of molecules can be studied by chemists and how chemists can study such molecules in a relatively simple experiment. The first of these works (chapter 5) studied a scattering interaction between entangled photons and two anesthetic molecules, a molecular system extremely important to biology and medicine that has not been studied with entangled photons before. Chapter 6 takes the ETPA experimental setup and shows how the experiment can actually be completed in a much smaller, simpler, and more cost-effective setup, with the additional benefit of increasing the signal-to-noise ratio of ETPA measurements. This development makes ETPA much more appealing and accessible to chemists. The final work (chapter 7) reveals an oversight regarding ETPA that had been missed in previous theoretical models, that of the importance of frequency-spatial coupling of SPDC. From this work, new uses for ETPA that had previously been neglected under the assumption that they were not practical experimentally are shown to have great potential for chemists, including new control over photochemical reactions.

Before detailing these works in the subsequent chapters, the remainder of this chapter will introduce the key concepts in quantum mechanics, optical spectroscopy, and prior work on ETPA that will be necessary to understand the work in this dissertation.

1.2 Correlations of Quantum States

1.2.1 Quantum States

When a measurement is performed on a quantum object, such as an atom, proton, or electron, the outcome, i.e. the specific value measured, is determined, in part, by the quantum state of the object. The *state* of an object is the description of the object's properties, such as position, energy, spin, etc., as they exist in reality. For example, an electron can spin counter-clockwise (called "spin up") or clockwise (called "spin down"). States can be manipulated or measured with operators that act on the state. When an operator acts on a state by extracting a piece of information, such as the spin of the electron, without changing the state of the object, the state is an *eigenstate* of that operator, and the information is a scalar called the *eigenvalue*.

Such eigenvalue problems are abundant in quantum mechanics. Some eigenvalue equations of the electron's spin can be written in a shorthand known as Dirac or bra-ket notation as:[13]

$$\hat{S}|\uparrow\rangle = \frac{\hbar}{2}|\uparrow\rangle \tag{1.1}$$

$$\hat{S}|\downarrow\rangle = -\frac{\hbar}{2}|\downarrow\rangle \tag{1.2}$$

When measuring the spin of the electron with the operator *S*, the state (also called a *ket*) in eq. 1.1 will always yield spin up, indicated by the eigenvalue $\hbar/2$, and the state in eq. 1.2 will always yield spin down, indicated by the eigenvalue $-\hbar/2$. However, objects do not have to start in an eigenstate of the operator. For example:

$$|\psi\rangle = a|\uparrow\rangle + b|\downarrow\rangle \tag{1.3}$$

The state in eq. 1.3 is in a *superposition* of the spin up state and spin down state. In this superposition, the electron's state has some character of the spin up state and some character of the spin down state, each weighted with the coefficients *a* and *b*, respectively, but the electron is not actually in either of the spin up or spin down states. If the electron's spin were measured while in this superposition, the state would collapse into either the spin up or spin down state, with the probability of each outcome equaling its coefficient squared (assuming the coefficients are normalized such that the sum of the squares is 1). All of the states in eq. 1.1-1.3 are examples of *pure states* because they express single, definable probability distributions for the outcome of a measurement.

Quantum states can also be written as *density operators*. For pure states, expressing the state in the ket form above or the density operator below provides the same information about the state. Other states, known as *mixed states*, can only be defined as a density operator. Mixed states are those that are a statistical mixture of multiple pure states, each of which define a unique probability distribution. The density operator is defined as:[14]

$$\rho = \sum_j^N p_j |\psi_j\rangle\langle\psi_j| \tag{1.4}$$

Here, p_j is the probability for the object to be in the *j*th state with the outer-product $|\psi_j><\psi_j|$, and each $|\psi_j>$ is a pure state. For pure states, $N = 1$ and $p_j = 1$. For mixed states, $N >$

1, and the summation of all the p_j's equals 1. As an example, a mixed state involving the pure states in eq. 1.1 and 1.2 can be:

$$\rho = \frac{1}{2}|\uparrow\rangle\langle\uparrow| + \frac{1}{2}|\downarrow\rangle\langle\downarrow| \tag{1.5}$$

A mixed state commonly occurs for a large ensemble, where each object in the ensemble, such as an electron, is in a pure state, such as spin up or spin down. However, when performing a measurement on one electron in the ensemble, it is not known before the measurement which pure state that particular electron is in. For the mixed state in eq. 1.5, the electron is in either the spin up or spin down state, with their probabilities both being 1/2. For both superposition states and mixed states, the outcome of the measurement is not known before the measurement is taken. The difference, however, is that with a superposition, the initial pure state of the electron is known; with a mixed state, the initial pure state is not known.

1.2.2 Classical Correlations

The initial state of a quantum object is important for understanding how two (or more) objects can be correlated. In general, *correlation* refers to the properties of one object influencing the properties of another object. Correlations can be classified as classical or quantum, with the difference being the initial joint state of the correlated objects. The joint state of two classically correlated objects is:

$$\rho_{AB} = \sum_j^{N>1} p_j |\psi_j\rangle_A \langle\psi_j|_A \otimes |\psi_j\rangle_B \langle\psi_j|_B = \sum_j^{N>1} p_j \rho_{j,A} \otimes \rho_{j,B} \tag{1.6}$$

Here, the density operators of objects A and B are separable, meaning that there is a defined density operator just for A and one just for B. Each object is in a pure state, and these pure states alone do not depend on each other. But, each object has multiple pure states it can be in, and the occupied states are correlated such that if object A is in $\rho_{j,A}$, then object B must be in $\rho_{j,B}$. Since it is not known which pure state each object is in, the joint system of both objects is a mixed state. Suppose there are 2 electrons labeled A and B. Each electron is in either the spin up or spin down pure state with the condition that one electron is spin up and the other spin down. Without you looking, the electrons are placed in separate boxes. The initial joint state of this system of electrons is:

$$\rho_{AB} = \frac{1}{2}|\uparrow\rangle_A\langle\uparrow|_A \otimes |\downarrow\rangle_B\langle\downarrow|_B + \frac{1}{2}|\downarrow\rangle_A\langle\downarrow|_A \otimes |\uparrow\rangle_B\langle\uparrow|_B \tag{1.7}$$

The left term says that if electron A is spin up, then electron B is spin down, and vice versa for the right term. Before opening a box, you do not know whether either electron is spin up or spin down. If you were to open the box with electron A, there is a 50 % chance of the electron being spin up or spin down, noted by the coefficients of ½. When you open the box with electron A, and see that the electron is spin up, you now know that electron B is spin down, even if you never open the box. By measuring the spin of electron A, you gained information about electron B without having to measure it because the two electrons were correlated.

1.2.3 Quantum Correlations and Entanglement

Quantum correlations have a different initial joint state:

$$\rho_{AB} = \sum_j^N p_j |\psi_j\rangle_A \otimes |\psi_j\rangle_B \cdot \langle\psi_j|_A \otimes \langle\psi_j|_B = \sum_j^N p_j \rho_{j,AB} \tag{1.8}$$

For this joint state, it is impossible to define a density operator just for A and just for B. There is only one density operator for each *j* that defines both objects together. An example joint state for two quantum correlated electrons A and B, with the condition that when measured one electron is spin up and the other is spin down, can be:

$$|\psi\rangle_A \otimes |\psi\rangle_B = \frac{1}{\sqrt{2}}\left(|\uparrow\rangle_A \otimes |\downarrow\rangle_B + |\downarrow\rangle_A \otimes |\uparrow\rangle_B\right) \tag{1.9}$$

This joint state is a superposition of the state where electron A is spin up and electron B is spin down, and vice versa. Substituting eq. 1.9 into eq. 1.8, with $N = 1$ and $p_j = 1$, would give the pure joint state of the quantum correlated electron pair. This kind of correlation is what is known as *quantum entanglement*. Suppose again that electrons A and B were placed in separate boxes without you looking, and the closed boxes resulted in the joint state in eq. 1.9. Before you open the box with electron A, both electrons are in a superposition of the spin up and spin down states. If you open the box for electron A and see that its state collapses to spin up, then you also know electron B has collapsed to spin down without ever having to open its box. Though this example may seem similar to the example for the classically correlated electrons, they are distinctly different. For the classically correlated electrons, electron A was always spin up, and electron B was always spin down, even when the boxes were closed and you had not yet looked at electron A. When you looked at electron A by opening its box, you

the observer gained more information about electron B, but the act of opening the box for electron A did not change anything about the state of electron B. For the quantum entangled electrons, neither electron was spin up nor spin down while the boxes were closed; they were both in superpositions. When you opened the box for electron A, you gained information about electron B, and the act of opening the box for electron A actually changed the state of electron B. This is what Einstein has famously referred to as "spooky action at a distance," because performing a measurement on one object actually changes the state of another distant object that has not been directly interacted with.

1.2.4 Hidden Variables

There is an important clarification regarding the nature of superpositions that must be understood. Some physicists, most notably Albert Einstein, believed there must be "hidden variables" that determine the collapsed value of a property's superposition before the measurement occurs.[15] Thus, the object was never in a superposition state in reality. The mathematical description of the superposition state merely reflects that the observer does not know which state the object is actually in. For example, before measuring the spin of an electron, the observer did not know whether the spin would be up or down after measuring it. But, the hidden variable theory states that the electron had some underlying variable which had already determined "this electron will be spin up when it is measured." The observer could not see this variable, and so represented the electron's state with a superposition, but Einstein and others believed the variable must exist.

While the debate of the existence of hidden variables continued, it was believed the theory could not be experimentally tested until John Bell proposed his eponymous theorem in 1964.[16] Bell showed that if the hidden variables were real, then the predicted statistical outcomes of measuring two entangled particles separately must obey an inequality, now referred to as Bell's inequalities. However, if there are no hidden variables, the predicted statistical outcomes would violate the inequality. Bell's theorem was first tested by Freedman and Clauser in 1972, and the results violated the inequality and confirmed the predictions of quantum mechanics without hidden variables.[17] The theory of hidden variables is thus incorrect, which leaves the original interpretation of the superposition intact.

While the hidden variable theory does not correctly explain the concept of superposition, the theory does provide an intuitive understanding of the difference between classical and quantum correlations. Supposing again that there are two electrons with correlated spins such that one is up and one is down, quantum correlations occur when the electrons are in a superposition of the spin up and spin down states. The spin state of each electron is not determined until the measurement of one of the electrons occurs. For classical correlations, one electron was always spin up, and the other was always spin down. However, the information of which electron was in which state was hidden to the observer before the measurement took place. Measurements of the quantum correlated electrons' spins would be consistent with quantum mechanics without hidden variables, while the hidden variable theory would be consistent with the measurements of the classically correlated electrons' spins.

1.3 Nonlinear Optics

1.3.1 Classical Second-Order Nonlinear Optics

There are a variety of particles that can be entangled, including the example of electrons used above. The particles relevant for this dissertation are entangled photons. Before explaining what entangled photons are and where they come from, a few concepts in nonlinear optics should be understood.

From a classical optics point-of-view, when a light field passes through a molecule, the electric field creates an oscillation of the molecule's electron density, known as a polarization. Assume the molecule is that of an optical crystal with its first electronic excited state far off resonance with the light field, as is common for optical crystals used experimentally. At low light intensities, the polarization, *P*, is linear, meaning the oscillation of the electron density contains only the frequency of the present light field(s):[18]

$$\vec{P}(t) = \varepsilon_0 \chi^{(1)} \vec{E}(t) \tag{1.10}$$

In eq. 1.10, ε_0 is the vacuum permittivity, $\chi^{(1)}$ is the linear or first-order susceptibility (a proportionality constant describing the molecule's ability to be polarized by the electric field), and E(t) is the electric field. For simplicity, assuming one electric field with frequency ω_1 and amplitude E_1 enters the crystal, the polarization oscillates according to:

$$\vec{P}(t) = \varepsilon_0 \chi^{(1)} E_1 e^{-i\omega_1 t} \tag{1.11}$$

When the molecule loses its polarization, it can emit a photon (in any direction) at the frequency it oscillates at: ω_1. This is known as Rayleigh scattering (Fig. 1.1a). If the molecule absorbs a small amount of energy and relaxes instead to a different vibrational state than it started in, the molecule emits a photon (in any direction) at a frequency very close to ω_1. This is known as Raman scattering (Fig. 1.1b).

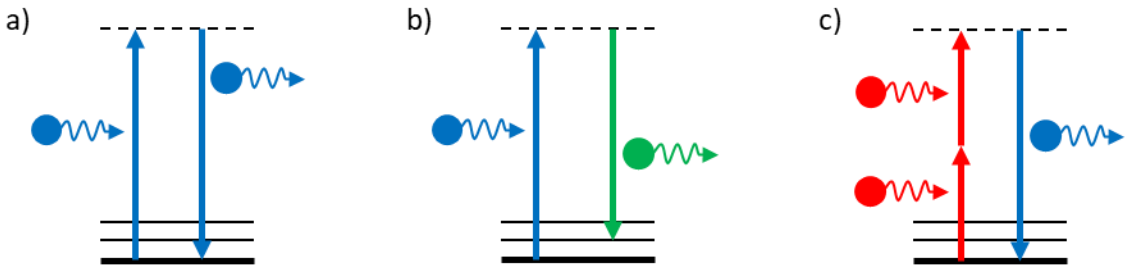

Figure 1.1. Energy level diagrams for: a) Rayleigh scattering; b) Raman scattering; c) second harmonic generation (SHG).

When the light field intensity is increased, the molecule can experience nonlinear polarizations, where the oscillation of the electron density contains frequencies not found in the present light field(s). This leads to several new nonlinear optical phenomena. Here, the polarization is written generally as:[18]

$$\vec{P}(t) = \varepsilon_0 \left[\chi^{(1)} \vec{E}(t) + \chi^{(2)} \vec{E}^2(t) + \cdots \right] \tag{1.12}$$

$\chi^{(2)}$ is the second-order susceptibility, and similar susceptibilities exist for higher-order terms as well. For relevancy to this dissertation, the polarization will be limited to second-order. Again assuming one electric field with frequency ω_1 and amplitude E_1 enters the crystal, the polarization oscillates according to:

$$\vec{P}(t) = \varepsilon_0 \left[\chi^{(1)} E_1 e^{-i\omega_1 t} + \chi^{(2)} E_1^2 e^{-i2\omega_1 t} \right] \tag{1.13}$$

In eq. 1.13, the first term is the Rayleigh scattering term found in eq. 1.11. The second term shows that the polarization can also oscillate at two times the frequency of ω_1. Thus, in addition to Rayleigh scattering, the crystal's molecules can also convert two photons of the electric field at frequency ω_1 into one photon at frequency $2\omega_1$ with amplitude E_1^2, known as second-harmonic generation (SHG), shown in Fig. 1.1c. There are other second-order

nonlinear processes that can occur if two electric fields at different frequencies are sent into the crystal, but those processes are outside the scope of this dissertation. All second-order nonlinear processes are also referred to as three-wave mixing since three waves (or three photons) are involved. For SHG, two photons are converted into a new third photon.

What eq. 1.13 says is that, from a classical nonlinear optics point-of-view, if one electric field is sent into a nonlinear crystal, only SHG (or Rayleigh scattering) can occur. Classically, it is not possible to send one electric field into a nonlinear crystal and for the crystal to convert one photon into two photons, even though such a process would be a second-order nonlinear, or three-wave mixing, process. (Note: if a second electric field of lower frequency than the first is also sent into the crystal, the second-order nonlinear process of difference frequency generation, or DFG, can convert the one photon from the first field into two photons, one at the second field's frequency and one at the difference in the first and second fields' frequencies. This is a classically-allowed process but REQUIRES the second electric field to already be present in the crystal to stimulate the process. In this dissertation, only one electric field is sent into the crystal.)

1.3.2 Quantum Second-Order Nonlinear Optics

Nonlinear optical processes can also be derived from a quantum optics point-of-view. In quantum optics, photons exist in *modes* with defined properties, such as frequency, wave vector, polarization, etc. In general, a mode *m* containing *n* number of photons is written as the state vector $|n_m\rangle$. Photons can be created in a mode or annihilated from a mode with the creation and annihilation operators, respectively:

$$\hat{a}^\dagger|n_m\rangle = \sqrt{n+1}|(n+1)_m\rangle \tag{1.14}$$

$$\hat{a}|n_m\rangle = \sqrt{n}|(n-1)_m\rangle \tag{1.15}$$

Quantization of the electromagnetic field is expressed as:[19]

$$\hat{E}_m(\vec{r},t) = i\sqrt{\frac{2\pi\hbar\omega_m}{V}}\left(\hat{a}_m e^{i\vec{k}\cdot\vec{r}-i\omega_m t} - \hat{a}_m^\dagger e^{-i\vec{k}\cdot\vec{r}+i\omega_m t}\right) \equiv \hat{E}_m^{(+)}(t) + \hat{E}_m^{(-)}(t) \tag{1.16}$$

The first term in eq. 1.16 is referred to as the *positive frequency component* of the electric field, and contains the annihilation operator, and the second term is referred to as the

negative frequency component of the electric field, and contains the creation operator. For a three-waving mixing process, three electric field operators must be included in the Hamiltonian operator. Since there must be at least one photon annihilated and at least one photon created, it can be assumed that E_1 will be annihilated and E_3 will be created. E_2 will be left possible to be annihilated or created. The Hamiltonian can then be written as:[20]

$$\hat{H}_{int} = \hat{E}_3^{(-)}\hat{E}_2\hat{E}_1^{(+)} = i\hbar\kappa\left(\hat{a}_3^\dagger\hat{a}_2\hat{a}_1 e^{-\Delta\vec{k}\cdot\Delta\vec{r}-i(\omega_1+\omega_2-\omega_3)t} + \hat{a}_3^\dagger\hat{a}_2^\dagger\hat{a}_1 e^{-\Delta\vec{k}\cdot\Delta\vec{r}-i(\omega_1-\omega_2-\omega_3)t}\right) \tag{1.17}$$

In the first term, two photons, one at frequency ω_1 and one at frequency ω_2, are annihilated, and one photon at frequency ω_3 is created. The probability of this process occurring is maximized when $\omega_1 + \omega_2 = \omega_3$. Since it was assumed that only one electric field entered the crystal, the two annihilated photons must be from the same electric field and have the same frequency. This first term, then, is SHG, just as seen with the classical nonlinear optics approach. Unlike the classical approach, a second term exists in eq. 1.17 from the quantum optics approach. This second term annihilates one photon at frequency ω_1 (called the *pump photon*) and creates two photons, one at frequency ω_2 and one at frequency ω_3. The probability of this process occurring is maximized when $\omega_1 = \omega_2 + \omega_3$. However, specific frequencies for ω_2 and ω_3 are not defined. As long as they sum to ω_1, the process can occur. This process is known as spontaneous parametric down-conversion (SPDC), and the two photons created, known as the *signal* and *idler* photons or *SPDC photons*, are entangled. SPDC is a purely quantum process since it cannot be explained using a classical approach. The process is shown in Fig. 1.2.

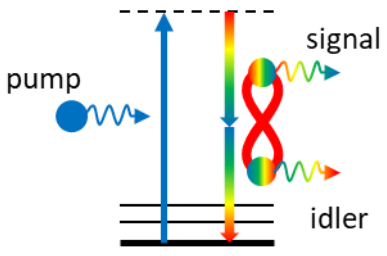

Figure 1.2. Energy level diagram and frequency spectrum for SPDC.

1.3.3 SPDC Phase-Matching

Eq. 1.17 clearly shows that energy must be conserved in SPDC. The factor Δk, which is the *phase mismatch*, should also equal 0 to maximize the probability of SPDC occurring. This factor takes momentum conservation into account since k_j is the wave vector of the j photon. The phase mismatch for SPDC is expressed as:

$$\Delta\vec{k} = \vec{k}_p - \vec{k}_s - \vec{k}_i \tag{1.18}$$

k_p, k_s, and k_i are the wave vectors of the pump, signal, and idler photons, respectively. Together, satisfying energy conservation and setting eq. 1.18 to 0 are known as the *phase-matching conditions*. As stated previously, the frequencies of the two SPDC photons must sum to the pump photon frequency, but neither individual frequency is specifically defined. However, these frequencies are also included in the phase mismatch in eq. 1.18 due to the dispersion relation that links the wave vector and frequency of a photon:

$$\vec{k}_j = n_j(\omega_j)\omega_j/c \tag{1.19}$$

n_j is the refractive index experienced by the photon, which is dependent upon the photon's frequency, ω_j, and c is the speed of light in vacuum. Substituting eq. 1.19 into eq. 1.18 yields:

$$\Delta\vec{k} = \left[n_p(\omega_p)\omega_p - n_s(\omega_s)\omega_s - n_i(\omega_i)\omega_i\right]/c \tag{1.20}$$

Though not necessary, assume for simplicity that the signal and idler have the same frequency. Conservation of energy then requires this frequency to be $\omega_p/2$, yielding:

$$\Delta\vec{k} = \left[n_p(\omega_p) - \frac{1}{2}\left[n_s(\omega_p/2) + n_i(\omega_p/2)\right]\right]\omega_p/c \tag{1.21}$$

If we consider a crystal where the refractive index only depends on photon frequency and not on polarization, then $n_s = n_i$ and:

$$\Delta\vec{k} = \left[n_p(\omega_p) - n_s(\omega_p/2)\right]\omega_p/c \tag{1.22}$$

Eq. 1.22 shows that in this crystal, the phase-matching conditions are only satisfied if the refractive index at half the pump frequency equals the refractive index at the pump frequency. However, assuming the pump photon is not close to resonance with an excited state in the crystal (as is the case for nonlinear crystals used in experiments), lower frequencies have lower refractive indices, so eq. 1.22 cannot be equal 0.

Birefringent crystals are typically used to create SPDC (and other nonlinear processes) since the refractive index will also depend on the polarizations of the photons relative to the axes of the crystal. A photon in the *ordinary ray* experiences a refractive index n_o, while a photon in the *extraordinary ray* experiences a refractive index n_e. These rays have orthogonal polarizations. While n_o is constant, n_e can be tuned by adjusting the angle between the pump beam and the *optical axis* of the birefringent crystal. This angle can be adjusted such that n_e has a value that satisfies the phase-matching condition. Thus, the birefringent crystal will generate the signal and idler into specific polarization directions that satisfy eq. 1.20. For SPDC (and all second-order nonlinear processes), there are three possible polarization combinations: Type-0, where all three photons have the same polarizations, or propagate in the same ray; Type-I, where the signal and idler have the same polarization and are orthogonal to the pump; Type-II, where the signal and idler have orthogonal polarizations and one of them is parallel to the pump.

1.4 SPDC Entanglement Properties

1.4.1 Frequency Entanglement

The angular dependence of the phase-matching condition conveniently ensures that both processes in the Hamiltonian in eq. 1.17 do not occur (strongly) at the same time. Each process requires a different angle between the pump beam and optical axis. Therefore, to describe the quantum state of the entangled photons, only the SPDC term in the Hamiltonian needs to be considered. The SPDC Hamiltonian, accounting for the volume of the crystal where SPDC occurs and considering each wave vector mode that the signal and idler can each be created into, is defined as:[8]

$$\hat{H}_{SPDC}(t) = \sum_{k_1}\sum_{k_2}\chi^{(2)}(\omega_p;\omega_1,\omega_2)\xi_p\frac{1}{V}\int_V d^3\vec{r}\, exp\left(i\Delta\vec{k}\cdot\vec{r}\right)exp(-i\Delta\omega t)\hat{a}^\dagger_{k_1}\hat{a}^\dagger_{k_2} + H.c. \tag{1.23}$$

In eq. 1.23, the pump electric field is treated classically since it is much stronger than the SPDC fields and the loss of pump photons is negligible compared to the incident intensity of the pump beam. The parameter ξ_p is the coherent amplitude of the pump beam. The phase-

matching conditions in the exponential functions and the creation operators are integrated over the entire volume of the crystal. *H.c.* is the Hermitian conjugate. In this dissertation, the pump propagation path will be defined as the z-axis and parallel to the optical table, with the x-axis being perpendicular to the z-axis and parallel to the plane of the optical table, and the y-axis being perpendicular to both the z-axis and plane of the optical table. The spatial dimension of the crystal in the x-axis is assumed to be much larger than the transverse profile of the pump beam, so the integration can be taken from -∞ to ∞:

$$\int_{\infty}^{-\infty} dx\, e^{i\Delta k_x \cdot x} = \delta(\Delta k_x) \tag{1.24}$$

The delta function in eq. 1.24 simply states that the pump, signal, and idler must be perfectly phase-matched in the x-axis. A similar integration occurs for the y-axis.

Integration along the z-axis is limited to the length of the crystal along the pump propagation path. Taking the entry plane of the crystal as z = 0 and the exit plane as z = L, the integration along the z-axis becomes:

$$\int_0^L dz e^{i\Delta k_z \cdot z} = \int_{-\infty}^{\infty} dz\, e^{i\Delta k_z \cdot z}\, rect\left(\frac{z-L/2}{L}\right) = sinc(\Delta k_z \cdot L) \tag{1.25}$$

While the sinc function in eq. 1.25 is maximized when the phase mismatch in the z-axis, Δk_z, equals 0, the function can still be non-zero even if the phase mismatch is non-zero. Because satisfying the phase-matching condition in a birefringent crystal is angular dependent, each angle will (typically) only have a perfect phase matching at one frequency. For SPDC, the angle between the pump beam and optical axis is usually chosen so that the phase-matching condition is satisfied exactly at the degenerate signal/idler frequency, i.e. $\omega_s = \omega_i = \omega_p/2$. The sinc function in eq. 1.25 states that signal/idler frequency pairs that are not degenerate, and therefore not perfectly phase-matched, can still have a non-zero probability of being created. As a result, the signal and idler both have a frequency spectrum upon their creation. Eq. 1.25 can be recast in terms of frequency by expanding Δk (along the z-axis) in terms of frequency:

$$\Delta k = k_p - k_s - k_i = K_p - \left(K_s + \nu \frac{dK_s}{d\omega_s}\Big|_{\Omega_s} + \frac{\nu^2}{2}\frac{d^2K_s}{d\omega_s{}^2}\Big|_{\Omega_s} + \cdots\right) - \left(K_i - \nu \frac{dK_i}{d\omega_i}\Big|_{\Omega_i} + \frac{\nu^2}{2}\frac{d^2K_i}{d\omega_i{}^2}\Big|_{\Omega_i} + \cdots\right)$$

(1.26)

In eq. 1.26, the signal (idler) frequency is rewritten in terms of its central frequency, Ω_s (Ω_i) = $\omega_p/2$, and a detuning frequency, v, from the central frequency: $\omega_s = \Omega_s + v$ ($\omega_i = \Omega_i - v$). K_p, K_s, and K_i are the central wave vector components of the pump, signal, and idler, respectively, along the z-axis. They follow the relation $K_p = K_s + K_i$. The signal and idler wave vectors are Taylor-expanded to show the deviations of the z-axis wave vector component from the central value. The term linear in v is the inverse group velocity, $1/u_s$ ($1/u_i$), for the signal (idler). The second-order term is the group velocity dispersion. Higher order terms are negligible. Substituting the expanded Δk_z into eq. 1.25 results in the sinc function recast into frequency terms:[21]

$$sinc\left(-vDL - \frac{v^2}{2}D''L\right) \tag{1.27}$$

D is the difference in the inverse group velocities of the signal and idler, and D'' is the sum of the group velocity dispersion of the signal and idler. As stated previously, this frequency spectrum is maximized when $v = 0$ since the birefringent crystal is perfectly phase-matched for this frequency pair. For the frequency pairs with a small phase mismatch ($v \neq 0$), their creation probability is determined by the bandwidth of the sinc frequency spectrum, which is determined by the length of the crystal, L, and the crystal's group velocity and group velocity dispersion.

The sinc function in eq. 1.27 is the general equation for the SPDC frequency spectrum. The spectrum can be further simplified when considering specific types of SPDC. For degenerate Type-0 or Type-I SPDC, where the signal and idler have the same polarization, the inverse group velocity of both photons is the same, so $D = 0$. The degenerate Type-0/Type-I SPDC frequency spectrum is thus:

$$sinc\left(-\frac{v^2}{2}D''L\right) \tag{1.28}$$

For Type-II SPDC and non-degenerate Type-0/Type-I SPDC, the inverse group velocities are different, so D is nonvanishing. The first-order term is then much larger than the second-order term, so the second-order term can be neglected, leaving:

$$sinc(-vDL) \tag{1.29}$$

With the volume integration completed in the Hamiltonian in eq. 1.17, the entangled photon state vector can be calculated. Using standard perturbation theory, the state vector (sometimes called the *twin state*) is calculated as:[7]

$$|twin\rangle = \left|0_{k_s}; 0_{k_i}\right\rangle - \frac{i}{\hbar}\int_{-\infty}^{\infty} dt\hat{H}_{SPDC}(t)\left|0_{k_s}; 0_{k_i}\right\rangle \tag{1.30}$$

$|0_{ks};0_{ki}\rangle$ is shorthand for the joint state of the tensor product of $|0_{ks}\rangle$ and $|0_{ki}\rangle$. The initial state vector contains no photons in the signal or idler mode. This state is also called the *vacuum state*. The first term in eq. 1.30 is the first-order perturbation where no interaction occurs. This term is commonly neglected since it plays no role in entangled photon interactions with molecules. The second term is the second-order perturbation that creates the SPDC. Higher order terms are negligible. Substituting eq. 1.17 for the Hamiltonian and integrating over the interaction time, *t*, yields:[7]

$$|twin\rangle = NL\sum_{k_s}\sum_{k_i} exp\left[-\frac{\left(\omega_p-\omega_s-\omega_i\right)^2}{\Delta\omega_p^2}\right] sinc\left[\frac{\Delta k_z \cdot L}{2\pi}\right]\left|1_{k_s}; 1_{k_i}\right\rangle \tag{1.31}$$

N is a normalization constant. The so-called *twin state* in eq. 1.31 is for SPDC in general. The appropriate simplified Δk_z can be inserted into the sinc function to obtain the specific twin state for Type-0/Type-I or Type-II SPDC.

The significance of the SPDC photons having a frequency spectrum, and not a single defined individual frequency, means the photons, before interacting with anything, are in frequency superpositions. However, the exponential in eq. 1.31 (conservation of energy with the pump) ensures that when one of the SPDC photons collapses its superposition, the other entangled photon must also collapse its superposition to conserve energy, even if this second photon has not interacted with anything. This phenomenon is known as frequency entanglement.

1.4.2 Temporal Entanglement

The bandwidth of the SPDC photons is extremely important for defining other entanglement properties in addition to frequency entanglement. It is well known in classical optics that a laser beam with a superposition of frequency yields a temporal pulse upon Fourier transform. Along similar lines, the superposition of frequency pairs of the signal and idler

yields a temporal width for the pair of photons. This temporal width, known as the second-order correlation time or *entanglement time*, T_e, defines the time window within which the pair of photons were created together.[7] As the photons travel along a path, if no delay is applied to either photon, then T_e states that when one photon is measured at a point in space, the second photon must arrive at the same point within a time T_e. This temporal entanglement can be ultrafast, with T_e as small as a few tens of femtoseconds using a ~1 mm long bulk nonlinear crystal to create the SPDC. The relationship between the frequency spectrum and T_e is shown in Fig. 1.3. If the photons are filtered in frequency, this filtering also affects the temporal correlation function following the properties of Fourier transform. Much of the early work in using entangled photon pairs for chemical sensing applications and experiments has focused on utilizing this ultrafast entanglement time, which is discussed more in a later section.

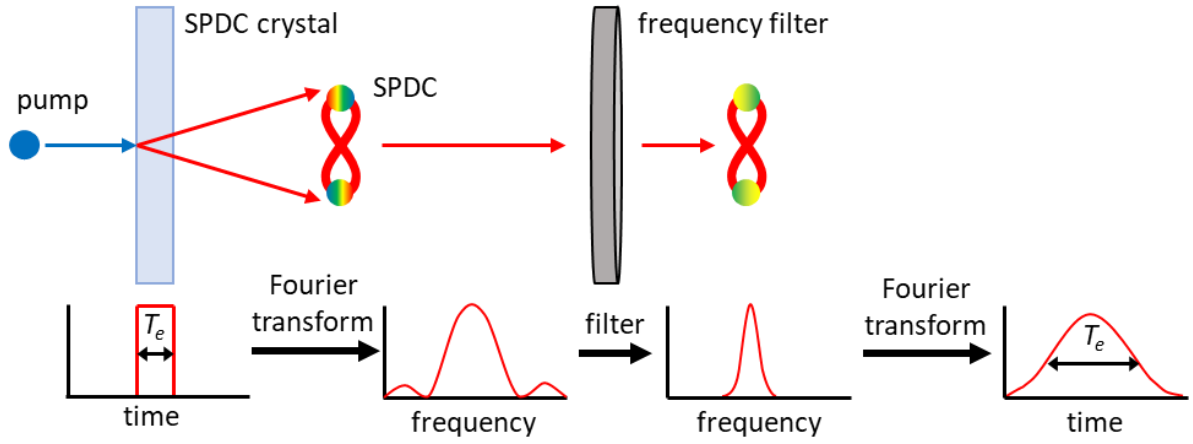

Figure 1.3. Generation and propagation of an SPDC pair highlighting the relationship between the frequency spectrum and temporal correlation.

1.4.3 Spatial Entanglement

The spatial properties of the SPDC photons are also coupled to the frequency spectrum.[22] In the SPDC crystal, each frequency experiences a different refractive index, causing each frequency component of the spectrum to propagate at a different angle in the crystal. When the SPDC photons reach the exit plane of the crystal, the frequency spectrum is spread out in space, shown in Fig. 1.4. This not only causes the transverse spatial location of the SPDC to be spread out but also creates an inherent structure to the transverse spatial profile. Each frequency component goes to one location, and each location has one frequency

component. Therefore, the frequency superposition of the individual photons creates a spatial superposition as well. So, when one photon has its frequency measured, its spatial location is also now determined. Frequency entanglement causes the second photon to collapse its frequency state, which means the second photon must also collapse its spatial state to a specific location. Thus, frequency entanglement also causes spatial entanglement, with the uncertainty of the transverse spatial location of the photons referred to as the second-order transverse spatial correlation or *entanglement area*, A_e.[7] As will be discussed in more detail in later chapters, A_e has historically been assumed to remain constant as the frequency spectrum of the SPDC changes.[7, 9, 23-25] However, work in this dissertation will show that the coupling of frequency and spatial entanglement is essential in properly modelling how entangled photons interact with a molecule. In fact, this coupling can be utilized to enhance the interaction.

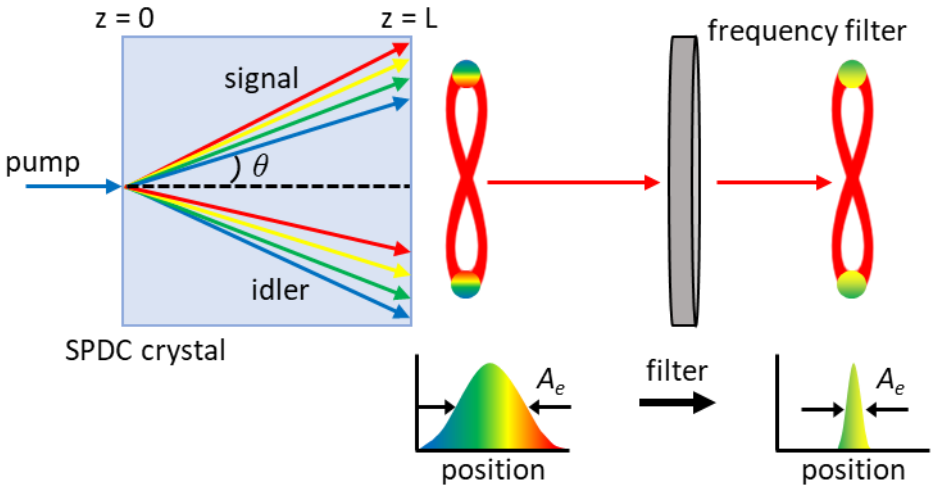

Figure 1.4. Generation and propagation of SPDC highlighting the relationship between the frequency spectrum and transverse spatial correlation.

The transverse spatial distribution of SPDC photons has a characteristic shape that results from the phase-matching conditions. As stated previously, the pump and SPDC photons are phase-matched by properly choosing an angle between the pump beam and optical axis of the crystal. If the pump beam propagates along the z-axis and in the x-z plane, then the emission angle of the SPDC, with respect to the pump beam, in the x-z plane is determined by the wave vector that meets the phase-matching condition. This angle, called the *opening half angle*, is typically labeled as the polar angle θ in spherical coordinates. The azimuthal angle φ, which is the angle in the x-y plane between the x-axis and the SPDC wave vector, is not dependent on

the phase-matching angle determined by the pump beam. As a result, φ can be any value between 0 and 2π. With φ being any value and θ being restricted to one value, the SPDC photons are emitted within a cone. The transverse cross-section then gives a ring. It should be noted that for Type-0/Type-I, where both signal and idler propagate along the ordinary (or extraordinary) ray, both the signal and idler are found within the same cone. They have the same θ but $\varphi_s = \pi + \varphi_i$ to conserve momentum. For Type-II SPDC, the signal and idler are each in one of the ordinary or extraordinary ray. The extraordinary ray does not follow Snell's law, so the ordinary and extraordinary rays propagate in different directions. As a result, SPDC photons emitted into the extraordinary ray form a cone that is different than the cone of SPDC photons in the ordinary ray. As such, Type-II SPDC has two cones, each containing one photon in a pair, and the transverse cross-section is a pair of rings. The angle of the pump beam with the optical axis determines whether these rings overlap in one, two, or zero points. When the two rings overlap, photons found in the overlapping points have polarization entanglement. Individually, the photons are in a superposition of the two polarization states. However, the phase-matching condition requires the photons to be orthogonally polarized. Measuring the polarization of one photon thus collapses the polarization superposition of the second photon as well. For the work in this dissertation that utilized Type-II SPDC, the two rings were made to overlap in two points, so polarization entanglement was present in the experiments.

Non-collinear phase-matching occurs when no SPDC photons propagate along the pump beam path. For Type-0/Type-I, this occurs when the opening half angle is non-zero. For Type-II, this occurs when the two rings intersect at two points. Collinear phase-matching occurs when some or all of the SPDC propagates along the same path as the pump. For Type-0/Type-I, this occurs when the opening half angle is zero. For Type-II, this occurs when the rings intersect at one point. These different phase-matching conditions are shown in Fig. 1.5.

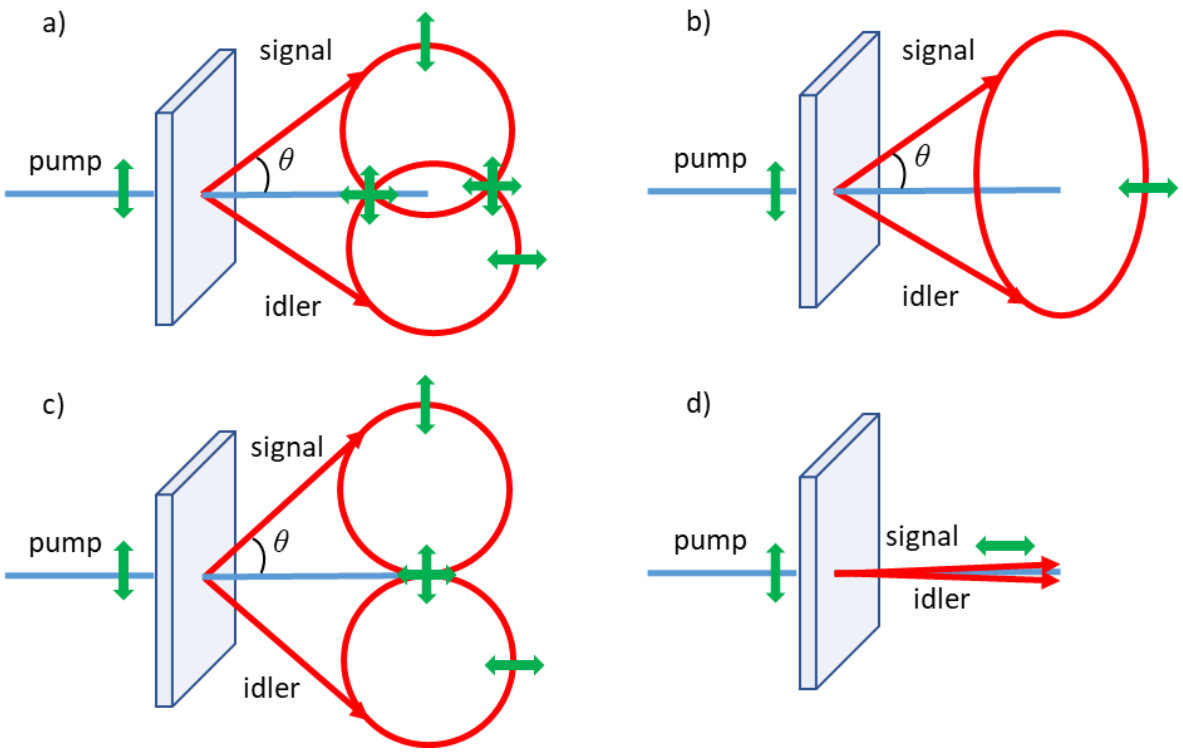

Figure 1.5. a) non-collinear Type-II SPDC spatial distribution; b) non-collinear Type-I SPDC spatial distribution; c) collinear Type-II SPDC spatial distribution; d) collinear Type-I SPDC spatial distribution. Green arrows represent the direction of the polarization. For Type-0 SPDC, the signal/idler polarization arrow is flipped in Type-I SPDC to be parallel to the pump.

1.4.4 Uses and Advantages of Entanglement

By being able to interact with one object and influence the state of another object opens the door for new technology that harnesses this unique ability of entanglement. One of the earliest known advantages of entanglement is that two entangled particles can be separated in time or space and still remain correlated with each other. In 2017, the record for longest open-air distance between two particles while still measuring entanglement between them was set at 1200 km.[26] Entangled photon pairs were generated on a satellite, split from each other, and sent to different receiving stations in China, where correlations between the photons received at each station were observed. This experiment shows the potential for long distance sensing using entangled photon pairs.

Entanglement is also utilized in a quantum sensing technique known as "ghost imaging."[27] In this experiment, one photon from an entangled pair interacts with an object, while the entangled partner does not. Although the second photon does not interact with the object, it reproduces the image of the object because of the photon's correlations with the photon that does interact with the object. Ghost imaging can also be applied to molecular studies, where one photon is sent into a sample to be absorbed while the partner photon remains outside of the sample.[28] The absorption spectrum of the sample can then be measured using the photon that never entered the sample.

Quantum sensing is also concerned with increasing the resolution of measurements beyond the limits of classical mechanics. In classical spectroscopy, today's laser technology can provide frequency resolution as small as a few kHz or time resolution as fast as a few hundreds of attoseconds. The major obstacle with classical spectroscopy is that these resolutions cannot be achieved simultaneously due to the Heisenberg uncertainty principle:

$$\Delta\omega\Delta t \geq \frac{\hbar}{2} \tag{1.32}$$

$\Delta\omega$ (Δt) is the frequency (time) uncertainty, and $\hbar$ is the reduced Planck's constant. Eq. 1.32 shows that as, $\Delta\omega$ gets smaller and the frequency is known with greater certainty, Δt must get larger and the time is known with less certainty. Thus for a classical laser pulse, decreasing the frequency bandwidth increases the temporal width of the pulse, and vice versa when increasing the frequency bandwidth. One may wish to study the energy of a particular excited state in a molecule and how that state evolves in time when it is populated. In a classical spectroscopy experiment, using a very narrow frequency laser pulse allows for high resolution of the energy of the state, but the laser pulse is too broad in time to measure the much faster dynamics of the state after excitation. Using an ultrafast pulse allows for these dynamics to be measured, but now the broad frequency bandwidth excites multiple nearby excited states as well, which can affect the measured dynamics.

Entangled photons provide a means to circumvent the uncertainty principle in spectroscopic measurements.[29] The joint frequency spectrum of the photon pair, shown in Fig. 1.6, defines the probability of the signal having frequency ω_s and the idler having frequency ω_i. There are two spectral widths: $\Delta\omega_+$ defined along the $\omega_+ = \omega_s+\omega_i$ axis, and $\Delta\omega_-$ defined

along the $\omega_- = \omega_s - \omega_i$ axis. $\Delta\omega_+$ is the range of possible summed frequencies of the photon pair, which is defined by the pump laser's spectral width since the photon pair must have a total frequency equal to the pump photon that created them. $\Delta\omega_-$ is the range of possible phase mismatched frequency combinations. There are several combinations of the signal/idler frequencies that can yield the same summed frequency, and $\Delta\omega_-$ defines how many of those combinations the photon pair can have. This width is closely related to the frequency spectrum width of the individual photons. The spectral widths $\Delta\omega_+$ and $\Delta\omega_-$ have Fourier-transformed temporal widths Δt_+ and Δt_-, respectively. Δt_+ is the range of time it takes for the photon pair to be created and arrive together at some point in space. Δt_- is the range of time it takes for the second photon to arrive at some point in space after the first photon arrived at that same point, i.e. Δt_- is the entanglement time, or T_e.

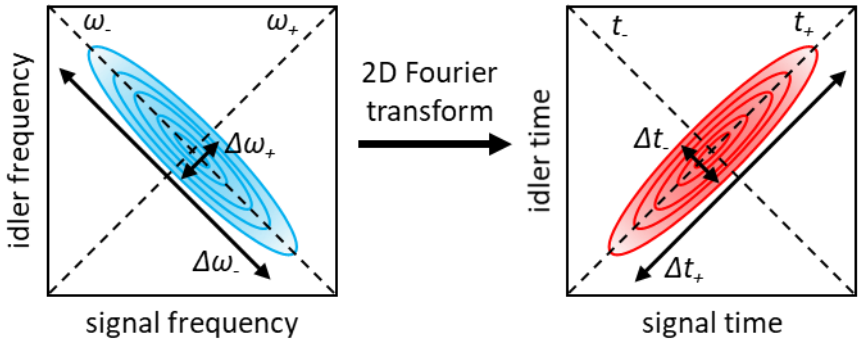

Figure 1.6. Joint frequency spectrum of entangled photon pairs and its 2D Fourier transform into the time domain.

When using an entangled photon pair to excite a molecule, the frequency resolution is determined by $\Delta\omega_+$ since the energy of the state that is excited is the energy of the total photon pair frequency. The temporal resolution is determined by Δt_- (T_e) since the delay between the two interactions with the molecule is the delay between the two photons' arrivals. Since $\Delta\omega_+$ and Δt_- are not Fourier conjugates, they do not limit each other. Both can be small at the same time, and the inequality in eq. 1.32 does not apply. Entangled photons thus provide a means for quantum metrology that can probe molecules beyond the limits of classical mechanics. It is possible to excite a specific excited state with extremely narrow energy precision while also monitoring the dynamics of the state upon excitation. Classical spectroscopy can do one or the other but not both at the same time.

1.4.5 Schmidt Decomposition

As explained, the initial two-photon state of entangled photon pairs is a superposition of many frequency pairs. Once the first photon interacts with an object, it is usually said for simplicity that the photon's frequency collapses to a single value and so does the second photon's frequency. This picture is a bit oversimplified since the photons' frequencies do not collapse to single values of monochromatic light. Rather, the superposition for each photon collapses to a single frequency state, which is still a probability amplitude for one or more frequencies. To understand exactly what a molecule is interacting with when exciting it with entangled photons, one must look at the frequency states that comprise the frequency entangled photons, not just the range of individual frequencies.

The joint frequency spectrum of entangled photons is most simply represented as a double Gaussian in the basis of the frequency states of $\omega_+ = \omega_s + \omega_i$ and $\omega_- = \omega_s - \omega_i$:[30, 31]

$$\Psi(\omega_+, \omega_-) \approx \frac{1}{\sqrt{2\pi\sigma_{\omega_+}\sigma_{\omega_-}}} exp\left[\frac{-\omega_+^2}{4\sigma_{\omega_+}^2}\right] exp\left[\frac{-\omega_-^2}{4\sigma_{\omega_-}^2}\right] \quad (1.33)$$

The widths of the Gaussians are given by $\sigma_{\omega+(-)}$. In this form, the frequencies of the photons are clearly linked, but the frequency states of the signal and idler are not clear. The joint frequency spectrum can instead be written in the eigenbasis of the signal and idler frequency states through the *Schmidt decomposition*:[32]

$$\Psi(\omega_s, \omega_i) = \sum_{n=1}^{n_{max}} \sqrt{\lambda_n}\psi_n(\omega_s)\phi_n(\omega_i) \quad (1.34)$$

In this form, the signal photon is in state ψ_n, and the idler photon is in state φ_n. If $n_{max} > 1$, then there is a superposition of frequency state pairs, and neither photon can be identified as being in a specific state without knowing the state of the other. In other words, if $n_{max} > 1$, the photons are entangled. For example, if $n_{max} = 2$, then before any interaction takes place, the photon pair is in a superposition of the $\psi_1\varphi_1$ and $\psi_2\varphi_2$ pairs of states. If the signal photon collapses to the state ψ_1 after an interaction, then the idler photon must also collapse to state φ_1. Here it is clearly seen what the frequency state of each individual photon is upon interaction with an object. Typically, the Laguerre-Gaussian or Hermite-Gaussian bases are used to define these states. Each of these pairs of states is referred to as a *Schmidt mode*. The probabilities that the photons collapse to each pair of states are λ_n. As coefficients for the Schmidt modes, the square

roots of λ_n are the *Schmidt coefficients*. The first three Schmidt modes of a typical SPDC joint frequency spectrum is shown in Fig. 1.7.

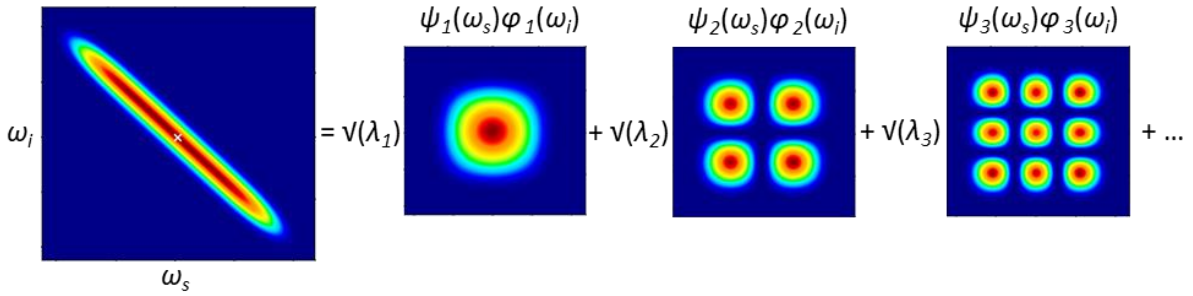

Figure 1.7. Schmidt decomposition of the joint frequency spectrum of SPDC showing the first 3 Schmidt modes.

Not only does the Schmidt decomposition more clearly show what a molecule perceives when interacting with an entangled photon pair, it is also convenient for quantifying "how entangled" the photons are. If multiple Schmidt modes have non-zero coefficients, then the photon pair is in a superposition of frequency states. It also becomes impossible to define the frequency state of one of the photons separate from the other. Therefore, the more non-zero Schmidt coefficients there are, the higher the degree of entanglement. If there is only one non-zero Schmidt mode, i.e. $n_{max} = 1$, then the signal has a defined frequency state and so does the idler. Neither photon's frequency state is dependent upon the other photon. These photons are not entangled.

Depending on the distribution of non-zero Schmidt coefficients, the coefficients may trend toward zero without ever reaching zero. The only restriction is that the sum of the coefficients squared must equal 1, since the photon pair must be in one of the Schmidt modes upon collapse. For example, the Schmidt coefficients may follow a Gaussian distribution, which never decreases to exactly zero. For this reason, the number of effective occupied Schmidt modes can be defined by the *Schmidt number*, K:[33]

$$K = \left(\sum_n^{n_{max}} \lambda_n^2\right)^{-1} \tag{1.35}$$

The value of K reveals that number of Schmidt modes that play a significant part of the frequency superposition. $K = 1$ for a classical pair of photons, and $K > 1$ for entangled pairs, with K increasing with the degree of entanglement. The degree of entanglement is sometimes

also quantified through the entanglement entropy, E, which is related to the von Neumann entropy:[30]

$$E = -\sum_{n}^{n_{max}} \lambda_n \log_2 \lambda_n \tag{1.36}$$

E = 0 for a classical pair of photons. E > 1 for entangled photons, with E increasing with the degree of entanglement.

1.5 Classical Two-Photon Absorption

The nonlinear optical processes described in the previous sections occur when the first excited electronic state of the media is far from resonance with the incident light field (or two photons within the incident light field). Other nonlinear processes occur when there is an excited state near resonance with two (or more) photons in the light field. One of the earliest known processes, and the most relevant to this dissertation, is *two-photon absorption* (TPA), shown in Fig. 1.8, first predicted by Maria Goeppert-Mayer in 1931.[34] Similar to SHG, in TPA, a polarization is created in a molecule, and the polarization includes an oscillation component at twice the frequency of the incident field. If the molecule has an excited state with energy close to resonance with the polarization, the molecule can absorb two photons from the field and use the energy to be excited from the ground to the excited state. After the absorption takes place, the non-stationary excited state can evolve dynamically until it relaxes back to the ground state. If the energy is released through a fluorescent photon, the process is known as *two-photon excited fluorescence* (TPEF).

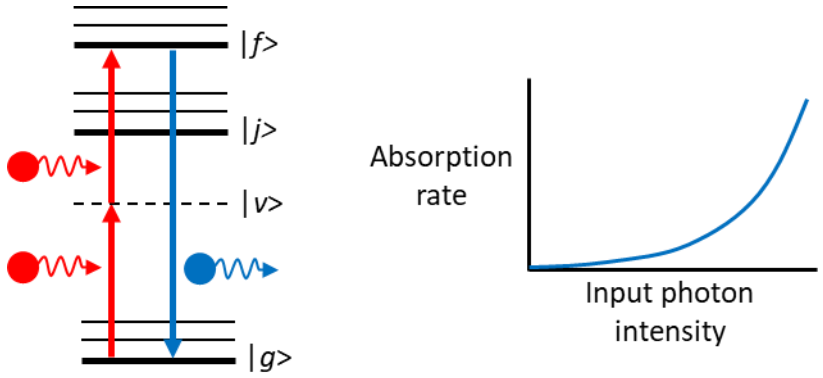

Figure 1.8. Classical TPA and fluorescence energy level diagram and absorption rate vs input photon intensity. *g*, *v*, *j*, and *f* are the ground, virtual, intermediate, and final states, respectively.

A three-level system is typically used to model TPA. The initial state of the molecule is typically assumed to be the ground state, and the two-photon excited state is labelled the final state. The third state, known as the intermediate state, is between the ground and final state. It is important to clarify that the intermediate state is not always excited during the TPA transition. In the special case where an intermediate state happens to be resonant with the first absorbed photon, TPA can then be modelled as two distinct absorption events: one exciting the molecule from the ground to intermediate state, and a second exciting the molecule from the intermediate to final state. This process is commonly called *two-step excitation* (TSE).

In most cases, the intermediate state is not near resonance with the first absorbed photon. In this case, TPA occurs through a *virtual state* acting as an intermediate. A virtual state is an extremely short-lived state that is not an energy eigenstate of the molecule. The virtual state is only formed in the presence of the light field and can be modelled as a superposition of the ground and excited eigenstates in the molecule. Because this superposition of states has a very broad energy range, it must be extremely short lived. Since the virtual state is a superposition of the eigenstates in the molecule, it takes on some character of those states, most notably the *transition dipole moments* (TDMs). TDMs are a quantification of the selection rules when considering whether a transition from one quantum state to another is allowed. TDM = 0 is a forbidden transition, and a non-zero TDM increases as the transition becomes allowed and more favorable. Excited states that can be excited with TPA are typically forbidden via a single transition. Instead, the first photon creates a coupling between the ground and virtual state, and the second photon creates a coupling between the virtual and final state, completing the TPA transition. In the superposition defining the virtual state, the coefficient for each state is proportional to the product of the TDMs between the ground-intermediate and intermediate-final states. As this product increases for a particular intermediate state, the virtual state takes on more character of that state. The superposition coefficients are also inversely proportional to the energy difference between the intermediate state and first photon, called the *detuning energy*. As this detuning energy decreases for a particular intermediate state, the virtual state takes on more character of that state.

The most distinct signature of TPA is the quadratic increase of the excitation rate vs input photon intensity.[35] For any absorption process, be it one- or two-photon, the rate of excitation is proportional to the probability of the necessary photon(s) being present. For one-photon absorption

(OPA), only one photon is needed, so the excitation rate is proportional to the intensity of the input light field. For TPA, the excitation rate is proportional to the probability of the first photon being present AND the second photon being present. So, the excitation rate is proportional to the intensity of the first light field times the intensity of the second light field. If both photons come from the same light field, the TPA rate is proportional to the intensity of the input field squared. Thus, as the intensity of the light field increases, the TPA rate increases quadratically. At low input intensities, the TPA rate is very low, and absorption/fluorescence signals are very small. At high intensities, the TPA rate increases very quickly, yielding very large absorption/fluorescence signals. Typically, measurable TPA signals are only obtained when using a focused pulsed laser beam since the peak intensity of the pulses provides a strong enough instantaneous intensity.

The probability that a molecule will undergo TPA to a particular excited state is quantified with the TPA *cross-section*, δ_r. Using a three-level system model for TPA, the cross-section is calculated using standard second-order perturbation theory as:[36]

$$\delta_r = \frac{B}{\hbar^2 \varepsilon_0^2} \omega_0^2 \delta(\varepsilon_f - \varepsilon_g - 2\omega_0) \times \left| \sum_j \frac{1}{(\omega_0 + \varepsilon_g - \varepsilon_j) - \frac{i\kappa_j}{2}} \mu_{fj} \cdot e \mu_{jg} \cdot e + \frac{1}{\omega_0 - \frac{i\kappa_g}{2}} \mu_{fg} \cdot e \mu_{gg} \cdot e + \frac{1}{-\omega_0 - i\kappa_f/2} \mu_{ff} \cdot e \mu_{fg} \cdot e \right|^2 \tag{1.37}$$

In eq. 1.37, the molecule's ground, intermediate, and final states have energies ε_g, ε_j, and ε_f with Lorentzian-broadened linewidths κ_g, κ_j, and κ_f, respectively. The TDM for the *j*-to-*k* transition is μ_{jk}, and the permanent dipole moment for the *j* state is μ_{jj}. The polarization of the SPDC photons are represented with the vector *e*. The photons are assumed to have degenerate frequency ω_0. A monochromatic light field is assumed. The TPA cross-section is expressed in units of cm^4s/photon/molecule, though often the units are expressed in GM, where 1 GM = 10^{-50} cm^4s/photon/molecule. The larger the cross-section, the higher the probability of the molecule undergoing TPA.

There are advantages for TPA compared to OPA. As mentioned, the symmetry of some excited states makes an OPA transition from the ground to this excited state forbidden. TPA can then be used to excite and probe this state.[37] As mentioned, high input intensities are required to obtain a measurable TPA signal due to the quadratic scaling of the TPA rate. Such high intensities only occur at the focal point of a focused pulsed laser beam, so in a bulk sample, TPA only occurs

at the focal point. This contrasts OPA, which can occur anywhere the light passes through the bulk sample. By limiting excitations to only the focal point, TPA offers greatly enhanced spatial resolution compared to OPA. This is particularly beneficial for using a microscope with TPA excitation since fluorescence will only occur at the focal point, which can be diffraction limited. Additionally, TPA uses lower frequency light fields than OPA since the light field should only be half of the frequency of the total transition. As energy increases, the density of excited states in molecules increases, making higher frequencies more likely to be absorbed than lower frequencies. Additionally, higher frequencies are more likely to be scattered. For both of these reasons, lower frequencies can penetrate deeper into solid samples to excite the target molecule. This gives TPA excitation more depth control than OPA excitation.

TPA also comes with disadvantages. While the need for high intensities helps improve the spatial resolution, it also comes with a catch. For many molecular samples, particularly photosensitive biological samples, the peak intensity of focused pulsed lasers damages the sample.[38] There can be a fine line between obtaining enough signal to effectively probe the sample and not damaging the sample, and sometimes an effective compromise cannot be found. Additionally, the need for laser pulses inherently decreases the frequency resolution of the experiment since a broad frequency superposition must be formed to create the laser pulses. It is also worth noting that pulsed laser systems are much larger, heavier, costlier, more temperamental, and require more expertise to operate than continuous-wave (CW) lasers. Most chemists would not have the access or experience to use these pulsed lasers in their labs.

1.6 Entangled Photon Spectroscopy

1.6.1 Entangled Two-Photon Absorption

Entangled photon pairs can also be used to excite a two-photon transition through the process of *entangled two-photon absorption* (ETPA), shown in Fig. 1.9.[39] In ETPA, the two absorbed photons are entangled with each other, which ensures that the two absorption events within the molecule are correlated with each other. In classical TPA, the two photons are not correlated with each other and so neither are the two absorption events. In this context, classical TPA is sometimes referred to as random TPA since the molecule randomly chooses two photons to absorb. The quantum correlated vs random nature of the two-photon transition for ETPA vs classical TPA, respectively, leads to significant differences in the defining features

of the two absorption processes. These differences allow ETPA to overcome the disadvantages of classical TPA and to obtain new information about molecules that classical TPA cannot reveal.

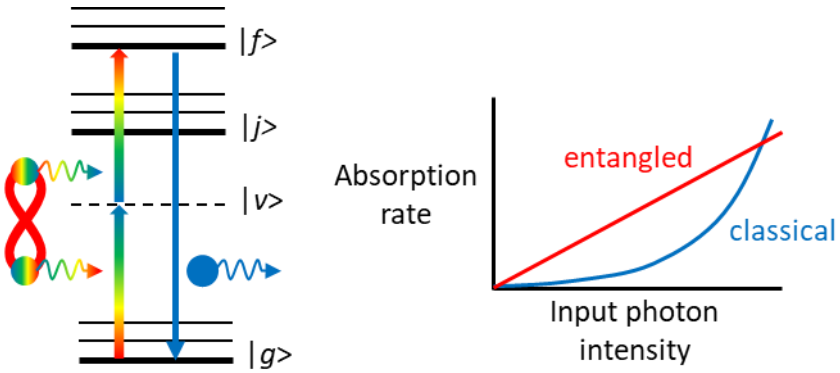

Figure 1.9. ETPA and fluorescence energy level diagram with absorption rate vs input photon intensity compared ETPA and classical TPA.

While ETPA has many remarkably different properties than classical TPA, there are a few aspects of their mechanism that are similar since both are two-photon transitions. Similar to classical TPA, the first photon establishes a coupling between the ground and virtual states, and the second photon establishes a coupling between the virtual and final state. The virtual state, which is not an eigenstate and only exists in the presence of the entangled light field, can be expressed as a superposition of the ground and excited eigenstates in the molecule. The stronger an intermediate state's TDM product for the ground-intermediate and intermediate-final transitions, the more the virtual state takes on the character of that state. Additionally, the closer an intermediate state is to the first photon energy, the more the virtual state takes on the character of that state. The energy difference between the intermediate *j* state and first photon is called the detuning energy, Δ_j. In special cases where an intermediate state is resonant with the first photon ($\Delta_j = 0$), the intermediate state would be directly excited as part of the process of *entangled two-step excitation* (ETSE).[40]

Although the energy level diagram for ETPA and classical TPA may look similar, the different correlations (or lack thereof) for ETPA vs classical TPA make the dynamics of the two processes strikingly different. For classical TPA, the transition probability is proportional to the probability of absorbing a first photon times the probability of absorbing a second photon. Since the two photons are absorbed at random, there is no guarantee that the second

photon will be present and get absorbed before the virtual state decays to the ground state. Taking a similar probabilistic approach, the ETPA cross-section, σ_e, would be viewed as similar to a random TPA transition, but with the temporal delay and spatial uncertainties more well defined by T_e and A_e, respectively. The probabilistic model for ETPA then states:[7]

$$\sigma_e = \frac{\delta_r}{A_e T_e} \tag{1.38}$$

However, for ETPA, temporal entanglement guarantees that the second photon will arrive within the time window set by T_e (assuming no additional delay has been applied to the second photon), so the second photon will always be present before the virtual state decays.[41] This correlation is represented mathematically with the g^2 function:

$$g^2(t) = \frac{\langle I_s(t) I_i(t)\rangle}{\langle I_s(t)\rangle\langle I_i(t)\rangle} = \frac{2}{\langle I_{SPDC}(t)\rangle} \tag{1.39}$$

$I_{s(i)}$ is the intensity of the signal (idler) beam, and I_{SPDC} is the intensity of the photon pairs. Since the probability of detecting a pair of entangled photons equals the probability of detecting one of the photons in the pair, all these intensities are equal, leading to the second equality in eq. 1.39. For classical coherent states of light:

$$g^2(t) = \frac{\langle I_A(t) I_B(t)\rangle}{\langle I_A(t)\rangle\langle I_B(t)\rangle} = \frac{\langle I_A(t)\rangle\langle I_B(t)\rangle}{\langle I_A(t)\rangle\langle I_B(t)\rangle} = 1 \tag{1.40}$$

The temporal correlation of entangled photons causes the two absorption events to be correlated so that the probability of the ETPA transition is not simply proportional to the product of the two absorption events occurring. Rather, there is an interference between the two absorption events which can enhance the ETPA cross-section to be greater than a simple probabilistic estimate. This interference is seen in the ETPA cross-section, σ_e, derived from standard second-order perturbation theory:[7, 23]

$$\sigma_e = \frac{A}{\hbar^2 \varepsilon_0^2 A_e T_e} \omega_0^2 \delta\left(\varepsilon_f - \varepsilon_g - 2\omega_0\right) \times \left| \frac{\frac{1-e^{-i\left(\omega_0+\varepsilon_g-\varepsilon_j\right)T_e-\frac{\kappa_j T_e}{2}}}{\left(\omega_0+\varepsilon_g-\varepsilon_j\right)-\frac{i\kappa_e}{2}} \mu_{fj}\cdot e_i \mu_{jg}\cdot e_s + \frac{1-e^{-i\omega_0 T_e-\kappa_g T_e/2}}{\omega_0-i\kappa_g/2} \mu_{fg}\cdot e_i \mu_{gg}\cdot e_s + \frac{1-e^{i\omega_0 T_e-\kappa_f T_e/2}}{-\omega_0-i\kappa_f/2} \mu_{ff}\cdot e_i \mu_{fg}\cdot e_s \right|^2 \tag{1.41}$$

This equation for the ETPA cross-section is similar to the classical TPA cross-section equation except for a few key factors. First, the constants out front show that σ_e is inversely proportional to A_e and T_e. Additionally, the complex exponentials in the modulus squared term are the interference factors between the two ETPA absorption events. These terms oscillate as a function of T_e, allowing the cross-section to be larger than the probabilistic estimate at certain T_e and smaller at other T_e. The enhanced cross-sections can be used to increase ETPA signals in weak absorbing excited states, and the decreased cross-sections can be used to turn off ETPA signals from unwanted states that provide noise in an experiment. ETPA-based sensors can utilize the selective nature of the constructive and destructive interference to turn the ETPA signal on and off without having to change the molecule itself or the wavelength or intensity of the light source.

The modulus squared factor in eq. 1.41 contains three terms. The first term is known as the *virtual state pathway*. Here, the first photon creates a coupling between the ground and virtual state, and the second photon creates a coupling between the virtual and final state. The TDMs determine the strength of these couplings. The second and third terms are known as the *permanent dipole pathways*. Here, the photon pair uses the direct coupling between the ground and final state to excite the molecule, with the strength of the transition also being determined by the strength of the permanent dipole moment of the ground (second term) or final state (third term). All of these pathways in the molecule compete with each other in the presence of the light field. This competition is analyzed in greater detail in subsequent chapters.

1.6.2 Advantages and Literature on ETPA

One of the earliest predicted hallmarks of ETPA was a linear excitation rate vs input photon intensity, even though ETPA is a two-photon process.[10] As stated previously, the absorption probability is proportional to the probability of the necessary photons being present. SPDC photons are guaranteed to exist in pairs from the Hamiltonian operator containing two creation operators.[42] When the first photon is present, the probability of the second photon being present is 1. Thus, the probability of both photons being present for the ETPA absorption is equal to the probability of the first photon being present, and the ETPA rate scales linearly with the input photon intensity. While the absorption of two entangled photons is linear, there is no guarantee that the molecule will always absorb two photons that form an entangled pair.

As the intensity of the SPDC photon beam increases, individual pairs are emitted closer and closer to each other in time. This increases the probability that the molecule will absorb one photon from one pair and then absorb a photon from a second pair arriving slightly later, if the time it takes for a second pair to arrive is comparable to T_e of the first pair. This scenario would be a classical TPA and would scale quadratically. To account for this competing process, the total TPA rate, R_{TPA}, is expressed as:[7, 10]

$$R_{TPA} = \sigma_e \Phi + \delta_r \Phi^2 \tag{1.42}$$

The input photon intensity is Φ. At very low intensity, the quadratic classical TPA term is negligible, so only ETPA is observed. The two processes become equally probable at the so-called critical flux, $\Phi = \sigma_e/\delta_r$. Above this flux, the measured TPA is quadratic since the second term will dominate. For this reason, ETPA experiments are always conducted below the critical flux.

The linear ETPA rate and transition to a quadratic dependence has been confirmed experimentally. Georgiades et. al. used a squeezed vacuum source of photon pairs, which have similar entanglement properties as SPDC pairs, to excite atomic cesium and measured the resulting fluorescence.[12] They obtained a fluorescence rate that included both linear and quadratic terms vs the input photon intensity. Lee et. al. later observed the linear ETPA, and transition to quadratic, in an organic chromophore solution using Type-II SPDC.[11]

The linear excitation rate of ETPA is advantageous in overcoming one of the major problems with classical TPA. Classical TPA is only observable with high intensities because the quadratic TPA rate makes the signal too small to measure at low intensities. At these low intensities, ETPA significantly enhances the TPA rate with its linear scaling (Fig. 1.9), allowing TPA to be measured at extremely small input intensities that have no risk of damaging a sample. The work from Lee et. al. observed ETPA using less than 10^7 photons/s. A study from Harpham et. al. compared the input photon intensities needed to measure ETPA and classical TPA.[43] While classical TPA required 10^{22} photons/s/cm^2, ETPA only required 10^{12} photons/s/cm^2, a ten orders of magnitude difference. Linear fluorescence intensity vs input photon intensity has also been experimentally confirmed.[44, 45]

Another advantage for ETPA comes with the new control knobs that entangled photons offer to modify the excitation of molecules. One of the earliest known control parameters is T_e. The complex exponential interference term between the two absorption events creates a sinusoidal transition probability as a function of T_e. By changing T_e, the ETPA cross-section can change by orders of magnitude, allowing one to turn the absorption signal on and off at will. The sinusoidal trend also gives unique control and information about the intermediate states involved in ETPA. The Fourier transform of the ETPA cross-section vs T_e reveals the frequencies of the different intermediate states that contribute to the formation of the virtual state.[9] This technique, known as *virtual state spectroscopy*, can identify intermediate states that may have too low oscillator strength to be excited directly and identified using linear absorption spectroscopy. Each of these intermediate state pathways in ETPA oscillate at a different frequency, determined by the detuning energy of that intermediate state with the first photon. With the energies of the intermediate states known, T_e can be tuned to turn off ETPA transitions involving undesired intermediate states and/or turn on ETPA transitions involving a specific, desired intermediate state. This would be a new form of control over the pathway of nonlinear transitions that classical spectroscopy does not offer.

It is important to note that T_e is not inherently a delay between the signal and idler photon wavepackets. For Type-II SPDC, the different polarizations of the photons cause them to propagate inside the SPDC crystal at different speeds because of the different refractive indices they experience. They will then have a delay when they exit the crystal, and this delay is the same magnitude as T_e. This delay can then be changed outside the crystal, by sending one photon through a delay line or birefringent prism, but T_e still remains the same as it originally was. This external delay of the entangled photons is often represented as τ. For Type-I SPDC, the photons leave the crystal with no delay because they have the same polarization. The external delay τ can then be changed outside the crystal. When taking τ into account in the ETPA cross-section, the complex exponential $e^{i\Delta jTe}$ is replaced with $e^{i\Delta jTe+\tau}+ e^{i\Delta jTe-\tau}$.[9] Changing τ can also be used to control the sinusoidal transition probability of ETPA. This has been confirmed experimentally as well, for both ETPA and ETPA-induced fluorescence.[11, 45-47] For the entangled twin state in eq. 1.31 used in calculating the ETPA cross-section, the SPDC photons have a rectangular temporal correlation function with width T_e. Thus, the delay τ cannot exceed T_e or else the photons are no longer temporally correlated, and ETPA cannot

occur. SPDC can also have a Gaussian temporal correlation function when the frequency spectrum is filtered with a Gaussian filter. In this case, the ETPA probability vs τ is Gaussian centered at $\tau = 0$ and with width T_e.

Another unique control parameter of ETPA is the spatial profile of the phase-matching condition. The effect of the phase-matching condition on ETPA using Type-II SPDC has been explored. It was shown that more overlap between the rings increases the ETPA cross-section, with no overlap at all yielding the weakest ETPA.[48] The explanation was that the ETPA cross-section may be proportional to the degree of distinguishability of the entangled photons. When the two SPDC cones overlap, the photons at the intersection(s) are indistinguishable since the polarization of the photons are superpositions of both possible states. Two overlapping points has more indistinguishability than one overlapping does, and no overlapping points has the least. This is the same trend observed for the ETPA cross-section. The effect of phase-matching on ETPA using Type-I SPDC has been explored in a later chapter of this dissertation.

Whether ETPA follows the same selection rules as classical TPA is still an open question. While the same TDMs are assumed in both derived cross-section equations, experiments have shown that the trend in classical TPA cross-sections for a group of molecules does not necessarily match the same group's trend in ETPA cross-sections.[44] Additionally, these experiments have shown that some molecules can have small classical TPA cross-sections but relatively large ETPA cross-sections. Other molecules have large classical TPA cross-sections but very small ETPA cross-sections.

More recent work on ETPA has focused on the variety of molecular systems that can be probed by entangled photons. A group of thienoacene chromophores with varying degrees of dipolar and quadrupolar character have been analyzed with ETPA.[47] It was found that the dipolar molecule, the only one with a permanent dipole moment, received an enhancement in its ETPA cross-section compared to its classical TPA cross-section. It was thus suggested that access to the permanent dipole pathway for the dipolar molecule provided this enhancement. ETPA has also been used to probe flavin chromophores in free solution and embedded in protein environments.[49] Results showed an increase in the ETPA cross-section for the flavin chromophores when they were embedded in protein environments. More interestingly, this enhancement in the cross-section was not found for classical TPA excitation, suggesting that

ETPA is a new tool to probe biological environments with more sensitivity than classical spectroscopy.

ETPA excitation is now being incorporated into microscopy experiments. The first microscope using ETPA excitation was used to obtain images of aggregates of a bis(styryl)benzene derivative.[46] ETPA excitation required 6 orders of magnitude lower input photon intensity compared to classical TPA excitation. The oscillations of ETPA vs τ were also observed.

There are several other promising theoretical proposals for using entangled photons to probe molecules for chemistry applications. Several reviews have been written on this topic.[50-52] Some highlights of these proposals include: 2D spectroscopy that eliminates background signal from uncorrelated processes[53]; enhancement in resonance energy transfer[54]; exciting dark states in cavity polaritons[55]; virtual-state spectroscopy without *a priori* knowledge of the molecule's excited states[56]; suppressing population transfer in the intermediate state of an exciton[57]; higher selectivity of double-exciton states in photosynthetic complexes[58]; stimulated Raman and pump-probe spectroscopy with simultaneous high frequency and time resolution[59, 60].

While these proposals are exciting, there are currently some obstacles and open questions regarding ETPA that is limiting their implementation. As mentioned, the selection rules that apply to ETPA transitions, particularly with how they compare to OPA and classical TPA selection rules, remains an open research question. It is also unknown how the excited state properties after ETPA excitation compare to using OPA or classical TPA excitation. While the ETPA cross-section is significantly larger than what would be expected from classical probabilistic theory, the ETPA cross-section is typically smaller than OPA cross-sections by a few orders of magnitude. The relatively smaller cross-sections with ETPA results in small absorption and fluorescence signals in experiments. These small signals require longer collection times. Finding ways to enhance ETPA cross-sections would benefit development of ETPA-induced fluorescence and microscopy applications greatly. It would also allow chemists to study the nonlinear properties of excited states with the same efficiency as studying linear absorption properties. Finally, due to the low efficiency of generating SPDC photon pairs, ETPA experiments have historically used pulsed lasers to create the SPDC. These experimental

setups make ETPA less accessible for chemists and biologists due to lack of expertise in nonlinear spectroscopy and quantum optics as well as size and cost restraints.

1.7 Overview of Remaining Chapters

The work completed in this dissertation seeks to develop ETPA specifically for its applications in chemistry research. The challenges and open questions that have been mentioned were studied in great detail, including: how chemical structure affects the transition pathways taken during ETPA, which helps to address the ETPA selection rules; how the excited state linewidth after ETPA excitation compares to classical TPA excitation, which relates to the unique excited state dynamics induced by ETPA; how to make ETPA experiments more accessible to chemists and improve the signal-to-noise ratio; how to increase the ETPA cross-section to make it more comparable to OPA cross-sections. A variety of molecular systems have been explored, some for the first time ever with entangled photons, ranging from small diatomic molecules to larger organic chromophores. This wide range of molecular systems explored speaks to the versatility of ETPA as a valuable tool for chemists.

Chapter 2 explains the methods, both experimental and theoretical, used throughout this dissertation. The experimental methods included the linear spectroscopic techniques of UV-vis absorption, fluorescence, and Raman spectroscopy and the nonlinear laser spectroscopic techniques of ETPA and classical TPA. The details regarding the experimental setups and how data was obtained is explained in this chapter. Theoretical methods provided by the help of collaborators included the novel electronic structure techniques of multi-reference configuration interaction (MRCI) with state-averaged complete active space self-consistent field (SA-CASSCF) to define the reference states and second linear response (SLR) time-dependent density functional theory (TDDFT).

Chapter 3 used a theoretical approach to examine how molecular structure affects the transition pathways taken during ETPA transitions. While prior literature has shown how the ETPA cross-section oscillates vs T_e, referred to as *non-monotonic behavior*, these previous works have focused mostly on the unique physics of entangled photons that give rise to these oscillations. It remained unclear how the structure of the molecule affects the observed oscillation pattern. This information would be useful so that molecules can be designed to optimize the oscillation pattern for a given application. For example, the orders of magnitude drops in the cross-section, known as

entanglement-induced transparencies, can be utilized in making ETPA-based sensors. A current challenge with developing such a sensor is that the oscillations observed thus far are on an ultrafast time-scale, making resolution of the cross-section maxima vs minima difficult. If molecular structure can be optimized to increase the period between the transparencies, the development of these ETPA sensors would become much more achievable. Additionally, learning how molecular structure correlates to the ETPA oscillation pattern would provide insight into the selection rules for ETPA. Each pathway in ETPA oscillates at its own frequency, with the strength of each pathway in the linear combination of pathways being determined by its TDMs with the ground and final states. These TDMs are directly related to the selection rules for optical transitions.

To complete this study, the ETPA cross-section was calculated vs T_e for a group of molecules with varying dipole properties. To calculate ETPA cross-sections, some information about the molecule must be known, including the energies and TDMs for the ground and several excited states. The accuracy of this molecular information directly impacts the accuracy of the ETPA calculations, so the high accuracy method of MRCI with SA-CASSCF was used to calculate these molecular parameters by collaborators from the Zimmerman group at the University of Michigan chemistry department. In particular, the calculation of the TDM between two excited states is difficult, but MRCI can complete this calculation very accurately. Since this theoretical method would be too computationally intensive to use large chromophores that are studied experimentally, diatomic molecules were used instead. These diatomic molecules also provided the advantage of being able to clearly define and vary the dipole character of the molecules. Nitric oxide (NO) was chosen as a molecule with a weak but non-zero permanent dipole moment. Hydrogen fluoride (HF) provided a strong permanent dipole moment. Dinitrogen (N_2) lacked a permanent dipole completely. To compare with prior literature, hydroxide (OH) was also studied.

The ETPA calculations showed a clear difference between the molecules that had a permanent dipole vs N_2 which did not. First, N_2 had a larger period between entanglement-induced transparencies. Additionally, the maxima in the cross-section for N_2 were 3-4 orders of magnitude larger than the cross-sections predicted from a classical probabilistic model, whereas the permanent dipole molecules had maxima within 1 order of magnitude of the probabilistic prediction. These results suggest that the virtual state pathway allows for more quantum behavior in the ETPA transition, meaning that intermediate states can interfere with each other to both

enhance the ETPA transition probability and increase the period between transparencies. Permanent dipole pathways lack this interference and lead to more "classical-like" behavior. It is clear then that for the application of ETPA sensors, molecules should be designed with strong virtual state pathways and weak or non-existent permanent dipole pathways. With regard to the selection rules for ETPA, it appears that molecules prefer to use the permanent dipole pathway if it exists. However, if the virtual state pathway can be enhanced by designing molecules with smaller detuning energies or larger TDMs, perhaps the permanent dipole pathway can be overcome.

Chapter 4 builds upon the work in chapter 3, extending the accurate calculation of ETPA cross-sections to larger organic chromophores that are used in experiments. This work also explores how the lineshape of the ETPA transition compares to that of classical TPA. The lineshape is an important insight into the excited state dynamics that are induced by a particular optical transition. The lineshape for ETPA has previously been assumed to match that of classical TPA. However, if the lineshape differs, this information is crucial for understanding how ETPA can be used to probe excited state dynamics and for designing molecules that can optimize the ETPA lineshape to enhance ETPA cross-sections.

Similar to chapter 3, molecular parameters needed to be calculated first in order to then calculate the ETPA cross-section. A pair of thiophene dendrimers that had previously been studied experimentally with ETPA were the molecules examined in this theoretical work. Development of SLR-TDDFT allowed the energies and TDMs of the molecules' ground and excited states to be calculated with much greater computational efficiency compared to other methods. The lineshape of ETPA was derived as well. The temporal entanglement and time-ordering of the SPDC photon pair yielded a different lineshape for ETPA than that of classical TPA. Specifically, the lineshape was significantly more narrow, defined by the spontaneous radiative lifetime of the final state.

Calculations of the ETPA cross-sections, performed by collaborators in the Schatz group at Northwestern University chemistry department, using the molecular parameters once again showed the expected oscillations vs T_e. The calculated cross-sections agreed with the experimentally measured cross-section to within a factor of 1.3, but only when the newly derived narrow lineshape for ETPA was used. Using the same lineshape as classical TPA, the calculated cross-sections were orders of magnitude smaller than the experimental values. These results show

that ETPA excitation induces unique dynamics for the final excited state. Additionally, the narrow lineshape enhances the ETPA cross-section compared to the classical TPA lineshape. This result encourages further study into how molecular structure can be designed to narrow ETPA lineshapes to enhance their cross-sections.

Chapter 5 highlights experimental work regarding a biological molecular system that has not before been explored with entangled photons. The interaction between entangled photons and halogenated anesthetic ethers was compared to that of weaker anesthetic ethers. The mechanism that anesthetic molecules take to induce temporary unconsciousness remains unknown. Theories based on classical physics and chemistry have attempted to explain the mechanism for decades, but the question remained unclear. As a result, new theories involving quantum mechanisms have been proposed. If the mechanism were quantum-based, then the anesthetic molecules would have to be sensitive to quantum objects and interact with them through a quantum mechanism. To date, no experiment had shown whether anesthetic molecules have this sensitivity. The work in this chapter was a proof-of-principle experiment to determine if some anesthetic molecules have the ability to interact with quantum objects, in this case the entangled photons.

The experiment consisted of measuring the transmission of entangled photons through two halogenated, strong anesthetic ethers sevoflurane (SEVO) and isoflurane (ISO). Compared to a solvent (methanol) that is known to be transparent to the entangled photons, both SEVO and ISO reduced the transmission of the entangled photons. Neither SEVO nor ISO showed sensitivity to classical photons at the same wavelength, even with much higher input photon intensities than that used for the entangled photon experiments. For comparison, the non-halogenated, weaker anesthetic diethyl ether showed no sensitivity to the entangled or classical photons. Linear absorption, fluorescence, and Raman spectroscopy was used to try to determine the mechanism that caused the entangled photon transmission to be reduced in SEVO and ISO. Electronic structure calculations were also completed. The results showed that no excited state is expected to be near the one- or two-photon resonance of the entangled photons, so OPA and ETPA was likely not possible. The strong Raman activity of the molecules suggests they scattered the entangled photons. Since they scattered the entangled photons and not the classical photons, it is clear that the quantum nature of the entangled photons is important to the molecules' sensitivity. This work

shows that entangled photons can be a very useful and unique tool for further explorations of how anesthetic molecules interact with the brain.

Chapter 6 focuses on how ETPA experiments can be improved and made more accessible for chemists. In previous ETPA literature, femtosecond pulsed lasers have been used to generate SPDC photons. While most chemists know how to use a UV-vis absorption or fluorescence spectrometer, not nearly as many have experience with high intensity pulsed lasers. ETPA has been heralded as a great new tool for chemists to probe their molecular compounds, but pulsed laser SPDC sources are not accessible to most chemists. Additionally, the current background noise, or baseline, of ETPA experiments is on the same order of magnitude as the ETPA signal itself, resulting in low signal-to-noise ratio (SNR). The SNR must be improved for chemists to be able to measure very small nonlinear signals in their compounds, which is one of the main benefits for chemists to use ETPA.

In this work, a continuous-wave (CW) laser was used to generate SPDC, which is much easier to operate, smaller in size and weight, and more cost effective than pulsed laser SPDC sources. The entire ETPA experiment, with SPDC source and detection, is much smaller and more realistic for a chemist to have in their lab, along the same line of a UV-vis absorption spectrometer. Additionally, this CW-pumped SPDC source yielded a 1-2 order of magnitude improvement in the SNR, setting a new standard for the smallest measurable ETPA cross-sections at ~10^{-21} cm^2/molecule. The role of the frequency Schmidt modes of SPDC were also analyzed, showing that by tuning the spatial shape of the pump, the joint frequency spectrum of the SPDC can be manipulated. This simple manipulation would allow chemists to control which excited states are populated by ETPA, offering a new control over photochemistry that classical light cannot offer.

Chapter 7 highlights a feature of ETPA that has previously been overlooked. From a physics perspective, the coupling between the frequency entanglement, temporal entanglement (T_e), and spatial entanglement (A_e) has been known. When the frequency spectrum is narrowed, A_e gets smaller and T_e gets larger. However, previous literature on ETPA has assumed that A_e remains constant. The ETPA cross-section expressed in eq. 1.41 would then get smaller as the frequency spectrum narrows since T_e increases. As a result, ETPA experiments have used femtosecond scale T_e so as not to decrease the ETPA cross-section.

This work shows experimentally that when the frequency spectrum is narrowed, the ETPA cross-section using Type-I SPDC actually increases. This result is explained by the frequency-spatial coupling of the SPDC. Here, A_e decreases quadratically because of the second-order dispersion properties of Type-I SPDC frequency spectrum. Since T_e only increases linearly, the net result on the ETPA cross-section is an increase. Conversely, Type-II SPDC causes the ETPA cross-section to plateau to a constant since A_e decreases linearly from the first-order dispersion properties of the frequency spectrum. The experimental data was fit to a theoretical model for how A_e changes with the frequency spectrum. The model shows the cross-section should continue increasing for Type-I SPDC until A_e reaches the diffraction limit, which occurs at T_e = 10 ps. At this maximum, the cross-section is an order of magnitude larger compared to the femtosecond T_e cross-sections reported in literature. Additionally, the cross-section at the maximum is 3-4 orders of magnitude larger than what the previous assumption of a constant A_e predicted.

The enhancement in the ETPA cross-section from the frequency-spatial coupling is an exciting development for chemists. ETPA is now expected to be measurable, and in fact stronger, at picosecond T_e. This would allow chemists to control photochemical reactions that require an intermediate process, such as an isomerization, proton transfer, or singlet-to-triplet energy transfer, between two photoexcitations. Additionally, A_e decreases by 4 orders of magnitude simply by filtering the SPDC, which would improve the spatial resolution of ETPA microscopy by 4 orders of magnitude. All of these advantages can be achieved today by using either a cavity-enhanced SPDC source, where the SPDC crystal is placed inside of a cavity so that only frequencies resonant with the cavity will be generated[61], or a periodically poled SPDC source that uses longer crystals with higher nonlinearities to generate much higher SPDC rates compared to thin BBO crystals.[62] Such a source would provide the necessary narrowband SPDC to reach the ETPA cross-section maximum.

References

1. Vedral, V., *Introduction to Quantum Information Science*. Oxford University Press: New York, 2006; p 182.
2. *The Physics of Quantum Information: Quantum Cryptography, Quantum Teleportationm Quantum Computation*. Springer: Berlin, Heidelberg, 2000.
3. Degen, C. L.; Reinhard, F.; Cappellaro, P., Quantum sensing. *Reviews of Modern Physics* **2017,** *89* (3), 035002.
4. Tóth, G.; Apellaniz, I., Quantum metrology from a quantum information science perspective. *Journal of Physics A: Mathematical and Theoretical* **2014,** *47* (42), 424006.
5. Fagaly, R. L., Superconducting quantum interference device instruments and applications. *Review of Scientific Instruments* **2006,** *77* (10), 101101.
6. Binnig, G.; Rohrer, H.; Gerber, C.; Weibel, E., Surface Studies by Scanning Tunneling Microscopy. *Physical Review Letters* **1982,** *49* (1), 57-61.
7. Fei, H.-B.; Jost, B. M.; Popescu, S.; Saleh, B. E. A.; Teich, M. C., Entanglement-Induced Two-Photon Transparency. *Physical Review Letters* **1997,** *78* (9), 1679-1682.
8. Peřina, J.; Saleh, B. E. A.; Teich, M. C., Multiphoton absorption cross section and virtual-state spectroscopy for the entangled n-photon state. *Physical Review A* **1998,** *57* (5), 3972-3986.
9. Saleh, B. E. A.; Jost, B. M.; Fei, H.-B.; Teich, M. C., Entangled-Photon Virtual-State Spectroscopy. *Physical Review Letters* **1998,** *80* (16), 3483-3486.
10. Javanainen, J.; Gould, P. L., Linear intensity dependence of a two-photon transition rate. *Physical Review A* **1990,** *41* (9), 5088-5091.
11. Lee, D.-I.; Goodson, T., Entangled Photon Absorption in an Organic Porphyrin Dendrimer. *Journal of Physical Chemistry B* **2006,** *110* (51), 25582-25585.
12. Georgiades, N. P.; Polzik, E. S.; Edamatsu, K.; Kimble, H. J.; Parkins, A. S., Nonclassical Excitation for Atoms in a Squeezed Vacuum. *Physical Review Letters* **1995,** *75* (19), 3426-3429.
13. Dirac, P. A. M., A new notation for quantum mechanics. *Mathematical Proceedings of the Cambridge Philosophical Society* **1939,** *35* (3), 416-418.
14. von Neumann, J., *Mathematical Foundations of Quantum Mechanics: New Edition*. Princeton University Press: Princeton, NJ, 1955.
15. Einstein, A.; Podolsky, B.; Rosen, N., Can Quantum-Mechanical Description of Physical Reality Be Considered Complete? *Physical Review* **1935,** *47* (10), 777-780.
16. Bell, J. S., On the einstein podolsky rosen paradox. *Physics Physique Fizika* **1964,** *1* (3), 195.
17. Freedman, S. J.; Clauser, J. F., Experimental test of local hidden-variable theories. *Physical Review Letters* **1972,** *28* (14), 938.
18. Shen, Y.-R., The principles of nonlinear optics. *New York* **1984**.
19. Itzykson, C.; Zuber, J.-B., *Quantum field theory*. Courier Corporation: 2012.
20. Couteau, C., Spontaneous parametric down-conversion. *Contemporary Physics* **2018,** *59* (3), 291-304.

21. Keller, T. E.; Rubin, M. H., Theory of two-photon entanglement for spontaneous parametric down-conversion driven by a narrow pump pulse. *Physical Review A* **1997,** *56* (2), 1534-1541.
22. Joobeur, A.; Saleh, B. E. A.; Larchuk, T. S.; Teich, M. C., Coherence properties of entangled light beams generated by parametric down-conversion: Theory and experiment. *Physical Review A* **1996,** *53* (6), 4360-4371.
23. Burdick, R. K.; Varnavski, O.; Molina, A.; Upton, L.; Zimmerman, P.; Goodson, T., Predicting and Controlling Entangled Two-Photon Absorption in Diatomic Molecules. *The Journal of Physical Chemistry A* **2018,** *122* (41), 8198-8212.
24. Kang, G.; Nasiri Avanaki, K.; Mosquera, M. A.; Burdick, R. K.; Villabona-Monsalve, J. P.; Goodson, T.; Schatz, G. C., Efficient Modeling of Organic Chromophores for Entangled Two-Photon Absorption. *Journal of the American Chemical Society* **2020,** *142* (23), 10446-10458.
25. Kojima, J.; Nguyen, Q.-V., Entangled biphoton virtual-state spectroscopy of the A2Σ+–X2Π system of OH. *Chemical Physics Letters* **2004,** *396* (4), 323-328.
26. Yin, J.; Cao, Y.; Li, Y.-H.; Liao, S.-K.; Zhang, L.; Ren, J.-G.; Cai, W.-Q.; Liu, W.-Y.; Li, B.; Dai, H.; Li, G.-B.; Lu, Q.-M.; Gong, Y.-H.; Xu, Y.; Li, S.-L.; Li, F.-Z.; Yin, Y.-Y.; Jiang, Z.-Q.; Li, M.; Jia, J.-J.; Ren, G.; He, D.; Zhou, Y.-L.; Zhang, X.-X.; Wang, N.; Chang, X.; Zhu, Z.-C.; Liu, N.-L.; Chen, Y.-A.; Lu, C.-Y.; Shu, R.; Peng, C.-Z.; Wang, J.-Y.; Pan, J.-W., Satellite-based entanglement distribution over 1200 kilometers. *Science* **2017,** *356* (6343), 1140.
27. Shapiro, J. H.; Boyd, R. W., The physics of ghost imaging. *Quantum Information Processing* **2012,** *11* (4), 949-993.
28. Yabushita, A.; Kobayashi, T., Spectroscopy by frequency-entangled photon pairs. *Physical Review A* **2004,** *69* (1), 013806.
29. Schlawin, F.; Dorfman, K. E.; Mukamel, S., Entangled Two-Photon Absorption Spectroscopy. *Accounts of Chemical Research* **2018,** *51* (9), 2207-2214.
30. Fedorov, M. V.; Miklin, N. I., Schmidt modes and entanglement. *Contemporary Physics* **2014,** *55* (2), 94-109.
31. Fedorov, M. V.; Mikhailova, Y. M.; Volkov, P. A., Gaussian modelling and Schmidt modes of SPDC biphoton states. *Journal of Physics B: Atomic, Molecular and Optical Physics* **2009,** *42* (17), 175503.
32. Ekert, A.; Knight, P. L., Entangled quantum systems and the Schmidt decomposition. *American Journal of Physics* **1995,** *63* (5), 415-423.
33. Terhal, B. M.; Horodecki, P., Schmidt number for density matrices. *Physical Review A* **2000,** *61* (4), 040301.
34. Göppert-Mayer, M., Über Elementarakte mit zwei Quantensprüngen. *Annalen der Physik* **1931,** *401* (3), 273-294.
35. Kaiser, W.; Garrett, C. G. B., Two-Photon Excitation in Ca${\mathrm{F}}_{2}$: ${\mathrm{Eu}}^{2+}$. *Physical Review Letters* **1961,** *7* (6), 229-231.
36. McClain, W. M.; Harris, R. A., Two-photon molecular spectroscopy in liquids and gases. *Excited states* **1977,** *3*, 1.
37. Bonin, K. D.; McIlrath, T. J., Two-photon electric-dipole selection rules. *Journal of the Optical Society of America B* **1984,** *1* (1), 52-55.
38. Hopt, A.; Neher, E., Highly nonlinear photodamage in two-photon fluorescence microscopy. *Biophysical journal* **2001,** *80* (4), 2029-2036.

39. Gea-Banacloche, J., Two-photon absorption of nonclassical light. *Physical Review Letters* **1989,** *62* (14), 1603-1606.
40. Oka, H., Enhanced vibrational-mode-selective two-step excitation using ultrabroadband frequency-entangled photons. *Physical Review A* **2018,** *97* (6), 063859.
41. Hong, C. K.; Mandel, L., Theory of parametric frequency down conversion of light. *Physical Review A* **1985,** *31* (4), 2409-2418.
42. Hong, C. K.; Mandel, L., Theory of parametric frequency down conversion of light. *Physical Review A* **1985,** *31* (4), 2409.
43. Harpham, M. R.; Süzer, Ö.; Ma, C.-Q.; Bäuerle, P.; Goodson, T., Thiophene Dendrimers as Entangled Photon Sensor Materials. *Journal of the American Chemical Society* **2009,** *131* (3), 973-979.
44. Upton, L.; Harpham, M.; Suzer, O.; Richter, M.; Mukamel, S.; Goodson, T., Optically Excited Entangled States in Organic Molecules Illuminate the Dark. *Journal of Physical Chemistry Letters* **2013,** *4* (12), 2046-2052.
45. Varnavski, O.; Pinsky, B.; Goodson, T., Entangled Photon Excited Fluorescence in Organic Materials: An Ultrafast Coincidence Detector. *Journal of Physical Chemistry Letters* **2017,** *8* (2), 388-393.
46. Varnavski, O.; Goodson, T., Two-Photon Fluorescence Microscopy at Extremely Low Excitation Intensity: The Power of Quantum Correlations. *Journal of the American Chemical Society* **2020,** *142* (30), 12966-12975.
47. Eshun, A.; Cai, Z.; Awies, M.; Yu, L.; Goodson, T., Investigations of Thienoacene Molecules for Classical and Entangled Two-Photon Absorption. *The Journal of Physical Chemistry A* **2018,** *122* (41), 8167-8182.
48. Guzman, A. R.; Harpham, M. R.; Süzer, Ö.; haley, M. M.; Goodson III, T., Spatial control of entangled two-photon absorption with organic chromophores. *J. Am. Chem. Soc.* **2010,** *132*, 7840-7841.
49. Villabona-Monsalve, J. P.; Varnavski, O.; Palfey, B. A.; Goodson, T. I., Two-Photon Excitation of Flavins and Flavoproteins with Classical and Quantum Light. *J. Am. Chem. Soc.* **2018,** *140* (44), 14562-14566.
50. Szoke, S.; Liu, H.; Hickam, B. P.; He, M.; Cushing, S. K., Entangled light–matter interactions and spectroscopy. *Journal of Materials Chemistry C* **2020,** *8* (31), 10732-10741.
51. Dorfman, K. E.; Schlawin, F.; Mukamel, S., Nonlinear optical signals and spectroscopy with quantum light. *Reviews of Modern Physics* **2016,** *88* (4), 045008.
52. Mukamel, S.; Freyberger, M.; Schleich, W.; Bellini, M.; Zavatta, A.; Leuchs, G.; Silberhorn, C.; Boyd, R. W.; Sánchez-Soto, L. L.; Stefanov, A.; Barbieri, M.; Paterova, A.; Krivitsky, L.; Shwartz, S.; Tamasaku, K.; Dorfman, K.; Schlawin, F.; Sandoghdar, V.; Raymer, M.; Marcus, A.; Varnavski, O.; Goodson, T.; Zhou, Z.-Y.; Shi, B.-S.; Asban, S.; Scully, M.; Agarwal, G.; Peng, T.; Sokolov, A. V.; Zhang, Z.-D.; Zubairy, M. S.; Vartanyants, I. A.; del Valle, E.; Laussy, F., Roadmap on quantum light spectroscopy. *Journal of Physics B: Atomic, Molecular and Optical Physics* **2020,** *53* (7), 072002.
53. Raymer, M. G.; Marcus, A. H.; Widom, J. R.; Vitullo, D. L. P., Entangled Photon-Pair Two-Dimensional Fluorescence Spectroscopy (EPP-2DFS). *The Journal of Physical Chemistry B* **2013,** *117* (49), 15559-15575.
54. Avanaki, K. N.; Schatz, G. C., Entangled Photon Resonance Energy Transfer in Arbitrary Media. *The Journal of Physical Chemistry Letters* **2019,** *10* (11), 3181-3188.

55. Gu, B.; Mukamel, S., Manipulating Two-Photon-Absorption of Cavity Polaritons by Entangled Light. *The Journal of Physical Chemistry Letters* **2020,** *11* (19), 8177-8182.
56. León-Montiel, R. d. J.; Svozilík, J.; Torres, J. P.; U'Ren, A. B., Temperature-Controlled Entangled-Photon Absorption Spectroscopy. *Physical Review Letters* **2019,** *123* (2), 023601.
57. Schlawin, F.; Dorfman, K. E.; Fingerhut, B. P.; Mukamel, S., Suppression of population transport and control of exciton distributions by entangled photons. *Nature Communications* **2013,** *4* (1), 1782.
58. Schlawin, F.; Dorfman, K. E.; Fingerhut, B. P.; Mukamel, S., Manipulation of two-photon-induced fluorescence spectra of chromophore aggregates with entangled photons: A simulation study. *Physical Review A* **2012,** *86* (2), 023851.
59. Dorfman, K. E.; Schlawin, F.; Mukamel, S., Stimulated Raman Spectroscopy with Entangled Light: Enhanced Resolution and Pathway Selection. *The Journal of Physical Chemistry Letters* **2014,** *5* (16), 2843-2849.
60. Schlawin, F.; Dorfman, K. E.; Mukamel, S., Pump-probe spectroscopy using quantum light with two-photon coincidence detection. *Physical Review A* **2016,** *93* (2), 023807.
61. Slattery, O.; Ma, L.; Zong, K.; Tang, X., Background and Review of Cavity-Enhanced Spontaneous Parametric Down-Conversion. *Journal of Research of the National Institute of Standards and Technology* **2019,** *124*, 1-18.
62. Jabir, M. V.; Samanta, G. K., Robust, high brightness, degenerate entangled photon source at room temperature. *Scientific Reports* **2017,** *7* (1), 12613.

CHAPTER 2
Experimental and Theoretical Methods

2.1 Overview

The experimental and theoretical methods used throughout this dissertation are outlined in this chapter. For the experimental methods, the information provided includes: what molecular information can be gained from the experiment, how the experimental setup looks, how the data is obtained, and any calculations necessary to obtain the molecular information from the data. For the theoretical methods, the information provided includes: what molecular information can be gained from the calculations, the main equations used in the technique, and the general process of how the calculations are performed.

2.2 Experimental Methods

2.2.1 Linear Absorption

Often the first spectroscopic experiment performed on a molecular sample is *steady-state linear absorption*. This technique measures the frequencies at which the molecule has a resonant eigenstate. By sending a broad range of frequencies into the molecular sample, any frequency that is resonant with an excited state will be attenuated due to the molecule absorbing that frequency of light to be excited from the ground to the excited state. The resulting spectrum then reveals the energies and energy widths of the molecule's excited states. The degree of attenuation of each frequency is related to the excited state's transition dipole moment (TDM) with the ground state.[1] The TDM is a quantitative measure of the one-photon selection rules between that particular excited state and ground state. Transitions that are more strongly allowed will have larger absorption intensities. The linear absorption spectrum therefore also reveals the TDMs of the one-photon allowed excited states. The absorbance signal is also dependent upon the concentration of the molecular solution and the molecule's *extinction coefficient, ε,* which is directly related to the TDM and one-photon absorption (OPA) cross-

section, a measure the molecule's ability to absorb light.[1] By measuring the absorbance and knowing either the concentration or ε, the other parameter can be easily calculated.

The range of frequencies measured cover the entire visible light range, as well as some frequencies in the low-UV and near-IR, leading to the common name of *UV-vis spectroscopy* for this technique as well. This range of frequencies corresponds to transitions to excited electronic states of the molecule. For the large organic chromophores used throughout this dissertation, the vibrational states within the excited electronic states have too much overlap to resolve them.

The optical elements within the Agilent 8453 spectrophotometer used throughout the work in this dissertation are shown in Fig. 2.1.

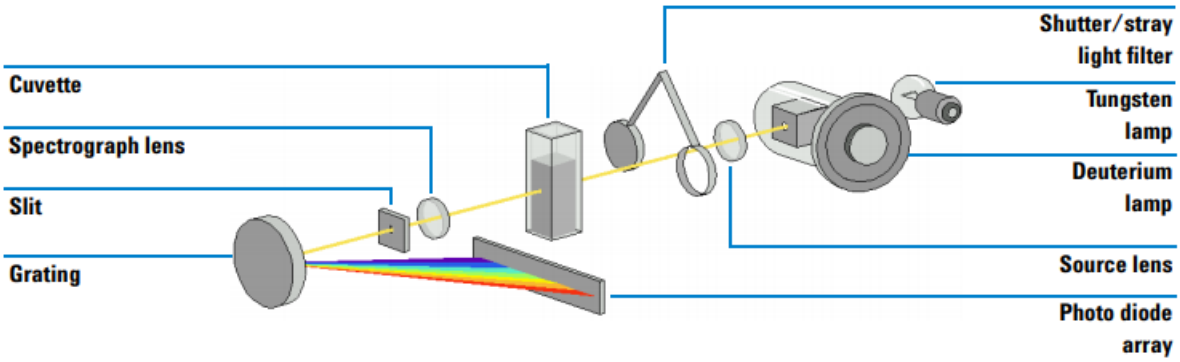

Figure 2.1. Optical elements and beam path of the Agilent 8453 spectrophotometer (image taken from the instrument's operator's manual).

Fig. 2.1 shows that two lamps are used to create the broad light source: a tungsten lamp for 370-1100 nm and a deuterium lamp for 190-800 nm. The light is collimated with a lens into a parallel beam. When the light is ready to be measured, the shutter opens, allowing the beam to pass through the cuvette containing the molecular solution (or solvent for a blank measurement). The beam that is transmitted through the cuvette is focused with a lens through a slit. The light then reflects off of a grating, which reflects each wavelength at a different angle. Therefore, each wavelength hits the photodiode array at a different spatial position. Each pixel in the photodiode array measures the intensity of the transmitted photons at the wavelength that hits it (with an interval of ~0.9 nm between each pixel). This array can thus measure the intensity of each wavelength across the 370-1100 nm wavelength range simultaneously.

To measure the absorption spectrum of the molecule, the intensity of each wavelength of light without the sample present needs to be known first. To measure this, clean solvent (the

same solvent used to prepare the molecular solution) is placed in the cuvette. The spectrophotometer is then blanked, where the intensity of the transmission through the solvent is measured for each wavelength. This information is stored within the spectrophotometer's software. The molecular solution is then placed in the cuvette, and the intensity of the transmission through the solution is measured for each wavelength. This transmission through the solution will be lower in intensity for wavelengths that are absorbed by the molecule. The transmittance, *T*, at each wavelength is then calculated as:[2]

$$T = \frac{I}{I_0} \tag{2.1}$$

I (I_0) is the intensity of the transmitted light through the solution (solvent). Plotting the transmittance vs wavelength would provide the transmission spectrum of the molecule. Here, the transmittance would be close to 1 at wavelengths where there is no excited state, and the transmittance will dip at wavelengths where there are excited states that absorbed the light. While the transmittance spectrum provides the information regarding the energies, linewidths, and TDMs of the molecule's excited states, the spectrum is usually converted into an absorption spectrum. The absorbance, *A*, is calculated as:[2]

$$A = log_{10}\frac{1}{T} \tag{2.2}$$

The absorbance is also commonly called the *optical density*, *OD*. By converting the transmittance into this log-scale of absorbance, states with weaker absorption can be more easily seen instead of being overwhelmed by stronger absorbing states on the linear scale of transmittance. It is also more intuitive to identify excited states based on the wavelengths the molecule absorbed vs the wavelengths that the molecule did not transmit. Additionally, absorbance has a linear relationship with the concentration, path length, *l*, and ε, compared to an exponential relationship with the transmittance. The linear relationship is simpler to deal with for further calculations than the transmittance. An example absorption spectrum measured for flavin adenine dinucleotide (FAD) is shown in Fig. 2.2.

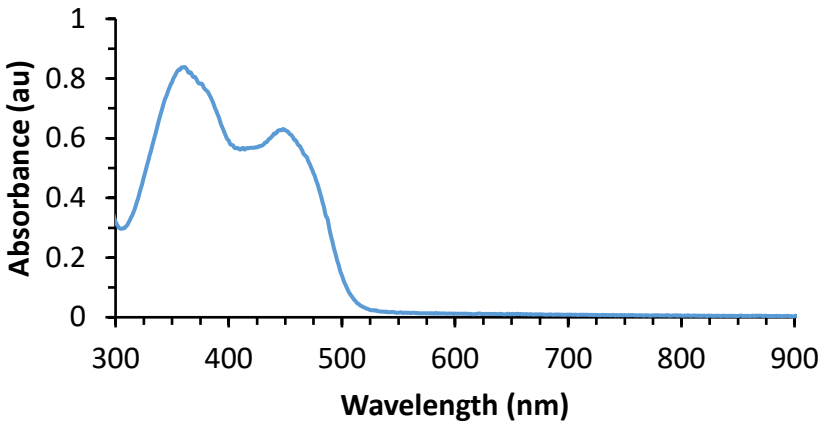

Figure 2.2. Absorption spectrum of flavin adenine dinucleotide.

The relationship between the absorbance, concentration, and ε is shown through the Beer-Lambert Law:[2]

$$A = \varepsilon lc \tag{2.3}$$

For molecules where ε is not known, a stock solution of the molecule is made with a known weight of solid and volume of solvent, allowing for calculating of the concentration of the solution. This stock solution is diluted several times through serial dilutions. A portion of the stock solution is placed in a new vial and a specific volume of solvent is added to this vial to dilute the solution. A portion of this new solution is placed into a new vial, and that solution is again diluted. With at least 3 such solutions prepared, the absorbance of each is measured using the same path length cuvette. ε is wavelength dependent, and the most accurate value comes from the wavelength at the peak of an absorption band, known as λ_{max}. Plotting absorbance at λ_{max} vs concentration yields a linear plot, with the slope equaling $\varepsilon * l$. Division by l leaves ε at λ_{max}.

When ε is known for a molecule, solutions for spectroscopic measurements in the later sections can prepared with known concentrations by dissolving some solid compound in solvent, measuring the absorbance at λ_{max}, and dividing that by ε and l. When a specific concentration is needed, the solution can be diluted until it yields the necessary absorbance at λ_{max}. To avoid aggregation between the molecules in solution, the absorbance is usually kept below 1.

The OPA cross-section, σ_1, is calculated through standard first-order perturbation theory as:[1]

$$\sigma_1(\omega) = \frac{2\pi^2 e^2 \omega_{ji}}{3\epsilon_0 hc} \frac{g_j}{g_i} g(\omega) \sum_j \left|\mu_{ji}\right|^2 = \frac{2.303\varepsilon c}{n} \quad (2.4)$$

Here, ω is the frequency of the light, g_i is the lineshape of the *i* state of the molecule (usually taken as Lorenztian), g is the lineshape of the light field, e is the charge of the electron, ω_{ji} is the frequency difference between the *i* and *j* states, μ_{ji} is the TDM between the *i* and *j* states, ϵ_0 is the permittivity of free space, h is Planck's constant, and c is the speed of light. The second equality relates the cross-section to the extinction coefficient, with n being the number of absorbing molecules.

2.2.2 Linear Fluorescence

When a molecule is in an excited electronic state, the molecule cannot remain in that higher energy state forever. The molecule will eventually return to the ground state upon releasing the energy through one of several mechanisms. The energy relaxation process relevant for this dissertation is fluorescence, where the molecule emits one photon of light, usually in the visible range, equal in frequency to the energy gap between the excited and ground states. Several properties of fluorescence are key pieces of information when trying to understand how a molecule behaves when it is in an excited state. These parameters include the wavelength spectrum, fluorescence lifetime (amount of time it takes, on average, for the excited state to emit a fluorescent photon), and quantum yield (probability the molecule will emit a fluorescent photon to decay to the ground state).[3]

Steady-state linear fluorescence measures the fluorescence intensity and spectrum from a molecule when it is excited at a particular wavelength. A diagram of the Horiba QuantaMaster fluorometer used in this work is shown in Fig. 2.3.

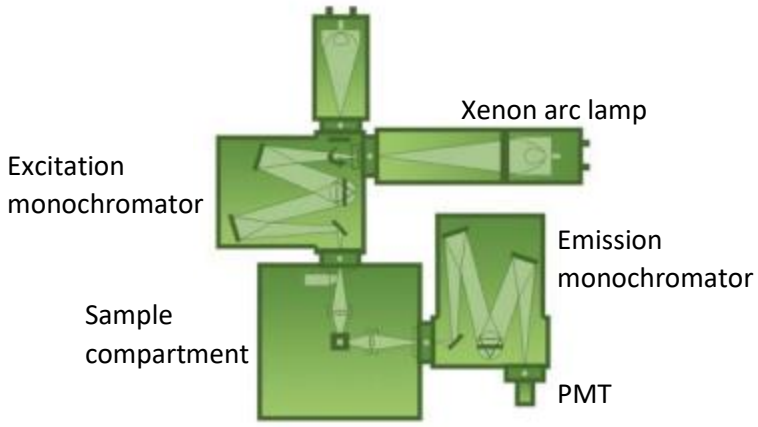

Figure 2.3. Horiba QuantaMaster fluorometer diagram (image from product brochure).

In the fluorimeter, a Xenon arc lamp is used as a broadband white light source. The white light is focused into a monochromator that uses a diffraction grating to reflect the wavelengths within the light source at different angles. The angle of the grating is chosen so that the desired excitation wavelength will be collected be focused through a narrow slit exiting the monochromator. All of the other wavelengths are blocked by the slit. The excitation light is then focused into a cuvette containing the molecular solution. Since the transmitted excitation light passes directly through the cuvette along a straight path, and fluorescence is emitted randomly in all directions, a lens is placed near the cuvette at a 90° angle from the excitation light beam. In this manner, only fluorescence light is collected by the lens for emission direction. The collected emission is focused into another monochromator that also contains a diffraction grating that reflects the wavelengths at different angles. The grating will reflect the emission toward another slit that leads to a photomultiplier tube (PMT). The grating will turn, allowing the intensity of each wavelength (with a bandwidth determined by the size of the slit) to be measured by the PMT one at a time. As the grating turns, the intensity for each wavelength is recorded by the software. The data is then plotted as fluorescence intensity vs wavelength. An example fluorescence spectrum of FAD is shown in Fig. 2.4.

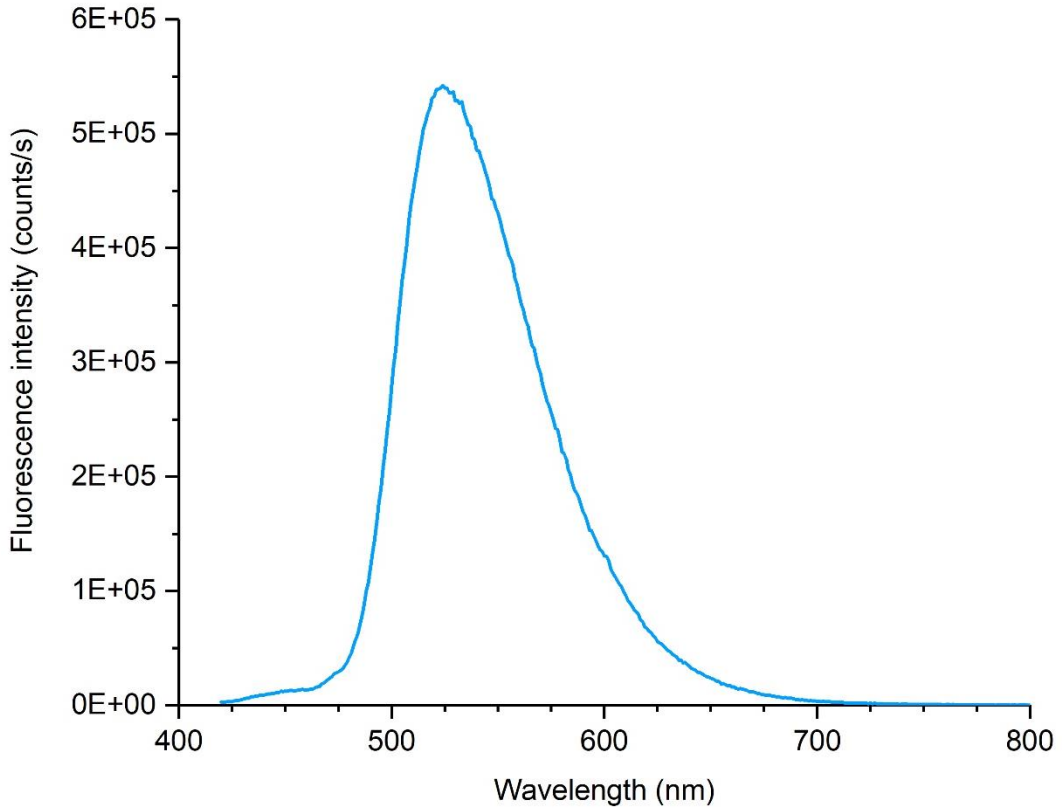

Figure 2.4. Steady-state linear fluorescence spectrum of flavin adenine dinucleotide.

Fluorescence measurements are commonly considered "background-free" since a fluorescence signal can only be obtained if the molecule is present and can absorb and emit photons. However, the solvent for a molecular solution can also scatter the excitation light through Rayleigh or Raman scattering.[3, 4] This scattered light can also be collected by the lens and measured with the fluorescence spectrum, yielding unexpected peaks in the fluorescence spectrum. These peaks, which are not from the molecule under study, can be subtracted out by collecting the mission spectrum of the pure solvent in the cuvette, similar to performing a blank during linear absorption. Subtraction of the solvent's emission spectrum from the molecule's emission spectrum yields the desired fluorescence spectrum free of solvent-scattered light.

Fluorescence typically only comes (appreciably) from the lowest excited electronic state in a molecule. Even if a higher electronic state is excited, the molecule was relax to the lowest excited state through vibrational relaxation or internal conversion before fluorescing. This is known as Kasha's rule.[5] As a result, fluorescence spectra typically only have one peak,

corresponding to the energy gap between the excited state and ground state. However, this energy gap is usually smaller than the energy gap measured by absorption spectroscopy. Treating each electronic state as a well with a minimum energy, a molecule will rest at the minimum of the ground state. The coordinate(s) along which the energy of the state changes is usually a conformational change of the nuclei of the molecule, such as a bond angle or stretch. When the molecule absorbs light, the electronic configuration of the molecule changes rapidly to that of the excited state. This change is in electron configuration is much faster than the nuclei can move.[6] As a result, when the molecule is first excited, the nuclei are not in the proper conformation that results in the minimum energy for the excited state's electron configuration. Over time, the nuclei will move toward this minimum energy conformation, which is different than the ground state's minimum energy conformation. The molecule will typically emit fluorescence when it is at this minimum energy in the excited state. The energy of the fluorescence photon is the energy between the excited state's minimum energy and the ground state's energy at that nuclei conformation, which is not the minimum energy conformation of the ground state. Emitting from the minimum energy of the excited state to return to a non-minimum energy of the ground state results in the fluorescence being lower in frequency than the absorbed light. The difference between the absorption and fluorescence energy is known as the Stokes shift.[3] Larger Stokes shifts indicate that the molecule's nuclei conformation changes more drastically upon absorption and relaxation to the excited state's energy minimum. This cycle of absorption and fluorescence is shown in Fig. 2.5.

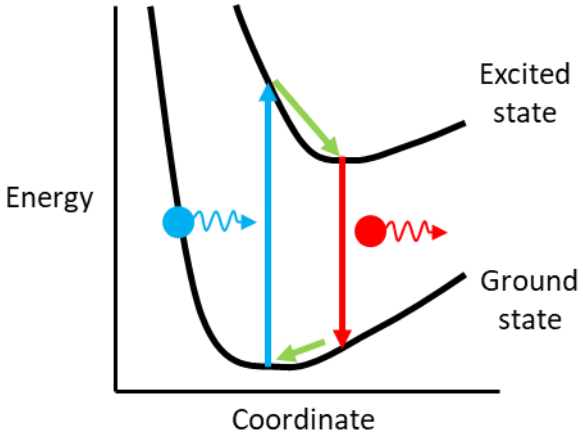

Figure 2.5. Energy level diagram for absorption and fluorescence on the potential energy curves of a molecule.

The quantum yield of a molecule can be measured from the fluorescence spectra of different concentrations of a molecular solution. The quantum yield is calculated as the percent of absorbed photons that result in a fluorescent photon. Since all relaxation processes compete with each other, larger quantum yields indicate that the molecule's fluorescence pathway is stronger than the other relaxation pathways.[3, 7] In theory, the quantum yield can simply be calculated by knowing the number of absorbed and fluoresced photons there are. However, determining these number accurately, particularly for fluorescence since only a portion of the actual fluorescence is collected and measured, can be difficult and only approximated at best. Additionally, pulsed light sources would be needed so that the excitation beam can be turned off while the fluorescence photons are counted. Otherwise, the molecule would continuously keep absorbing more light.

A much easier method to calculate the quantum yield is through the comparison method.[7] In this method, the fluorescence signal as a function of the absorbance for the target molecule is compared to the trend for a standard with a known quantum yield. The fluorescence spectrum is integrated to calculate the total fluorescence intensity measured with the PMT. This intensity is plotted versus the absorbance of that concentration. This is repeated for at least 3 concentrations. Since fluorescence is linearly proportional to absorbance, the resulting plot should be a linear regression. The slope of the line is proportional to the quantum yield (though not equal to the quantum yield) since both the slope and quantum yield are measures of the fluorescence obtained per absorption. Therefore, the ratio of the target molecule's slope, m_t, to standard's slope, m_s, should equal the ratio of the target's quantum yield, φ_t, to standard's quantum yield,φ_s. The target's quantum yield is then simply calculated as:

$$\phi_t = \frac{\phi_s m_t}{m_s} \tag{2.5}$$

The fluorescence spectrum can be an indicator of the quality of a sample. If a sample starts to degrade, whether from it being a naturally unstable compound, damage due to laser radiation, etc., the bonds within the molecule begin to break. Breaking bonds can change the excited states of the molecule, such as changing what the minimum energy nuclei conformation for the lowest excited state is. If this conformation changes, the fluorescence spectrum will look different compared to how it normally looked before it degraded. The fluorescence spectrum can also help identify impurities within a sample or solution, since the impurities will emit light at a different wavelength than the sample.

2.2.3 Classical Two-Photon Absorption

Classical two-photon absorption (TPA) is the nonlinear transitions where a molecule absorbs two photons whose summed frequencies are resonant with an excited state in the molecule.[8] Much of the background and advantages of TPA has been explained in Chapter 1.5. Briefly, the TPA rate is proportional to the intensity of the input electric field squared. The quadratic dependence yields very low TPA signals at low input intensity, requiring focused, high intensity laser pulses to produce a measurable signal. The spatial resolution of TPA is superior to OPA since TPA only occurs (measurably) at the focal point, which can be diffraction-limited.[9, 10] The lower laser field frequencies used for TPA compared to OPA allow for deeper penetration into samples.[11, 12] Finally, excited states that are OPA-forbidden from selection rules can be allowed by TPA, allowing these states to be excited and probed.[13]

In terms of molecular information that can be gained from TPA, the main molecular parameter probed with TPA is the TDMs between excited states.[13] Since the first absorbed photon only creates a coupling between the ground and intermediate states (via a virtual state if the intermediate states are not resonant with the first photon), the second photon must create a coupling between the intermediate and final excited states. These latter TDMs cannot be probed with steady-state linear absorption. Excited-to-excited state TDMs are helpful to define the strength of charge transfer between excited states, which is a crucial dynamical process for applications such as fluorescence-based sensors, solar cells, and OLEDs.[14-17] By measuring the TPA cross-section of a molecule, some insight into the potential strength of charge transfer can be gained.

The TPA cross-section can be measured through a transmittance-based technique similar to linear absorption. This technique, know as a *z-scan*, measures the transmitted power of a focused pulsed laser as the molecular solution is scanned across the laser beam path (z-axis) through the focal point.[18] Because the focal point has a much higher intensity than the converging or diverging beam, the transmittance will drop as the solution gets closer to and enters the focal point. The TPA cross-section can be extracted from the rate at which the transmittance drops vs position.

Though the z-scan technique can measure the TPA cross-section, a fluorescence-based technique can provide better accuracy since it is inherently a background-free measurement.[19]

This technique, known as *two-photon excited fluorescence*, *TPEF*, was used throughout the work of this dissertation and will be explained it further detail. The diagram of the experimental setup used to measure the TPA cross-section via TPEF is shown in Fig. 2.6.

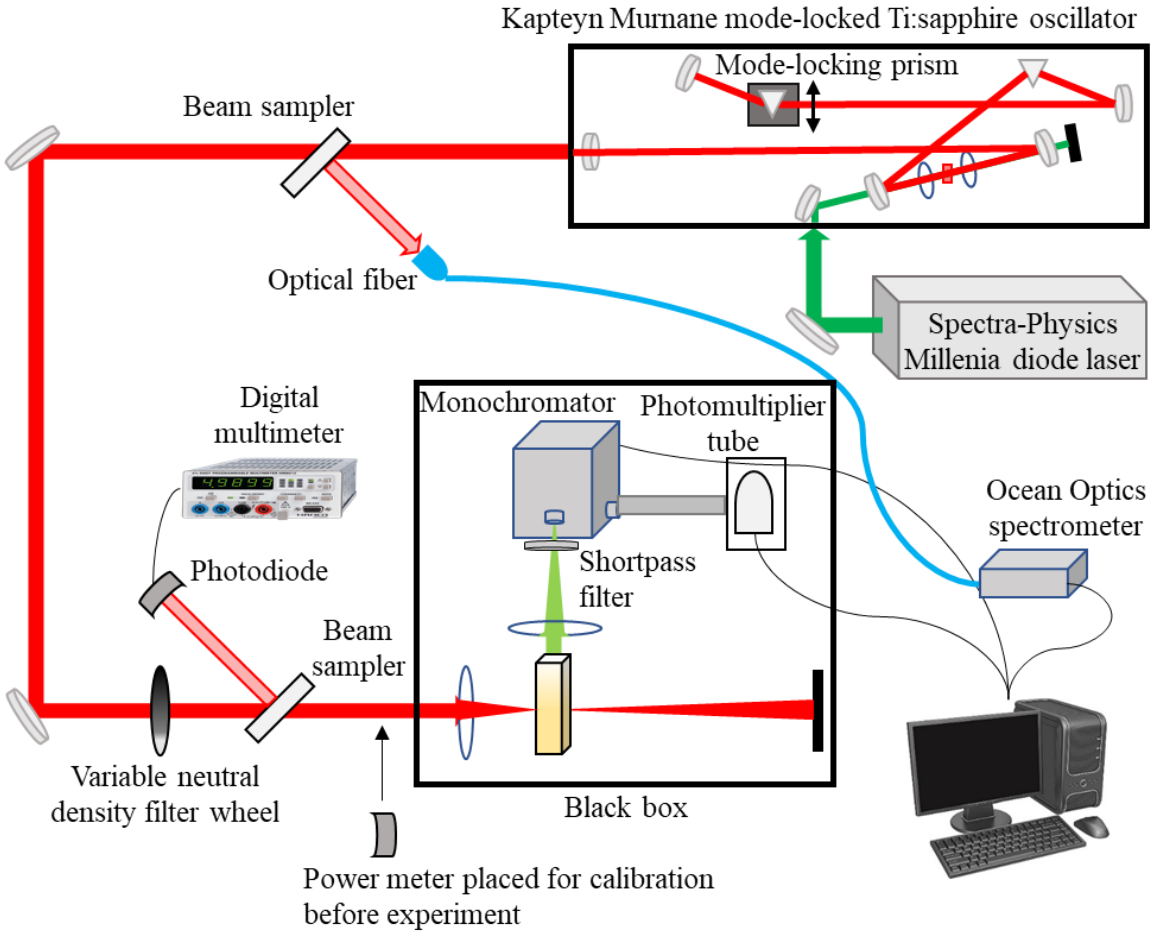

Figure 2.6. Experimental setup used to measure two-photon excited fluorescence.

A Spectra-Physics Millenia CW laser with 4 W of 532 nm emission is sent into a KMLabs Ti:sapphire oscillator. The oscillator emits fs laser pulses, typically centered around 800 nm with ~100 fs temporal width and 80 MHz repetition rate. The central wavelength and temporal width has some tunability. The output of the oscillator is sent through a beam sampler, which reflects a very small amount of the light into an Ocean Optics spectrometer to measure the spectrum. The oscillator is mode-locked by monitoring the spectrum while adjusting a prism inside the cavity. Before the oscillator is mode-locked, the emission will be CW, which appears as a tall, narrow emission peak at the central wavelength. By slightly pushing the prism's

spring-loaded translational stage, the beam within the cavity is temporally misaligned. Releasing the stage back to its original position returns the alignment, allowing the light field mode-lock. When it mode-locks, the spectrum will become flatter and broader. The oscillator is now producing fs pulses.

A pair of mirrors redirects the pulses toward the sample compartment. Another beam sampler reflects a small portion of the light toward a photodiode, which measures a voltage signal proportional to the intensity of the light field. This signal is calibrated to the power of the light field with a power meter. A variable neutral density filter wheel is placed in the beam path before the beam sampler. The wheel is rotated to different positions to change the transmitted laser power. The light transmitted through the beam sampler is measured with a power meter. A linear calibration curve of the voltage vs power is recorded across the entire power range needed for the experiment, typically 10-100 mW. The power meter is then removed, and the power throughout the experiment is measured by recording the voltage signal from the photodiode and converting the signal to power.

The beam is sent into a black box containing the sample holder, monochromator, and photomultiplier tube (PMT) detector. A lens focuses the light into the sample holder where the cuvette with the molecular solution is placed. Similar to the fluorimeter setup, a lens is placed near the sample holder at a 90° angle to the input light beam. This lens collects the TPEF and focuses it into the monochromator. A shortpass filter before the monochromator entrance blocks scattered light from the input beam, allowing only the fluorescence to enter. The output of the monochromator is sent to a PMT to measure the count rate.

To measure the TPA cross-section, a comparison method with a standard of known TPA cross-section is used, similar to the quantum yield measurement.[20] First, the TPEF spectrum is measured for the target molecule and standard by scanning the monochromator and measuring the intensity at each wavelength with the PMT. The TPEF spectrum should resemble the linear fluorescence spectrum, though small shifts in the peak wavelength are possible since the excited state dynamics for TPA vs OPA can be different. The λ_{max} of the TPEF spectrum is used as the detection wavelength for the power scan. In the power scan, the TPEF intensity over a range of input light powers is measured. The filter wheel is turned to change the power, and ~10 measurements of the TPEF intensity are collected between 10-100 mW. The TPEF intensity vs power is then plotted.

Since the TPEF is created with fs pulses, the resulting fluorescence from each pulse is too quick for a detector to resolve the fluorescence signal temporally. The time-averaged fluorescence signal, $\langle F(t)\rangle$, is related to the input laser power, $\langle P(t)\rangle$ by:[21]

$$\langle F(t)\rangle \approx \frac{1}{2} g\phi\eta c\delta_r \frac{8n\langle P(t)\rangle^2}{\pi\lambda} \tag{2.6}$$

g is the second-order temporal coherence of the laser beam, φ is the fluorescence quantum yield (assumed to be the same as for linear fluorescence), η is fluorescence collection efficiency of the experimental setup, c is the concentration of the solution, n is the solution's refractive index (assumed to be that of the solvent for dilute solutions), and λ is the wavelength of the laser. While direct calculation of the target's TPA cross-section is possible with eq. 2.6, such calculation requires accurate knowledge of g and η. By using the comparison method with a standard of known TPA cross-section, and using the same experimental setup and laser properties (central wavelength, bandwidth, etc.), these factors will be the same for standard's fluorescence intensity as for the target's fluorescence intensity. Therefore, once accounting for the concentrations and quantum yields of the target and standard, the ratio of the fluorescence intensities equals the ratios of the TPA cross-sections. Since eq. 2.6 is a quadratic function, the calculation can be further simplified by making a log-log plot of the TPEF intensity vs input power for the target and standard. The log-log plot is then governed by:

$$log[\langle F(t)\rangle] = 2log[\langle P(t)\rangle] + log\left[\frac{1}{2} g\phi\eta c\delta_r \frac{8n}{\pi\lambda}\right] \equiv 2log[\langle P(t)\rangle] + b \tag{2.7}$$

This log-log equation is linear and has a slope of 2 since the fluorescence intensity is proportional to the input power squared for a TPA. Ensuring that the measured log-log plot has a slope of 2 is a good check that the fluorescence signal measured is indeed from TPEF. The log of all the other parameters is the y-intercept term, b. Since the TPA cross-section is within the y-intercept, comparison of the y-intercepts for the target and standard yields the target's TPA cross-section by dividing the target's y-intercept by the standard's y-intercept:

$$\frac{\frac{1}{2} g\phi_t\eta c_t\delta_{r,t}\frac{8n_t}{\pi\lambda}}{\frac{1}{2} g\phi_s\eta c_s\delta_{r,s}\frac{8n_s}{\pi\lambda}} = \frac{10^{b_t}}{10^{b_s}} \tag{2.8}$$

Rearranging eq. 2.8 and cancelling the parameters that are only laser-dependent, which were kept the same for both the target and standard measurement, results in:

$$\delta_{r,t} = \frac{10^{b_t - b_s}\phi_s c_s \delta_{r,s} n_s}{\phi_t c_t n_t} \tag{2.9}$$

2.2.4 Entangled Two-Photon Absorption

Entangled two-photon absorption (ETPA) is the two-photon optical transition where a molecule absorbs a pair of entangled photons to create population on an excited state. The mechanism for this transition, from ground to intermediate/virtual to final state, looks similar to that of classical TPA, but the quantum correlations of the entangled photons induces unique photophysics during the ETPA transition.[22] The notable differences and advantages of ETPA are explained in greater detail in Chapter 1.6. Briefly, the pair of photons are defined as a single quantum object since the properties of one photon cannot be described without the properties of the other photon.[23, 24] As a single object for the molecule to absorb, ETPA scales linearly with the input photon rate, rather than quadratically for classical TPA.[25] The linear trend yields an enhancement in the absorption rate at low input intensities compared to classical TPA, allowing two-photon transitions to be probed at extremely small photon rates where the molecule cannot be damaged.[26] The TPA rate enhancement also improves the sensitivity of ETPA compared to classical TPA since the same absorption/fluorescence signal can be obtained using orders of magnitude lower light intensities.

The quantum correlations of the entangled photons also yield unique quantum signatures in ETPA signals. Most notably, the two absorption events, first from ground to virtual state and second form virtual to final state, interfere with each other.[22] Constructive interference enhances the ETPA cross-section, and the Fourier transform of the non-monotonic signal reveals the energies of excited states in the molecule, even if they cannot be directly excited by light.[27] ETPA is also not bound by the uncertainty principle for energy and time resolution.[28] Both variables can have high resolution simultaneously, which classical TPA cannot reproduce.

The ETPA experiments in this work involved measuring the ETPA cross-section in a variety of molecules and with different entangled photon properties, most notably the frequency bandwidth and spatial phase-matching condition. The entangled photon source was spontaneous parametric down-conversion (SPDC). While previous theoretical and experimental work has shown some unique benefits of ETPA,[29, 30] there is still many lingering questions regarding how the ETPA cross-section is dependent upon, including CW SPDC pumping vs pulsed laser pumping, Type-I SPDC vs Type-II SPDC, collinear vs non-collinear SPDC, and Gaussian frequency spectra vs sinc frequency spectra. For all of these studies, the

ETPA cross-section was measured using a transmittance-based technique. The basic layout and experimental procedure for measuring the ETPA cross-section using this technique is explained below. Modifications to the setup needed to complete these studies and to characterize the SPDC sources are explained after.

The first ETPA experimental setup used in this work is shown in Fig. 2.7.

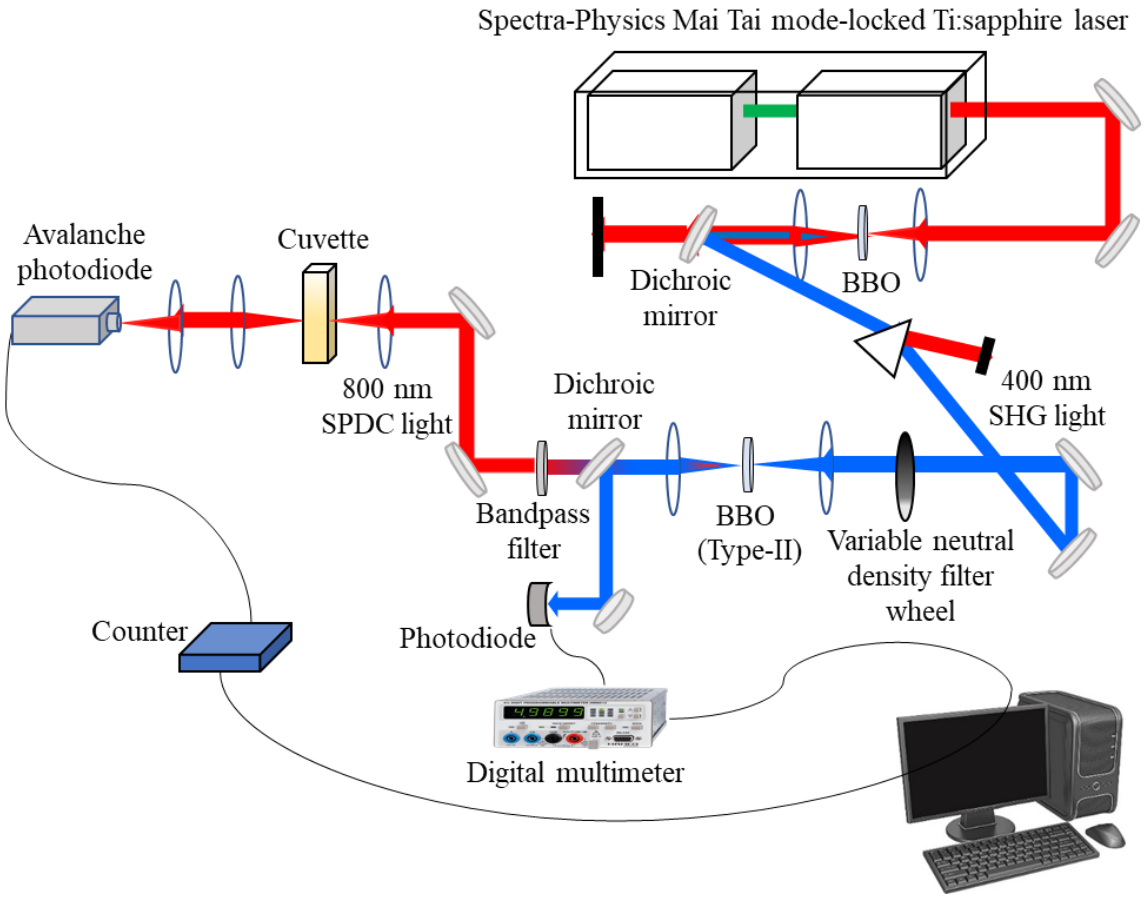

Figure 2.7. ETPA experimental setup using Type-II SPDC with fs pulse pumping.

A Ti:sapphire oscillator (Spectra-Physics Mai Tai) produces laser pulses centered at 800 nm with temporal width of ~100 fs with a 80 MHz repetition rate. The output power is typically ~1 W. This beam is directed toward a second-harmonic generation (SHG) BBO crystal to double the frequency to 400 nm pulses. A prism separates the 400 nm beam from any residual 800 nm light. The 400 nm beam is the pump for the SPDC process. The beam first passes through a variable neutral density filter wheel to control the pump power. The beam is then focused with a lens into a Type-II BBO SPDC crystal with length 0.5 mm to create the

entangled photons. A lens collimates the output of the crystal. A dichroic mirror reflects the residual 400 nm beam and allows the 800 nm-centered SPDC to pass through. The reflected 400 nm beam is directed to a photodiode that measures a voltage signal. Similar to the classical TPA experiment, a calibration curve between pump power and voltage is measured. Then, the voltage signal is measured throughout the ETPA experiment and converted to pump power. After being transmitted through the dichroic mirror, the SPDC passes through a longpass filter with cut-on wavelength of 700 nm and a bandpass filter centered at 800 nm with a 12 nm bandwidth. The SPDC is directed toward the sample holder, where a lens focuses the SPDC into the center of a cuvette containing the molecular solution (or solvent for a blank). The transmitted SPDC is collimated and then focused onto an avalanche photodiode (APD). The APD has single photon detection sensitivity, producing a TTL pulse for every photon that hits the sensor. The TTL pulse is sent to a counter which counts the number of pulses received within a given time window (usually 1 s). This count rate is recorded in a Labview program, along with the voltage signal that is passed from the photodiode to a digital multimeter (Kiethley). Because the APD can detect single photons, it is crucial that the entire experiment to be covered with black boxes to prevent room light and scattered light from the pump laser from reaching the APD. The room lights must also remain off throughout the entire experiment.

Measurement of the ETPA cross-section consists of three power scans. First, the cuvette is filled with pure solvent that is used for the molecular solution. The pump laser is blocked from entering the SPDC crystal so that no entangled photons are created, and no photons should reach the APD. The count rate is measured, which will be non-zero due to the APD producing false positive TTL pulses. These "dark counts" are from electrons in the APD spontaneously exciting thermally and producing a TTL pulse. These dark counts should be on the order of 10^2-10^3 counts/s. If they are higher, the experimental setup needs to be covered more from room light/scattered laser light. The filter wheel is then set to its minimum transmission position and the laser is unblocked to allow SPDC to be produced. The count rate transmitted through the pure solvent is measured, along with the voltage signal. A total of 5 measurements are collected, each with a 1 s collection window. The average of these 5 measurements is the count rate used for further calculations explained below. The standard deviation of the 5 measurements is the error. The filter wheel is slightly turned to allow more

pump light into the crystal, and the measurement is repeated. A total of ~10 count rates at increasing pump power should be measured. The total scan range in terms of count rate should cover a minimum of 10^6 counts/s and up to a maximum of 10^7 counts/s, though lower minimum count rates can be collected if the filter wheel can provide enough attenuation to reach 10^5 counts/s.

The second power scan is another scan of the transmitted count rate through the pure solvent in the cuvette. Without moving the cuvette from the sample holder, the original solvent can be removed with a pipette, and new solvent can be added. Or to save solvent, a pipette can be used to mimic the process of removing the solvent and adding new solvent. The pipette is placed inside the filled cuvette, some solvent is collected in the pipette, and the pipette is carefully pulled out of the cuvette. With the solvent still in the pipette, the pipette is placed back into the cuvette, and the solvent is released. This process is repeated 3 times to mimic replacing the solvent. The purpose of this step is to measure how the transmitted count rate changes due to mechanical movement of experimental equipment while removing the solvent and adding the molecular solution in the before the third and final scan. Such movement would slightly alter the beam alignment on the APD, causing the count rate to drop and appear as an absorption signal. This step also accounts for how the laser power might fluctuate during the time between each scan. If the laser power slightly drops, the count rate would also drop and appear as an absorption signal. Both of these count rate drops are false positives. Measurement of this count rate drop establishes the baseline for the experiment. For the molecular solution in the next step, the count rate must drop more than this baseline to say there is an ETPA signal.

Without moving the cuvette from the sample holder, the solvent is completely removed from the cuvette with a pipette, and the molecular solution is added to the cuvette. The power scan completed for the solvent is then repeated for the solution. With the 3 power scans completed, the ETPA rate vs input photon rate is calculated as follows:

First, the count rates measured with the APD must be corrected to account for the dead time and quantum efficiency of the detector. The dead time refers to the brief period of time immediately after the APD detects a photon during which the APD cannot detect another photon until the electrons settle. This time is typically a few ns and is specified in the data sheet provided by the APD manufacturer. The quantum efficiency is the probability that the APD will detect a photon that hits the sensitive area, which is dependent upon the wavelength of the

photon. For 800 nm, the APD used has a quantum efficiency of ~60 %. Both of these factors are corrected for using the equation:

$$R_{corr} = \frac{(R_{meas} - R_{dark})/\phi_e}{1-(R_{meas} - R_{dark})T_D/\phi_e} \quad (2.10)$$

R_{meas}, R_{dark}, and R_{corr} are the measured, dark, and corrected count rates, respectively, φ_e is the quantum efficiency of the APD, and T_D is the dead time. Using the corrected count rates, the count rates at each pump power for the two solvent scans are subtracted. The difference between them is the ETPA baseline, quantifying the sensitivity and detection limit of the experiment. The standard deviations for both scans are used to calculate the error of the subtraction through standard error propagation. These baselines rates are plotted vs the transmitted count rate for one of the solvent scans. Since the solvent does not have an electronic energy level close to resonance with the one-photon frequency or summed frequency of the entangled photons, it is assumed that the solvent does not absorb any entangled photons in the experiment. With this assumption, the transmitted count rate equals the input photon rate. Then, the transmitted count rate for the solution power scan is subtracted from the transmitted count rate for the second solvent scan. The difference between them is the baseline difference plus the drop due to the solutions absorbing some of the entangled photons. The difference between the scans is plotted vs the count rate for the solvent (which is assumed to equal the input photon rate). An example plot of the ETPA rate and baseline vs input photon rate is shown in Fig. 2.8.

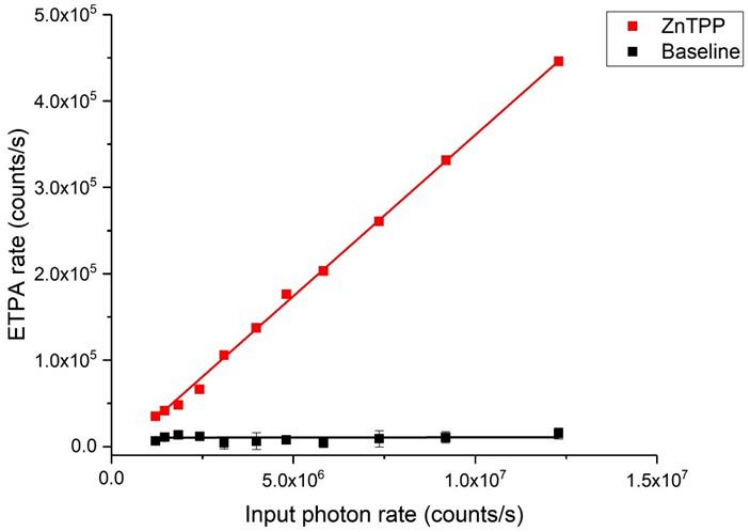

Figure 2.8. ETPA rate for zinc tetraphenylporphyrin (ZnTPP) and baseline vs input photon rate.

The baseline is then subtracted from the ETPA rate to correct for the count drop due to mechanical movement and laser power fluctuations. The result is the corrected ETPA rate vs input photon rate, which should have a clear linear trend given the low input photon rates used, which are well below the critical flux where the total TPA rate becomes quadratic. The slope of this line is the percentage of entangled photons that were absorbed by the sample. This percentage is concentration dependent, and for solutions with concentrations below ~200 μM, the percentage is typically between 1 and 5 %. The baseline for the experiment using the setup in Fig. 2.7 (Type-II SPDC, fs pulse pumping) is 1 %, resulting in a signal-to-noise ratio (SNR) of 1-5.

To calculate the ETPA cross-section from this plot, the cross-section equations starts from the standard linear absorption rate:

$$\frac{N_{abs}}{N_{in}} = 1 - e^{-\sigma_e lc} \tag{2.11}$$

N_{abs} (N_{in}) is the photon rate absorbed by (input to) the solution, σ_e is the ETPA cross-section, l is the cuvette path length, and c is the concentration. The exponential function can be Taylor expanded and truncated to first order in σ_e, which results in the approximation:

$$\frac{N_{abs}}{N_{in}} \approx \sigma_e lc \tag{2.12}$$

The left-hand term is the percent of entangled photons absorbed, i.e. the slope (m) of the ETPA rate vs input photon rate. Rearranging eq. 2.12 results in the expression for the ETPA cross-section:

$$\sigma_e = \frac{m}{lcN_A} \tag{2.13}$$

N_A is Avogadro's number to calculate the cross-section in units of cm^2/molecule. Note, c should be converted to units of mol/cm^3.

Chapter 6 of this dissertation shows the use of a newly built ETPA experiment that uses a CW pump laser and Type-I SPDC. The experimental setup is shown in Fig. 2.9.

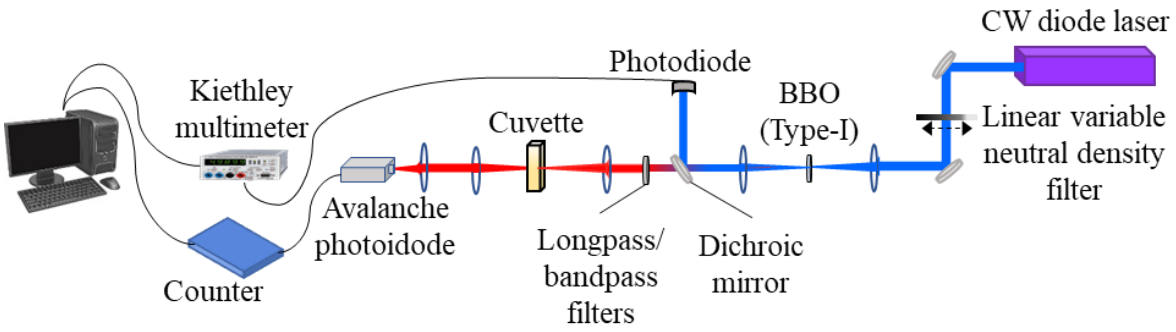

Figure 2.9. ETPA experimental setup for CW pumping of Type-I SPDC.

In this setup, a CW diode laser (Crystalaser) with 250 mW of 405 nm light is used to pump the SPDC process. A linear variable neutral density filter is mounted on a translation stage oriented perpendicular to the laser beam. Moving the translational stage with the filter changes the attenuation of the pump beam. The pump is focused into a Type-I BBO SPDC crystal with length 1 mm. The output from the crystal is collimated with a lens. A dichroic mirror reflects the residual 405 nm beam toward a photodiode that measures a voltage signal, similar as in the setup in Fig. 2.7. The transmitted SPDC is passed through a longpass filter cut-on 700 nm and a bandpass filter centered at 810 nm. A variety of filters are used with bandwidths of 10, 30, and 80 nm. The SPDC is focused into the cuvette containing the molecular solution (or solvent for the blank), and the transmitted SPDC is collimated after. The SPDC is then focused onto an APD that sends TTL pulses to a counter to measure the count rate as in the setup in Fig. 2.7. The entire experimental setup is covered in black boxes to prevent room light and scattered laser light from hitting the APD.

The procedure for collecting data and calculating the ETPA cross-section is the same as explained previously. As noted in greater detail in Chapter 6, this setup using CW pumping yields a typical ETPA percentage of 1-10 %, with a baseline of 0.1 %, resulting in an improved SNR of 10-100 compared to the previous setup's SNR of 1-5.

The ETPA rate can also be measured by detecting coincidence counts instead of singles counts. For this experiment, the entangled photon pair is split, sending one photon to one APD and the other photon to a different APD. For Type-II SPDC, the pairs are split using a polarizing beam-splitter since one polarization is reflected and the other transmitted. For Type-I collinear SPDC, a non-poalrizing 50:50 beam splitter is used, where each photon has a 50:50 chance of being reflected or transmitted. With this method, the photon pairs may not always

be separated since both can be reflected (or transmitted) together. Probabilistically, the coincidence rate measured will only be half of the total number of photon pairs present. For this reason, it is better to use non-collinear phase-matching for Type-I SPDC, shown in Fig. 2.10.

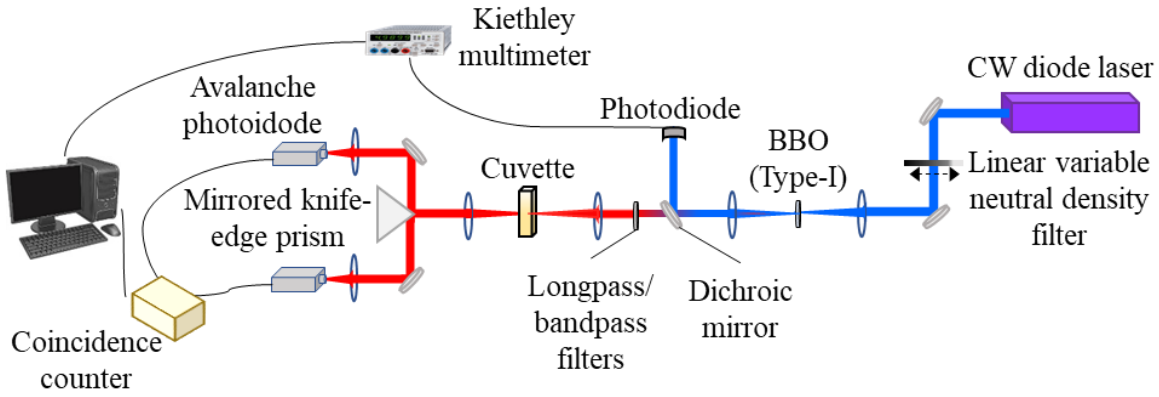

Figure 2.10. Experimental setup for measuring coincidence counts with non-collinear Type-I SPDC.

Because non-collinear Type-I SPDC pairs are spatially separated from each other 180° around the ring to conserve momentum, a mirrored knife-edge prism can separate each photon pair. When the SPDC ring is centered on the edge of the prism, each photon within the pair is reflected in opposite directions. Then the photons can be focused onto their own APDs. It is essential for the experimental setup that the total path distance for each photon from the point where they are separated to their respective APDs is the same, and that the BNC cables that connect the APDs to the coincidence counter are the same length. Any difference in either of these lengths will add an artificial delay to the TTL pulses arriving at the coincidence counter, resulting in an inaccurate measurement of the coincidence count rate.

Once the entangled pairs are separated and aligned to their respective APDS, the two APDS send TTL pulses to a coincidence counter each time they detect a photon. The coincidence counter has a specific coincidence window, in this case 5 ns. If the two APDs both send a TTL pulse to the coincidence counter within this coincidence window, the counter registers 1 coincidence count. If the counter receives a TTL pulse from only 1 APD, it does not register a coincidence count (though the counter can keep track of the singles counts from each APD as well). The probability for an entangled pair to have both photons arrive at their

respective APDs within the coincidence window is determined by their entanglement time, T_e, and any potential delay added to the pair after their generation. In this case, no delay is added, so the two photons must arrive at their respective detectors within a time window of width T_e. As long as T_e is shorter than the coincidence window, the entangled pair is guaranteed to arrive at the APDs within enough time for the APDs to register a coincidence count with the counter (though the dead time and quantum efficiency of the APDs still apply, so not every single entangled pair will be detected).

As mentioned in Chapter 1.4.3, both Type-I and Type-II SPDC have multiple spatial phase-matching conditions which yield different spatial distributions of the SPDC rings. To optimize SPDC generation, the crystals are cut such that when the crystal face is orthogonal to the pump beam, one of the phase-matching conditions will be met by the angle that the pump beam is making with the optical axis. To change the spatial phase-matching, the crystal can be slightly tilted around the axis that is orthogonal to the pump beam and parallel to the optical table. Adding this tilt changes the angle between the pump beam and optical axis, which changes the spatial phase-matching condition.

Chapter 7 details work on measuring the ETPA cross-section using different SPDC frequency bandwidths. To control the bandwidth, the SPDC generated from the crystal is filtered using either a bandpass filter (80, 30, 10 nm bandwidths) or a monochromator (5, 4, 3, 2.5, 2 nm bandwidths). For the broader bandwidths, the appropriate bandpass filter is placed in the SPDC path with the 700 nm longpass filter after the dichroic mirror in Fig. 2.10. No additional alignment is needed. For the narrower bandwidths, the monochromator is placed after the dichroic mirror and before the lens that focuses the SPDC into the cuvette. A focusing (collimating) lens should be placed immediately before (after) the monochromator to optimize coupling of the SPDC into and out of the monochromator. The grating in the monochromator is turned so that 810 nm light is centered on the exit slit. The entrance and exit slit widths control the bandwidth that exits the monochromator. The exact bandwidth is calculated from the grating's dispersion, d, in nm/mm and the slit width, w, as:

$$\Delta\lambda = d \times w \tag{2.14}$$

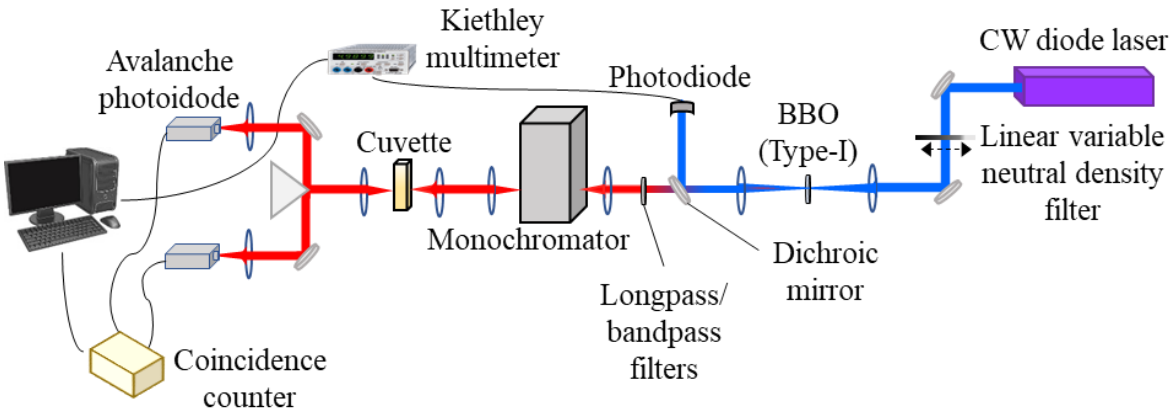

Figure 2.11. Experimental setup for adjusting the SPDC frequency bandwidth with a monochromator.

An important part of building an ETPA setup is characterizing the entanglement of the photon source. In this work, the frequency entanglement was measured. To complete this characterization, a monochromator was placed in the beam path of each photon within an entangled pair after they have been separated from each other, shown in Fig. 2.12.

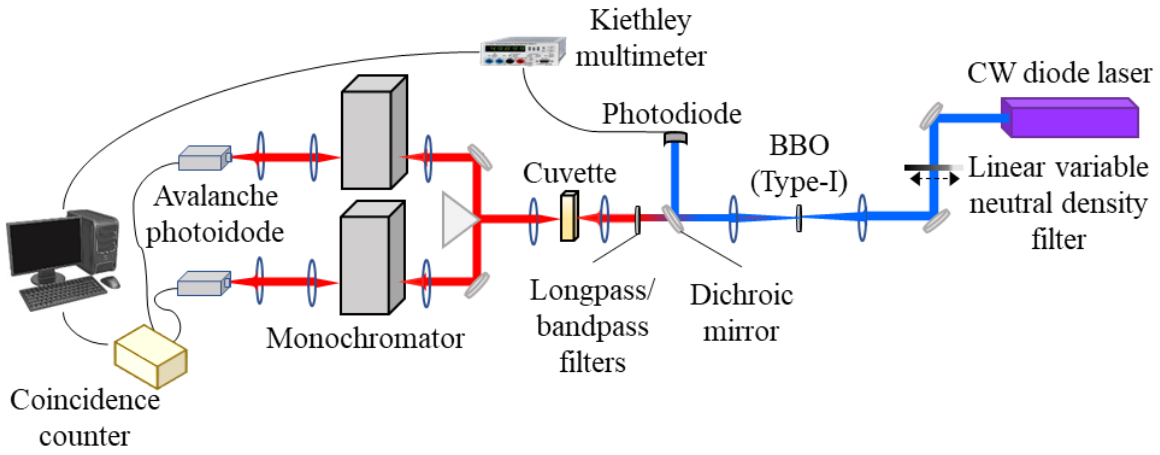

Figure 2.12. Experimental setup for measuring the joint frequency spectrum.

As with using the monochromator as a frequency filter, a lens focuses the light into the monochromator and another lens collimates the output. The output is then focused onto the APD, and coincidence counts are measured between the two APDs. The SPDC joint frequency spectrum, which is a 2D spectrum with signal photon frequency on the x-axis and idler photon frequency on the y-axis, was measured using the following procedure. A bandpass filter

centered at 810 nm with 80 nm bandwidth is placed in the SPDC path before the photons are split. The monochromators and APDs do not have sufficient quantum efficiency across the entire SPDC spectrum to accurately measure the entire unfiltered SPDC frequency spectrum. The bandpass filter keeps the frequency bandwidth within the detection range while also providing a large enough bandwidth for accurate extrapolation in a later step. With the bandpass filter in place, the entrance and exit slits for both monochromators are adjusted to the smallest possible width that allows enough photons to be transmitted for accurate coincidence count detection. In this work, the slits were adjusted to achieve at least 10^3 coincidence counts/s when both monochromators are set to 810 nm, which corresponded to a frequency bandwidth of ~ 3 nm. The monochromator (Alice) for the signal photon is then set to a central wavelength outside the bandpass filter range (ex.: 750 nm). The other monochromator (Bob) for the idler photon is scanned across the entire bandpass filter range (ex.: 750-870 nm). The coincidence counts are measured 3 times for 1 s each at 1 nm increments. The average of the 3 measurements for each wavelength is recorded in a Labview program. Alice's monochromator is then changed to a new central wavelength (ex.: 760 nm), and Bob's scan is repeated. This procedure is repeated until Alice's central wavelength is past the bandpass filter range (ex.: 870 nm).

The collected spectra are cross-sections of the 2D joint frequency spectrum of the SPDC. The peak in each spectra that Bob measures during his scans occurs at the wavelength that conserves energy from the pump beam with Alice's current central wavelength. Therefore, whenever Alice changes her central wavelength, Bob measures a peak at a different wavelength than his previous scan. The width of Bob's spectrum is determined by the pump laser spectral width (1 nm) and the spectral resolution of the monochromators (3 nm). Since the monochromator bandwidth was greater than the pump spectral width, the measured spectral width of Bob's scans are broader than what the actual spectral width of the SPDC is expected to be. To obtain the full joint frequency spectrum, the collected spectra was plotted in Origin and fit with the following double-Gaussian:

$$z = A \cdot exp\left[\begin{matrix} -\frac{1}{2}\left(\frac{x\cdot cos(\theta)+y\cdot sin(\theta)-x_c\cdot cos(\theta)-y_c\cdot sin(\theta)}{\omega_+}\right)^2 \\ -\frac{1}{2}\left(\frac{-x\cdot sin(\theta)+y\cdot cos(\theta)+x_c\cdot sin(\theta)-y_c\cdot cos(\theta)}{\omega_-}\right)^2 \end{matrix}\right] \tag{2.15}$$

Here, A is the amplitude, x (y) is the frequency along the x-(y-)axis, which have centers x_c (y_c), and θ is the angle between the anti-diagonal and the x-axis. An example is shown in Fig. 2.13.

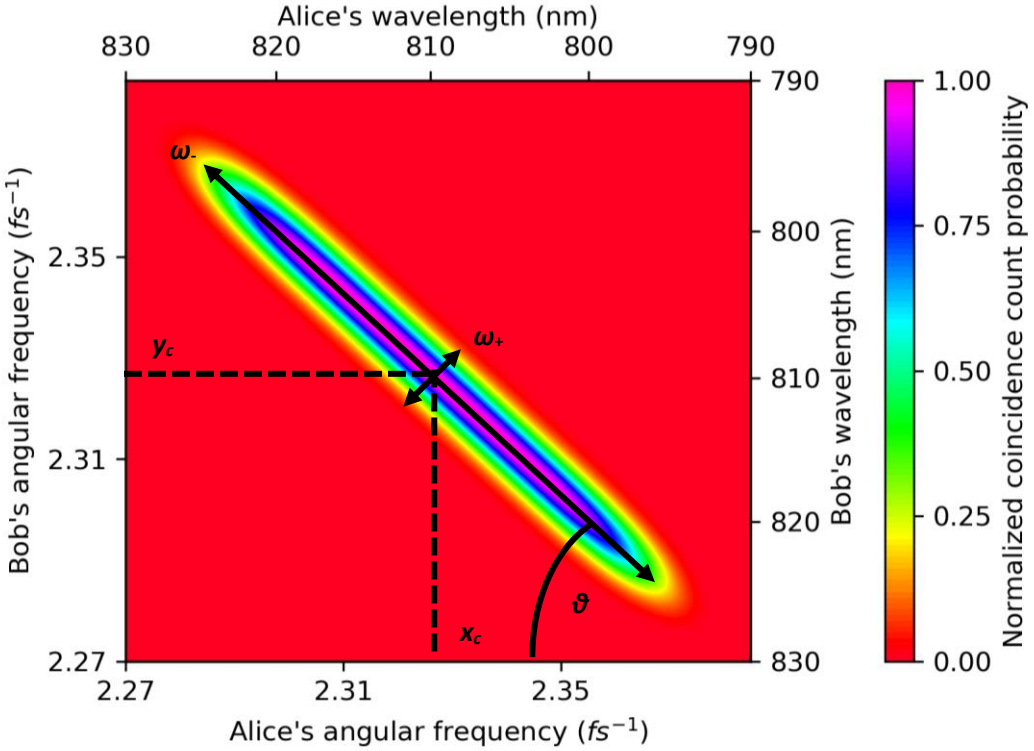

Figure 2.13. Example of a double-Gaussian of the form in eq. 2.15.

The width ω_- is the Fourier conjugate of T_e. Therefore, T_e can be calculated from the inverse of ω_-. Additionally, from this double-Gaussian, the widths along the diagonal and anti-diagonal can be used to approximate the degree of frequency entanglement. The Fedorov ratio, R, is calculated as:[31]

$$R = \frac{\omega_-}{\omega_+} \tag{2.16}$$

A more accurate calculation of the degree of frequency entanglement is through the Schmidt decomposition. As explained in Chapter 1.4.5, the Schmidt decomposition reveals the actual frequency states that the two photons are in once they interact with an object.[32] Before the interaction, the photons are in superpositions of these possible states. The more states in the superposition, the stronger the entanglement. The Schmidt decomposition of the fitted double-Gaussian in eq. 2.15 was performed using a free-to-use Python program.[33] Mathematically, the Schmidt decomposition is the continuous function form of the singular value decomposition

(SVD), which decomposes matrices into a basis set. The Schmidt decomposition is easiest calculated by converting the double-Gaussian obtained from the fitting with eq. 2.15 into matrix form. The SVD is then performed on the matrix using the svd function in the numpy.linalg module. The columns in the *U* and *V* matrices of the SVD are the vectors for the signal and idler frequency eigenstates. Their products are the Schmidt modes. The singular values are the Schmidt coefficients. To quantify the degree of frequency entanglement, the number of effective occupied Schmidt modes is calculated using eq. 1.35 and/or the entropy of entanglement using eq. 1.36.

2.3 Theoretical Methods

2.3.1 Multireference Configuration Interaction

The properties of molecular states can be calculated if one knows the correct wave function to describe the state of interest. In particular, the states of interest for quantum chemistry calculations are the energy eigenstates of the Hamiltonian, *H*, operator. With the eigenstates, Ψ_i, known, their energies, E_i, can be calculated as:

$$E_i = \frac{\langle \Psi_i | \hat{H} | \Psi_i \rangle}{\langle \Psi_i | \Psi_i \rangle} \tag{2.17}$$

The dipole moments, μ_{ji}, between states Ψ_i and Ψ_j can also be calculated with the dipole operator, μ, as:

$$\mu_{ji} = \langle \Psi_j | \hat{\mu} | \Psi_i \rangle \tag{2.18}$$

If $i \neq j$, the dipole is the transition dipole moment (TDM) between states Ψ_i and Ψ_j. If $i = j$, the dipole is the permanent dipole moment of state Ψ_i.

The challenge for quantum chemistry calculations is obtaining the correct wave functions to substitute into eq. 2.17-2.18. One of the best methods for calculating these wave functions is through configuration interaction (CI).[34] In this method, a reference electronic configuration (obtained from the method in the next section) for the eigenstate of the interest, say the ground state, is used as a starting point. Additional configurations are determined by exciting electrons from the reference configuration to unoccupied higher energy states. For example, the singly excited configurations are those that have one electron from the reference configuration excited to a higher state, doubly excited configurations have two electrons

excited, etc. The reference configuration and all of the excitation configurations are "interacted" by forming a linear combination of the configurations:[34]

$$|\Psi_i\rangle = \sum_k c_k|\psi_k\rangle + \sum_a c_a|\psi^a\rangle + \sum_{ab} c_{ab}|\psi^{ab}\rangle + \cdots \quad (2.19)$$

The states ψ^a and ψ^{ab} are the singly and doubly excited configurations. The coefficients for the linear combination are optimized such that the resulting wave function will produce the minimum possible energy in the Schrodinger equation:[34]

$$\hat{H}\vec{c} = \varepsilon\hat{S}\vec{c} \quad (2.20)$$

Here, c is the eigenvector of the coefficients c_k, S is the matrix with elements of the overlap between the states $|\psi_k\rangle$, and ε is the energy eigenvalue. In general, multiple eigenstates of the molecule can be solved for, turning c into a matrix whose columns are the eigenvectors for each eigenstate and turning ε into a diagonal matrix of the energies.

If one were to consider every possible excitation configuration in eq. 2.19, the method is known as *full CI* and results in the exact wave function for the eigenstate. In reality, full CI is only possible for the smallest of molecules due to the computational cost being too large as the molecule grows in size and number of electrons. Truncated CI methods provide a compromise between computational cost and wave function accuracy. Truncated CI methods limit the excitations considered, such as only considering the singly excited configurations (CIS) or only considering the singly and doubly excited configurations (CISD). When using truncated CI methods, the accuracy of the energies of ground and excited eigenstates can be improved by considering how these eigenstates can be correlated with each other. This is accomplished by using multiple reference configurations in the CI method, known as multireference CI (MRCI).[35] In MRCI, the excitations from the ground reference configuration are considered, and well as excitations from excited state reference configurations:[36-38]

$$|\Psi_i\rangle = \sum_k c_k|\psi_k\rangle + \sum_S \sum_a (\vec{c}_S)_a|\psi_S^a\rangle + \sum_P \sum_{ab} (C_P)_{ab}\left|\psi_P^{ab}\right\rangle + \cdots \quad (2.21)$$

Here, S and P refer to states that have N-1 and N-2 electron holes, respectively. This linear combination is then optimized to minimize the energy eigenvalues. MRCI is better at calculating the energy gap between states since it is better at considering how the ground state may have some correlation with the excited states. Single reference CI will typically overestimate the excitation energies.

2.3.2 State-Averaged Complete Active Space Self-Consistent Field

To complete the MRCI calculations, reference configurations must be chosen as the starting point for the excitation configurations. One of the earliest methods to approximate the wave function of a many-body system was Hartree-Fock.[34] This method assumes that the wave function can be described as a single Slater determinant, where the determinant represents each electron, e_N, being in a spin orbital, φ_N:[34]

$$|\psi_k\rangle = \frac{1}{\sqrt{N!}}\begin{vmatrix} \phi_1(e_1) & \cdots & \phi_N(e_1) \\ \vdots & \ddots & \vdots \\ \phi_1(e_N) & \cdots & \phi_N(e_N) \end{vmatrix} \tag{2.22}$$

The Slater determinant follows the antisymmetric rule for fermions, where swapping two electrons in their respective spin orbitals results in a sign flip of the wave function. Hartree-Fock is the *self-consistent field* (SCF) method that optimizes the spin orbitals to produce the Slater determinant that minimizes the energy when solving the Schrodinger equation. Where Hartree-Fock fails is in considering how the electrons are correlated with each other. To consider the correlations, *multi-configurational* SCF (MCSCF) uses a set of Slater determinants to approximate the wave function, where each Slater determinant is for an excited electron configuration. There are multiple methods for completing MCSCF, and the one used in this work was *complete active space* SCF (CASSCF). In CASSCF, an active space is defined where the orbitals with occupied electrons can have their electrons excited, and unoccupied orbitals can receive an excited electron.[36, 38] Orbitals below the active space are "frozen" such that their electrons are never excited. Orbitals above the active space of "virtual" such that they will never receive an excited electron. Each combination of electrons with the active space has a Slater determinant, and the linear combination of these determinants is optimized to have the lowest possible energy. State-averaged CASSCF means that the minimized energy is the average energy of the molecular eigenstates being calculated. The final configurations calculated from CASSCF for the ground and excited eigenstates are used as the reference configurations for MRCI.

2.3.3 Second-Linear Response Time-Dependent Density Functional Theory

While MRCI provides very accurate approximations of the molecular eigenstates' wave functions, the calculations can only be applied to very small systems to complete the calculation in a reasonable amount of time and memory. Other quantum chemistry methods

attempt to calculate accurate approximations of wave functions for larger molecules. One of the most common approaches is *density functional theory* (DFT).[39, 40] In DFT, instead of considering how each electron in the molecule is configured, this many-body problem is mapped into a single-body problem by defining an electron density functional. The density functional, $n(r)$, which is a function of the wave function Ψ, describes the probability of finding an electron at each point in space across the structure of the molecule:[40]

$$n(\vec{r}) = \int d^3\vec{r}_2 \dots \int d^3\vec{r}_N \Psi^*(\vec{r}, \vec{r}_2, \dots \vec{r}_N)\Psi(\vec{r}, \vec{r}_2, \dots \vec{r}_N) \tag{2.23}$$

By knowing how the electron density is arranged for an eigenstate, eq. 2.23 can be reversed to extract the wave function. As with MRCI, the procedure for DFT is to minimize the energy. This is accomplished by calculating the eigenvalues for each energy operator of the Hamiltonian (potential energy, *V*, kinetic energy, *T*, and electron-electron interaction energy, *U*). The kinetic energy, $\varepsilon_{k,I}$, is calculated using the classical kinetic energy operator:[40]

$$-\frac{\hbar^2}{2m}\nabla^2\varphi_i(\vec{r}) = \varepsilon_{k,i}\varphi_i(\vec{r}) \tag{2.24}$$

Here, the orbitals φ_i comprise the density functional as:[40]

$$n(\vec{r}) = \sum_i |\varphi_i(\vec{r})|^2 \tag{2.25}$$

The potential energy and electron-electron interaction energy can be expressed:[39]

$$V_s(\vec{r}) = V_{ext}(\vec{r}) + \sum_k \frac{Z_k}{|\vec{r}-\vec{r}_k|} + \int \frac{n(\vec{r}\prime)}{|\vec{r}-\vec{r}\prime|} d^3\vec{r} + V_{XC}[n(\vec{r})] \tag{2.26}$$

Here, $V_{ext}(r)$ is the potential energy from an external field (such as a light field), the second term is the electron-nucleus attraction potential energy, the third term as the classical electron-electron repulsion potential, and V_{XC} is the exchange-correlation potential. V_{XC} provides corrections to the classical kinetic energy and classical electron-electron repulsion energy that accounts for the true quantum nature of the electrons, namely the exchange and correlation energies. The exchange energy results from the electrons being fermions, meaning no two electrons can have the exact same state, so electrons with the same spin will remain further apart in space than would be predicted using just the classical repulsion energy. The correlation energy considers how the position, momentum, etc. of one electron in the molecule affects the same properties of the other electrons. This last term is what limits the accuracy of DFT since it is usually not known explicitly. Many approximations exist, though discussion of them is outside the scope of this dissertation. The potential energy is thus calculated as:[40]

$$V_s(\vec{r})\varphi_i(\vec{r}) = \varepsilon_{s,i}\varphi_i(\vec{r}) \tag{2.27}$$

Optimizing the orbitals φ_i to minimize the total energy $E_s = \varepsilon_k + \varepsilon_s$ results in the final $n(r)$. Of course, the third term in eq. 2.26 contains the density functional, and solving eq. 2.26 is part of the process in optimizing the density functional. DFT is thus self-consistent and is solved iteratively until the calculated density functional matches the input density functional for that same iteration through the loop.

DFT is used principally to calculate the ground state wave function of a molecule. To calculate the wave functions for excited states, which are time-dependent states, *time-dependent* DFT (TDDFT) is required. TDDFT is analogous to solving DFT, with the exception that the external potential, $V(r,t)$ is now time-dependent. As a result, $n(r,t)$ becomes time-dependent. Now, one solves the time-dependent Schrodinger equation to calculate the energy:[40]

$$\hat{H}(t)|\Psi(t)\rangle = i\hbar\frac{\partial}{\partial t}|\Psi(t)\rangle \tag{2.28}$$

Solving for the density functional with TDDFT can be quite computationally expensive. To simplify the calculation and minimize the computational cost, if the perturbation with the light field is assumed to be small enough that the ground state is not completely destroyed, the TDDFT calculation can be limited to first-order in the perturbation, hence *linear response* TDDFT (LR-TDDFT). In other words, when the light field is sufficiently weak, the density functional will retain much of its ground state character with the addition of some new, small perturbed ground state character. The Hamiltonian can then be described as:[40]

$$\hat{H}(t) = \hat{H}_0 + \hat{V}_{ext}(t) \tag{2.29}$$

The total Hamiltonian is simply the ground state Hamiltonian with no field applied, H_0, plus the Hamiltonian for the external field, V_{ext}(t), which is time-dependent.

LR-TDDFT can be used to calculate the properties of a singly excited state in a molecule, such as with one-photon absorption. However, for calculating the properties of a state excited by a two-photon absorption, two interactions between the density functional and light field must be considered. Perhaps the most intuitive way to accomplish this is to take the TDDFT calculation to second-order in the density functional response, known as quadratic TDDFT. However, quadratic TDDFT scales as N^6, where N is the number of electrons, making calculation for large organic chromophores too computationally intensive.[41] A new approach from the Schatz group in the Northwestern University chemistry department is *second linear response* TDDFT (SLR-TDDFT), which scales as N^4.[41, 42] The idea is to complete LR-TDDFT

twice. The first time it is completed as explained above. The resulting output state from the first LR-TDDFT, which is the ground orbitals plus some perturbation of the ground orbitals, is used as the input reference state for the second LR-TDDFT. The degree to which to include the perturbed part is controlled with the scalar λ:[41]

$$\varphi_{i,SLR}(\vec{\boldsymbol{r}}) = \varphi_i(\vec{\boldsymbol{r}}) + \lambda \sum_a X_{ai}^I \varphi_a(\vec{\boldsymbol{r}}) \tag{2.30}$$

Here, φ_i are the ground state orbitals and φ_a are the virtual orbitals that can receive an electron from the perturbation. The perturbation is a linear combination of the virtual orbitals, with coefficients X_a. To calculate SLR-TDDFT for a particular excited state, the virtual orbitals for that chosen excited state are used for φ_a. They are added to the ground state orbitals to some degree, determined by λ, resulting in the input orbitals for the second LR-TDDFT, $\varphi_{i,SLR}$.

References

1. Hilborn, R. C., Einstein coefficients, cross sections, f values, dipole moments, and all that. *American Journal of Physics* **1982,** *50* (11), 982-986.
2. Swinehart, D. F., The Beer-Lambert Law. *Journal of Chemical Education* **1962,** *39* (7), 333.
3. Lakowicz, J. R., *Principles of fluorescence spectroscopy*. Springer science & business media: 2013.
4. Weber, G.; Teale, F. W. J., Determination of the absolute quantum yield of fluorescent solutions. *Transactions of the Faraday Society* **1957,** *53* (0), 646-655.
5. Kasha, M., Characterization of electronic transitions in complex molecules. *Discussions of the Faraday Society* **1950,** *9* (0), 14-19.
6. Born, M.; Oppenheimer, R., Zur Quantentheorie der Molekeln. *Annalen der Physik* **1927,** *389* (20), 457-484.
7. Birks, J. B., Fluorescence Quantum Yield Measurements. *Journal of research of the National Bureau of Standards. Section A, Physics and chemistry* **1976,** *80A* (3), 389-399.
8. Göppert-Mayer, M., Über Elementarakte mit zwei Quantensprüngen. *Annalen der Physik* **1931,** *401* (3), 273-294.
9. Denk, W.; Piston, D. W.; Webb, W. W., Two-photon molecular excitation in laser-scanning microscopy. In *Handbook of biological confocal microscopy*, Springer: 1995; pp 445-458.
10. Denk, W.; Strickler, J. H.; Webb, W. W., Two-photon laser scanning fluorescence microscopy. *Science* **1990,** *248* (4951), 73.
11. Ash, C.; Dubec, M.; Donne, K.; Bashford, T., Effect of wavelength and beam width on penetration in light-tissue interaction using computational methods. *Lasers in medical science* **2017,** *32* (8), 1909-1918.
12. Kwon, K.; Son, T.; Lee, K.-J.; Jung, B., Enhancement of light propagation depth in skin: cross-validation of mathematical modeling methods. *Lasers in Medical Science* **2009,** *24* (4), 605-615.
13. Bonin, K. D.; McIlrath, T. J., Two-photon electric-dipole selection rules. *Journal of the Optical Society of America B* **1984,** *1* (1), 52-55.
14. Ansbacher, T.; Srivastava, H. K.; Stein, T.; Baer, R.; Merkx, M.; Shurki, A., Calculation of transition dipole moment in fluorescent proteins—towards efficient energy transfer. *Physical Chemistry Chemical Physics* **2012,** *14* (12), 4109-4117.
15. Deibel, C.; Strobel, T.; Dyakonov, V., Role of the Charge Transfer State in Organic Donor–Acceptor Solar Cells. *Advanced Materials* **2010,** *22* (37), 4097-4111.
16. Falke, S. M.; Rozzi, C. A.; Brida, D.; Maiuri, M.; Amato, M.; Sommer, E.; De Sio, A.; Rubio, A.; Cerullo, G.; Molinari, E.; Lienau, C., Coherent ultrafast charge transfer in an organic photovoltaic blend. *Science* **2014,** *344* (6187), 1001.
17. Dias, F. B.; Bourdakos, K. N.; Jankus, V.; Moss, K. C.; Kamtekar, K. T.; Bhalla, V.; Santos, J.; Bryce, M. R.; Monkman, A. P., Triplet Harvesting with 100% Efficiency by Way of Thermally Activated Delayed Fluorescence in Charge Transfer OLED Emitters. *Advanced Materials* **2013,** *25* (27), 3707-3714.

18. Yin, M.; Li, H. P.; Tang, S. H.; Ji, W., Determination of nonlinear absorption and refraction by single Z-scan method. *Applied Physics B* **2000,** *70* (4), 587-591.
19. Kaiser, W.; Garrett, C. G. B., Two-Photon Excitation in Ca${\mathrm{F}}_{2}$: ${\mathrm{Eu}}^{2+}$. *Physical Review Letters* **1961,** *7* (6), 229-231.
20. Albota, M. A.; Xu, C.; Webb, W. W., Two-photon fluorescence excitation cross sections of biomolecular probes from 690 to 960 nm. *Applied Optics* **1998,** *37* (31), 7352-7356.
21. Xu, C.; Webb, W. W., Measurement of two-photon excitation cross sections of molecular fluorophores with data from 690 to 1050 nm. *Journal of the Optical Society of America B* **1996,** *13* (3), 481-491.
22. Fei, H.-B.; Jost, B. M.; Popescu, S.; Saleh, B. E. A.; Teich, M. C., Entanglement-Induced Two-Photon Transparency. *Physical Review Letters* **1997,** *78* (9), 1679-1682.
23. Klyshko, D. N.; Penin, A. N.; Polkovnikov, B. F., Parametric Luminescence and Light Scattering by Polaritons. *Soviet Journal of Experimental and Theoretical Physics Letters* **1970,** *11*, 5.
24. Burnham, D. C.; Weinberg, D. L., Observation of Simultaneity in Parametric Production of Optical Photon Pairs. *Physical Review Letters* **1970,** *25* (2), 84-87.
25. Javanainen, J.; Gould, P. L., Linear intensity dependence of a two-photon transition rate. *Physical Review A* **1990,** *41* (9), 5088-5091.
26. Harpham, M. R.; Süzer, Ö.; Ma, C.-Q.; Bäuerle, P.; Goodson, T., Thiophene Dendrimers as Entangled Photon Sensor Materials. *Journal of the American Chemical Society* **2009,** *131* (3), 973-979.
27. Saleh, B. E. A.; Jost, B. M.; Fei, H.-B.; Teich, M. C., Entangled-Photon Virtual-State Spectroscopy. *Physical Review Letters* **1998,** *80* (16), 3483-3486.
28. Schlawin, F.; Dorfman, K. E.; Mukamel, S., Entangled Two-Photon Absorption Spectroscopy. *Accounts of Chemical Research* **2018,** *51* (9), 2207-2214.
29. Dorfman, K. E.; Schlawin, F.; Mukamel, S., Nonlinear optical signals and spectroscopy with quantum light. *Reviews of Modern Physics* **2016,** *88* (4), 045008.
30. Mukamel, S.; Freyberger, M.; Schleich, W.; Bellini, M.; Zavatta, A.; Leuchs, G.; Silberhorn, C.; Boyd, R. W.; Sánchez-Soto, L. L.; Stefanov, A.; Barbieri, M.; Paterova, A.; Krivitsky, L.; Shwartz, S.; Tamasaku, K.; Dorfman, K.; Schlawin, F.; Sandoghdar, V.; Raymer, M.; Marcus, A.; Varnavski, O.; Goodson, T.; Zhou, Z.-Y.; Shi, B.-S.; Asban, S.; Scully, M.; Agarwal, G.; Peng, T.; Sokolov, A. V.; Zhang, Z.-D.; Zubairy, M. S.; Vartanyants, I. A.; del Valle, E.; Laussy, F., Roadmap on quantum light spectroscopy. *Journal of Physics B: Atomic, Molecular and Optical Physics* **2020,** *53* (7), 072002.
31. Fedorov, M. V.; Miklin, N. I., Schmidt modes and entanglement. *Contemporary Physics* **2014,** *55* (2), 94-109.
32. Ekert, A.; Knight, P. L., Entangled quantum systems and the Schmidt decomposition. *American Journal of Physics* **1995,** *63* (5), 415-423.
33. Ho, K.-Y. *pyqentangle*, 3.1.7; 2020.
34. Shavitt, I., The method of configuration interaction. In *Methods of electronic structure theory*, Springer: 1977; pp 189-275.
35. Szalay, P. G.; Müller, T.; Gidofalvi, G.; Lischka, H.; Shepard, R., Multiconfiguration Self-Consistent Field and Multireference Configuration Interaction Methods and Applications. *Chemical Reviews* **2012,** *112* (1), 108-181.
36. Werner, H. J., Molecular properties from MCSCF-SCEP wave functions. II. Calculation of electronic transition moments. *The Journal of Chemical Physics* **1984,** *80* (10), 5080-5084.

37. Werner, H. J.; Knowles, P. J., An efficient internally contracted multiconfiguration–reference configuration interaction method. *The Journal of Chemical Physics* **1988,** *89* (9), 5803-5814.
38. Werner, H. J.; Reinsch, E. A., The self-consistent electron pairs method for multiconfiguration reference state functions. *The Journal of Chemical Physics* **1982,** *76* (6), 3144-3156.
39. Burke, K., Perspective on density functional theory. *The Journal of Chemical Physics* **2012,** *136* (15), 150901.
40. Engel, E.; Dreizler, R. M., *Density functional theory*. Springer: 2013.
41. Mosquera, M. A.; Chen, L. X.; Ratner, M. A.; Schatz, G. C., Sequential double excitations from linear-response time-dependent density functional theory. *J. Chem. Phys.* **2016,** *144* (20), 204105.
42. Mosquera, M. A.; Jackson, N. E.; Fauvell, T. J.; Kelley, M. S.; Chen, L. X.; Schatz, G. C.; Ratner, M. A., Exciton Absorption Spectra by Linear Response Methods: Application to Conjugated Polymers. *J. Am. Chem. Soc.* **2017,** *139* (10), 3728-3735.

CHAPTER 3

Predicting and Controlling Entangled Two-Photon Absorption in Diatomic Molecules

The work in this chapter was published as the journal article:

Burdick, R. K.; Varnavski, O.; Molina, A.; Upton, L.; Zimmerman, P.; Goodson, T.: Predicting and Controlling Entangled Two-Photon Absorption in Diatomic Molecules." *The Journal of Physical Chemistry A* **2018,** *122* (41), 8198-8212.

Modifications have been made for the style and content of this dissertation. References and supporting information for the manuscript are included in this chapter.

In this chapter, I calculated all of the ETPA cross-sections vs the entanglement time, T_e, using the molecular parameters that were calculated by Andrew Molina and Paul Zimmerman. I completed the analysis of how the wave nature of each of the ETPA pathways interfere with each other and contribute to the ETPA cross-section. I performed the approximation calculations for using a one or two dominant pathways and compared the resulting oscillation periods to the full calculation oscillation periods.

3.1 Abstract

The use of nonclassical states of light to probe organic molecules has received great attention due to the possibility of providing new and detailed information regarding molecular excitations. Experimental and theoretical results have been reported which show large enhancements of the nonlinear optical responses in organic materials due to possible virtual electronic state interactions with entangled photons. In order to predict molecular excitations with nonclassical light, more detailed investigations of the parameters involved must be carried out. In this report we investigate the details of the state-to-state parameters important in calculating the contribution of particular transitions involved in the entangled two-photon absorption process for diatomic molecules. The theoretical discussion of the entangled two-photon process is described for a set of diatomic molecules. Specifically, we provide detailed quantum chemical calculations which give accurate energies and transition moments for selection-rule allowed intermediate states

important in the entangled nonlinear effect for the diatomic molecules. These results are used to estimate in a more accurate manner the nonmonotonic behavior of the entangled two-photon absorption cross-section. We also derive accurate approximations that can be used to predict the period between entanglement-induced transparencies without needing exact values of the transition dipole moments. These results suggest that with the additional parameters allotted by the entangled two-photon absorption (in comparison to the classical case), it may be possible to predict and later control the nonlinear absorption and transparency of a molecule at a constant incident photon frequency.

3.2 Introduction

The interaction of light with organic matter has led to the discovery of many applications.[1] The linear (as well as nonlinear) optical responses of organic materials can be explained to a great extent by considering the electronic states of the molecular selection rules regarding the population of various transitions in organic molecules as a result of the interaction with light.[2-7] These processes are well described with the application of classical light. There has been rising interest in the use of non-classical states of light for the purposes of exciting organic molecules as well.[8-14] Generation of entangled photons was first reported by Kocher and Commins[15] where a calcium atomic cascade emitted polarization-correlated photons in a non-Poissonian distribution. Basché et al.[16] later extended emission of entangled photons to a molecular system by exciting a single pentacene molecule in a *p*-terphenyl crystal, leading to anti-bunching fluorescence. In most experiments today, entangled photons are generated from the process of spontaneous parametric downconversion (SPDC), first shown by Klyshko et. al.[17] SPDC has allotted new insights into the possibility of exciting electronic states with entangled photons where the population is extremely low.[11,12,18-21] In particular, nonlinear optical methods which require relatively large excitation flux densities may be carried out at orders of magnitude smaller flux densities with non-classical light, with experimental results showing a difference of up to 10 orders of magnitude.[8-11,14,22,23] The results and discussions of these possibilities have led to many suggestions regarding the use of entangled photons in spectroscopy and to creation of a very sensitive detection methodology.[9,11,13,14,24-30] For example, there have been reported proposals of novel spectroscopic techniques such as femtosecond stimulated Raman spectroscopy which offers the possibility of combining entangled photons with interference detection to select matter pathways.[31] This would

ultimately offer enhanced resolution aided by the use of entangled photons. From such reports it is now accepted that entangled photons may provide a unique temporal and spectral detection window that can better resolve fast excited-state dynamics compared to classical and correlated disentangled states of light.[10,14,27,28,32,33] However, there is much to learn about the nature of the interaction of electronic states in organic molecules with non-classical states of light. It has been shown that the entangled two-photon absorption (ETPA) process is sensitive to the pathway and available excited states of the molecules investigated.[11,13,18,25,26,29,30,34] It was further found that there are additional parameters which can drive the population of particular optical transitions when one utilizes entangled photons. The entanglement time, delay, and area are critical parameters which are connected to the nonmonotonic absorption process observed in the entangled two-photon experiments.[8-11,14,25,26,34] Recent reports have also observed the nonmonotonic behavior in the resulting fluorescence from excitation with non-classical light.[11,14]

Theoretically, there have been reports of the connection of the fourth-order correlation function with the calculation of the ETPA cross-section.[24-26,34] In order to describe these interactions between light and matter one often employs higher order optical coherence theory. Classical two-photon absorption (TPA) can be described with a second order correlation function. The classical two-photon absorption cross-section, δ_R, is given by:[11]

$$\delta_R = \frac{B}{\hbar^2\varepsilon_0^2}\omega_0^2\delta(\varepsilon_f - \varepsilon_g - 2\omega_0) \times \left|\frac{1}{(\omega_0+\varepsilon_g-\varepsilon_e)-i\kappa_e/2}\mu_{fe}\cdot e\mu_{eg}\cdot e + \frac{1}{\omega_0-i\kappa_g/2}\mu_{fg}\cdot e\mu_{gg}\cdot e + \frac{1}{-\omega_0-i\kappa_f/2}\mu_{ff}\cdot e\mu_{fg}\cdot e\right|^2 \quad (3.1)$$

where ω_0 is the energy of each photon, e is the polarization of the field, ε_g, ε_e, and ε_f are the energies of the ground, intermediate, and excited state, respectively, μ_{ij} are the transition dipole matrix elements, and κ_j are the state linewidths. This equation assumes that both photons in this process have the same polarization and frequency. The first term in eq. 3.1 describes TPA occurring through an intermediate level. The second and third terms describe a process involving permanent dipoles. In the classical case these two terms can be simplified to one contribution proportional to the permanent dipole difference $\Delta\mu_{fg} = \mu_{ff} - \mu_{gg}$. The description beyond the classical regime of nonlinear optical responses of organic materials, which involves the effects of quantum correlated photons in spectroscopy, gives rise to the quantum effects caused by entangling the excitation source and a change in the interaction mechanism between the field and

the material system.[24-26] Not only is the cross-section modified, but also the interactions are no longer intensity-squared dependent.[24-26] The effects of the interactions between entangled photon states and matter have not yet been exploited to the same extent as classical photons utilizing quantum computational methods for the electronic structure of organic molecules.

As mentioned above, in order to describe the fields generated by entangled photons, fourth-order correlation functions are needed.[24-26,34] Developing theoretical models to describe this mechanism in certain organic systems with particular electronic (virtual) states is a key critical step in understanding and controlling the entangled photon absorption process.[24-26,34] The ETPA cross-section has been found to have a dependence on the detuning energy (Δ_j) between the entangled photon and the intermediate state, as well as on the intermediate state linewidth, and the transition matrix elements.[22,24-26,34] For a system with ground, intermediate, and excited state wavefunctions, in the Dirac notation $|g\rangle$, $|e\rangle$, and $|f\rangle$, respectively, and under the simplified case of a monochromatic pump beam, without a delay between signal and idler beam, one finds for σ_e:[11]

$$\sigma_e = \frac{A}{\hbar^2 \varepsilon_0^2 A_e T_e} \omega_0^2 \delta(\varepsilon_f - \varepsilon_g - 2\omega_0) \times \left| \frac{1-e^{-i(\omega_0+\varepsilon_g-\varepsilon_e)T_e-\kappa_e T_e/2}}{(\omega_0+\varepsilon_g-\varepsilon_e)-i\kappa_e/2} \mu_{fe} \cdot e_i \mu_{eg} \cdot e_s + \right.$$
$$\left. \frac{1-e^{-i\omega_0 T_e-\kappa_g T_e/2}}{\omega_0-i\kappa_g/2} \mu_{fg} \cdot e_i \mu_{gg} \cdot e_s + \frac{1-e^{i\omega_0 T_e-\kappa_f T_e/2}}{-\omega_0-i\kappa_f/2} \mu_{ff} \cdot e_i \mu_{fg} \cdot e_s \right|^2 \quad (3.2)$$

where A_e and T_e are entanglement area and entanglement time, respectively, ω_0 is the energy of each photon, e_s and e_i are the polarizations of signal and idler photons, respectively, ε_g, ε_e, and ε_f are the energies of the ground, intermediate, and excited state, respectively, μ_{ij} are the transition dipole matrix elements, and κ_j are the state linewidths. A level scheme as depicting two different pathways may be suggested where the ETPA could occur through an intermediate level "e," or the ETPA could result from the utilization of permanent dipoles between the initial state "g" and final state "f."[11] Interestingly, it is these pathways, combined with good estimates of the populations of virtual states, which could give rise to new and interesting features related to the use of non-classical light for spectroscopy as well as quantum sensing.[11,12,18,20,23-26,30]

The terms inside the modulus squared in eq. 3.2 can be rearranged to highlight the wave nature of each entangled two-photon transition pathway:

$$\sigma_e \propto \left| \frac{\mu_{fe}\cdot e_i \mu_{eg}\cdot e_s}{(\omega_0+\varepsilon_g-\varepsilon_e)-\frac{i\kappa_e}{2}} - \frac{\mu_{fe}\cdot e_i \mu_{eg}\cdot e_s}{(\omega_0+\varepsilon_g-\varepsilon_e)-\frac{i\kappa_e}{2}} e^{-i(\omega_0+\varepsilon_g-\varepsilon_e)T_e-\frac{\kappa_e T_e}{2}} + \frac{\mu_{fg}\cdot e_i \mu_{gg}\cdot e_s}{\omega_0-\frac{i\kappa_g}{2}} - \right.$$

$$\left. \frac{\mu_{fg}\cdot e_i \mu_{gg}\cdot e_s}{\omega_0-\frac{i\kappa_g}{2}} e^{-i\omega_0 T_e-\frac{\kappa_g T_e}{2}} + \frac{\mu_{ff}\cdot e_i \mu_{fg}\cdot e_s}{-\omega_0-\frac{i\kappa_f}{2}} - \frac{\mu_{ff}\cdot e_i \mu_{fg}\cdot e_s}{-\omega_0-\frac{i\kappa_f}{2}} e^{i\omega_0 T_e-\kappa_f T_e/2} \right|^2 \quad (3.3)$$

In eq. 3.3 above, each pathway can be expressed in a simplified wave form such that:

$$\sigma_e \propto \left| \sum_j A_j - A_j e^{i\omega_j T_e} \right|^2 \quad (3.4)$$

where A_j is the amplitude of each wave and ω_j is the frequency. Each wave is also offset from oscillating around 0 by its amplitude. Therefore, the ETPA cross-section is proportional to a sum of waves offset from oscillating around 0 by the sum of the amplitudes of the waves. This wave nature of the transition pathways is purely a quantum effect that does not appear in the classical TPA process in eq. 3.1. For the virtual-state pathways, the frequency of the ETPA transition in wave form is the negative of the detuning energy. For the two permanent dipole pathways, the frequency of the wave is the negative (positive) of the frequency of one of the incident photons. These different pathways and their frequencies, ω_j, are shown in the energy level diagrams in Fig. 3.1 below. The state linewidths of these BO atomic states are assumed to be $\kappa_j << 1$.

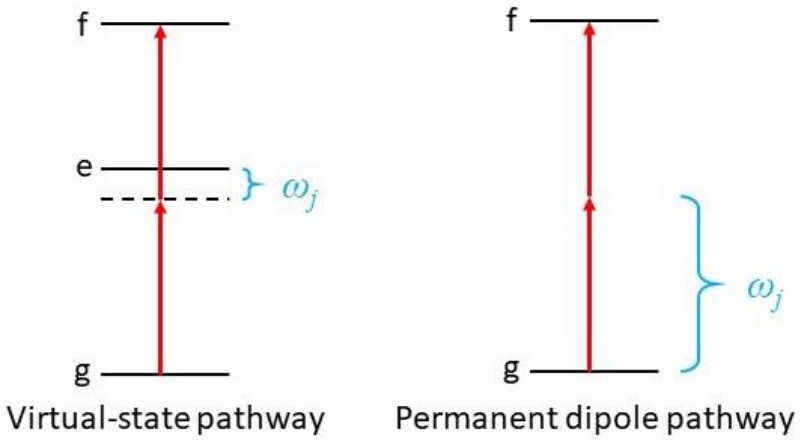

Figure 3.1. Energy level diagrams for the two pathways in ETPA, with the quantity that represents ω_j in eq. 3.4 labeled for each pathway.

The use of EPTA may allow a more detailed interrogation of the electronic behavior of molecules interacting with non-classical light. With knowledge of the possible ETPA transitions occurring in a molecule, it may be possible to manipulate the unique quantum optical behavior of a molecule by controlling the entanglement beam parameters.[11,25,26,29,30,34] Among the unique

quantum optical behavior are entanglement-induced transparencies, where the ETPA cross-section significantly drops in magnitude compared to the maximum cross-section. This unique behavior from using entangled photons may provide a means to create an ETPA "switch," where the absorption/fluorescence signal can be "turned on" or "turned off" without changing anything about the molecule itself. In order for this application to be achievable, we must be able to identify at which specific entanglement times the transparencies will occur and how much the magnitude will drop relative to the maximum cross-section. Since these transparencies arise from the wave nature of the ETPA transitions in eq. 3.2-3.4, a complete description of the different transition pathways, including both the interband and intraband transitions, is necessary. In order to fully describe these transitions, exact values of the electronic properties in molecules are required. One of these properties, Δ_j, offers a new handle on the population of particular electronic states by use of non-classical states of light.[22] In more chemical terms, the detuning is the energy difference between the time-dependent 'virtual' state induced by the absorbed photon (dotted line in Fig. 3.1 above) and nearby Born-Oppenheimer (BO) states (solid line labeled "e" in Fig. 3.1 above).[22] Thus, creating a model of the relationship between the targeted virtual state and the observed quantum optical behavior requires accurate knowledge of the Born-Oppenheimer state properties.[22,25,26,34] Such properties include the state energies, as well as permanent and transition dipole moments between all of the involved electronic states. While the potential energies and transition dipole moments for interband transitions are readily obtained using standard methods, calculating reliable transition dipole moments for intraband transitions is a non-trivial process and requires careful selection of the calculation parameters.

To date, these electronic properties have not been reported with the degree of completeness and accuracy necessary for modeling ETPA spectroscopy. While databases such as LIFBASE include some electronic properties of small molecules, these values are only approximations.[35] The databases are also limited to interband transitions in the molecules.[35] In order to more accurately describe the ETPA process in small molecules, we wanted exact values for the electronic properties of both interband and intraband states in the molecules. Even for diatomic molecules, this information is not widely known nor easily attainable, from either a computational or experimental approach. Prior simulations of the electronic structure and dipole moments for diatomic molecules were performed at the multi-configurational self-consistent field (MCSCF) and multireference configuration interaction (MRCI) levels by Knowles and Werner in the 1980s.[36-39] These

simulations are qualitatively similar to the MRCI simulations of the present study, but the differences reflect a substantial change in computational power over the last 30 years. In our study, large active spaces (where all electronic correlations are treated exactly) were utilized for all examples. Prior studies used small active spaces, which were then truncated further (i.e. from complete to incomplete active spaces, in terms of electronic configurations) to save computational cost.[36-39] Where the earlier studies could afford small basis sets (double zeta, polarized), our study uses a polarized triple zeta basis augmented with diffuse functions. Both factors make the present simulations substantially more accurate, as MRCI theories are variational and therefore more closely approach the exact electronic wave functions as the sizes of basis set and active space increase. In addition, the early work studying dipole moments of diatomics was performed at a single geometry for each species (i.e the equilibrium geometry).[36-38] In our present work, the ground and excited states were characterized along the diatomic bonding axis, including compressed and stretched structures. In total, our present work was able to go far beyond earlier studies due to great increases in computational ability over the years, although the spirit of the simulations is quite similar.

Using high-level MRCI calculations, we are able to identify the Born-Oppenheimer states that meet the energy and symmetry requirements to be involved in ETPA transitions in diatomic molecules. We have completed this work for diatomics first since a complete characterization of the ETPA mechanism requires highly accurate calculations of the BO states' electronic properties, an accuracy that is currently not achievable for larger molecules. However, with a complete characterization of the ETPA mechanism in diatomic molecules, we can probe the parameters of the molecules and their BO states in order to identify the specific parameters that most significantly impact the molecules' ETPA abilities. This methodology will allow us to understand and describe the ETPA process in a more complete way than ever before. With a more detailed understanding of the ETPA process in small molecules, it is hoped that we may be able to probe the same process in larger molecules in a way that is achievable with current computational and/or experimental technology.

3.3 Theoretical Details

3.3.1 Electronic Structure Simulations

Despite the existence of databases such as LIFBASE[35] containing energies, transition moments, and lifetimes for many small molecules, many of the transitions needed for this work were not available, most notably the intraband transitions between two excited states in a molecule. Therefore, approaches to calculate these values were carried out. Potential energy curves, transition dipole moments (TDMs), and permanent dipole moments for nitric oxide (NO), hydrogen fluoride (HF), and dinitrogen (N_2) were computed using state-averaged complete active space self-consistent field (SA-CASSCF)[36,40-42] and multireference configuration interaction (MR-CI),[37-39] as implemented in MOLPRO.[43,44] All calculations were performed with the augmented polarized valence triple zeta (aug-cc-pVTZ)[40] basis set. Results previously reported for carbon monoxide (CO) were replicated to confirm our methodology.[41] We only consider electronic transitions in this work.

For the heteronuclear systems NO and HF, the active space included all valence occupied orbitals and the corresponding unoccupied orbitals. Thus, the active space for NO is $[1\sigma^2\ 2\sigma^2\ 3\sigma^{\{0-2\}}\ 4\sigma^{\{0-2\}}\ 1\pi^{\{0-4\}}5\sigma^{\{0-2\}}2\pi^{\{0-4\}}6\sigma^{\{0-2\}}]$, which contains four A_1, two B_1, and two B_2 orbitals (CAS(11,8)). For HF, a CAS(6,7) was used. Due to the high density of the states in N_2, a larger CAS(10,12) active space including four additional orbitals (two A_g and two B_u) was utilized. To maintain consistent results across the different interatomic distances, orbitals from proximate geometries are used as initial guesses for each SA-CASSCF procedure.

Due to point group limitations in the program, heteronuclear diatomics ($C_{\infty v}$) were treated in the C_{2v} symmetry group and N_2 ($D_{\infty h}$) in D_{2h}. Because of the lowered symmetry assignments, states of Π symmetry (resulting from $\sigma \rightarrow \pi$ excitations) are described as B_1 or B_2 symmetry depending on whether the excitation involves a π_x or π_y orbital. A similar relationship exists between the Δ and $\{A_1, A_2\}$ groups. For a given two-photon transition, only electronic states with appropriate symmetry as allowed by selection rules were considered as potential intermediate states. In ETPA,[26,34] states higher in energy than the final state's energy can be intermediate states, and therefore states with energies below 1.5 times $\Delta E_{i\rightarrow f}$ were subject to TDM analysis. Due to the arbitrariness in the overall sign of each excited-state wave function, the TDMs have been corrected to maintain the same sign at neighboring geometries.

3.3.2 TDM Averaging

Since we calculated a range of TDMs for each pair of states as a function of interatomic distance, it was necessary to condense this information down to a single parameter that could be applied in the ETPA model equations. A weighted average was therefore taken using the ground state harmonic oscillator probability distribution. Using the natural length, n_l, of the quantum harmonic oscillator, the discrete data points along each curve are weighted according to the following formula:

$$D_{avg} = \frac{\sum_i (h(x_i))^2 D(x_i)}{\sum_i (h(x_i))^2} \tag{3.6}$$

where $h(x_i)$ is the amplitude of the zero-order harmonic wavefunction:

$$h(x) = Ae^{-\left(\frac{x-x_e}{n_l}\right)^2} \tag{3.7}$$

Since $h(x_i)^2$ appears in the numerator and denominator, the normalization factor, *A*, cancels and the equilibrium bond length, x_e and natural length are provided by the Morse parameters.

The potential energy curves generated with this methodology provide vertical excitation energies for each excited state in the molecules. These energies and the weighted-average dipole moments from eq. 3.6 can then be used as the necessary input for the ETPA model in eq. 3.2.

3.4 Results

The electronic structure methodology explained above provides highly accurate calculations of the energies and transition dipole moments for BO states in a molecule. Such high accuracy is needed in order to yield the most accurate and complete description of the ETPA process in a molecule, since the results of the electronic structure calculations are needed as input in the ETPA model in eq. 3.2. However, this methodology is only feasible for small molecules, so we chose a few diatomic molecules with different electronic properties as our models. Since ETPA can occur through a permanent dipole pathway, as explained above, we wanted to see how the relative strength of the dipole moment in a molecule affects its ETPA activity. Therefore, we chose NO as a molecule with a weak dipole moment, HF as a molecule with a strong dipole moment, and N_2 as a molecule with no dipole moment.

3.4.1 NO Potential Energy Curves and TDMs

NO acts a good model for a molecule that has a weak, but nonzero, permanent dipole moment. This molecule can reveal how the virtual-state pathway in ETPA interferes with a weak permanent dipole pathway. The notation for a two-photon transition used in this paper describes the transition as: ground electronic state → intermediate electronic state → final electronic state. The two-photon absorption process for NO is described by a $^2\Pi \rightarrow {}^2\Sigma^+ \rightarrow {}^2\Pi$ transition.[45,46] The dominant electronic configuration of the intermediate $^2\Sigma^+$ state is $(\ldots)5\sigma^1 2\pi^2$ and the final $^2\Pi$ state $(\ldots)1\pi^3 5\sigma^2 2\pi^2$. Due to the use of an Abelian symmetry group (C_{2v} rather than $C_{\infty h}$), the calculation distinguishes the $2\pi_x$ or $2\pi_y$ orbitals. Regardless, the pathways are identical in the full symmetry group, and it is only necessary to calculate one of these pathways, for the states X $1B_1$, A $1A_1$ and C $2B_1$. As shown in Fig. 3.2a below, the vertical excitation to the only active intermediate state is 8.35 eV (compared to 8.32 eV from experiment).[47] Over the span of ground state energies shown in Fig. 3.2, the dissociation energy, D_e, and well-width parameter, L, were found to be 7.25 eV and 2.62 Å, respectively (experiment: D_e = 6.62 eV, L = 2.83 Å).[48] Dipole moments for these transitions in NO are presented in Fig. 3.2b below.

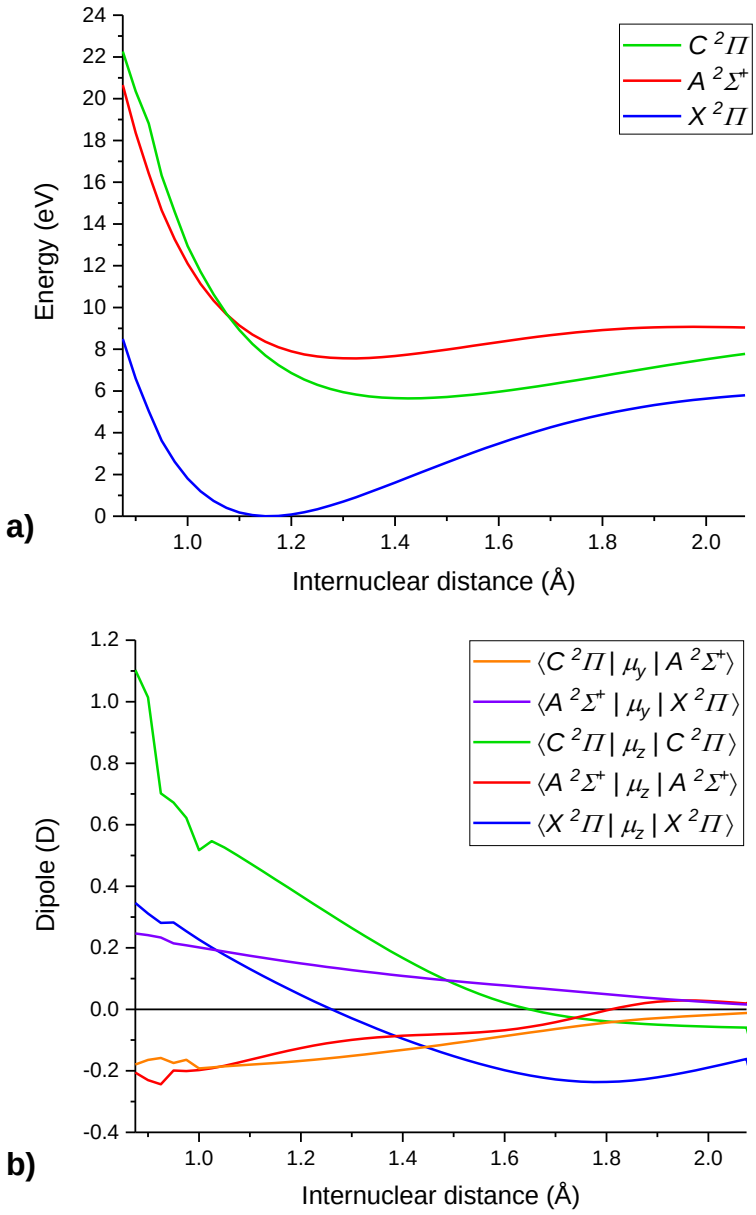

Figure 3.2. a) Potential energy curves and **b)** dipole strength for the three examined states in NO. The polarization of the dipoles is based upon the z-axis being aligned along the internuclear axis.

3.4.2 HF Potential Energy Curves and TDMs

HF represents a molecule with a strong permanent dipole moment that should compete with the virtual-state pathway more strongly. The expected TPA mechanism is $X\ ^1\Sigma^+ \rightarrow\ ^1\Pi \rightarrow\ ^1\Sigma^+$, representing an overall $\sigma \rightarrow \sigma^*$ electronic excitation.[49] Energy gaps to the active states are 10.28 eV (10.51 eV)[50,51] for the $^1\Sigma^+$state and 14.38 eV (13.03 eV)[51] for the $^1\Pi$ state. The Morse parameters D_e and L are 5.78 eV and 2.33 Å, respectively (experiment: D_e = 6.08 eV,

L = 2.25 Å).[52] The potential energy curves and dipole moments for HF are presented in Fig. 3.3a-b, respectively, below.

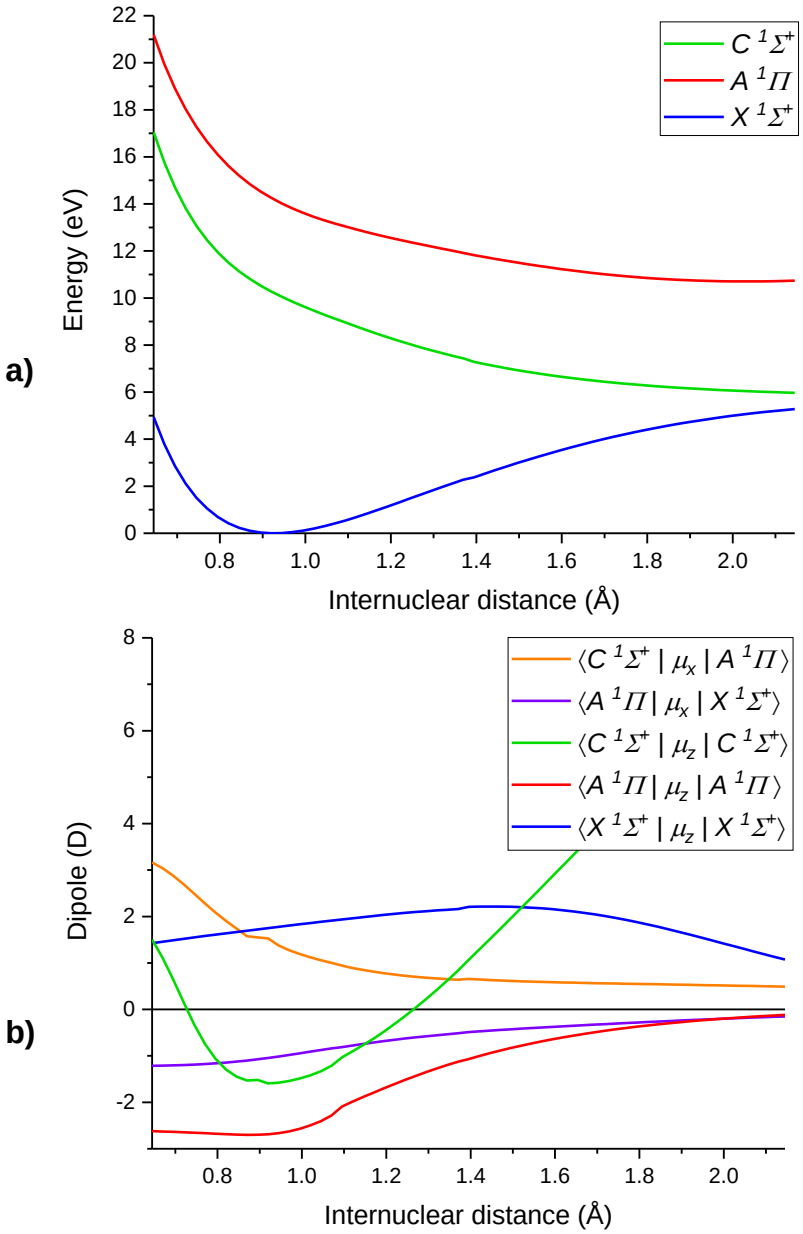

Figure 3.3. a) Potential energy curves and **b)** dipole strength for the three examined states in HF. The z-axis is aligned along the internuclear axis.

3.4.3 N_2 Potential Energy Curves and TDMs

N_2 represents a molecule that has no competition with its virtual-state pathways since the homonuclear diatomic lacks a permanent dipole. Because of the high density of the excited state manifold in dinitrogen, a number of avoided crossings occur where states of the same symmetry become nearly degenerate. To ensure that the electronic properties are accurately treated, four additional states of A_u and B_{2g} symmetries were computed in addition to the states of interest. For the TPA transition, the initial state is $^1\Sigma_g^+$ (A_g in the D_{2h} representation) and the final state has $^1\Pi_g$ (B_{2g}) symmetry, and these can be connected by states with $^1\Pi_u$ or $^1\Sigma_u^+$ (B_{2u} or A_u) symmetry.[43] At the minimum energy geometry, the virtual states are all above the final $^1\Pi_g$ state (Fig. 3.4). Four total states, 2 $^1\Sigma_u^+$ states and 2 $^1\Pi_u$ states, are relevant for the TPA mechanism based on energy and symmetry selection-rules. The Morse parameters for the ground state are D_e = 9.86 eV and L 2.69 Å, respectively (experiment: D_e = 9.90 eV, L = 2.85 Å).[48] The potential energy curves and dipole moments for N_2 are presented in Fig. 3.4a-b, respectively, below.

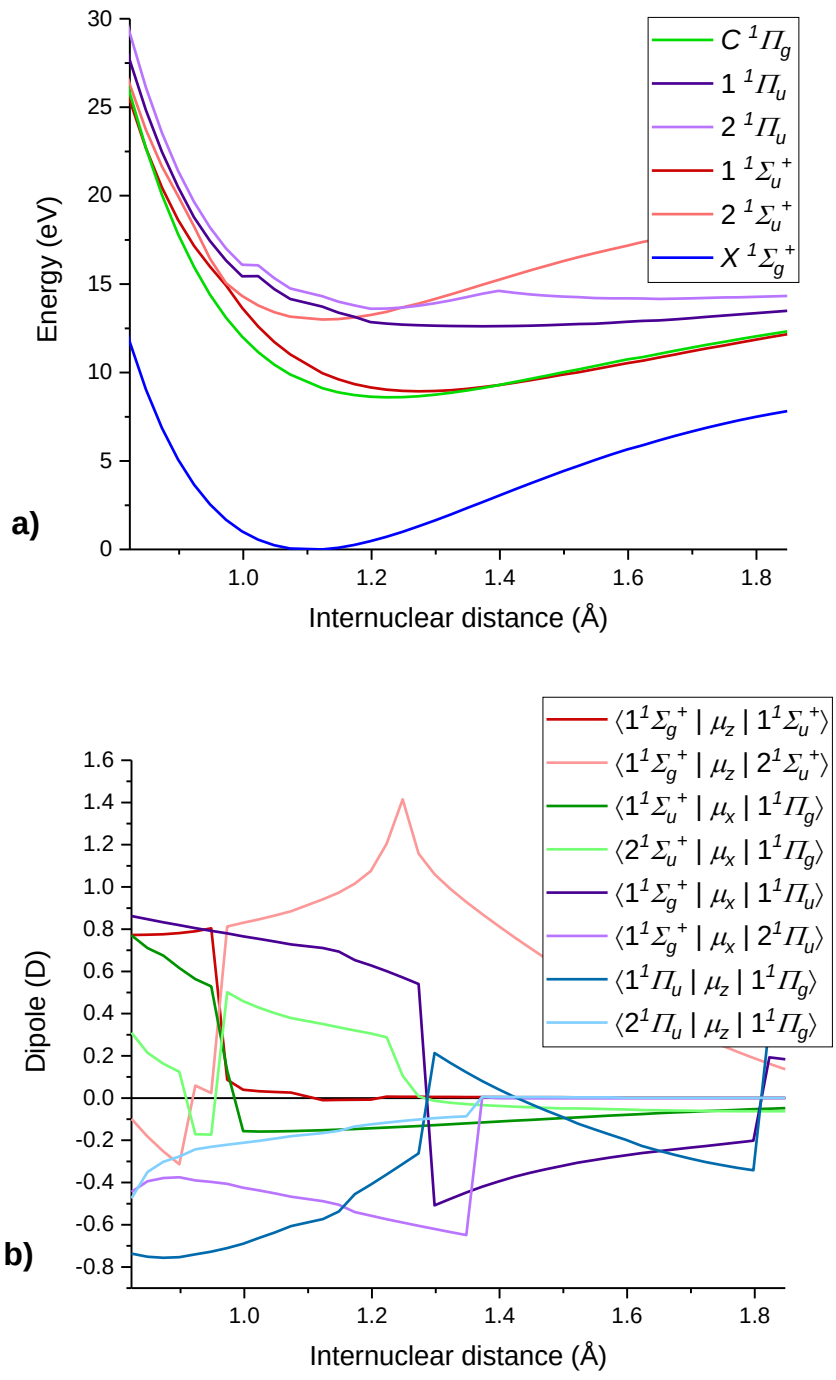

Figure 3.4. a) Potential energy curves and **b)** dipole strength for the six examined states in N_2. The z-axis is aligned along the internuclear axis.

3.4.4 Transition Dipole Analysis for ETPA Calculations

The potential energy curves in Fig. 3.2-3.4 above provide the energies of all the excited states involved in the ETPA process for each molecule. The range of transition dipole moments in Fig. 3.2-3.4 were averaged into a single parameter using eq. 3.6. The weight-averaged dipole moment values are reported below for use in the ETPA cross-section calculations. The dipole moments for HF and NO are presented in Table 3.1 while N_2 data is presented in Table 3.2.

Table 3.1. Permanent and transition dipole moments (Debye) in NO and HF. Notation for the transition dipoles in the table uses **X** to represent the ground state, **C** represents the final excited state, and **A** is the virtual state.

	$\langle X\|\mu_z\|X\rangle$	$\langle A\|\mu_z\|A\rangle$	$\langle C\|\mu_z\|C\rangle$	$\langle A\|\mu_x\|X\rangle$	$\langle C\|\mu_x\|A\rangle$
NO	0.086	-0.144	0.419	-0.174	0.161
HF	1.750	-2.588	-1.301	-1.027	1.533

In N_2, the significant number of low-lying excited states means there is more than one possible virtual state. For each pathway, the dipole moments of the first and second transitions are always orthogonally polarized in order to maintain the correct excited state symmetry. For example, for the $^1\Sigma_u^+$ virtual states, the ground-to-virtual state transition, $^1\Sigma_g^+ \rightarrow {}^1\Sigma_u^+$, have dipole moments along the z-axis whereas for the virtual-to-final state transition, $^1\Sigma_u^+ \rightarrow {}^1\Pi_g$, it is along the x-axis. For the $^1\Pi_u$ virtual states, the opposite trend exists, where the ground-to-virtual state transition is along the x-axis and the virtual-to-final state transition is along the z-axis.

Table 3.2. Transition dipole moments for dinitrogen (Debye). Notation for the transition dipoles in the table uses **X** to represent the ground $^1\Sigma_g^+$ state, **C** represents the final $^1\Pi_g$ excited state, and **A** is the virtual state corresponding to the column in which the value is found.

	$1\ ^1\Sigma_u^+$	$2\ ^1\Sigma_u^+$	$1\ ^1\Pi_u$	$2\ ^1\Pi_u$
$\langle A\|\mu_x\|X\rangle$	0.0	0.0	0.714	-0.481
$\langle C\|\mu_x\|A\rangle$	-0.147	0.368	0.0	0.0
$\langle A\|\mu_z\|X\rangle$	0.014	0.921	0.0	0.0
$\langle C\|\mu_z\|A\rangle$	0.0	0.0	-0.580	-0.173

The results reported in Chapters 3.4.1-4 show that we can use MRCI calculations to identify intermediate states that are allowed by both energy and symmetry requirements for ETPA transitions, including both interband and intraband transitions. The energies and dipole moments involving all of these intermediate states are necessary to calculate the ETPA cross-section using eq. 3.2.

3.5 Discussion

The results of our MRCI calculations of the energies and transition dipole moments for intermediate states in NO, HF, and N_2 above have been shown to be highly accurate through comparison with experimental literature values, which we have provided in Chapters 3.4.1-3 above for each molecule.[47,48,50-52] With these results, we can compare the contributions to the ETPA process associated with each intermediate state separately and the ETPA cross-section for each molecule when all transition pathways are considered. It is important to note that our ETPA cross-section expression in eq. 3.2 differs from previously reported expressions in that our expression also considers the permanent dipole pathway in heteronuclear diatomics.[25,26] We first compare the accuracy of our expression to the previously reported expression by calculating the ETPA cross-section in the hydroxyl radical (OH) and comparing our results to that obtained by Kojima et. al.[34] using the expression derived by Fei et. al.[25,26] We then calculate the ETPA cross-section for NO, HF, and N_2 to characterize how the different electronic properties of these three diatomics affect their ability to absorb entangled photons.

3.5.1 ETPA cross-section of OH

A theoretical study on the heteronuclear diatomic molecule OH showed the presence of entanglement-induced transparency in the hydroxyl radical (OH).[34] This was demonstrated using an entangled two-photon absorption cross-section expression derived using second-order perturbation theory and neglecting the intermediate state linewidths.[25,26] The selection rules for allowed two-photon transitions were determined for the $R_1(5)$ rotational line of the $A\,^2\Sigma^+$-$X\,^2\Pi_i$ transition in OH, where the population is excited from the ground $X\,^2\Pi_{3/2}$ ($v'' = 0$, $N'' = 5$) state (544.21 cm^{-1}) to an intermediate state, and from the intermediate state to the excited $A\,^2\Sigma^+$ ($v' = 0$, $N' = 6$) state (33,150.15 cm^{-1}).[34] The selection-rule allowed pathways include both electronic and rovibronic transitions, as the possible intermediates states are different

rovibronic levels on the *X* or *A* electronic states.[34] The energies were calculated based on the Hamiltonian derived by Luque and Crosley.[53] Both electronic ($X \rightarrow A$) and vibrational ($X \rightarrow X$ or $A \rightarrow A$) transition moments, energies and lifetimes were calculated and included in this database as well.[53] The wave functions were found from solving the radial Schrodinger equation using the potential curves calculated with the Rydberg–Klein–Rees (RKR) method, which included the rotational centrifugal term.[34] Neither the wavefunction nor RKR calculations accounted for Λ-doubling or spin-orbit coupling, but it was reported that this does not significantly impact the simulation.[34]

Kojima et. al. calculated the ETPA cross-section using 53 different rovibronic intermediate states.[54] As a starting point, we utilized their data and ETPA cross-section expression and calculated the cross-section using only 5 different electronic intermediate states, as opposed to all rovibronic states.[34] Their ETPA cross-section expression differs from eq. 3.2 in that it does not include the permanent dipole terms.[25,26,34] By not including the dipolar terms, some important physics may have been missed within the ETPA cross-section.[4,5,55] The calculated and plotted ETPA cross-section is shown in Fig. 3.5a with an entanglement time of 0-200 fs. The entanglement time was extended to 2,000 fs in Fig. 3.5b. We then used the same data and parameters to calculate the ETPA cross-section using eq. 3.2 to compare the effect that the permanent dipole terms have on the cross-section. The new plot is shown in Fig. 3.5c with an entanglement time of 0-200 fs. The entanglement time was extended to 2,000 fs in Fig. 3.5d.

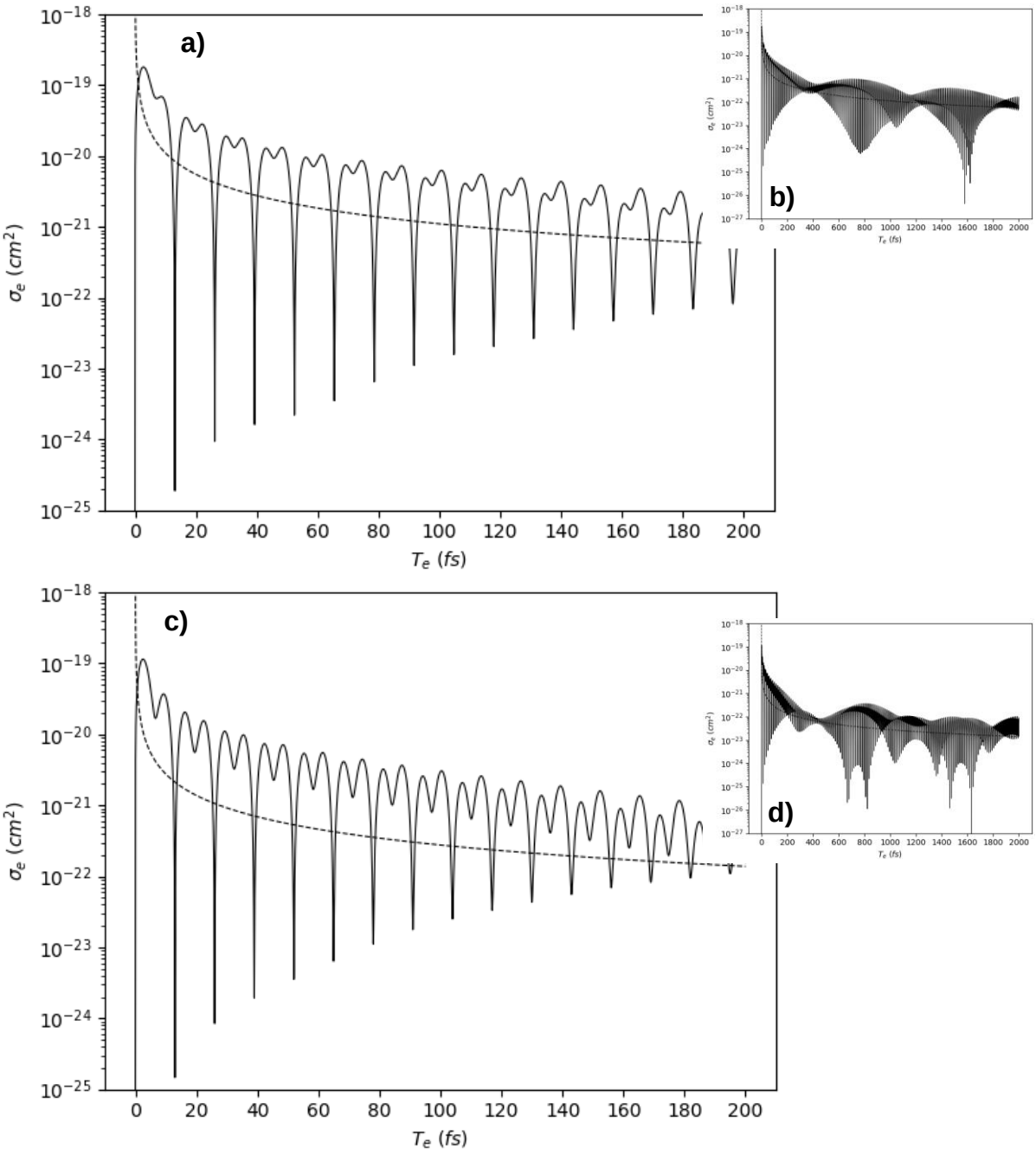

Figure 3.5. The ETPA cross-section for the *A*-*X* transition in OH as a function of entanglement time. The pump is degenerate. This is based on the data by Kojima et. al.[34] **(a)** previously reported ETPA cross-section equation (solid line) and a probabilistic particle analysis approximation (dashed line) derived by Fei et. al.[25], entanglement time = 0-200 fs; **(b)** same equation as **(a)**, entanglement time = 0-2,000 fs; **(c)** modified ETPA cross-section equation given by eq. 3.2 (solid line) and a probabilistic particle analysis approximation (dashed line)[25], entanglement time = 0-200 fs; **(d)** same equation as **(c)**, entanglement time = 0-2,000 fs.

Our plot in Fig. 3.5a, which uses the same expression as Kojima et. al.[34], shows the same cross-section magnitude and period between entanglement-induced transparencies as Kojima et. al.[34], confirming the accuracy of our plot. However, our plot also shows a splitting at each maxima in the cross-section that does not appear in Kojima et. al.'s[34] plot. This can be attributed to our use of only electronic transitions, while Kojima et. al. considered additional rovibronic transitions in their work, offering them more resolution in their plot.[34] For the purposes of this paper, we wanted to compare how the inclusion of the permanent dipole pathway affects the nonmonotonic behavior of the ETPA cross-section, making our simplification to considering only electronic transitions sufficient for comparing the results of the previously reported ETPA cross-section expression with the results from our expression in eq. 3.2.

Fig. 3.5a-c show that both ETPA cross-section expressions yield similar periods of entanglement-induced transparencies: 13.10 fs for the previously derived expression vs 13.00 fs for eq. 3.2. Both expressions also yield similar maximum cross-sections: 1.811×10^{-19} cm^2 for the previously derived expression vs 1.147×10^{-19} cm^2 for eq. 3.2. In both plots, the splitting at the maxima show the interference pattern created by the competing pathways. This interference is stronger when the permanent dipole pathways are included with eq. 3.2, shown in Fig. 3.5c. Fig. 3.5b and 3.5d show the ETPA cross-section out to entanglement times of 2,000 fs. The interference pattern at the maxima in both plots is almost identical, while the pattern at the minima in Fig. 3.5d clearly shows a more complex interference pattern resulting from the addition of the permanent dipole pathways using eq. 3.2. While the intensity of the ETPA cross-section does not change much when permanent dipole pathways are included, the interference pattern is clearly affected, which may change when entanglement-induced transparencies occur in other molecules.

3.5.2 ETPA cross-section of NO

Using eq. 3.2 as our expression for the ETPA cross-section, we now use the calculated excitation energies from the potentials energy curves in Fig. 3.2-3.4 and the transition dipole moments in Tables 3.1 and 3.2 to compare the entangled two-photon absorption cross-sections of the three diatomic molecules. The cross-sections were calculated and plotted as functions of the entanglement time. Entanglement times at which the cross-section drops by at least 1 order

of magnitude can be considered entanglement-induced transparencies. For NO, we probe the $^2\Pi \rightarrow {}^2\Sigma^+$ and $^2\Sigma^+ \rightarrow {}^2\Pi$ transitions which occur via the $^2\Sigma^+$ intermediate state.[45,46] The permanent dipole for NO is 0.159 D,[56] and the excited state lifetime is 1.95 ps.[57] The ETPA cross-section for NO is plotted in Fig. 3.6, with entanglement times out to 200 fs in Fig. 3.6a and out to 2,000 fs in Fig. 3.6b.

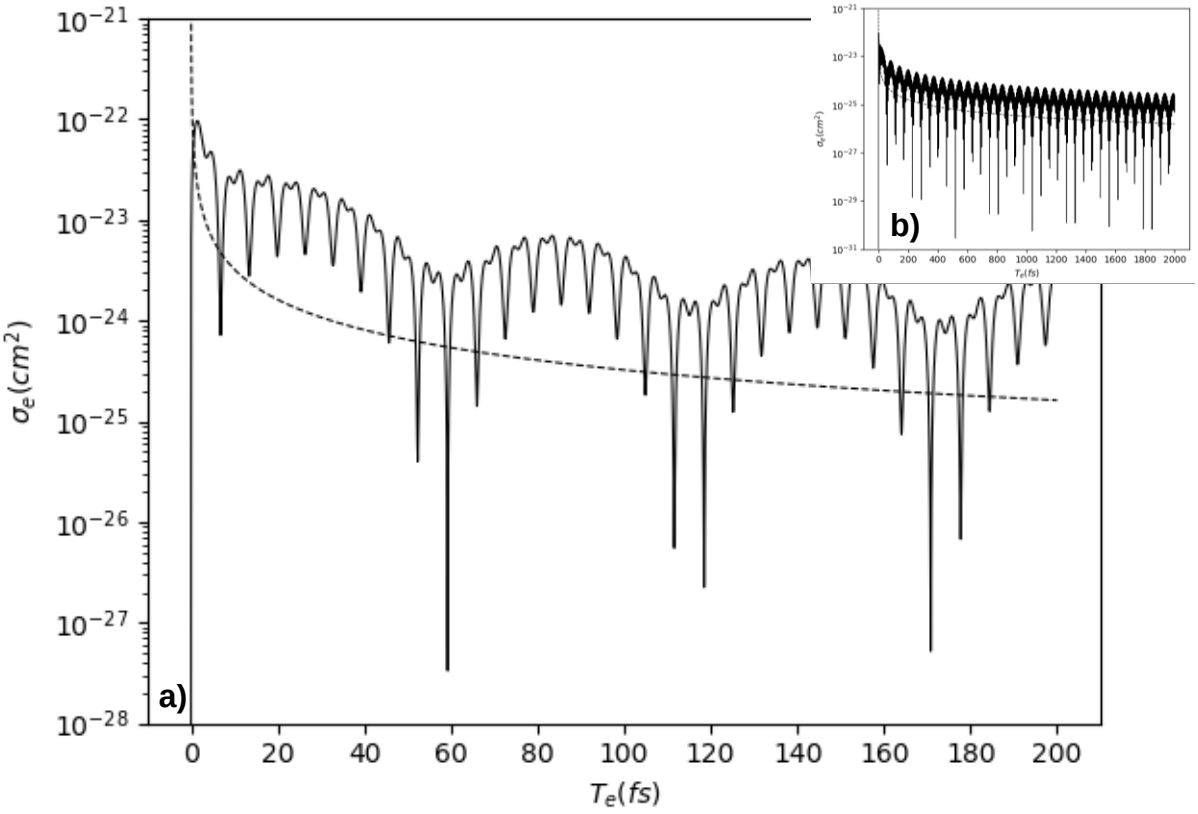

Figure 3.6. The ETPA cross-section of NO as a function of entanglement time, ranging from **(a)** entanglement time = 0-200 fs, and **(b)** entanglement time = 0-2,000 fs. The probabilistic particle analysis approximation (dashed line) derived by Fei et. al. is shown for comparison.[25]

The maximum cross-section in Fig. 3.6, found at T_e = 1.47 fs, is 9.636x10^{-23} cm^2. There are significant drops in cross-section magnitude (3 or more orders) occurring every 59.25 fs. Between each of these large drops in magnitude, there are more frequent relative minima that occur every 6.84 fs. Since each of these more frequent minima are approximately 1 order of magnitude less than their nearby maxima, all of these minima can be considered entanglement-induced transparencies, making the period between transparencies 6.84 fs in NO.

3.5.3 ETPA cross-section of HF

For HF, we probe the $^1\Sigma^+ \rightarrow {}^1\Pi$ and $^1\Pi \rightarrow {}^1\Sigma^+$ transitions.[49] HF has a dipole moment of 1.83 D,[56] and the excited state lifetime is 30 fs.[58] The ETPA cross-section for HF is shown in Fig. 3.7, out to entanglement times of 200 fs in Fig. 3.7a and 2,000 fs in Fig. 3.7b.

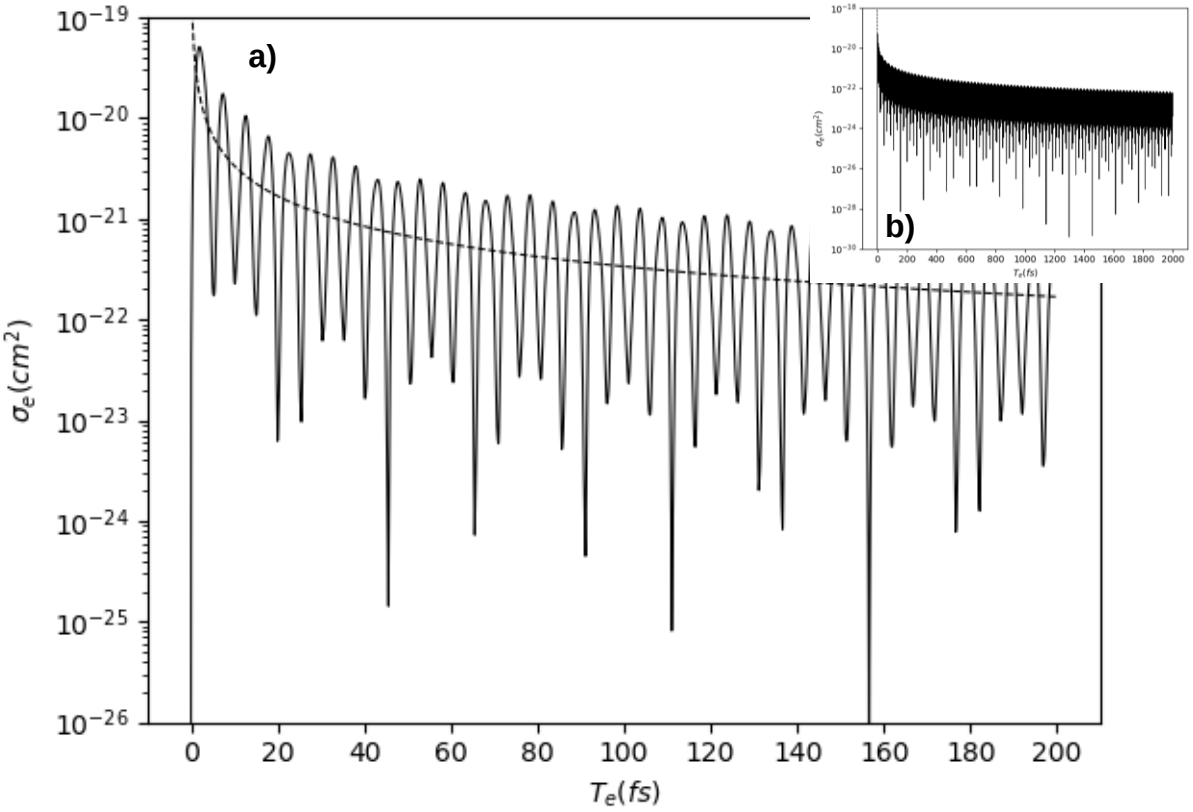

Figure 3.7. The entangled two-photon absorption cross-section of HF as a function of entanglement time, ranging from **(a)** entanglement time = 0-200 fs, and **(b)** entanglement time = 0-2,000 fs. The probabilistic particle analysis approximation (dashed line) derived by Fei et. al. is shown for comparison.[25]

The maximum cross-section in Fig. 3.7, found at T_e = 1.95 fs, is 5.112x10^{-20} cm^2. The cross-section drops by at least 2 orders of magnitude every 5.28 fs, making the period of entanglement-induced transparencies 5.28 fs in HF.

3.5.4 ETPA cross-section of N_2

For N_2, we probe two transition pathways: the $X^1\Sigma_g \rightarrow a'^1\Sigma_u$ and $a'^1\Sigma_u \rightarrow a\ ^1\Pi_g$ transition which occurs via the $a'^1\Sigma_u$ transition state, and the $X^1\Sigma_g \rightarrow {}^1\Pi_u$ and $^1\Pi_u \rightarrow a\ ^1\Pi_g$

transition which occurs via the $^1\Pi_u$ transition state.[43] N_2 has no permanent dipole, and the excited state lifetime is 115 μs for N_2.[43] The ETPA cross-section, calculated with eq. 3.2, is shown in Fig. 3.8, out to entanglement times of 200 fs in Fig. 3.8a and 2,000 fs in Fig. 3.8b.

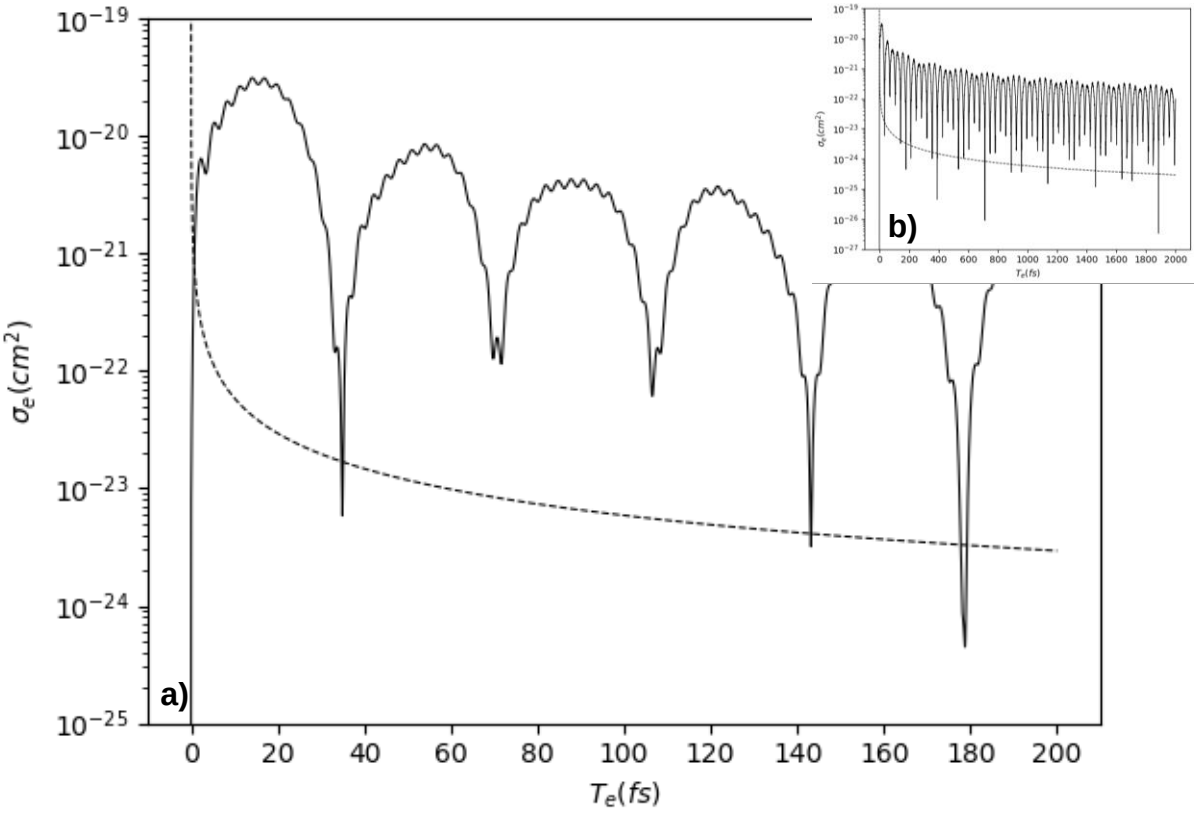

Figure 3.8. The entangled two-photon absorption cross-section of N_2 as a function of entanglement time, ranging from **(a)** entanglement time = 0-200 fs, and **(b)** entanglement time = 0-2,000 fs. The probabilistic particle analysis approximation (dashed line) derived by Fei et. al. is shown for comparison.[25]

The maximum cross-section in Fig. 3.8, found at 14.14 fs, is 3.122×10^{-20} cm^2. While there are relative minima in the cross-section that occur every 3.42 fs, these minima have almost the same magnitude cross-section as the nearby maxima and are not considered transparencies. There are much more significant minima that occur every 34.96 fs, with these minima dropping by up to 3 orders of magnitude compared to the maxima. The period of entanglement-induced transparencies in N_2 is thus 34.96 fs.

Fig. 3.8 also highlights a very unique feature to entangled photon spectroscopy: the ability to utilize Born-Oppenheimer intermediate states that are higher in energy than the final

state. The potential energy curves for N_2 in Fig. 3.4a show that all the intermediate states are higher in energy than the final state at the minimum energy geometry. If the utilization of intermediate states above the final state were not allowed, Fig. 3.8a would not show any ETPA activity for N_2. The fact that the plot does show ETPA activity shows that entangled photon spectroscopy can utilize these higher energy intermediate states, unlike spectroscopy using a classical light source.

Table 3.3. Summary of MRCI and ETPA results for OH, NO, HF, and N_2. ETPA cross-sections were calculated using eq. 3.2. OH transition probabilities and intermediate state energies for detunings were obtained from Kojima et. al.[34]

					virtual-state pathways		
molecule	total transition symmetry	max σ_e (10^{-23} cm^2)	period (fs)	permanent dipole (D)	virtual-state symmetry	transition probability (D^2)	detuning (cm^{-1})
OH	$^2\Pi_{3/2} \rightarrow {}^2\Sigma^+$	11.470	13.00	1.655	$^2\Sigma^+$	1.3	16101
					$^2\Pi_{3/2}$	0.00796	12755
					$^2\Pi_{3/2}$	1.24	16079
					$^2\Pi_{1/2}$	1.24	16023
					$^2\Pi_{1/2}$	1.24	15769
NO	$^2\Pi \rightarrow {}^2\Pi$	9.636	6.84	0.153	$^2\Sigma^+$	0.028	35488
HF	$^1\Sigma^+ \rightarrow {}^1\Sigma^+$	5,112	5.28	1.910	$^1\Pi$	1.574	73558
N_2	$^1\Sigma_g^+ \rightarrow {}^1\Pi_g$	3,122	34.96	0	$^1\Sigma_u^+$	0.002	43635
					$^1\Sigma_u^+$	0.339	68073
					$^1\Pi_u$	0.414	73961
					$^1\Pi_u$	0.083	78720

Table 3.3 summarizes the results of our MRCI calculations for NO, HF, and N_2 and our ETPA calculations using eq. 3.2 for OH, NO, HF, and N_2. In first comparing the effect that the presence of a permanent dipole pathway has on a molecule, the additional competition from the permanent dipole pathway seems to keep the period between entanglement-induced transparencies very short. N_2, which is the only molecule in Table 3.3 that does not have a permanent dipole, has a period that is several times longer than OH, NO, and HF. The lack of a permanent dipole in N_2 does not appear to affect the magnitude of the cross-section, since N_2's maximum cross-section is larger than NO's maximum cross-section (weak permanent dipole) but smaller than OH's and HF's maximum cross-sections (strong permanent dipoles). The ETPA behavior reported in Table 3.3 is more directly affected by the virtual-state pathway properties in the molecules. Most significantly, the presence of multiple virtual-state pathways in a molecule increases the period between transparencies, as evidenced by OH and N_2, which have multiple virtual states, having longer periods than NO and HF, which only have one

virtual state. Even though OH has 5 virtual states compared to the 4 virtual states in N_2, N_2 has a much longer period than OH. This is likely due to the permanent dipole pathway in OH decreasing the period. These results suggest that when a molecule undergoes ETPA, two (or more) virtual-state pathways will interfere constructively to increase the period between transparencies while a virtual-state pathway and a permanent dipole pathway will not significantly interfere to change the period between transparencies.

The magnitude of the ETPA cross-section has more factors at play. Based on eq. 3.2, we expect the cross-section to be proportional to the transition probability and permanent dipole and inversely proportional to the detuning, which the results in Table 3.3 confirm. The molecules with the largest permanent dipoles and transition probabilities, OH and HF, have the largest magnitude cross-sections. When comparing OH and HF to each other, the much smaller detunings in OH lead to a larger cross-section. In addition, the constructive interference between virtual-state pathways also seems to increase the cross-section magnitude. For example, N_2 and HF have similar detunings, but HF has a much larger transition probability, so HF would be expected to have a much larger cross-section than N_2. However, the cross-sections of the two molecules are roughly the same, which can be attributed to the virtual-state pathways' constructive interference in N_2, a property that HF does not have because it only has one virtual state. This enhancement in the ETPA activity of N_2 arising from the interference between its virtual-state pathways may be viewed as a coupling between the pathways' respective transition dipole moments. Hanczyc et. al.[59] recently reported a similar phenomenon where the classical TPA activity of amyloid fibers was enhanced due to exciton coupling from the symmetric transition dipole moments in tyrosine chromophores. The coupling in the amyloid fibers is an intermolecular interaction between the same transition dipole moment in multiple tyrosine chromophores. However, the coupling in N_2 is an intramolecular interaction between different transition dipole moments in a single molecule.

Each of the dotted curves in Fig. 3.5-3.8 show the result of using the probabilistic particle analysis derived by Fei et. al.[25,26] This approximation estimates the ETPA cross-section (eq. 3.2) to be proportional to the classical TPA cross-section (eq. 3.1) by the expression:[25,26]

$$\sigma_e = \frac{\delta_r}{2A_eT_e} \tag{3.8}$$

Since the magnitude of both the ETPA cross-section, σ_e, and classical TPA cross-section, δ_r, depend upon the transition probabilities and detunings, the probabilistic particle analysis in eq.

3.8 may provide a reasonable estimate of the magnitude of the ETPA cross-section. But since the approximation does not account for the wave nature of ETPA transitions, a purely quantum effect, this approximation should be viewed as showing "classical-like" behavior that does not account for quantum interference effects. It is therefore expected that the exact quantum calculation of the ETPA cross-section by eq. 3.2 should oscillate around this classical approximation, with constructive interference causing the cross-section to be larger at certain entanglement times and destructive interference causing the cross-section to be smaller at certain entanglement times. The more the exact quantum ETPA cross-section deviates from this classical approximation, the more significant are the quantum effects of the ETPA process. Looking at the cross-sections for OH and HF in Fig. 3.5 and 3.7, respectively, the probabilistic particle analysis ETPA cross-section is always within 1 order of magnitude from the maxima of the exact ETPA cross-section, with the transparencies dropping below the classical approximation as expected. But in NO and N_2, even many of the minima in the exact ETPA cross-section are larger in magnitude than the probabilistic particle analysis, showing much stronger deviation from the classical approximation. This may be attributed to the relative strength of the permanent dipoles in the molecules. The molecules with larger permanent dipoles (OH and HF) see more "classical-like" behavior. NO, which has a small permanent dipole, sees more deviation from the "classical-like" behavior than OH and HF. N_2, which has no permanent dipole, sees the most deviation from "classical-like" behavior. In fact, out to entanglement times of 2,000 fs in Fig. 3.8b, the exact ETPA cross-section is almost always larger in magnitude than the probabilistic particle analysis ETPA cross-section, with the maxima being 3 or more orders of magnitude larger than the classical approximation[25,26]. This is evidence that the virtual-state pathways in ETPA lead to more quantum behavior, while permanent dipole pathways cause the molecule to behave more "classical-like." As the permanent dipole becomes weaker, the deviation from classical behavior becomes stronger. Thus, in order to take advantage of the quantum effects from using entangled photons, the permanent dipole pathway contribution to ETPA must be minimized, or ideally, be non-existent, as is the case with N_2.

3.5.5 Sum-of-waves Analysis for Transition Pathways in ETPA

The results in Fig. 3.5-3.8 and Table 3.3 clearly show that the wave nature of an ETPA transition largely affects a molecule's ability to absorb entangled photons. In order to more fully understand the quantum interference among the different transition pathways, we sought a complete description of the wave mechanics of the transitions and interference patterns. With a more complete understanding of the quantum interference in these diatomic molecules, we hope to extend this knowledge to be able to describe the interference effects in larger molecules undergoing ETPA.

Looking at the transition pathways individually, since each wave is offset from 0 by the value of its amplitude, as shown in eq. 3.3 and 3.4, the wave will equal zero at its minima, if the amplitude is negative, or at its maxima, if the amplitude is positive. When the wave equals 0, its intensity, i.e. the amplitude squared, which is proportional to the ETPA cross-section in eq. 3.4, will also be 0, thus creating a transparency in the cross-section. Since these transparencies will always occur at the minima of the intensity, they occur at the same frequency of the wave itself. Therefore, transparencies resulting from individual pathways occur at entanglement times of:

$$T_e = \frac{2n\pi}{\omega_j} \quad n = 0, 1, 2, \ldots \tag{3.9}$$

The period of transparencies will therefore increase as the frequency, i.e. the detuning energy for virtual-state pathways or the incident photon energy for permanent dipole pathways, decreases. Eq. 3.9 matches that derived by Fei et. al.[25] where they assumed one intermediate state dominated the summation over all intermediate state pathways.

Analysis of the individual pathways in the four molecules we studied can explain more thoroughly why N_2 has a much larger period between entanglement-induced transparencies compared to OH, NO, and HF. Table 3.4 below shows the amplitudes, transition probabilities, and magnitude of the frequencies for each individual pathway in each molecule. For each molecule, the pathway(s) with the largest amplitude will dominate the ETPA transition. In chemical terms, the amplitude of each virtual-state pathway (labeled with a "V" in Table 3.4) is proportional to its transition probability (product of the transition dipole moments) and inversely proportional to its detuning energy. The amplitude of each permanent dipole pathway (labeled with a "P" in Table 3.4) is proportional to its transition probability (permanent dipole strength) and inversely proportional to the energy of the incident photons. As a result of these

two dependencies in each pathway, there can be a trade-off that one must consider when identifying the most dominant transition pathway in ETPA. While one pathway may have a large transition probability, the pathway may also have a large detuning, which would negatively affect its amplitude. In order to compare the relative strength of two or more pathways in an ETPA process using a single parameter, the total amplitude of each pathway's wave equation (as in eq. 3.3 and 3.4) must be considered. However, the frequencies shown in Table 3.4 are all very large, with even the smallest frequency being over 12,000 cm^{-1}. Javanainen and Gould have reported that a detuning of less than 50 cm^{-1} is necessary to see ETPA activity experimentally.[22] Because each transition that we have studied has a detuning/incident photon energy >> 50 cm^{-1}, we can reasonably assume for these specific molecules that the amplitude of each transition will only be dependent on the magnitude of its transition probability, or dipole moments. Thus, when comparing the amplitudes of two transitions in Table 3.4, we are really comparing their transition probabilities, to a very reasonable approximation. This may not be the case for other molecules that have very small detunings. From the data in Table 3.4 below, OH, HF and N_2 each have two dominant pathways: pathways P6 and P7 in OH, pathways P2 and P3 in HF, and pathways V2 and V3 in N_2. NO only has one dominant pathway: pathway P3.

Table 3.4. The amplitudes (A_j), transition probabilities, and magnitude of the frequencies ($|\omega_j|$) for each individual pathway's wave equation in all four molecules studied. For virtual-state pathways, denoted by "V#," the frequency is the detuning energy for the pathway's virtual state. For permanent dipole pathways, denoted by "P#," the frequency is the energy of the incident photons. OH transition probabilities and intermediate state energies for detunings were obtained from Kojima et. al.[34]

Molecule	**Pathway**	A_j **(D^2·cm^{-1})**	**Transition probability (D^2)**	$\|\omega_j\|$ **(cm^{-1})**
OH	V1	8.074E-05	1.3	16101
	V2	6.241E-07	0.00796	12755
	V3	7.712E-05	1.24	16079
	V4	7.739E-05	1.24	16023
	V5	7.864E-05	1.24	15769
	P6	1.015E-04	1.655	16303
	P7	1.015E-04	1.655	16303
NO	V1	7.890E-07	0.028	35488
	P2	4.080E-07	0.013	31859
	P3	2.009E-06	0.064	31859
HF	V1	2.140E-05	1.574	73558
	P2	8.064E-05	3.343	41457
	P3	5.994E-05	2.485	41457
N_2	V1	4.583E-08	0.002	43635
	V2	4.980E-06	0.339	68073
	V3	5.598E-06	0.414	73961
	V4	1.054E-06	0.083	78720

Since NO only has one dominant pathway in its ETPA process, we can approximate the period between its entanglement-induced transparencies using eq. 3.9: 6.57 fs, compared to its exact period of 6.84 fs in Fig. 3.6a. OH and HF are both dominated by their permanent dipole pathways, and Table 3.4 shows that the permanent dipole pathways in each molecule will have the same wave frequency. As a result, no beat pattern forms from their interference, and the period between transparencies when the permanent dipole pathways interfere is the same as the period in each individual pathway. Thus, we can approximate the period between entanglement-induced transparencies in OH and HF using eq. 3.9: 12.85 fs in OH, compared to its exact period of 13.00 fs in Fig. 3.5c; 5.05 fs in HF, compared to its exact period of 5.28 fs in Fig. 3.7a.

Since the two dominant pathways in N_2 are virtual-state pathways with slightly different frequencies, a complex beat pattern forms when they interfere, producing a carrier wave whose amplitude oscillates according to upper and lower limit modulating waves. The

resulting ETPA cross-section is thus the part of the carrier wave that is contained within the envelope created by the modulating waves. The oscillations of the amplitude of the beat pattern can be characterized by this envelope, i.e. the modulus of the sum of the waves involved. The envelope of the beating pattern for two arbitrary pathways (pathway 1 = $A_1 e^{i\omega_1 T_e}$ and pathway 2 = $A_2 e^{i\omega_2 T_e}$) can be characterized as (see Supporting Information for full derivation):

$$\pm\sqrt{(A_1 e^{i\omega_1 T_e} + A_2 e^{i\omega_2 T_e}) \times c.c.} \tag{3.10}$$

$$= \pm\sqrt{{A_1}^2 + {A_2}^2 + 2A_1 A_2 \cos[(\omega_1 - \omega_2)T_e]} \tag{3.11}$$

These two equations for the upper and lower limit of the envelope must be offset by $A_1 + A_2$, as shown by the original expression in eq. 3.4. The carrier wave that oscillates between the two envelope waves in eq. 3.11 will have relative minima occurring at every entanglement time that the carrier wave hits the lower limit envelope. When the lower limit envelope equals 0, an absolute minima can occur in the carrier wave. Since the ETPA cross-section is proportional to the sum of pathways involved (eq. 3.4), the locations of entanglement-induced transparencies can occur at these relative and absolute minima. The entanglement times at which the absolute minima occur can be calculated (see Supporting Information for full derivation):

$$\left(A_1 + A_2 \pm \sqrt{{A_1}^2 + {A_2}^2 + 2A_1 A_2 \cos[(|\omega_1| - |\omega_2|)T_e]}\right)^2 = 0 \tag{3.12}$$

$$T_e = \frac{2n\pi}{||\omega_1| - |\omega_2||} \qquad n = 0, 1, 2, \ldots \tag{3.13}$$

The relative minima can only be considered transparencies if their magnitude is significantly smaller than the magnitude of the nearby maxima. One way to compare the intensity of the relative minima in the ETPA cross-section to its nearby maxima is by calculating the ratio between the two envelope waves at the maximum of the lower limit envelope, i.e. one-half of the period of the absolute minima calculated above. This value represents the largest that a relative minimum in the ETPA cross-section can be. Thus, at $T_e = \frac{n\pi}{||\omega_1| - |\omega_2||}$, the ratio of the intensities of the envelope waves are (see Supporting Information for full derivation):

$$\frac{\left(A_1+A_2+\sqrt{{A_1}^2+{A_2}^2+2A_1A_2\cos\left[(|\omega_1|-|\omega_2|)\frac{\pi}{||\omega_1|-|\omega_2||}\right]}\right)^2}{\left(A_1+A_2-\sqrt{{A_1}^2+{A_2}^2+2A_1A_2\cos\left[(|\omega_1|-|\omega_2|)\frac{\pi}{||\omega_1|-|\omega_2||}\right]}\right)^2} \tag{3.14}$$

$$= \frac{{A_1}^2}{{A_2}^2} \tag{3.15}$$

If A_2 is chosen to be the larger amplitude, then eq. 3.15 can be expressed as a percentage. Only when this percentage is large will the relative minima be similar in magnitude to the maxima, thus allowing us to neglect the relative minima as true transparencies. In chemical terms, a large percentage from eq. 3.15 reveals that significant constructive interference occurs between the two ETPA transitions pathways. Fig. 3.9 below shows the sum of the two dominant pathways in N_2, along with the envelope waves.

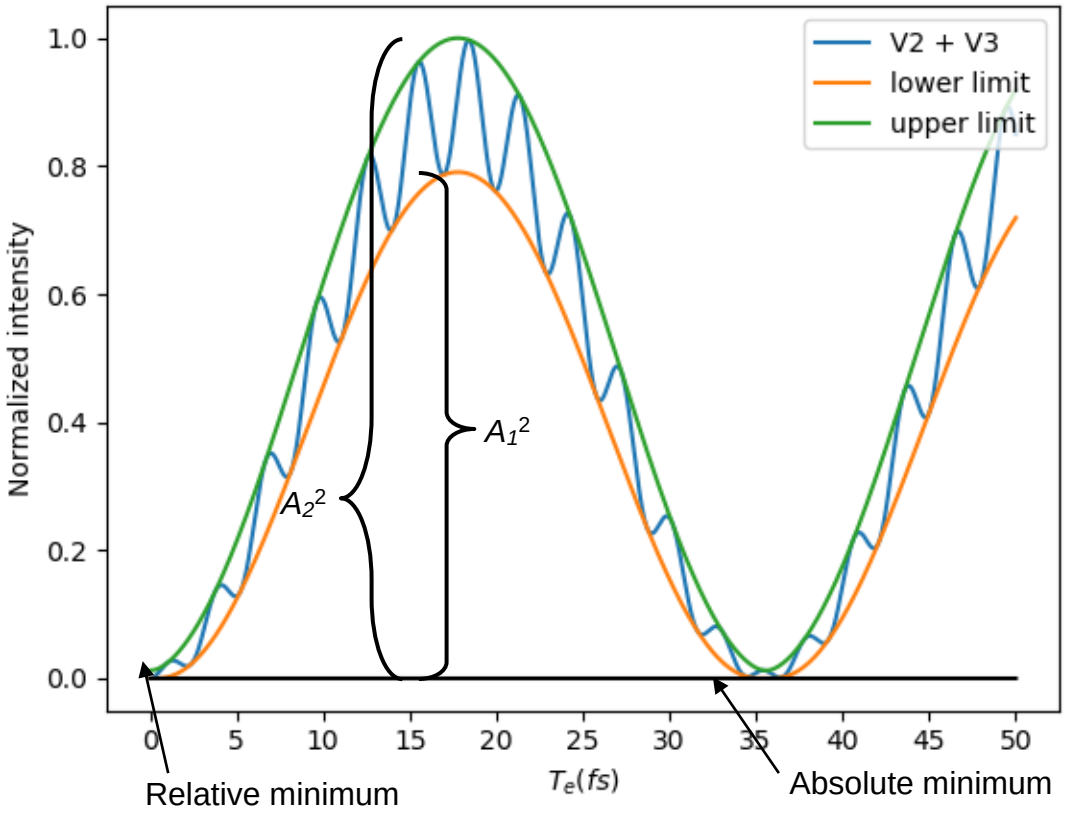

Figure 3.9. The beat pattern formed by adding pathways V2 and V3 in N_2. The upper and lower limit envelope waves are shown.

In Fig. 3.9, the sum of pathways V2 and V3 in N_2 shows that the lower limit envelope (orange) is close in magnitude to the upper limit envelope (green). At $T_e = \frac{n\pi}{||\omega_1|-|\omega_2||} = 17.79$ fs, eq. 3.15 calculates that the lower limit envelope is ~79 % as intense as the upper limit envelope. As a result, the relative minima of the sum of the pathways (blue) are similar in intensity to the nearby maxima. For these two pathways, the relative minima are close enough in magnitude to the maxima that they should not be considered transparencies. Only the absolute minima, when the lower limit envelope reaches zero, will show transparencies in the ETPA signal. These entanglement times can be calculated using eq. 3.13: 35.57 fs, compared to its exact period of 34.96 fs in Fig. 3.8a. This period, which is much longer than the periods in OH, NO, and HF, results from the significant constructive interference between the two dominant pathways in N_2, which can only occur because the intermediate states for the two pathways have very similar transition probabilities. This is confirmed from the TDM data for N_2 in Table 3.3: pathway V2, which uses a $^1\Sigma^+$ virtual state, has a transition probability of 0.339 D^2; pathway V3, which uses a $^1\Pi_u$ virtual state, has a transition probability of 0.414 D^2.

Table 3.5 below summarizes what we calculated the period between entanglement-induced transparencies to be based on our approximations above. These predictions are compared to the exact periods found in the plotted ETPA cross-sections in Fig. 3.5-3.8 for OH, NO, HF, and N_2, respectively.

Table 3.5. The dominant ETPA transition pathways in each molecule studied, used to calculate the approximated period between entanglement-induced transparencies. The exact periods were obtained from the plotted ETPA cross-sections in Fig. 3.5-3.8 for OH, NO, HF, and N_2, respectively.

Molecule	**Dominant pathway(s)**	**Approximated period (fs)**	**Exact period (fs)**
OH	P6 + P7	12.85	13.00
NO	P3	6.57	6.84
HF	P2 + P3	5.05	5.28
N_2	V2 + V3	35.57	34.96

The results in Table 3.5 confirm the accuracy of the approximations in our sum-of-waves methodology and the derived expressions for when one or two pathways dominate the ETPA process. All of our calculated periods based on our approximations are within 1 fs of the exact plotted period when all pathways are considered. Since our approximations only

require the energies of the Born-Oppenheimer states in each molecule, which can be easily obtained with current computational techniques or experimental data, these approximations may allow for the calculation of the periods of entanglement-induced transparencies in much larger molecules where a full ETPA calculation using eq. 3.2 would not be feasible with current computational technology. The transition dipole moments for interband and especially intraband transitions are much harder to calculate than the energies of the BO states. Using our approximations, exact values for the dipole moments are no longer required. As long as one can reasonably compare the relative strengths of the dipole moments for two BO states in a molecule, one can then identify which pathway(s) are most dominant in the ETPA process. This comparison would be much less computationally-intensive than the high-level MRCI calculations we completed in this work, allowing our methodology to be applied to much larger molecules.

Our modeling of the ETPA cross-section for OH, NO, and HF show that ETPA transitions can occur through permanent dipole pathways in addition to virtual-state pathways. However, molecules with permanent dipole pathways and large detuning energies for the virtual-state pathways will have short periods between entanglement-induced transparencies, as seen with OH, NO, and HF in this work. Other molecules not studied here that have permanent dipoles and small detuning energies can have long periods between entanglement-induced transparencies. In this case, the virtual-state pathway would have a much smaller frequency, and therefore much higher amplitude, in eq. 3.4 than the permanent dipole pathway, making the virtual-state pathway dominate the ETPA transition. Thus, the detuning energy of the virtual-state pathway would be used in eq. 3.9 to determine the period between entanglement-induced transparencies, and since the detuning energy would be small, the period between entanglement-induced transparencies would be long. In general, for molecules with large detuning energies, the permanent dipole pathway must be reduced or eliminated if a long period between transparencies is desired; otherwise, the virtual-state pathways will be overshadowed, and the period will be short. For molecules with small detuning energies, a permanent dipole pathway will not present an issue to increasing the period between transparencies since the virtual-state pathways will dominate the ETPA transition anyway.

While N_2 has a longer period between transparencies than the other diatomics studied here, this molecule does not represent the maximum limit. Eq. 3.9 and 3.13 show that the period

is only dependent upon the detunings of the virtual states. N_2 has very large detunings for all of its virtual states, thus limiting how long its period can be. If a molecule had smaller detunings than N_2, the period between transparencies would be longer. If a molecule has more than one such intermediate state, the virtual-state pathways would constructively interfere and increase the period between transparencies even more, making resolution between cross-section maxima and minima experimentally achievable with current technology.

3.6 Conclusions

Unlike classical two-photon absorption, the ways in which the competing transition pathways of ETPA interfere greatly impact their absorption signal. The number of competing virtual-state pathways, the magnitude of their transition dipoles, and the strength of any permanent dipole pathways all impact this signal. Maximizing these parameters in novel organic molecules to increase constructive interference may be the key to rational material design and the development of molecules with maximized ETPA cross-sections. In order to study these parameters, highly accurate descriptions of the electronic states in the molecule are needed.

We have shown that we can identify Born-Oppenheimer intermediate states in molecules that meet both energy and symmetry requirements to be involved in ETPA transitions. Specifically for each molecule: NO can have intraband transitions with the $^2\Sigma^+$ state in the $^2\Pi \rightarrow {}^2\Pi$ transition; HF can have intraband transitions with the $^1\Pi$ state in the $^1\Sigma^+ \rightarrow {}^1\Sigma^+$ transition; N_2 can have intraband transitions with the $^1\Sigma_u^+$ or $^1\Pi_u$ states in the $^1\Sigma_g^+ \rightarrow {}^1\Pi_g$ transition. Using the accurately calculated vertical excitation energies and dipole moments for these states, we have completely modeled the ETPA cross-section as a function of entanglement time for each molecule's transition, taking into account the permanent dipole pathways in addition to the virtual-state pathways, an analysis that has not been completed before. With this complete model of the ETPA process in these small molecules, we were then able to probe the specific parameters in the molecules that most significantly impact its ETPA transitions in order to gain a deeper understanding of the ETPA process. This description of the ETPA process in small molecules may be extended to the ETPA process in large molecules without the need for exact electronic state calculations that would be too computationally intensive for large molecules.

To a greater extent than previous studies, we have analyzed the origin of the nonmonotonic behavior of the ETPA cross-section as a function of entanglement time. We have derived

expressions to characterize the complex beat pattern that arises from the quantum interference between competing transition pathways. Using these expressions, we have determined when an ETPA process can be reasonably approximated to one or two dominant pathways. These dominant pathways determine the magnitude of the ETPA cross-section and the period of entanglement-induced transparencies. When multiple electronic states in a molecule have similar transition pathway amplitudes, the pathways associated with those states constructively interfere to increase the period between entanglement-induced transparencies. These transition pathway amplitudes are proportional to the transition probabilities and inversely proportional to the detuning energies in virtual-state pathways or the incident photon energies in the permanent dipole pathways. We have shown that virtual-state pathways lead to stronger quantum interference effects that deviate from classical behavior, while permanent dipole pathways induce more "classical-like" behavior. Thus, molecules with weaker permanent dipole moments can more strongly exhibit the quantum effects that are unique to using entangled photons. In particular, N_2 deviates from the classical approximation by 3 or more orders of magnitude because it only has virtual-state pathways.

Using only the dominant pathways' energies, we can now calculate when entanglement-induced transparencies will occur in molecules with two significant advantages: 1) the ETPA cross-section does not need to be calculated over a large range of entanglement times to determine when transparencies will occur; 2) precise calculations of the dipole moments are no longer needed, which are extremely difficult for intraband transitions and become increasingly complex when scaling up the size of the molecule under study. We have confirmed the accuracy of our approximations by comparing the approximated period to the exact period when a full ETPA calculation is completed, and our approximated period was within 1 fs of the exact period of all four molecules studied. These accurate approximations may be applied to larger molecules to calculate the locations of their entanglement-induced transparencies without needing to complete a full ETPA calculations with transition dipole moments.

The implication of these unique behaviors in the ETPA cross-section is that it may be possible to design a molecule to act as an ETPA "switch," a molecule that can exhibit ETPA behavior (signal "turned on") or be ETPA transparent (signal "turned off") without having to change anything about the molecule itself. In order to make this experiment feasible with current technology, the period between entanglement-induced transparencies will have to be larger than current technology's resolution limit. Increasing the period between transparencies can be

achieved through constructive interference between virtual-state pathways. Because permanent dipole pathways often dominate the ETPA process in molecules with large detuning energies, longer periods between transparencies are easier to achieve with molecules that do not have permanent dipoles, such as N_2. However, we have also explained how a molecule with a small detuning energy will have a long period between transparencies regardless of whether or not it has a permanent dipole. When the virtual-state pathways dominate the ETPA transition over the permanent dipole pathways, a longer period between transparencies is achieved.

References

1. Pathak, A.; Ghatak, A. Classical Light vs. Nonclassical Light: Characterizations and Interesting Applications. *J. Electromagnet. Wave.* **2018**, *32*, 229-264.
2. Pawlicki, M.; Collins, H. A.; Denning, R. G.; Anderson, H. L. Two-Photon Absorption and the Design of Two-Photon Dyes. *Angew. Chem. Int. Ed.* **2009**, *48*, 3244-3266.
3. Kogej, T.; Beljonne, D.; Meyers, F.; Perry, J. W.; Marder, S. R.; Brédas, J. L. Mechanisms for Enhancement of Two-Photon Absorption in Donor–Acceptor Conjugated Chromophores. *Chem. Phys. Lett.* **1998**, *298*, 1-6.
4. Jagatap, B. N.; Meath, W. J. On the Competition between Permanent Dipole and Virtual State Two-Photon Excitation Mechanisms, and Two-Photon Optical Excitation Pathways, in Molecular Excitation. *Chem. Phys. Lett.* **1996**, *258*, 293-300.
5. Drobizhev, M.; Meng, F. Q.; Rebane, A.; Stepanenko, Y.; Nickel, E.; Spangler, C. W. Strong Two-Photon Absorption in New Asymmetrically Substituted Porphyrins: Interference between Charge-Transfer and Intermediate-Resonance Pathways. *J. Phys. Chem. B* **2006**, *110*, 9802-9814.
6. Bhaskar, A.; Guda, R.; Haley, M. M.; Goodson, T. III. Building Symmetric Two-Dimensional Two-Photon Materials *J. Am. Chem. Soc.* **2006**, *128*, 13972– 13973.
7. Albota, M.; Beljonne, D.; Brédas, J.-L.; Ehrlich, J. E.; Fu, J.-Y.; Heikal, A. A.; Hess, S. E.; Kogej, T.; Levin, M. D.; Marder, S. R.; et al. Design of Organic Molecules with Large Two-Photon Absorption Cross-Sections. *Science* **1998**, *281*, 1653– 1656.
8. Lee, D. I.; Goodson, T. III. Entangled Photon Absorption in an Organic Porphyrin Dendrimer. *J. Phys. Chem. B* **2006**, *110*, 25582-25585.
9. Harpham, M. R.; Süzer, O.; Ma, C. Q.; Bäuerle, P.; Goodson, T. III. Thiophene Dendrimers as Entangled Photon Sensor Materials. *J. Am. Chem. Soc.* **2009**, *131*, 973-979.
10. Guzman, A. R.; Harpham, M. R.; Süzer, O.; Haley, M. M.; Goodson, T. III. Spatial Control of Entangled Two-Photon Absorption with Organic Chromophores. *J. Am. Chem. Soc.* **2010**, *132*, 7840-7841.
11. Upton, L.; Harpham, M.; Suzer, O.; Richter, M.; Mukamel, S.; Goodson, T. III. Optically Excited Entangled States in Organic Molecules Illuminate the Dark. *J. Phys. Chem. Lett.* **2013**, *4*, 2046-2052.
12. Schlawin, F.; Mukamel, S. Two-photon Spectroscopy of Excitons with Entangled Photons *J. Chem. Phys.* **2013**, *139*, 244110.
13. Dorfman, K. E.; Fingerhut, B. P.; Mukamel, S. Manipulation of Two-Photon-Induced Fluorescence Spectra of Chromophore Aggregates with Entangled Photons: A Simulation Study. *Phy. Rev. B* **2012**, *86*, 023851.
14. Varnavski, O.; Pinsky, B.; Goodson, T. III. Entangled Photon Excited Fluorescence in Organic Materials: An Ultrafast Coincidence Detector. *J. Phys. Chem. Lett.* **2017**, *8*, 388-393.
15. Kocher, C. A.; Commins, E. D. Polarization Correlation of Photons Emitted in an Atomic Cascade. *Phys. Rev. Lett.* **1967**, *18*, 575-577.
16. Basché, T.; Moerner, W. E.; Orrit, M.; Talon, H. Photon Antibunching in the Fluorescence of a Single Dye Molecule Trapped in a Solid. *Phys. Rev. Lett.* **1992**, *69*, 1516-1519.

17. Klyshko, D. N.; Penin, A. N.; Polkovnikov, B. F. Parametric Luminescence and Light Scattering by Polaritons. *JETP Lett.* **1969**, *11*, 5-8.
18. Roslyak, O.; Marx, C. A.; Mukamel, S. Nonlinear Spectroscopy with Entangled Photons: Manipulating Quantum Pathways of Matter. *Phys. Rev. A: At., Mol., Opt. Phys.* **2009**, *79*, 033832.
19. Rubin, M. H.; Klyshko, D. N.; Shih, Y. H.; Sergienko, A. V. Theory of Two-Photon Entanglement in Type-II Optical Parametric Down-Conversion *Phys. Rev. A* **1994**, *50*, 5122– 5133.
20. Gea-Banacloche, J. Two-Photon Absorption of Nonclassical Light. *Phys. Rev. Lett.* **1989**, *62*, 1603– 1606.
21. Schlawin, F. Tutorial Entangled Photon Spectroscopy. *J. Phys. B* **2017**, *50*, 203001.
22. Javanainen, J.; Gould, P. L. Linear Intensity Dependence of a Two-Photon Transition Rate. *Phys. Rev. A* **1990**, *41*, 5088-5091.
23. Dorfman, K. E.; Schlawin, F.; Mukamel, S. Nonlinear Optical Signals and Spectroscopy with Quantum Light. *Rev. Mod. Phys.* **2016**, *88*, 045008.
24. Lissandrin, F.; Saleh, B. E. A.; Sergienko, A. V.; Teich, M. C. Quantum Theory of Entangled-Photon Photoemission. *Phys. Rev. B* **2004**, *69*, 165317.
25. Fei, H. B.; Jost, B. M.; Popescu, S.; Saleh, B. E. A.; Teich, M. C. Entanglement-Induced Two-Photon Transparency. *Phys. Rev. Lett.* **1997**, 78, 1679-1682.
26. Saleh, B. E. A.; Jost, B. M.; Fei, H. B.; Teich, M. C. Entangled-Photon Virtual-State Spectroscopy. *Phys. Rev. Lett.* **1998**, *80*, 3483-3486.
27. Hong, C. K.; Ou, Z. Y.; Mandel, L. Measurement of Subpicosecond Time Intervals between Two Photons by Interference *Phys. Rev. Lett.* **1987**, *59*, 2044– 2046.
28. Richter, M.; Mukamel, S. Ultrafast Double-Quantum-Coherence Spectroscopy of Excitons with Entangled Photons *Phys. Rev. A* **2010**, *82*, 013820.
29. Peřina, J.; Saleh, B. E. A.; Teich, M. C. Multiphoton Absorption Cross Section and Virtual-State Spectroscopy for the Entangled N-Photon State *Phys.Rev. A* **1998**, *57*, 3972– 3986.
30. Svozilik, J.; Perina, J.; Leon-Montiel, R. D. Virtual-State Spectroscopy with Frequency-Tailored Intense Entangled Beams. *J. Opt. Soc. Am. B* **2018**, *35*, 460-467.
31. Dorfman, K. E.; Schlawin, F.; Mukamel, S. Stimulated Raman Spectroscopy with Entangled Light: Enhanced Resolution and Pathway Selection. *J. Phys. Chem. Lett.* **2014**, *5*, 2843-2849.
32. Leon-Montiel, R. de J.; Svozilik, J.; Salazar-Serrano, L. J.; Torres, J. P. Role of the Spectral Shape of Quantum Correlations in Two-Photon Virtual-State Spectroscopy *New J. Phys.* **2013**, *15*, 053023.
33. Oka, H. Two-Photon Absorption by Spectrally Shaped Entangled Photons. *Phys. Rev. A* **2018**, *97*, 033814.
34. Kojima, J.; Nguyen, Q. V. Entangled Biphoton Virtual-State Spectroscopy of the $A^2\Sigma^+$–$X^2\Pi$ System of OH. *Chem. Phys. Lett*. **2004**, *396*, 323-328.
35. Luque, J.; Crosley, D. R. LIFBASE: Database and Spectral Simulation (Version 1.5). *SRI International Report MP 99-009* **1999**.
36. Werner, H. J. Molecular Properties from MCSCF-SCEP Wave Functions. II. Calculation of Electronic Transition Moments. *J. Chem. Phys.* **1984**, *80*, 5080-5084.
37. Werner, H. J.; Knowles, P. J. A Second Order Multiconfiguration SCF Procedure with Optimum Convergence. *J. Chem. Phys.* **1985**, *82*, 5053-5063.
38. Werner, H. J.; Knowles, P. J. An Efficient Internally Contracted Multiconfiguration–Reference Configuration Interaction Method. *J. Chem. Phys.* **1988**, *89*, 5803-5814.

39. Werner, H. J.; Reinsch, E. A. The Self-Consistent Electron Pairs Method for Multiconfiguration Reference State Functions. *J. Chem. Phys.* **1982**, *76*, 3144-3156.
40. Dunning, T. H. Gaussian Basis Sets for Use in Correlated Molecular Calculations. I. The Atoms Boron through Neon and Hydrogen," *J. Chem. Phys.* **1989**, *90*, 1007-1023.
41. Lu, P. F.; Yan, L.; Yu, Z. Y.; Gao, Y. F.; Gao, T. An Accurate Calculation of Potential Energy Curves and Transition Dipole Moment for Low-Lying Electronic States of CO. *Commun. Theor. Phys.* **2013**, *59*, 193.
42. Knowles, P. J.; Werner, H. J. An Efficient Method for the Evaluation of Coupling Coefficients in Configuration Interaction Calculations. *Chem. Phys. Lett.* **1988**, *145*, 514-522.
43. Lofthus, A.; Krupenie, P. H. The Spectrum of Molecular Nitrogen. *J. Phys. Chem. Ref. Data*, **1977**, *6*, 113-307.
44. Werner, H. J.; Knowles, P. J.; Knizia, G.; Manby, F. R.; Schütz, M. Molpro: A General-Purpose Quantum Chemistry Program Package. *Wiley Interdiscip. Rev. Comput. Mol. Sci.* **2012**, *2*, 242-253.
45. Lefebvre-Brion, H.; Field, R. W. *The Spectra and Dynamics of Diatomic Molecules*; Elsevier Academic Press: Amsterdam, **2004**.
46. Hippler, M. Interference in Two-Photon Rotational Line Strengths of Diatomic Molecules. *Mol. Phys.* **1999**, *97*, 105-116.
47. Dressler, K.; Miescher, E. Absorption Spectrum of the NO Molecule. V. Survey of Excited States and Their Interactions. *Astrophys. J.* **1964**, *141*, 1266-1283.
48. Konowalow, D. D.; Hirschfelder, J. O. Morse Potential Parameters for O-O, N-N, and N-O Interactions. *Phys. Fluids* **1961**, *4*, 637-642.
49. Cacelli, I.; Carravetta, V.; Moccia, R.; Rizzo, A. The Photon Bound-Bound Electronic Transition Calculations in Molecules. *Mol. Phys.* **1986**, *59*, 403-419.
50. Nee, J. B.; Suto, M.; Lee, L. C. Photoabsorption Cross Section of HF at 107-145 nm. *J. Phys. B* **1985**, *18*, L293-L294.
51. Hitchcock, A. P.; Williams, G. R. J.; Brion, C. E.; Langhoff, P. W. Experimental and Theoretical Studies of the Valence-Shell Dipole Excitation Spectrum and Absolute Photoabsorption Cross Section of Hydrogen Fluoride. *Chem. Phys.* **1984**, *88*, 65-80.
52. Lonardo, G. Di; Douglas, A. E. The Electronic Spectrum of HF. I. The $B^1\Sigma^+$-$X^1\Sigma^+$ Band System. *Can. J. Phys*, **1973**, *51*, 434-445.
53. Luque, J.; Crosley, D. R. Transition Probabilities in the $A\,^2\Sigma^+ - X\,^2\Pi_i$ Electronic System of OH. *J. Chem. Phys.* **1998**, *109*, 439-448.
54. Cageao, R. P.; Ha, Y. L.; Jiang, Y.; Morgan, M. F.; Yung, Y. L.; Sander, S. P. Calculated Hydroxyl $A^2\sum \rightarrow X^2\Pi$ (0,0) Band Emission Rate Factors Applicable to Atmospheric Spectroscopy. *J. Quant. Spectrosc. Radiat. Transfer* **1997**, *57*, 703-717.
55. Jagatap, B. N.; Meath, W. J. Contributions of Permanent Dipole Moments to Molecular Multiphoton Excitation Cross Sections. *J. Opt. Soc. Am. B* **2002**, *19*, 2673-2681.
56. *Landolt-Börnstein: Numerical Data and Functional Relationships in Science and Technology - New Series*; Springer-Verlag: Heidelberg, 1974; Vol. 11/6.
57. Jeunehomme, M.; Duncan, A. B. F. Lifetime Measurements of Some Excited States of Nitrogen, Nitric Oxide, and Formaldehyde. *J. Chem. Phys.* **1964**, *41*, 1692-1699.
58. Huang, Z. S.; Jucks, K. W.; Miller, R. E. The Vibrational Predissociation Lifetime of the HF Dimer upon Exciting the "Free-H" Stretching Vibration. *J. Chem. Phys.* **1986**, *85*, 3338-3341.
59. Hanczyc, P.; Samoc, M.; Norden, B. Multiphoton Absorption in Amyloid Protein Fibres. *Nat. Photonics* **2013**, *7*, 969-972.

3.7 Supporting Information

Sum-of-Waves Analysis for Transition Pathways in ETPA

When two ETPA transition pathways compete with each other, their wave nature creates an interference pattern in the ETPA cross-section as a function of entanglement time. If the pathways have different frequencies, a beat pattern results, where the amplitude of the summation oscillates according to an envelope wave. This envelope, which characterizes the upper and lower limit of the sum of waves, can be expressed as the modulus of the sum of the waves, as in eq. 3.16 below for two generic pathways, pathway 1 = $A_1 e^{i\omega_1 T_e}$ and pathway 2 = $A_2 e^{i\omega_2 T_e}$. Multiplying out by the complex conjugate in eq. 3.S16 results in eq. 3.17. The complex exponential terms can be rearranged so that there is one exponential function added with it complex conjugate (eq. 3.18), which is the same as the real part of the function, i.e. the cosine (eq. 3.19). Eq. 3.19 can be used as a simpler expression for the upper and lower limit envelope waves when two pathways interfere.

$$\pm\sqrt{(A_1 e^{i\omega_1 T_e} + A_2 e^{i\omega_2 T_e}) \times c.c.} \tag{3.16}$$

$$= \pm\sqrt{{A_1}^2 + {A_2}^2 + A_1 A_2 e^{i\omega_1 T_e} e^{-i\omega_2 T_e} + A_1 A_2 e^{-i\omega_1 T_e} e^{i\omega_2 T_e}} \tag{3.17}$$

$$= \pm\sqrt{{A_1}^2 + {A_2}^2 + A_1 A_2 (e^{i(\omega_1 - \omega_2) T_e} + e^{-i(\omega_1 - \omega_2) T_e})} \tag{3.18}$$

$$= \pm\sqrt{{A_1}^2 + {A_2}^2 + 2A_1 A_2 \cos[(\omega_1 - \omega_2) T_e]} \tag{3.19}$$

When two pathways in ETPA have significant constructive interference, the period of entanglement-induced transparencies can be calculated to occur whenever the envelope wave squared equals 0, since the ETPA cross-section is proportional to the envelope squared. The envelope wave must first be offset from 0 by the amplitudes of the two waves that are interfering, as seen in eq. 3.3 and 3.4 in the article. Thus, the entanglement times can be calculated by squaring this envelope wave and setting it equal to 0, as shown in eq. 3.20. Note: only the absolute values of the frequencies are needed since cosine is an even function. Eq. 3.21 results from taking the square root and subtracting A_1 and A_2 from both sides. After squaring both sides (eq. 3.22), all the amplitudes will cancel from both sides, resulting in the cosine expression in eq. 3.23. Solving for T_e results in eq. 3.24.

$$\left(A_1 + A_2 \pm \sqrt{{A_1}^2 + {A_2}^2 + 2A_1 A_2 \cos[(|\omega_1| - |\omega_2|) T_e]}\right)^2 = 0 \tag{3.20}$$

$$\pm\sqrt{{A_1}^2 + {A_2}^2 + 2A_1A_2\cos[(|\omega_1| - |\omega_2|)T_e]} = -(A_1 + A_2) \tag{3.21}$$

$${A_1}^2 + {A_2}^2 + 2A_1A_2\cos[(|\omega_1| - |\omega_2|)T_e] = (A_1 + A_2)^2 = {A_1}^2 + {A_2}^2 + 2A_1A_2 \tag{3.22}$$

$$\cos[(\omega_1 - \omega_2)T_e] = 1 \tag{3.23}$$

$$T_e = \frac{2n\pi}{||\omega_1| - |\omega_2||} \qquad n = 0, 1, 2, \ldots \tag{3.24}$$

To determine whether or not there is significant constructive interference between two competing pathways, we can compare the magnitudes of the upper and lower limit envelopes at the entanglement time $T_e = \frac{n\pi}{||\omega_1| - |\omega_2||}$. At this entanglement time, the lower limit will be at a maximum, yielding the largest value that a relative minimum in the ETPA cross-section can be. If this relative minimum is still significantly smaller than the maximum of the cross-section, then the relative minima are considered entanglement-induced transparencies. If the relative minimum is roughly the same magnitude as the maxima, the relative minima are not transparencies. We begin this comparison of the magnitudes of the upper and lower limit by dividing the lower limit envelope wave squared by the upper limit envelope wave squared, both at the entanglement time $T_e = \frac{n\pi}{||\omega_1| - |\omega_2||}$, shown in eq. 3.25. Since cos(π)=1, eq. 3.25 reduces to eq. 3.26. The simplification steps in eq. 3.27-3.28 are straightforward, with eq. 3.30 showing the most simplified result. The ratio of the upper and lower limit envelope waves is equal to the ratio of the square of the amplitudes of the two pathways that are competing.

$$\frac{\left(A_1 + A_2 + \sqrt{{A_1}^2 + {A_2}^2 + 2A_1A_2\cos\left[(|\omega_1| - |\omega_2|)\frac{\pi}{||\omega_1| - |\omega_2||}\right]}\right)^2}{\left(A_1 + A_2 - \sqrt{{A_1}^2 + {A_2}^2 + 2A_1A_2\cos\left[(|\omega_1| - |\omega_2|)\frac{\pi}{||\omega_1| - |\omega_2||}\right]}\right)^2} \tag{3.25}$$

$$= \frac{\left(A_1 + A_2 + \sqrt{{A_1}^2 + {A_2}^2 - 2A_1A_2}\right)^2}{\left(A_1 + A_2 - \sqrt{{A_1}^2 + {A_2}^2 - 2A_1A_2}\right)^2} \tag{3.26}$$

$$= \frac{\left(A_1 + A_2 + \sqrt{(A_1 - A_2)^2}\right)^2}{\left(A_1 + A_2 - \sqrt{(A_1 - A_2)^2}\right)^2} \tag{3.27}$$

$$= \frac{(A_1 + A_2 + A_1 - A_2)^2}{(A_1 + A_2 - A_1 + A_2)^2} \tag{3.28}$$

$$= \frac{(2A_1)^2}{(2A_2)^2} \tag{3.29}$$

$$= \frac{{A_1}^2}{{A_2}^2} \qquad (3.30)$$

CHAPTER 4

Efficient Modeling of Organic Chromophores for Entangled Two-photon Interferometry

The work in this chapter was published as the journal article:

Kang, G.; Nasiri Avanaki, K.; Mosquera, M. A.; Burdick, R. K.; Villabona-Monsalve, J. P.; Goodson, T.; Schatz, G. C., "Efficient Modeling of Organic Chromophores for Entangled Two-Photon Absorption." *Journal of the American Chemical Society* **2020**, *142* (23), 10446-10458.

Modifications have been made for the style and content of this dissertation. References and supporting information for the manuscript are included in this chapter.

In this chapter, I provided the understanding of how the calculated ETPA linewidth relates to the ETPA cross-section when performing ETPA experimentally. Namely, I connected the arrival time uncertainty of the entangled photon pair to the absorption time uncertainty in the molecule, which is what effectively narrows the final state linewidth when using ETPA excitation. This connection justifies the use of the newly derived narrow ETPA linewidth for calculating ETPA cross-sections even though the molecules studied are large and in solution (experimentally), which would result in many collisions and relaxation mechanisms that would normally be expected to broaden the excited state linewidth.

4.1 Abstract

The use of a nonclassical light source for studying molecular electronic structure has been of great interest in many applications. Here we report a theoretical study of entangled two-photon absorption (ETPA) in organic chromophores, and we provide new insight into the quantitative relation between ETPA and the corresponding unentangled TPA based on the significantly different line widths associated with entangled and unentangled processes. A sum-over-states approach is used to obtain classical TPA and ETPA cross sections and to explore the contribution of each electronic state to the ETPA process. The transition moments and energies needed for this calculation were obtained from a second linear-response (SLR) TDDFT method [*J. Chem. Phys*.,

2016, *144*, 204105], which enables the treatment of relatively large polythiophene dendrimers that serve as two-photon absorbers. In addition, the SLR calculations provide estimates of the excited state radiative line width, which we relate to the entangled two-photon density of states using a quantum electrodynamic analysis. This analysis shows that for the dendrimers being studied, the line width for ETPA is orders of magnitude narrower than for TPA, corresponding to highly entangled photons with a large Schmidt number. The calculated cross sections are in good agreement with the experimentally reported values. We also carried out a state-resolved analysis to unveil pathways for the ETPA process, and these demonstrate significant interference behavior. We emphasize that the use of entangled photons in TPA process plays a critical role in probing the detailed electronic structure of a molecule by probing light-matter interference nature in the quantum limit.

4.2 Introduction

Since the initial discovery of two-photon absorption (TPA) in the 1930s, TPA has attracted significant interest in studying fundamental aspects of light–matter interaction.[1,2] In addition, the use of two-photon sources has been considered in a variety of applications including photopolymerization,[3-4] optical data storage,[5,6] microfabrication,[3,6,7] and light harvesting.[8,9] With classical light sources, TPA is a second-order nonlinear optical process (Rate = $\delta_r \phi^2$, where δ_r is the cross section, and ϕ is the photon flux), thus a very high ϕ ($\sim 10^{22}$ photons cm^{-2} s^{-1}) is required to overcome the small TPA cross-sections. Typical cross-sections for TPA in most organic chromophores are on the order of 10^{-48} cm^4 s photon^{-1}, and are usually quoted in the units of Goeppert-Mayer (GM), where 1 GM is 10^{-50} cm^4 s photon^{-1}.

Important technical developments in the past decades have occurred to facilitate TPA for the purpose of demonstrating quantum optical effects. Specifically, recent advances in nonclassical light sources of entangled photons have enabled new directions in nonlinear spectroscopy for investigating quantum effects in light–matter interaction and developing optical quantum computers.[10-12] The first discovery of entangled photons was reported by Kocher and Commins in 1967, where polarization correlation of two photons simultaneously emitted in the atomic cascade in calcium was observed.[13] Since then, thorough studies of the properties of entangled photons have been carried out both experimentally[14-17] and theoretically.[18,19] Further improvements in photon detection instruments in the past decades have enabled the application of entangled photons

to broader problems including entangled two-photon absorption (ETPA) spectroscopy applied to molecules. Indeed, the unique nonclassical spectral and temporal features of entangled photons make them a potentially powerful probe of molecular electronic structure.

In many ETPA experiments, entangled photons are generated through a nonlinear process called spontaneous parametric down-conversion (SPDC). In SPDC, one photon of higher energy from a pump laser is converted into a pair of photons (namely, signal and idler photons) of lower energy through interaction with a nonlinear crystal. Both energy and momentum are conserved through this process as the combined energy and momentum of an entangled photon pair are the same as those of a pump photon. The twin photons can exit the nonlinear crystal at different times that are dictated by the time needed to propagate the length of the crystal. Entanglement time (T_e) is the largest estimate of this range of times, as dictated by the dimensions of the crystal, which can be further tuned by placing a quartz plate to adjust the refractive index of the medium. More accurately, T_e is determined by the width of the fourth-order temporal coherence function of the entangled photon pair.[20] In addition to the temporal coherence, polarization entanglement is produced for the photon pairs generated using SPDC. Among two types of SPDC processes (Type-I and II), Type-II SPDC generates perpendicularly polarized photon pairs using a BBO (β-barium borate) crystal. Recently entangled photons from the Type-II SPDC process have been extensively applied to the study of various two-photon absorbing chromophores by Goodson and co-workers.[21-25] In these works, the correlated photon pairs arrive at the absorbing medium with a flux density, ϕ_e, per photon pair (photons cm^{-2} s^{-1}). The overall ETPA rate, R_e, is known to be linearly dependent on the input flux:[21,22,24,26]

$$R_e = \sigma_e \phi_e \tag{4.1}$$

where σ_e is the ETPA cross-section. The ETPA cross-sections are reported on the order of 10^{-17} cm^2 using low photon fluxes (10^{12} photons cm^{-2} s^{-1}). The cross sections are many orders of magnitude higher than those which would be obtained from TPA using high photon fluxes (10^{22} photons cm^{-2} s^{-1} × 10^{-48} cm^4 s $photons^{-1}$ = 10^{-26} cm^2).[21-24]

There have been a few theoretical studies in which ETPA cross-sections were evaluated for atoms and small molecules. Fei et al. derived a Kramers-Heisenberg-like expression for the ETPA cross-section expression for the first time and used it to obtain the ETPA cross section of atoms.[26,27] Recently, Burdick et al. have provided detailed quantum chemical descriptions of ETPA for diatomic molecules.[28] In addition, extensive work to simulate the frequency-resolved

absorption of model systems by entangled photons through a pump–probe scheme has been proposed by the Mukamel group.[29-31] Although these previous theoretical studies provided meaningful insights for understanding ETPA for model systems, a quantitative description of entangled photon interactions with large organic chromophores has been lacking, yet it is important for understanding the applicability of ETPA. In addition, future experiments may be able to better control the entanglement beam parameters based on a detailed understanding of entangled photon generation, including sources other than SPDC.[32,33] Since the electronic structure of a molecule becomes more complicated with increasing size of the molecule, a systematic and efficient approach to obtain ETPA cross-sections is required.

Motivated by the above discussion, we use a recently developed approach[34,35] called second linear response time-dependent density functional theory (SLR-TDDFT), in combination with a new approach to the determination of line shape functions for entangled photons, to calculate both TPA and ETPA cross-sections, and to make quantitative comparisons with experiment for large organic molecules. SLR-TDDFT is an extension of traditional linear response TDDFT for the description of excited state properties, including transition multipoles and permanent dipole moments involving excited states. SLR-TDDFT is in principle exact (in practice approximate depending on the choice of exchange-correlation approximation). Formally it involves examining the response of the initial state of the system to a weak external perturbation. This analysis is performed in the linear response regime. SLR-TDDFT is a different approach with respect to standard (linear response) TDDFT as the latter refers to excitations only from the ground electronic state of the molecule being studied. SLR-TDDFT is designed to rigorously determine transition moments between two excited states by doing two calculations, first a conventional TDDFT (ground state) calculation, and then a second in which the initial state is described by the ground state plus a small amount of the excited state of interest. There are other ways to calculate transition moments between different excited states, such as quadratic TDDFT, however SLR-TDDFT has superior scaling properties that are useful for the large molecules being studied in this work. An advantage of the SLR-TDDFT algorithm is that the energy spectrum obtained from standard (or first) linear response TDDFT can be used to compute the excited-state-to-excited-state excitation frequencies, so if the energy spectrum is accurate so are spectroscopic properties. Furthermore, in the algorithm developed by Mosquera et al.,[34] the calculation of a single excited

state has the same cost of a standard LR-TDDFT computation, thus offering computational advantages to the calculation of the ETPA and TPA cross sections for large molecules.

In this work, we apply SLR-TDDFT to the efficient calculation of TPA and ETPA cross-sections for thiophene dendrimers, making comparison with experimental results which have been determined previously. In addition, we describe methods for determining the line shape functions for TPA and ETPA (needed for evaluating cross-sections) in which we take into account the different excited state densities associated with classical and entangled excitation. We justify this analysis by examining the quantum electrodynamics of a three level model of ETPA, where we show that high degrees of entanglement arise when the radiative lifetime of the two-photon excited state is much smaller than that for the one-photon excited states that serve as intermediates in ETPA. The calculated cross-sections show good agreement with the experimental values, indicating the accuracy of both our SLR-TDDFT approach and our model for estimating line shapes. Further, we provide a state-resolved analysis of the interference patterns in the ETPA cross-section over varying entanglement time, and show that the quantum light source provides new information about molecular electronic states that is not available with classical photons.

4.3 Theoretical Details

4.3.1 Classical Two-Photon Absorption Cross-Section

The TPA cross section for a classical two-photon source, δ_r, is given by the following equation under near-resonance conditions:[36-38]

$$\delta_r = \frac{\pi}{2}\omega_1\omega_2\langle S_r^2\rangle g_r(\omega_0, \Gamma) \tag{4.2}$$

where ω_1 and ω_2 are the signal and idler frequencies, respectively. In most TPA and ETPA measurements, the frequencies of the two sources are degenerate ($\omega_1 = \omega_2 = \omega_p/2$). $g_r(\omega_0, \Gamma)$ is the line shape function for excitation by classical photons. The line shape broadening is determined by the excited state damping factor Γ and is often chosen to be 0.1 eV for TPA, corresponding to the measured two-photon line shape for many molecules.[38-41] Later we show that this choice of damping factor provides reasonable quantitative agreement between measured and calculated cross-sections, but one could argue that values larger or smaller by a factor of 2 could also have been used, indicating the level of uncertainty of our results (consistent with previous work[42]). Here we assume a Lorentzian line shape function for $g_r(\omega_0, \Gamma)$:[38]

$$g_r(\omega_0, \Gamma) = \frac{1}{\pi} \frac{\Gamma}{(\omega_1+\omega_2-\omega_0)^2+\Gamma^2} \tag{4.3}$$

Under the two-photon resonance condition, $g_r(\omega_0, \Gamma) = 1/\pi\Gamma$. If the half width is 0.1 eV, then the resulting line shape function yields a value of 13 fs for the effective excited state lifetime. $\langle S_r^2 \rangle$ is the rotationally averaged TPA strength in the molecular coordinate to account for ensemble averaging in bulk samples. This term is expressed as a sum of two-photon transition matrix elements $S_{r,ab}$ with polarization-dependent parameters (F, G, and H):[43]

$$\langle S_r^2 \rangle = \frac{1}{30} \sum_{ab} \left(F S_{r,aa} \bar{S}_{r,bb} + G S_{r,ab} \bar{S}_{r,ab} + H S_{r,ab} \bar{S}_{r,ba} \right) \tag{4.4}$$

For linearly polarized light with parallel polarization, $F = G = H = 2$, whereas $F = H = -1$ and $G = 4$ for perpendicularly polarized light. In the experiment, parallel polarization is generally used for classical TPA measurements whereas perpendicular polarization generated through the Type-II SPDC process is used for ETPA measurements. The classical two-photon transition probability between the initial state $|i\rangle$ and final state $|f\rangle$, S_{ab}, is expressed as the following sum-over-states expression:

$$S_{r,ab}^{if} = \sum_j \left[\frac{D_{ab}^{(j)}}{\Delta_1^{(j)} - i\kappa_j/2} + \frac{D_{ba}^{(j)}}{\Delta_2^{(j)} - i\kappa_j/2} \right] \tag{4.5}$$

where κ_j is a phenomenological line width of the intermediate state $|j\rangle$ which can be considered a constant for a sufficiently weak photon-flux density. This is also referred to as a dephasing factor due to various effects including vibronic and solvent effects. Because of the technical difficulty in accurately obtaining the value both experimentally and theoretically, we will study the cases, where (1) κ_j is zero and (2) has a commonly accepted upper limit which is 0.1 eV. Later in this work, we conclude that the cross-sections are not sensitive to this range of values of κ_j. The transition matrix element with the molecular electric dipole moment components in the molecular coordinates is given by $D_{ab}^{(j)} = \langle f|\mu_b|j\rangle\langle j|\mu_a|i\rangle$. Energy mismatches are defined as $\Delta_1^{(j)} = \epsilon_j - \epsilon_i - \omega_1$ and $\Delta_2^{(j)} = \epsilon_j - \epsilon_f + \omega_2$, where the phase matching condition is $\omega_p = \omega_1 + \omega_2$. Note that the denominators in the first and the second summation terms of the transition matrix element are identical only if the energy sum of the signal and idler photons is resonant with the energy difference between the final and initial states: $\epsilon_f - \epsilon_i = \omega_1 + \omega_2$. One should note that the transition probability for either entangled or unentangled absorption does not necessarily require a summation over molecular electronic states; instead, these molecular states provide a convenient expansion for the virtual states that are the intermediates. However, we have adopted the sum-over-states formulation derived by Teich and co-workers[26,27] for the purpose

of providing a practical tool for probing the molecular electronic structure in this work. Especially for ETPA, this formalism is found to provide a rapidly converging representation of the virtual states, including interferences that arise from the entangled photons. Also, we assume the electronic resonance condition in which both energy mismatch expressions can be generalized as $\Delta_k^{(j)} = \epsilon_j - \epsilon_i - \omega_k$. The terms inside the brackets of the above transition probability element are summed over all electronic states including the ground and final states ($j \geq i$). Under the two-photon resonance condition with degenerate photon energies, eq. 4.5 reduces to the following form:

$$S_{r,ab}^{if} = 2\sum_j \frac{D_{ab}^{(j)}}{\Delta^{(j)} - i\kappa_j/2} = \sum_j \beta_{ab}^{(j)} \tag{4.6}$$

In eq. 4.6, we introduced a single-state transition probability element, $\beta_{ab}^{(j)}$, to resolve the role of each intermediate state and the interaction among multiple states.

4.3.2 Entangled Two-Photon Absorption Cross-Section

The ETPA cross-section was determined quantum mechanically for a time-entangled twin state wave packet.[26,27] Analogous geometrical considerations used in the simplified probabilistic model yield the following expression for the ETPA cross-section:

$$\sigma_e = \frac{\pi}{4A_eT_e}\omega_1\omega_2\langle S_e^2\rangle g_e(\omega_f) \tag{4.7}$$

where A_e is the entanglement area which we assume has the value $A_e = 10^{-6}$ cm^2 based on previous work with SPDC sources.[26] T_e is the entanglement time between the photon pairs which is determined by the experimental setup within the range of 50–100 fs. The line shape function for ETPA is $g_e(\omega_f)$ which will be discussed in detail below. We assume that the entangled photon pairs are created by parametric Type-II down-conversion, where the polarization of the signal photon is orthogonal to that of the idler photon. Using second-order time-dependent perturbation theory with an entangled twin state yields the following transition probability matrix element from the ground state $|i\rangle$ to the final excited state $|f\rangle$:

$$S_{e,ab}^{if} = \sum_j \left[D_{ab}^{(j)} \frac{1-exp\left[-iT_e\Delta_1^{(j)} - T_e\kappa_j/2\right]}{\Delta_1^{(j)} - i\kappa_j/2} + D_{ba}^{(j)} \frac{1-exp\left[-iT_e\Delta_2^{(j)} - T_e\kappa_j/2\right]}{\Delta_2^{(j)} - i\kappa_j/2} \right] \tag{4.8}$$

Using $\beta_{ab}^{(j)}$ defined in eq. 4.6, the above expression can be reduced to the following:

$$S_{e,ab}^{if} = \sum_j \beta_{ab}^{(j)} \left[1 - exp\left[-iT_e\Delta^{(j)} - T_e\kappa_j/2\right]\right] \tag{4.9}$$

Three parameters dependent on the choice of intermediate state $|j\rangle$ are included in this expression: the transition matrix element $D^{(j)}$, the energy mismatch $\Delta^{(j)}$ and the line width of the state κ_j. The strengths of the transition matrix elements and the transition symmetry are critical in determining $D^{(j)}$, as this depends on the dot product of two transition elements. The excited state energies relative to the excitation energy are determined by $\Delta^{(j)}$. Since the evaluation of κ_j is not straightforward for molecules with large numbers of degrees of freedom, we assume a constant line width parameter in this work. Although the entanglement time T_e is not a material dependent factor (it depends on the source properties), the variation in the ETPA cross section on T_e will be also considered due to uncertainty in its value.

4.3.3 ETPA Line Shape

It is important to emphasize that the line shape for ETPA, g_e, is different from the classical TPA line shape function, g_r. The line width associated with g_r is associated with rapid dephasing of the two-photon excited state by any process, while that for g_e reflects decay via entangled photons. There are certain excited states of atoms where these two line widths can be the same, so previous studies of atomic systems have not considered this issue, but in the present case the differences are many orders of magnitude. To understand how this works, we consider two-photon excitation in the three-level model shown in Fig. 4.1.

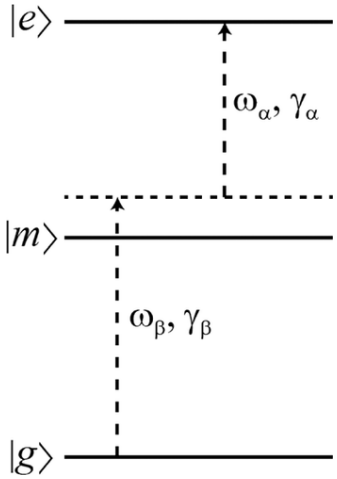

Figure 4.1. Three-level model used for the description of two-photon absorption. The molecule initially is in its ground state and may absorb a photon with excitation energy ω_β and absorption rate γ_β, followed by the absorption of a second photon with excitation energy ω_α and rate γ_α.

In this model, the molecule in its ground state may absorb a photon with excitation energy of ω_β and absorption rate γ_β, followed by absorption of a second photon with excitation

energy of ω_α and rate γ_α. In this version of the analysis we consider unentangled photons. The interaction Hamiltonian, in the rotating-wave approximation, for this system is expressed as follows:

$$\hat{H}_I = \hbar g_\alpha^* \hat{\psi}_{me}^\dagger \hat{a} e^{-i\Omega_\alpha t} + \hbar g_\beta^* \hat{\psi}_{gm}^\dagger \hat{a} e^{-i\Omega_\beta t} + H.c. \tag{4.10}$$

where $\omega - \omega_i = \Omega_i$. The molecule-field couplings in the dipole approximation are given by $g_\alpha^* = \langle \boldsymbol{\mu}_{me} \cdot \mathbf{E}(\mathbf{r}) \rangle$ and $g_\beta^* = \langle \boldsymbol{\mu}_{gm} \cdot \mathbf{E}(\mathbf{r}) \rangle$, where $\boldsymbol{\mu}_{me}$ and $\boldsymbol{\mu}_{gm}$ are the corresponding dipole matrix elements and $\mathbf{E}(\mathbf{r})$ is the electric field interacting with the system. It should be noted that the coupling matrix elements are assumed to be averaged over all possible orientations. The transition operators for the absorption scheme shown in Fig. 4.1 are defined by the following:

$$\begin{aligned} \hat{\psi}_{me}^\dagger &= |e\rangle\langle m|, \hat{\psi}_{gm}^\dagger = |m\rangle\langle g| \\ \hat{\psi}_{me} &= |m\rangle\langle e|, \hat{\psi}_{gm} = |g\rangle\langle m| \end{aligned} \tag{4.11}$$

The overall set of basis functions is given by $|0\rangle \otimes |g\rangle$, $|0\rangle \otimes |m\rangle$, and $|0\rangle \otimes |e\rangle$ and we use this basis to construct the interaction Hamiltonian,

$$\hat{H}_I = \hbar \begin{bmatrix} 0 & g_\beta e^{-i\Omega_\beta t} & 0 \\ g_\beta^* e^{-i\Omega_\beta t} & 0 & g_\alpha e^{-i\Omega_\alpha t} \\ 0 & g_\alpha^* e^{-i\Omega_\alpha t} & 0 \end{bmatrix} \tag{4.12}$$

Given this Hamiltonian, the time evolution of the density matrix is specified by the Liouville equation as follows:

$$\frac{\partial \rho_{ij}}{\partial t} = -\frac{i}{\hbar} \sum_k \left(H_{ik}\rho_{kj} - \rho_{ik}H_{kj} \right) - \left(\gamma_i \rho_{ij} - \rho_{ij}\gamma_j \right) \tag{4.13}$$

where we include for the relaxation of each state using $\langle i|\hat{\gamma}|j\rangle = \gamma_i \delta_{ij}$. The decay rates of the populations of the first and second excited states will be denoted γ_α and γ_β, respectively. It should be noted that here have not included dephasing in eq. 4.13 (as can be done using the Lindblad equation) so as to simplify the analysis. In order to obtain the solution to these equations of motion, it is more convenient to reformulate it using the transition operators $\rho_{ij}(t) = \hat{\phi}_i(t)\hat{\phi}_j^*(t)$ as follows:[44]

$$\frac{\partial \hat{\phi}_i(t)}{\partial t} = -\frac{i}{\hbar} \sum_j H_{ij} \hat{\phi}_j(t) - \gamma_i \hat{\phi}_i(t) \tag{4.14}$$

which can be simplified in a matrix form,

$$\begin{bmatrix} \dot{\phi}_g \\ \dot{\phi}_m \\ \dot{\phi}_e \end{bmatrix} = \begin{bmatrix} -i\omega_g & -ig_\beta & 0 \\ -ig_\beta^* & -(\gamma_\beta + i\omega_m) & -ig_\alpha \\ 0 & -ig_\alpha^* & -(\gamma_\alpha + i\omega_e) \end{bmatrix} \begin{bmatrix} \phi_g \\ \phi_m \\ \phi_e \end{bmatrix} \tag{4.15}$$

With no further approximations, the above coupled set of equations can be solved numerically. However, it is more instructive and sufficiently accurate at low intensities to assume that we are in a weak interaction regime so that the population of the intermediate state does not change over time, i.e., $\dot{\phi}_m = 0$, therefore we have the following:

$$\phi_m = \frac{ig_\beta^*}{\gamma_\beta - i\omega_m}\phi_g - \frac{ig_\alpha}{\gamma_\beta - i\omega_m}\phi_e \tag{4.16}$$

Substituting the above expression in eq. 4.15 and diagonalizing the matrix, the general solution for this set of differential equations with the initial condition of $\rho_{ee}(t = 0) = \rho_{mm}(t = 0) = 0$ and $\rho_{gg}(t = 0) = 1$, is given by:

$$\rho_{gg}(t) = \phi_g\,(t)\phi_g^*(t) = e^{-2\theta t}, \text{ where } \theta = \frac{\gamma_\beta |g_\beta|^2}{\gamma_\beta^2 + \omega_\beta^2}$$

$$\rho_{ee}(t) = \phi_e\,(t)\phi_e^*(t) = K_e\left[e^{-2\gamma_\alpha t} - 2e^{-(\gamma_\alpha+\theta)t}cos\left(\omega_\beta t\right) + e^{-2\theta t}\right] \tag{4.17}$$

where,

$$K_e = \frac{|g_\alpha g_\beta|^2}{\left(\omega_\alpha\omega_\beta + \omega_\beta^2 + \gamma_\alpha\gamma_\beta - |g_\beta|^2\right)^2 + \left(\omega_\alpha\gamma_\beta + \omega_\beta\gamma_\beta + \omega_\beta\gamma_\alpha\right)^2}.$$

We obtained the above expressions assuming $\omega_g = 0$, $\omega_m = \omega_\beta$, and $\omega_e = \omega_\alpha + \omega_\beta$. Note that here ρ_{gg}, ρ_{mm}, and ρ_{ee} are the density of ground, intermediate and excited states, respectively. We see that the excited state probability $\rho_{ee}(t)$ involves the competition between two time scales, one determined by γ_α and the other by θ. Here, θ is determined by the pumping rate to the intermediate state. If this is fast enough, then the time dependence of ρ_{ee} is governed by θ. Alternatively for slower pumping, γ_α determines the time scale for populating the excited state. Below we show that the parameters relevant to the present work are where γ_α dominates. We may determine the ground and excited state densities in the frequency domain for a more advanced analysis,

$$\rho_{gg}(\omega) = \frac{4\theta}{4\theta^2 + \left(\omega - \omega_\beta\right)^2}$$

$$\rho_{gg}(\omega) = \frac{4\gamma_\alpha}{4\gamma_\alpha^2 + (\omega-\omega_\alpha)^2} - \frac{2(\gamma_\alpha+\theta)}{\omega_\beta^2 + (\gamma_\alpha+\theta)^2 + (\omega-\omega_\alpha)^2} + \frac{4\theta}{4\theta^2 + (\omega-\omega_\alpha)^2} \tag{4.18}$$

In Fig. 4.2 we plot ρ_{gg} and ρ_{ee} as a function of frequency using parameters discussed later for the planar 6T molecule. This shows the extremely narrow line shape for ρ_{ee} near $\omega = \omega_\alpha$ that arises using the small value of γ_α that results from the SLR-TDDFT calculations.

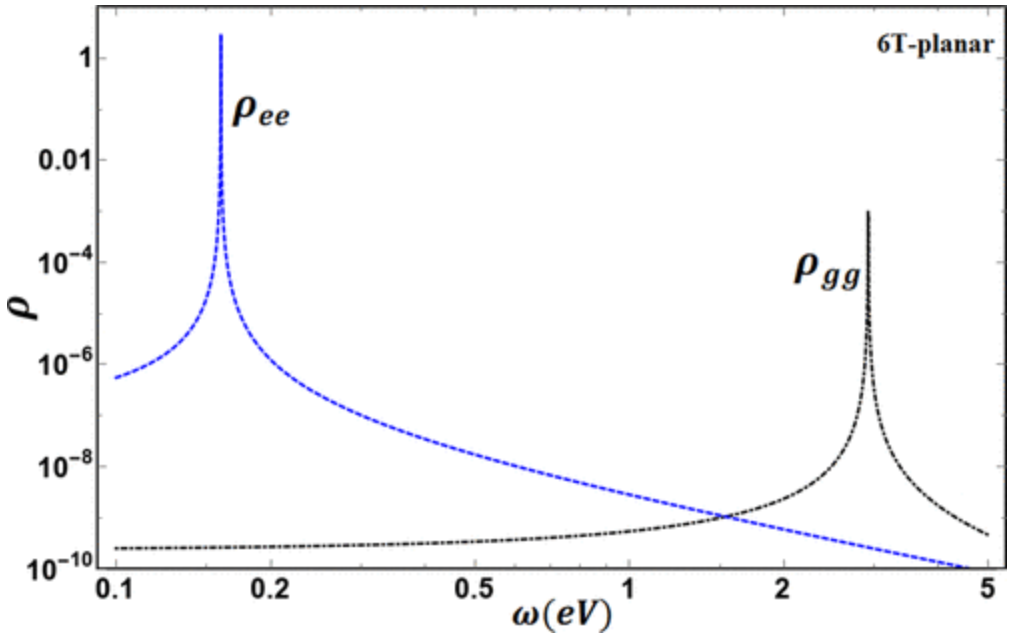

Figure 4.2. Population of ground and two-photon excited states for the three-level model. In the calculations, we used the values in Tables 4.1 and 4.3 for the excitation energies of 6T-planar (ω_α, ω_β), and the widths $\gamma_\alpha = 0.001$ and $\gamma_\beta = 1.6$ MHz.

In the supporting information (SI), we present a similar analysis of the Liouville equation within the context of quantum electrodynamics, as applied to emission process starting from the two-photon excited state. In this case, the emission line width is determined by the second order frequency correlation function of the emitted photons:

$$g_x^{(2)}(\omega) = \gamma_\alpha\gamma_\beta\left[\frac{\gamma_\beta}{\gamma_\alpha} - 1\right]\frac{1}{(\omega-\omega_\alpha-\omega_\beta)^2+\gamma_\alpha^2} \times \frac{1}{(\omega-\omega_\beta)^2+\gamma_\beta^2} \tag{4.19}$$

The width of resonances in this correlation function, which determines the characteristic width of the frequency anticorrelation, is governed by γ_α as long as $\gamma_\alpha \ll \gamma_\beta$. The spectra associated with $g_x^{(2)}$ are plotted in Fig. 4.10 using the calculated values for the molecules of interest in this work. Note that two sharp peaks are associated with the emission process. The peaks represent the detection of one and two emitted photons where the width corresponding to the two-photon process is much narrower than that of the one-photon process. Therefore, γ_α can be interpreted as a width factor while it is the emission rate of the first photon. We also note that $\gamma_\alpha \ll \gamma_\beta$ is required for producing a highly entangled state (large Schmidt number) in two-photon emission.[45]

It is interesting to note that the molecule does not broaden the line width due to collisions with its environment, relaxation through non-radiative processes, etc. This rather

unusual result stems from not being able to define exactly when ETPA took place. Though the time difference of the two absorption events is well-defined as less than or equal to T_e, the time at which the pair as a whole arrives at the molecule, and therefore the time at which the first photon is absorbed, is not well defined. From the monochromatic pump beam assumed here, the entangled photons can be created at any time in the crystal since the pump beam is always on inside the crystal, as opposed to being a pulsed beam whose intensity comes and goes with the repetition rate. There is therefore great uncertainty in when the entangled photons were created. Note that the creation time of the pair as a whole is the Fourier conjugate of the pump bandwidth, since smaller pump bandwidths are broader in time and therefore spend more time in the crystal. Since the time at which the photons were absorbed has a large uncertainty, the time at which the excited state in the molecule relaxes must also have a large uncertainty. Therefore, the line width in frequency must be very narrow as the Fourier conjugate. It is expected that broadening the pump laser in frequency would shorten the excited state life time and broaden the line width. More work to confirm this is required.

We conclude that the width γ_α of the two-photon state ρ_{ee} shows up equivalently in both the absorption and emission processes. We note that this use of the spontaneous radiative emission lifetime of the two-photon excited state to determine the line width for the ETPA cross section was used previously for the OH molecule.[46] In the present applications, we determined the ETPA line shape using the spontaneous radiative lifetime from Fermi's golden rule:

$$g_e\left(\omega_f\right) = \tau_r = \left[\sum_{j<f} \frac{4}{3\hbar}\left(\frac{|\omega_{if}|}{c}\right)^3 \left|\mu_{if}\right|^2\right]^{-1} \tag{4.20}$$

based on results for the two-photon excited state from the SLR-TDDFT calculations. In addition, we have verified from our calculations that the two-photon allowed excited state has a much longer radiative lifetime than the intermediate states produced after emission of the first photon. Due to this huge difference in lifetimes, two-photon absorbing dyes are an ideal system for maximum ETPA efficiency.

4.4 Computational Details

The geometries of the molecules investigated in this work were first optimized with the B3LYP hybrid functional and the 6-31G* basis set. This same level of theory was used for the

excited state calculations, as for 18T this is the highest level that is feasible with the facilities available to us. For each molecule, a SLR-TDDFT calculation was carried out to generate the 15 lowest-lying excited states. DFT and TDDFT calculations were performed using the NWChem computational package version 6.6 modified by Mosquera et al. to calculate oscillator strengths and transition dipole matrix elements for intraband transitions between two excited states.[34,35] In this approach, the intraband transition dipoles are effectively calculated by running two steps of TDDFT. In the first step, a standard linear response TDDFT calculation is run, and the ground state orbitals are redefined as follows (the Tamm-Dancoff approximation is used here):

$$\varphi_{i\sigma}(\vec{\boldsymbol{r}}) \leftarrow \varphi_{i\sigma}(\vec{\boldsymbol{r}}) + \lambda \sum_a X^I_{ai\sigma}\varphi_{a\sigma}(\vec{\boldsymbol{r}})$$
`
$$\varphi_{a\sigma}(\vec{\boldsymbol{r}}) \leftarrow \varphi_{a\sigma}(\vec{\boldsymbol{r}}) - \lambda \sum_i X^I_{ai\sigma}\varphi_{i\sigma}(\vec{\boldsymbol{r}}) \quad (4.21)$$

where the indices *i* and *a* denote occupied and virtual orbitals, respectively, σ denotes the *z*-spin, $X_{ai\sigma}^I$ is the excitation vector from standard TDDFT for the excited state labeled *I*, and λ is a small number (in spin-restricted calculations we set $\varphi_{p,\uparrow} = \varphi_{p,\downarrow}$). These new orbitals, with the exact XC potentials, could represent the density of the linear combination $\Psi_0 + \lambda\Psi_I$, where Ψ_0 is the true ground-state wave function, and Ψ_I is the true excited state of interest. With the redefined orbitals, the LR-TDDFT equations are solved once again, and the transition dipoles of the perturbed and original LR-TDDFT calculations are compared. In ref. [34], we showed that the numerical derivative

$$\boldsymbol{d}_{j,I} = \frac{\boldsymbol{d}_{j,0}(\lambda) - \boldsymbol{d}_{j,0}(\lambda=0)}{\lambda} \quad (4.22)$$

can be used to compute the transition dipole ($\mathbf{d}_{J,I}$) for the excitation from state *I* to state *J* (where *J* is in a chosen energy window). In the above equation, $\mathbf{d}_{J,0}$ denotes the transition dipoles for excitation from the reference to the state labeled *J*. On the basis of our previous calculations on oligomers of polythiophene,[35] we determined that $\lambda = 10^{-2}$ is appropriate for calculations of the above derivative (the results do not change significantly by further reducing this value). The SLR-TDDFT calculation yields a new family of excitation vectors, which we refer to as SLR vectors. However, if some roots are degenerate, then the SLR-TDDFT calculation can slightly break the degeneracy, and the SLR vectors have to be rematched with their first LR counterparts. To reorganize the roots, we used the following criterion: a first linear response vector $\mathbf{X}$ and an SLR vector $\bar{\mathbf{X}}$ correspond to one another if $1 - C_r < |\mathbf{X} \cdot \bar{\mathbf{X}}| < 1 + C_r$. We use the value $C_r = 0.05$. We thus have two sets of transition dipoles, one for the ground-state reference, and another for the perturbed reference, constructed with the formula shown in eq. 4.22; these

transition dipoles are computed using the first and second LR excitation vectors, respectively. Once the transition dipoles are obtained, both TPA and ETPA cross sections were calculated using a home-built Python code.

4.5 Results and Discussion

In order to study a model system to obtain TPA and ETPA cross sections, structures of thiophene monomer (1T) and two thiophene dendrimers with 6 and 18 monomers (6T and 18T) were optimized using DFT and the corresponding optimized geometries are shown in Fig. 4.3.

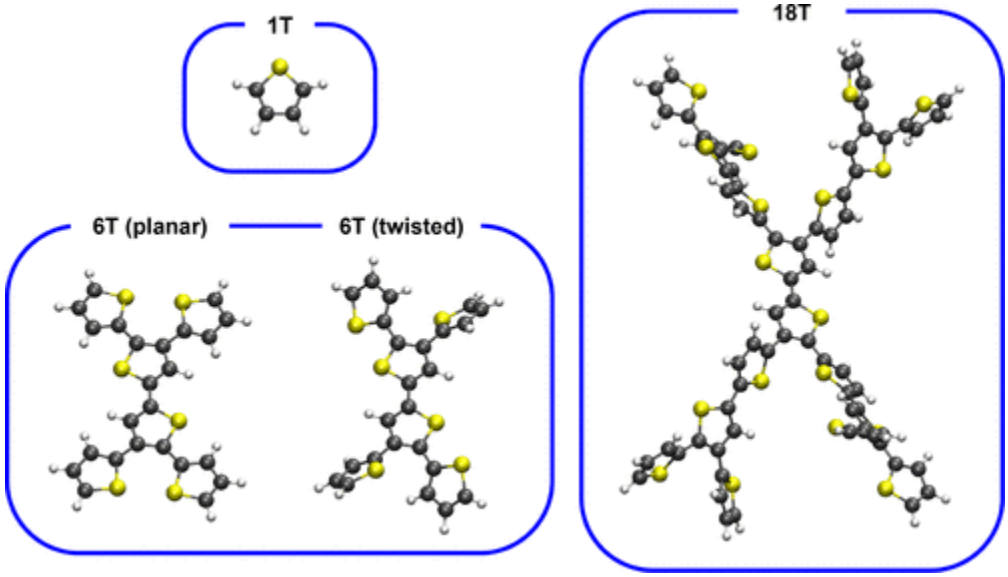

Figure 4.3. DFT optimized structures of thiophene dendrimers with 1, 6, and 18 thiophene monomers. Two different conformers of the 6T molecule were optimized with planar and twisted geometries (white: hydrogen; gray: carbon; and yellow: sulfur).

These thiophene dendrimers were selected because experimental measurements on both TPA and ETPA cross sections were reported by the Goodson group.[22] 1T was not experimentally studied, but we included this molecule for comparison. These molecules can serve as a good model system due to structural simplicity as well as chemical similarity among the molecules as dictated by the thiophene unit. Two structural conformers of 6T were generated so as to test the effects of a torsional geometry change and changes in delocalization of the π electrons on the results. The planar structure in which all atoms are positioned in a single plane is more energetically stable by 29 meV than the twisted structure. However, the thermodynamic barrier between the two structures is small enough for 6T to undergo dynamic structural evolution between different conformers at room temperature. The same issue arises for 18T, but to keep the calculations manageable we will only consider the structure presented in Fig. 4.3.

Absorption spectra of thiophene dendrimers were first simulated to estimate the optically allowed transitions and compare them to UV–vis spectra. In Fig. 4.4, the absorption peaks are broadened using a Lorentzian broadening function with a full-width half-maximum (FWHM) of 0.1 eV. The simulated spectra are compared with the previously reported experimental absorption spectra.[22]

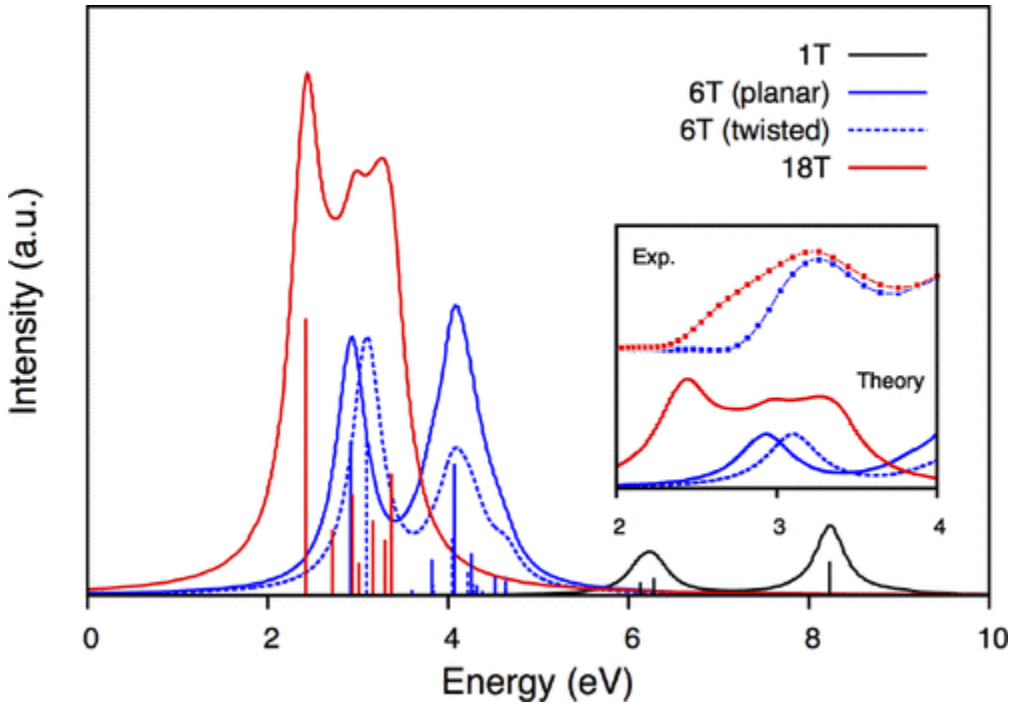

Figure 4.4. Calculated absorption spectra of 1T (black), 6T (blue), and 18T (red) using LR-TDDFT. The vertical lines indicate positions and oscillator strengths of excitation. Experimental absorption spectra are shown in the inset as a comparison.[22]

As shown in the simulated spectra, the first absorption bands at 2.92 and 3.10 eV, corresponding to planar and twisted 6T, respectively, match well with the experimental peak at 3.2 eV. The torsional twist in 6T slightly blue-shifts absorption energies as a result of the reduced planar π-conjugated structure, as expected. However, the small twist in the geometry does not impact the optical transitions significantly. The major absorption peak for 18T experimentally observed at 3.2 eV is likely due to the peaks in the range of 2.7 to 3.1 eV. Also, the first absorption peak at 2.42 eV can be matched with the shoulder peak at ~2.7 eV in the experiment. This shoulder peak is attributed to absorption by α-thiophene chains of longer lengths within the dendron. Even though the TDDFT calculations are performed for isolated molecules, the simulated absorption spectra predict the energies for optically allowed transitions fairly well compared with the experiment carried out in solution. We also note that the absorption peaks of the thiophene

monomer are located well above 6 eV, so dendrimer formation (and the expected delocalization of the π electrons) is important for meaningful two-photon absorption spectroscopy experiments. In Table 4.1, the energy, dipole moment, and oscillator strength of each transition for the ten lowest excited states of 6T and 18T are listed. The first transitions are dipole-allowed transitions with significant oscillator strengths for both molecules. Some calculated transitions are dipole-forbidden with zero dipole moment and not shown in the absorption spectra in Fig. 4.4. However, these states play an important role in determining the TPA cross section as the transition symmetry is different for the two-photon process. Therefore, all excited states from both dipole-allowed and dipole-forbidden transitions were included in the cross section calculations.

Table 4.1. Transition Energy, Dipole, and Oscillator Strength for the Ten Lowest Singlet Transitions of 6T and 18T[a]

	6T (planar)			6T (twisted)			18T		
no.	energy (eV)	$\mu^{i\to f}$ (a.u.)	$f^{i\to f}$	energy (eV)	$\mu^{i\to f}$ (a.u.)	$f^{i\to f}$	energy (eV)	$\mu^{i\to f}$ (a.u.)	$f^{i\to f}$
ES1	2.92	1.66, −3.45, 0.0	1.05	3.10	1.37, −3.49, −0.26	1.07	2.42	2.88, −4.83, −0.28	1.88
ES2	3.08	0.0, 0.0, 0.0	0.0	3.41	0.0, 0.0, 0.0	0.0	2.62	0.0, 0.02, −0.02	0.0
ES3	3.56	−0.01, −0.01, 0.0	0.0	3.65	0.0, 0.0, 0.0	0.0	2.72	0.01, 0.16, 0.02	0.0
ES4	3.60	−0.06, −0.65, 0.0	0.04	3.84	−0.14, −0.84, −0.02	0.07	2.72	−0.08, −2.59, 0.04	0.45
ES5	3.83	−1.25, 1.02, 0.0	0.24	4.03	0.0, 0.0, 0.0	0.0	2.82	0.01, −0.01, 0.01	0.0
ES6	3.83	−0.10, 0.11, 0.0	0.0	4.05	−0.86, −1.78, 0.08	0.39	2.94	−1.49, −2.70, 0.11	0.69
ES7	4.07	2.45, 1.72, 0.0	0.89	4.22	−1.18, −0.49, 0.24	0.17	3.01	−1.72, 0.19, 0.20	0.22
ES8	4.17	0.01, −0.01, 0.0	0.0	4.28	−0.35, 0.76, −0.07	0.07	3.03	−0.02, 0.0, 0.0	0.0
ES9	4.26	−0.69, −1.51, 0.0	0.29	4.31	0.0, 0.0, 0.0	0.0	3.11	−0.17, −0.14, 0.05	0.0
ES10	4.31	−0.13, −0.04, 0.0	0.0	4.38	−0.52, 0.04, −0.17	0.03	3.17	−0.47, 2.52, 0.09	0.51

[a]ES refers to excited state for each transition.

In Fig. 4.5, TPA cross-sections for 6T and 18T are plotted as a function of pump energy ω_p. Three cross-sections are presented for each molecule, corresponding to choosing the first three excited states as the two-photon excited state.

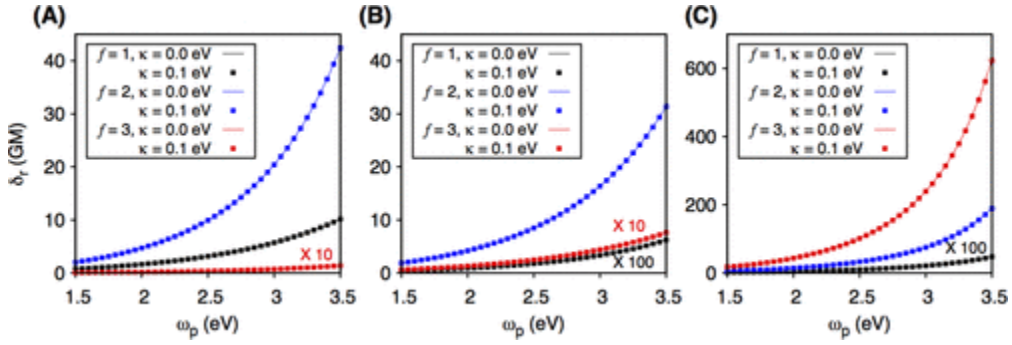

Figure 4.5. TPA cross section plots for (A) planar 6T, (B) twisted 6T and (C) 18T with three lowest excited states chosen as the two-photon excited state. Solid lines and squared dots represent cross sections with excited state line widths κ_j = 0.0 and 0.1 eV, respectively.

As expected from eq. 4.2, a quadratic relationship between the TPA cross section and ω_p is observed for both molecules. The quadratic relationship breaks if the intermediate state is resonant

for one photon excitation, however this is not the case for the molecules considered in this work. For both planar and twisted 6T, the second excited state (ES2), located at 3.08 and 3.52 eV, respectively, yields the highest TPA cross-sections when it is chosen as the final state. (24 and 19 GM at ω_p = 3.1 eV for planar and twisted structures, respectively). When ES1 is chosen as the final state, the TPA cross-section is smaller by a factor of 4 with a value of 6 GM for the planar structure. However, with ES2 as the final state, the TPA cross-section becomes negligible for the twisted geometry. Regardless of the structure of 6T, the choice of ES3 as the final state shows a minimal effect in the TPA cross-section. For 18T, the highest TPA cross-section is found when ES3 is selected as the final state (288 GM at ω_p = 3.1 eV). A negligible contribution by ES1 to the cross-section is observed, whereas ES2 yields a meaningful cross-section value of 90 GM. Note that the states yielding high TPA cross-sections for every molecule are dipole-forbidden for one-photon transitions as shown in Table 4.1. The symmetry of each transition is visualized as a transition density in Fig. 4.11 (SI). Although the transition densities from the ground state (GS) to ES1 for both 6T and 18T are localized along a linear dendrimer chain, they are distributed from one end of the molecule to the other. However, the two-photon allowed transitions for 6T (GS to ES2) are localized around the thiophene dimer moiety at the center, and this decreases the linearity of the transition density distribution. For 18T, the transition density is more delocalized over the dendrimer complex for two-photon allowed transitions (GS to ES2 and ES3). This analysis indicates that assigning the final state for calculating the TPA cross section requires close attention.

The squared dots in Fig. 4.5 show the trend in the TPA cross section with a finite line width value (κ_j) of 0.1 eV. Surprisingly, no significant difference in the cross-section value with variation in κ_j was observed for any of the cases even though this value is toward the upper limit of typical line widths for organic molecules. This is because the energy mismatch $\Delta_k^{(j)}$ in the denominator of the two-photon transition probability (eq. 4.5) is much greater than $\kappa_j/2$ unless a real state exists near the one photon energy. This infers that the existence of real states between the ground and the final states can impact the TPA cross-section significantly. However, this condition does not apply to thiophene dendrimers and many organic chromophores as two-photon allowed states are usually higher in energy than the one-photon allowed state by a minimal amount. The TPA cross-section values for the experimental excitation energy ω_p = 3.1 eV were calculated and are shown in Table 4.2. The comparison between experiment and theory shows excellent agreement (never worse than a factor of 4) for both 6T and 18T. The theoretical values slightly overestimate the TPA cross-

section, which could arise from a variety of factors including the existence of multiple structural conformers, intermolecular interactions, dielectric medium effects, issues with the choice of excited state line width, and errors in the SLR-TDDFT results.

Table 4.2. Comparison between Experimental[22] and Theoretical TPA Cross Sections for 6T and 18T[a]

	experiment[22]	theory	
molecule	δ_r (10^{-50} cm^4 s)	f	δ_r (10^{-50} cm^4 s)
6T (planar)	6	ES2	24
6T (twisted)		ES2	19
18T	230	ES2	90
		ES3	288

[a] Theoretical cross sections were calculated with ω_p = 3.1 eV and κ_j = 0.0 eV.

In order to calculate the ETPA cross-section σ_e, the final states chosen for the TPA cross section calculation (Table 4.2) were used. Calculated σ_e values as a function of the entanglement time T_e and pump energy ω_p are shown as the colormap in Fig. 4.6 for two values of the excited state line widths (κ_j = 0.0 (left) and 0.1 eV (right)).

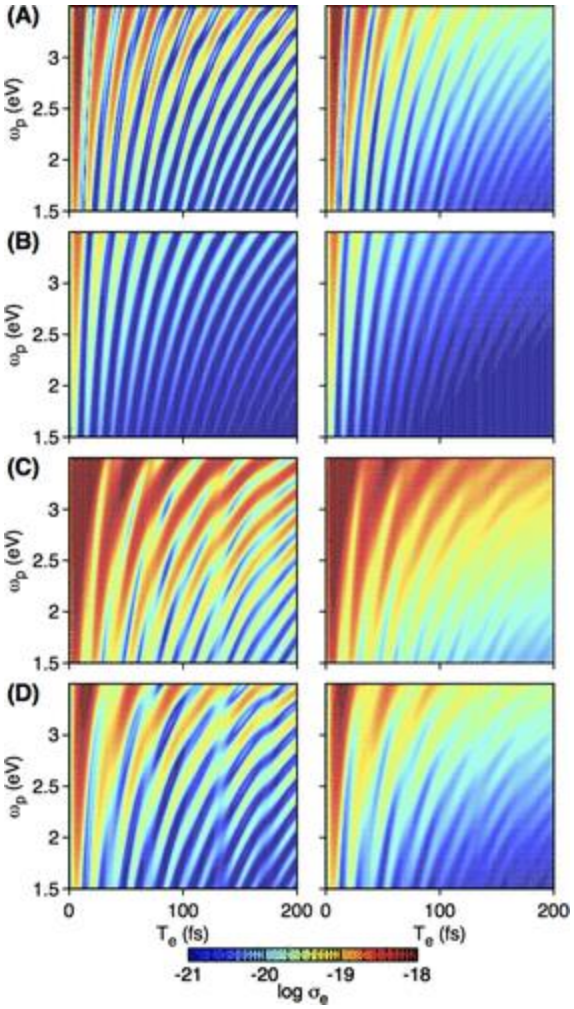

Figure 4.6. ETPA cross section (σ_e) colormaps as a function of T_e (x-axis) and ω_p (y-axis) for (A) planar 6T (f = ES2), (B) twisted 6T (f = ES2), (C) 18T (f = ES2), and (D) 18T (f = ES3). The excited state line width is κ_j = 0.0 and 0.1 eV for the left and right colormaps, respectively. The colormaps are represented in the log scale of σ_e.

As reported in previous works,[26-28] σ_e oscillates with T_e due to the exponential in the cross section expression in eq. 4.8. Since the oscillating nature of this formula originates from interference between the nonclassical photons and the electronic states of the molecule, detailed analysis of the pattern is desired. For both planar and twisted 6T (Fig. 4.6a-b), one wave dominates the oscillation, with small distortions due to interference with other minor features. When the geometry is twisted, the ETPA cross-section is attenuated as in the TPA case with shorter oscillation periods by 1–2 fs, regardless of T_e and ω_p. Unlike 6T, multiple waves with slightly different oscillation periods are overlapped with each other for 18T with either ES2 or ES3 chosen as the final state (Fig. 4.6c-d). The waves interfere all together and result in some irregular local maxima and minima in the cross section colormaps. Also, it is clear that longer oscillation periods

are observed for 18T than for 6T. This is due to energy mismatch values ($\Delta_k^{(j)}$) that are smaller for the larger molecule, as will be discussed later in detail. Note that higher ETPA cross-sections are obtained with ES2 than ES3 chosen as the final state. This is an unexpected result since the TPA cross section is higher by a factor of 3 when ES3 is the final state. Such discrepancy is due to the difference in the lifewidth for random and entangled TPA processes. As discussed in the Theoretical Details (Chapter 4.3), the line width for the ETPA process is related to the radiative emission lifetime of the two-photon excited state, whereas that for random TPA (the 0.1 eV width) is assumed independent of the final state.

Calculated ETPA cross sections as well as line widths for chosen final states are listed in Table 4.3. Due to a large variation in the ETPA cross section, we chose local maximum values at ~100 fs and ω_p = 3.1 eV in the colormaps for the comparison between experiment and theory.

Table 4.3. Comparison between Experimental and Theoretical ETPA Cross Sections for 6T and 18T[a]

	experiment[22]	theory			
molecule	σ_e (10^{-19} cm^2)	f	σ_e (10^{-19} cm^2)	g_e (μs)	γ_f/γ_1
6T (planar)	1.3	ES2	1.7	988	6×10^{-4}
6T (twisted)		ES2	0.18	175	3×10^{-3}
18T	7.1	ES2	5.3	853	6×10^{-4}
		ES3	1.2	84	6×10^{-3}

[a]Local maximum values at ~100 fs are chosen at ω_p = 3.1 eV in the colormaps in Fig. 4.6. (κ_j = 0.0).

The excited state lifetime values (which determine the line width for ETPA) vary within the temporal range from 100 to 1000 μs depending on the choice of the final state. These lifetimes are extremely long compared with typical one-photon excited state radiative lifetimes, due to the small frequency associated with transition between the intermediate state and the two-photon excited state. This is also supported by the obtained line width ratios of the final and the first excited states listed in Table 4.3 where we see $\gamma_f \ll \gamma_1$ which is in line with our assumptions from the quantum electrodynamic analysis for the presence of a highly entangled state. The existence of a long-lived state excited by the entangled photon pair boosts the cross section significantly compared to the unentangled result. For 6T, the lifetime of the entangled two-photon excited state (ES2) becomes shorter for the twisted geometry, resulting in a decreased ETPA cross section. It is

noticeable that ES2 results in a higher ETPA cross section than ES3 does for 18T due to the significantly longer lifetime value. This emphasizes that both the magnitude of the transition matrix element $D_{ab}^{(j)}$ and the lifetime of the excited state induced by the entangled photons play critical roles in determining the ETPA cross-section.

In addition to the wave-like features of the ETPA cross-section, the dependence of cross section on the finite state line width κ_j is notable. A comparison between the left (κ_j = 0.0 eV) and right (κ_j = 0.1 eV) colormaps in Fig. 4.6 shows the attenuation of the ETPA cross-section with a finite value of κ_j. Without any changes in the oscillation pattern of the cross-section, only the magnitude of the ETPA cross-section decreases for a nonzero κ_j. This is in contrast to classical TPA in which the finite value of κ_j barely affects the cross-section value. This is because of the presence of the dephasing factor in the exponential in eq. 4.8, indicating that the transition probability is more sensitive to dephasing of the intermediate states when the two photons responsible for excitation are entangled. In addition, the ETPA cross-section further decreases with increasing T_e for a nonzero κ_j. This is somewhat intuitive as the dephasing effect becomes more significant with increasing temporal coherence between the two photons. The correlation between κ_j and T_e in the ETPA cross-section hints that even more detailed information such as vibronic features can be obtained using a source with a precise temporal resolution.

We now analyze the oscillating behavior of the ETPA cross-sections in more detail. Specifically, it is essential to understand the relationship between the cross-section behavior and the properties of each excited state. To do so, we used the single-state transition probability element suggested in eq. 4.6 to distinguish the contribution from different intermediate states in the TPA cross-section. Note that we used the classical TPA cross-section values for the state-resolved analysis to ignore the dependence on the entanglement time and line width of the ETPA cross-section. Since the TPA cross-section is proportional to the square of the two-photon transition probability, it can be expressed as a double summation over the intermediate states:

$$\delta_r \propto \langle S_r^2 \rangle = \sum_{j,k} \langle \beta^{(j)} \beta^{(k)} \rangle \propto \sum_{j,k} \delta_r^{jk} \tag{4.23}$$

The coupling between two intermediate states is included in the above expression, and a fractional TPA cross-section δ_r^{jk} is introduced which is dependent on the choice of two intermediate states. The fractional TPA cross-section is positive when $j = k$, but can be negative otherwise. In Fig. 4.7, couplings between states $|j\rangle$ and $|k\rangle$ are represented by the fractional TPA cross-section δ_r^{jk} in the colormaps. Red spots represent the most dominant interstate coupling terms.

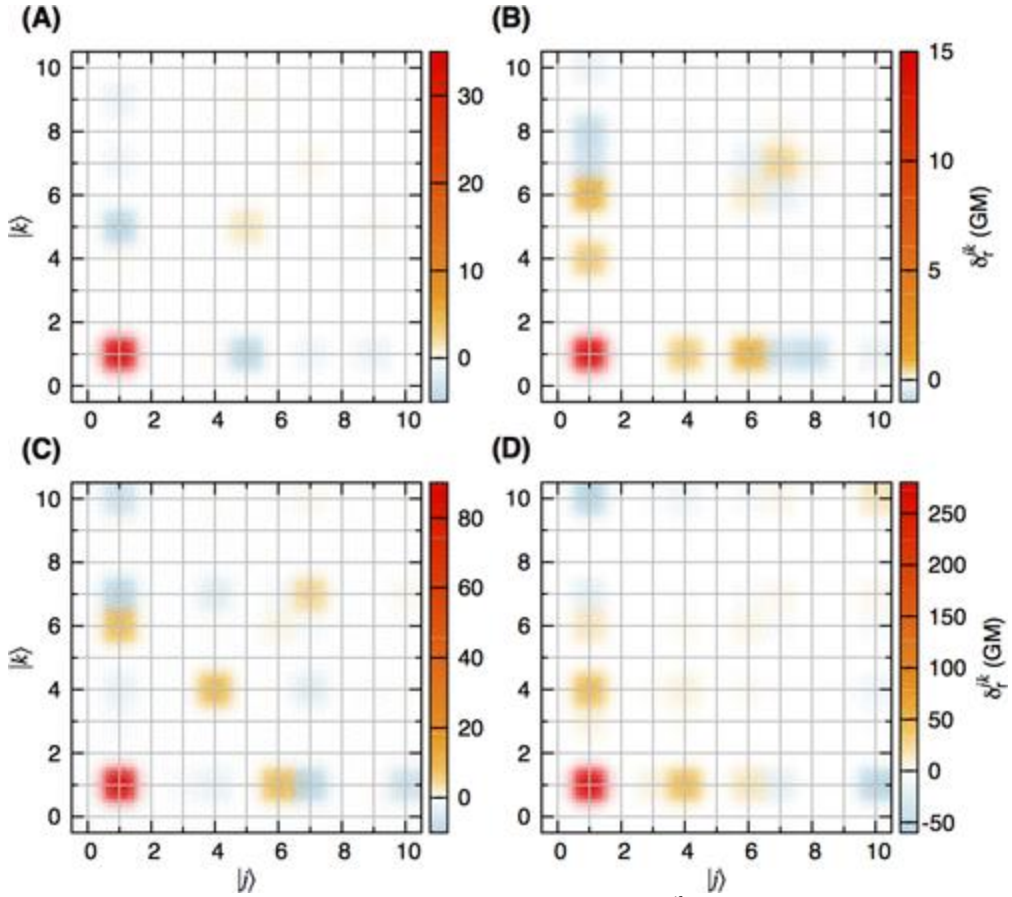

Figure 4.7. Distributions of fractional TPA cross section, δ_r^{jk}, between states $|j\rangle$ and $|k\rangle$ for (A) planar 6T (f = ES2), (B) twisted 6T (f = ES2), (C) 18T (f = ES2), and (D) 18T (f = ES3). (κ_j = 0.0).

In all cases, the diagonal term involving ES1, δ_r^{11}, is the most dominant contributing term to the TPA cross-section. In addition, cross coupling terms between ES1 and other states show minor contributions to the cross section, as represented with orange and blue spots for positive and negative values, respectively. The positive and negative contributions to the cross-section are attributed to constructive and destructive interference among states, respectively. Specifically, destructive interference is observed if two transition matrix elements have different signs as a result of different symmetry. Despite the existence of multiple negative fractional cross-sections originating from destructive interference, the sum of all contributions is always positive as a single term dominates over the others. This result justifies the approximation of using one or two intermediate states in calculating cross-section values.

The state-resolved analysis also shows how molecular structure and size affect the distribution of fractional cross-sections for different states. A comparison between Fig. 4.7A-B shows that the δ_r^{11} value for 6T becomes less dominant compared to other fractional cross-sections

when the molecule is twisted. This is because the distorted structure results in a weaker transition matrix element between GS and ES1 which leads to a lower δ_r[11] value. For a larger molecular size, the distributions of fractional cross-sections for 18T (Fig. 4.7C-D) show that more states are involved in the total cross-section as expected from the higher density of states. The choice of different final states (ES2 and ES3) yields a similar pattern of fractional TPA cross-sections in which ES1 contributes dominantly and ES6 shows minor positive contributions, whereas ES7 and ES10 yield minor negative fractional cross-sections. This hints that ES2 and ES3 play similar roles as the final state in determining the TPA cross-section in terms of symmetry. However, the transition probability from ES1 is higher to ES3 than to ES2 and thereby results in a higher cross-section. The transition density distributions for the first excitations (Fig. 4.11 (SI)) obviously form linearly distributed dipoles along the molecules. However, upper states with zero transition dipole moments are centrosymmetric.

Unlike classical TPA, the fractional ETPA cross-sections provide significant information due to their strong oscillation with varying entanglement time. Specifically, different temporal behaviors are expected depending on the choice of intermediate states. In analogy to the fractional TPA cross-section in eq. 4.23, the fractional ETPA cross section is defined as follows:

$$\sigma_e \propto \langle S_e^2 \rangle = \sum_{j,k} \langle \beta^{(j)} \beta^{(k)} \rangle \left[1 - exp\left[-iT_e\Delta^{(j)} - \frac{T_e\kappa_j}{2}\right]\right] \times \left[1 - exp\left[-iT_e\Delta^{(k)} - \frac{T_e\kappa_k}{2}\right]\right]$$
$$\propto \sum_{j,k} \sigma_e^{jk} \quad (4.24)$$

In Fig. 4.8, total and fractional ETPA cross-sections for 6T and 18T are plotted as a function of T_e for ω = 3.1 eV and κ = 0.0 eV.

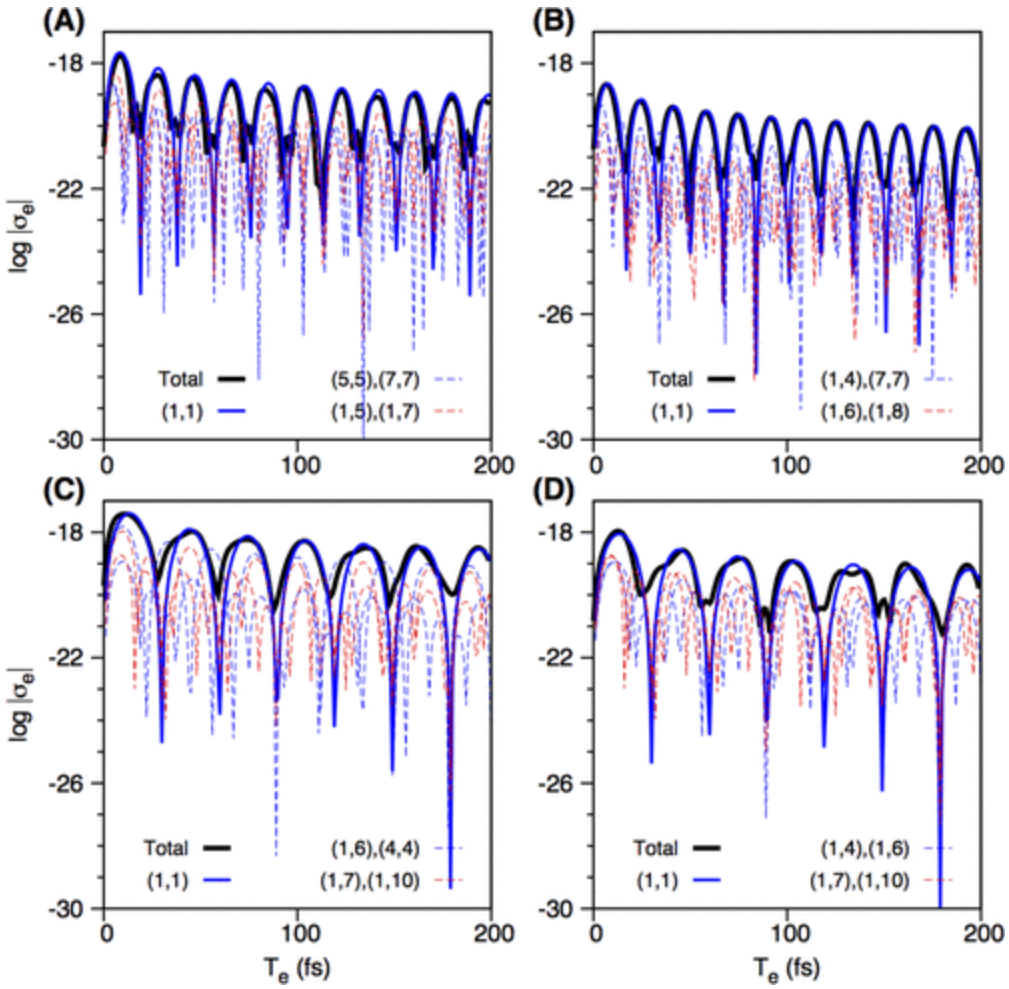

Figure 4.8. ETPA cross section plots for ω_p = 3.1 eV and κ_j = 0.0 eV for (A) planar 6T (f = ES2), (B) twisted 6T (f = ES2) and (C) 18T (f = ES2), and (D) 18T (f = ES3). Bold black curve: total σ_e, bold blue curve: major σ_e^{jk}, blue dashed curve: minor positive σ_e^{jk}, and red dashed curve: absolute value of minor negative σ_e^{jk}. The unit of σ_e is cm^2 and the y-value is plotted in a log scale for σ_e.

A careful look at the peaks and dips of the total cross-section (bold black curves) indicates that a single wave dominates the behavior of the total ETPA cross-section, with minor interference with other small waves. As is the case with classical TPA, σ_e^{11} (blue bold curves) is the most dominant fractional cross-section for both 6T and 18T. Therefore, the oscillation period of the total ETPA cross section can be approximated to that of σ_e^{11}. When the coupling states are identical ($|j\rangle = |k\rangle$), the fractional ETPA cross-section can be written as follows:

$$\sigma_e^{jj} \propto \langle \beta^{(j)2} \rangle \left[1 + e^{-T_e \kappa_j} - 2e^{-T_e \kappa_j / 2} cos\left(T_e \Delta_k^{(j)} \right) \right] \tag{4.25}$$

According to eq. 4.25, the cross section oscillates with a period of $2\pi/\Delta_k^{(j)}$. As discussed in Fig. 4.6, the ETPA cross sections oscillate with shorter periods for 6T than for 18T. The calculated periods with j = ES1 are 19 and 17 fs for planar and twisted 6T, respectively. (Fig. 4.8A-B)

However, longer periods of oscillation with a value of 30 fs are observed for 18T when either ES2 or ES3 is chosen as the final state. (Fig. 4.8C-D) Although the oscillations in total cross sections are dominated by a single state, attenuation of the peak intensities is observed due to multiple minor contributions. Thus, we expect the peaks and dips in the ETPA cross-section as a function of T_e to be less sharp as the size of the molecule increases. The dependence of the ETPA oscillations on the excited state line widths κ_j is even more dramatic. In Fig. 4.12 (SI), ETPA cross-sections are plotted as a function of T_e with κ_j = 0.1 eV. The dephasing in the excited states leads to a decrease in the coherence between the entangled photons and the electronic states. Therefore, oscillations in the ETPA cross-section become featureless with increasing entanglement time. As the amount of coherence between the photonic and electronic states diminishes, the magnitude of the transition matrix elements dominates in determining the ETPA cross-section, approaching the classical limit. Here we conclude that the increased molecular size and broader state line width can lead to decreased coherence in the ETPA process. In addition, any factors that increase the degrees of freedom of the molecule such as vibronic coupling, interactions with surrounding medium, and intermolecular interaction are likely to result in further decoherence. Experimentally, the dependence of the ETPA cross-section on T_e is poorly studied due to technical limitations. Further experimental improvements with a better temporal resolution will offer detailed information regarding the relationship between the ETPA cross-sections and the electronic structure of a molecule.

4.6 Conclusions

In summary, we developed a new theoretical method for calculating TPA and ETPA cross-sections for relatively large organic chromophores and have used it to provide a quantitative interpretation of TPA/ETPA measurements. The second linear response TDDFT method was used to efficiently calculate the transition dipoles and excitation frequencies for the dominant excited states that correspond to absorption of the first or second photon. For both unentangled TPA and ETPA, the calculated cross-sections were in good agreement with previously determined experimental values. A new feature in this work is that we use the radiative lifetime of the two-photon excited state to define the line width used in calculating the ETPA cross section. We justify this result by examining the interaction of an entangled photon pair with a three level system, showing that the two-photon radiative lifetime defines the entangled line shape as long as this lifetime is much

longer than the intermediate state lifetime. The difference between the radiative lifetime of the entangled and unentangled states plays a major role in making the ETPA cross-section many orders of magnitude larger than the TPA result. Finally we have examined the role of each intermediate state in the TPA and EPTA cross-sections. This shows that various factors including molecular size, shape, excited state line width, and the choice of the excited state can affect oscillation patterns in the ETPA cross-section. Such factors can be studied by resolving the ETPA cross-section into two components: one related to the contribution of transition probabilities which scales with the TPA cross section, and one which scales with the two-photon radiative lifetime. Our results in this work show that the first term grows larger with increasing molecular size, but in general the second one shows a nonsystematic variation with molecular size. This conclusion indicates that in future work it will be important to search for rules governing the radiative lifetimes of two-photon excited states. In conclusion, our study successfully provides a pathway to interpret the interaction between entangled photons and relatively large molecules, which is of relevance to a number of chemical applications related to quantum light.

References

1. Göppert-Mayer, M. Über elementarakte mit zwei quantensprüngen. *Ann. Phys.* **1931**, *401*, 273– 294.
2. Schlawin, F.; Dorfman, K. E.; Mukamel, S. Entangled two-photon absorption spectroscopy. *Acc. Chem. Res.* **2018**, *51*, 2207– 2214.
3. Maruo, S.; Nakamura, O.; Kawata, S. Three-dimensional microfabrication with two-photon-absorbed photopolymerization. *Opt. Lett.* **1997**, *22*, 132– 134.
4. Ueno, K.; Juodkazis, S.; Shibuya, T.; Yokota, Y.; Mizeikis, V.; Sasaki, K.; Misawa, H. Nanoparticle plasmon-assisted two-photon polymerization induced by incoherent excitation source. *J. Am. Chem. Soc.* **2008**, *130*, 6928– 6929.
5. Strickler, J. H.; Webb, W. W. Three-dimensional optical data storage in refractive media by two-photon point excitation. *Opt. Lett.* **1991**, *16*, 1780– 1782.
6. Cumpston, B. H.; Ananthavel, S. P.; Barlow, S.; Dyer, D. L.; Ehrlich, J. E.; Erskine, L. L.; Heikal, A. A.; Kuebler, S. M.; Lee, I.-Y. S.; McCord-Maughon, D.; Qin, J.; Röckel, H.; Rumi, M.; Wu, X.-L.; Marder, S. R.; Perry, J. W. Two-photon polymerization initiators for three-dimensional optical data storage and microfabrication. *Nature* **1999**, *398*, 51.
7. Zhou, W.; Kuebler, S. M.; Braun, K. L.; Yu, T.; Cammack, J. K.; Ober, C. K.; Perry, J. W.; Marder, S. R. An efficient two-photon-generated photoacid applied to positive-tone 3D microfabrication. *Science* **2002**, *296*, 1106– 1109.
8. Walla, P. J.; Linden, P. A.; Hsu, C.-P.; Scholes, G. D.; Fleming, G. R. Femtosecond dynamics of the forbidden carotenoid S1 state in light-harvesting complexes of purple bacteria observed after two-photon excitation. *Proc. Natl. Acad. Sci. U. S. A.* **2000**, *97*, 10808– 10813.
9. Oar, M. A.; Dichtel, W. R.; Serin, J. M.; Fréchet, J. M.; Rogers, J. E.; Slagle, J. E.; Fleitz, P. A.; Tan, L.-S.; Ohulchanskyy, T. Y.; Prasad, P. N. Light-harvesting chromophores with metalated porphyrin cores for tuned photosensitization of singlet oxygen via two-photon excited FRET. *Chem. Mater.* **2006**, *18*, 3682– 3692.
10. O'brien, J. L. Optical quantum computing. *Science* **2007**, *318*, 1567– 1570.
11. Hadfield, R. H. Single-photon detectors for optical quantum information applications. *Nat. Photonics* **2009**, *3*, 696.
12. O'brien, J. L.; Furusawa, A.; Vučković, J. Photonic quantum technologies. *Nat. Photonics* **2009**, *3*, 687.
13. Kocher, C. A.; Commins, E. D. Polarization correlation of photons emitted in an atomic cascade. *Phys. Rev. Lett.* **1967**, *18*, 575.
14. Benson, O.; Santori, C.; Pelton, M.; Yamamoto, Y. Regulated and entangled photons from a single quantum dot. *Phys. Rev. Lett.* **2000**, *84*, 2513.
15. Akopian, N.; Lindner, N.; Poem, E.; Berlatzky, Y.; Avron, J.; Gershoni, D.; Gerardot, B.; Petroff, P. Entangled photon pairs from semiconductor quantum dots. *Phys. Rev. Lett.* **2006**, *96*, 130501.
16. Salter, C.; Stevenson, R.; Farrer, I.; Nicoll, C.; Ritchie, D.; Shields, A. An entangled-light-emitting diode. *Nature* **2010**, *465*, 594.

17. Stevenson, R. M.; Young, R. J.; Atkinson, P.; Cooper, K.; Ritchie, D. A.; Shields, A. J. A semiconductor source of triggered entangled photon pairs. *Nature* **2006**, *439*, 179.
18. Troiani, F.; Tejedor, C. Entangled photon pairs from a quantum-dot cascade decay: The effect of time reordering. *Phys. Rev. B: Condens. Matter Mater. Phys.* **2008**, *78*, 155305.
19. Avanaki, K. N.; Schatz, G. C. Entangled photon resonance energy transfer in arbitrary media. *J. Phys. Chem. Lett.* **2019**, *10*, 3181– 3188.
20. Saleh, B. E.; Jost, B. M.; Fei, H.-B.; Teich, M. C. Entangled-photon virtual-state spectroscopy. *Phys. Rev. Lett.* **1998**, *80*, 3483.
21. Lee, D.-I.; Goodson, T. Entangled photon absorption in an organic porphyrin dendrimer. *J. Phys. Chem. B* **2006**, *110*, 25582– 25585.
22. Harpham, M. R.; Süzer, O.; Ma, C.-Q.; Bäuerle, P.; Goodson, T., III Thiophene dendrimers as entangled photon sensor materials. *J. Am. Chem. Soc.* **2009**, *131*, 973– 979.
23. Guzman, A. R.; Harpham, M. R.; Süzer, O.; Haley, M. M.; Goodson, T. G., III Spatial control of entangled two-photon absorption with organic chromophores. *J. Am. Chem. Soc.* **2010**, *132*, 7840– 7841.
24. Upton, L.; Harpham, M.; Suzer, O.; Richter, M.; Mukamel, S.; Goodson, T., III Optically excited entangled states in organic molecules illuminate the dark. *J. Phys. Chem. Lett.* **2013**, *4*, 2046– 2052.
25. Eshun, A.; Cai, Z.; Awies, M.; Yu, L.; Goodson, T., III Investigations of thienoacene molecules for classical and entangled two-photon absorption. *J. Phys. Chem. A* **2018**, *122*, 8167– 8182.
26. Fei, H.-B.; Jost, B. M.; Popescu, S.; Saleh, B. E.; Teich, M. C. Entanglement-induced two-photon transparency. *Phys. Rev. Lett.* **1997**, *78*, 1679.
27. Peřina, J.; Saleh, B. E.; Teich, M. C. Multiphoton absorption cross section and virtual-state spectroscopy for the entangled n-photon state. *Phys. Rev. A: At., Mol., Opt. Phys.* **1998**, *57*, 3972.
28. Burdick, R. K.; Varnavski, O.; Molina, A.; Upton, L.; Zimmerman, P.; Goodson, T., III Predicting and controlling entangled two-photon absorption in diatomic molecules. *J. Phys. Chem. A* **2018**, *122*, 8198– 8212.
29. Roslyak, O.; Marx, C. A.; Mukamel, S. Nonlinear spectroscopy with entangled photons: Manipulating quantum pathways of matter. *Phys. Rev. A: At., Mol., Opt. Phys.* **2009**, *79*, 033832.
30. Schlawin, F.; Dorfman, K. E.; Fingerhut, B. P.; Mukamel, S. Manipulation of two-photon-induced fluorescence spectra of chromophore aggregates with entangled photons: A simulation study. *Phys. Rev. A: At., Mol., Opt. Phys.* **2012**, *86*, 023851.
31. Schlawin, F.; Mukamel, S. Two-photon spectroscopy of excitons with entangled photons. *J. Chem. Phys.* **2013**, *139*, 244110.
32. Jechow, A.; Seefeldt, M.; Kurzke, H.; Heuer, A.; Menzel, R. Enhanced two-photon excited fluorescence from imaging agents using true thermal light. *Nat. Photonics* **2013**, *7*, 973.
33. Dayan, B.; Pe'Er, A.; Friesem, A. A.; Silberberg, Y. Two photon absorption and coherent control with broadband down-converted light. *Phys. Rev. Lett.* **2004**, *93*, 023005.
34. Mosquera, M. A.; Chen, L. X.; Ratner, M. A.; Schatz, G. C. Sequential double excitations from linear-response time-dependent density functional theory. *J. Chem. Phys.* **2016**, *144*, 204105.

35. Mosquera, M. A.; Jackson, N. E.; Fauvell, T. J.; Kelley, M. S.; Chen, L. X.; Schatz, G. C.; Ratner, M. A. Exciton absorption spectra by linear response methods: application to conjugated polymers. *J. Am. Chem. Soc.* **2017**, *139*, 3728– 3735.
36. Bebb, H. B.; Gold, A. Multiphoton ionization of hydrogen and rare-gas atoms. *Phys. Rev.* **1966**, *143*, 1.
37. Peticolas, W. L. Multiphoton spectroscopy. *Annu. Rev. Phys. Chem.* **1967**, *18*, 233– 260.
38. Beerepoot, M. T.; Friese, D. H.; List, N. H.; Kongsted, J.; Ruud, K. Benchmarking two-photon absorption cross sections: performance of CC2 and CAM-B3LYP. *Phys. Chem. Chem. Phys.* **2015**, *17*, 19306– 19314.
39. Albota, M.; Beljonne, D.; Brédas, J.-L.; Ehrlich, J. E.; Fu, J.-Y.; Heikal, A. A.; Hess, S. E.; Kogej, T.; Levin, M. D.; Marder, S. R.; McCord-Maughon, D.; Perry, R. H.; Joseph, W.; Rumi, M.; Subramaniam, G.; Webb, W. W.; Wu, X.-L.; Xu, C. Design of organic molecules with large two-photon absorption cross sections. *Science* **1998**, *281*, 1653– 1656.
40. Beverina, L.; Fu, J.; Leclercq, A.; Zojer, E.; Pacher, P.; Barlow, S.; Van Stryland, E. W.; Hagan, D. J.; Brédas, J.-L.; Marder, S. R. Two-photon absorption at telecommunications wavelengths in a dipolar chromophore with a pyrrole auxiliary donor and thiazole auxiliary acceptor. *J. Am. Chem. Soc.* **2005**, *127*, 7282– 7283.
41. Zheng, S.; Leclercq, A.; Fu, J.; Beverina, L.; Padilha, L. A.; Zojer, E.; Schmidt, K.; Barlow, S.; Luo, J.; Jiang, S.-H.; Jen, A. K.-Y.; Yi, Y.; Shuai, Z.; Van Stryland, E. W.; Hagan, D. J.; Brédas, J.-L.; Marder, S. R. Two-photon absorption in quadrupolar bis (acceptor)-terminated chromophores with electron-rich bis (heterocycle) vinylene bridges. *Chem. Mater.* **2007**, *19*, 432– 442.
42. Masunov, A.; Tretiak, S. Prediction of two-photon absorption properties for organic chromophores using time-dependent density-functional theory. *J. Phys. Chem. B* **2004**, *108*, 899– 907.
43. Monson, P.; McClain, W. Polarization dependence of the two-photon absorption of tumbling molecules with application to liquid 1-chloronaphthalene and benzene. *J. Chem. Phys.* **1970**, *53*, 29– 37.
44. Scully, M.; Zubairy, M. S. *Quantum Optics*; Cambridge University Press: Cambridge, UK, 1997.
45. Muthukrishnan, A.; Agarwal, G. S.; Scully, M. O. Inducing disallowed two-atom transitions with temporally entangled photons. *Phys. Rev. Lett.* **2004**, *93*, 093002.
46. Kojima, J.; Nguyen, Q.-V. Entangled biphoton virtual-state spectroscopy of the A2Σ+–X2Π system of OH. *Chem. Phys. Lett.* **2004**, *396*, 323– 328.

4.7 Supporting Information

Here we consider the quantum electrodynamics of two-photon emission, rather than absorption, with the goal of determining parameters of the three-level model that leads to the generation of highly entangled photons. In the cascade emission model, we define the excited molecule as a three-level system (see Fig. 4.9) generating a photon pair as a result of cascading from excited state |*e*> through the intermediate state |*m*> and to the ground state |*g*>. The molecule is initially excited at t = 0 to the top level |*e*> with the energy ħ($\omega_\alpha + \omega_\beta$) and width γ_α which means it can stay on this state for a duration of γ_α^{-1}.

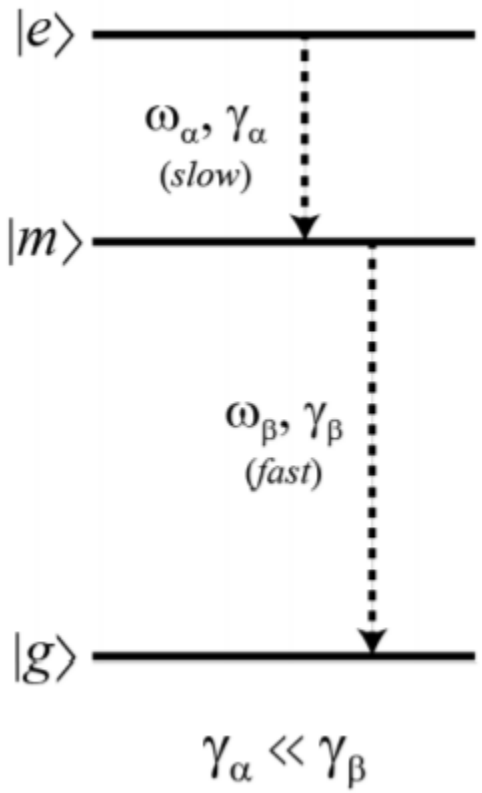

Figure 4.9. Three-level configuration used for the observation of two-photon cascade emission.

For the two-photon emission process, the molecule is in the excited state |ei and the field modes are in the vacuum state |0> at t = 0. Then the state vector of the molecule-field system can be described by:

$$|\psi(t)\rangle = \eta_e(t)|e;0\rangle + \sum_k \eta_{m.k}(t)|m;1_k\rangle + \sum_{kq} \eta_{g;kq}(t)\big|g;1_k,1_q\big\rangle \qquad (4.26)$$

where the symbol |1_k, 1_q> represents the tensor product |1_k> ⊗ |1_q> of two single-photon states in the frequency mode $\omega_{k(q)}$ of a subsystem α (or β) with the probability amplitude of $\eta(\omega_k, \omega q) \equiv \eta_{kq}$.

We can determine the states of the molecule and the radiation field at time t when the molecule starts to emit photons following Weisskopf-Wigner theory. By substituting eq. 4.26 into the time-dependent Schrödinger equation, the following equations of motions for the probability amplitudes η_e, $\eta_{m,k}$, and $\eta_{g.k.q}$ are obtained:

$$\dot{\eta}_e = -i\sum_k g_{\alpha_k}\eta_{m.k}e^{i(\omega_\alpha-\omega_k)t}$$

$$\dot{\eta}_{m,k} = -ig_{\alpha_k}\eta_e e^{-i(\omega_\alpha-\omega_k)t} - i\sum_q g_{\beta_q}\eta_{g,kq}e^{i(\omega_\beta-\omega_q)t}$$

$$\dot{\eta}_{g,kq} = -ig_{\beta_q}\eta_{m.k}e^{-i(\omega_\beta-\omega_q)t} \qquad (4.27)$$

With an assumption that the modes of the field are closely spaced in frequency, we can replace the summation over k and q with an integral:

$$\sum_k \rightarrow 2\frac{V}{(2\pi)^3}\int_0^{2\pi} d\phi \int_0^{\pi} sin\theta d\theta \int_0^{\infty} k^2 dk \qquad (4.28)$$

The radiative decay constants are determined according to Fermi's golden rule:

$$\gamma_\alpha = \frac{\Gamma_\alpha}{2} = \frac{4\omega_\alpha^3\mu_{em}^2}{3\hbar c^3}$$

$$\gamma_\beta = \frac{\Gamma_\beta}{2} = \frac{4\omega_\beta^3\mu_{mg}^2}{3\hbar c^3} \qquad (4.29)$$

Solving the integration implied by eq. 4.26[1,2] one obtains the probability amplitudes as follows:

$$\eta_{m,k}(t) = -g_{\alpha,k}\frac{e^{-i(\omega_k-\omega_\alpha)t-\gamma_\alpha t}-e^{-\gamma_\beta t}}{(\omega_k-\omega_\alpha)+i(\gamma_\alpha-\gamma_\beta)} \qquad (4.30a)$$

$$\eta_{g,kq}(t) = \frac{g_{\alpha,k}g_{\beta,q}}{(\omega_k-\omega_\alpha)+i(\gamma_\alpha-\gamma_\beta)}\left\{\frac{1-e^{-i(\omega_k-\omega_\alpha)t-\gamma_\alpha t}}{\omega_q-\omega_\beta+i\gamma_\beta} - \frac{1-e^{i(\omega_k+\omega_q-\omega_\alpha-\omega_\beta)t-\gamma_\alpha t}}{\omega_k+\omega_q-\omega_\alpha-\omega_\beta+i\gamma_\alpha}\right\} \qquad (4.30b)$$

The first term in eq. 4.30b is dominated by γ_β, which is related to the unentangled component of the evolution with a fast decay rate. As time proceeds the second term in eq. 4.30b, controlled by γ_α, dominates the probability amplitude. In fact this term shows how the ground state population amplitude rises up with time as is determined by $e^{-\gamma\alpha t}$. We may simplify the two-photon state in the long time limit ($t >> \gamma_\alpha^{-1}, \gamma_\beta^{-1}$):

$$|II, Cas\rangle = \sum_{kq}\eta_{cas}|1_k,\alpha;1_q,\beta\rangle \qquad (4.31)$$

where both $\eta_{m,k}(t)$ and $\eta_e(t)$ are zero and we used $\eta_{cas} = \eta_{g,k,q}(\infty)$. Recall that for a linearly polarized field $E^{(+)}(\mathbf{r}_i, t_i) = \sum_k a_k e^{-i\omega kti+i\mathbf{k}\cdot\mathbf{r}i}$, the second order correlation function for the two-photon process is recast as:

$$G^{(2)}(t,\tau) = \langle II, Cas | E^{(-)}(\tau)E^{(-)}(t)E^{(+)}(t)E^{(+)}(\tau) | II, Cas \rangle$$
$$= \sum_{\{a\}} \left\langle II, Cas \middle| E_\alpha^{(-)}(\tau)E_\beta^{(-)}(t) \middle| \{n\} \right\rangle \left\langle \{n\} \middle| E_\alpha^{(+)}(t)E_\beta^{(+)}(\tau) \middle| II, Cas \right\rangle$$
$$= \left\langle II, Cas \middle| E_\alpha^{(-)}E_\beta^{(-)} \middle| 0 \right\rangle \left\langle 0 \middle| E_\alpha^{(+)}E_\beta^{(+)} \middle| II, Cas \right\rangle \quad (4.32)$$

Here a complete set of states *n* is used, but only the vacuum state survives while the others lead to zero. Using the two-photon wave function introduced earlier in eq. 4.31 and defining:[1]

$$\Psi^{(2)}(t,\tau) = \left\langle 0 \middle| E_\alpha^{(+)}(t)E_\beta^{(+)}(\tau) \middle| II, Cas \right\rangle$$
$$= \sum_{kq} \eta_{cas} e^{-i\omega_k \tau - i\omega_q t}$$
$$= -\frac{2L\sqrt{\gamma_\alpha \gamma_\beta}}{c} e^{-(i\omega_\alpha + i\omega_\beta + \gamma_\alpha)\tau} \Theta(\tau) e^{-(i\omega_\beta + \gamma_\beta)(t-\tau)} \Theta(t-\tau) \quad (4.33)$$

and substituting the above result into eq. 4.32, we obtain following correlation function:

$$G^{(2)}(t,\tau) = \left|\Psi^{(2)}(t,\tau)\right|^2 = \frac{4L^2\gamma_\alpha\gamma_\beta}{c^2} \Theta(t)\Theta(t-\tau) e^{-2\gamma_\alpha \tau} e^{-2\gamma_\beta(t-\tau)} \quad (4.34)$$

For a bipartite system, the correlation between parts can be determined by following the normalized cross temporal correlation function:

$$g_x^{(2)}(t,\tau) = \frac{\langle II, Cas | E_\alpha^{(-)}(\tau)E_\beta^{(-)}(t)E_\alpha^{(+)}(t)E_\beta^{(+)}(\tau) | II, Cas \rangle}{\langle II, Cas | E_\alpha^{(-)}(t)E_\alpha^{(+)}(t) | II, Cas \rangle \langle II, Cas | E_\beta^{(-)}(t)E_\beta^{(+)}(\tau) | II, Cas \rangle}$$
$$\approx \gamma_\alpha \gamma_\beta \left(\frac{\gamma_\beta}{\gamma_\alpha} - 1\right) \Theta(t)\Theta(t-\tau) e^{-2\gamma_\alpha \tau} e^{-2\gamma_\beta(t-\tau)} \quad (4.35)$$

A Fourier transform of the above equation leads to:

$$g_x^{(2)}(\omega) \approx \gamma_\alpha \gamma_\beta \left(\frac{\gamma_\beta}{\gamma_\alpha} - 1\right) \frac{1}{(\omega - \omega_\alpha - \omega_\beta)^2 + \gamma_\alpha^2} \times \frac{1}{(\omega - \omega_\beta)^2 + \gamma_\beta^2} \quad (4.36)$$

As a result, we obtain the final expression for $g_x^{(2)}(t, \tau)$ assuming double resonance; $\Delta = |\omega_\alpha - \omega_1| \cong |\omega_\beta - \omega_2| \rightarrow 0$. The correlation function, which gives the characteristic width of the frequency anticorrelation, is equal to γ_α. The spectra associated with $g_x^{(2)}$ are plotted in Fig. 4.10 using the calculated values for the molecules of interest in the main manuscript. Note that two sharp peaks arise due to the presence of two Lorentzians in the expression. Each peak represents the detection of one and two emitted photons where the width corresponding to the two-photon process is much narrower than that of the one-photon process. Here γ_α can be interpreted as a width factor while it is the emission rate of the first photon. Then it is convincing to say that the light

emission is dominated by γ_α as long as $\gamma_\alpha << \gamma_\beta$. Thus γ_α is the linewidth factor associated with emission of two highly entangled photons.

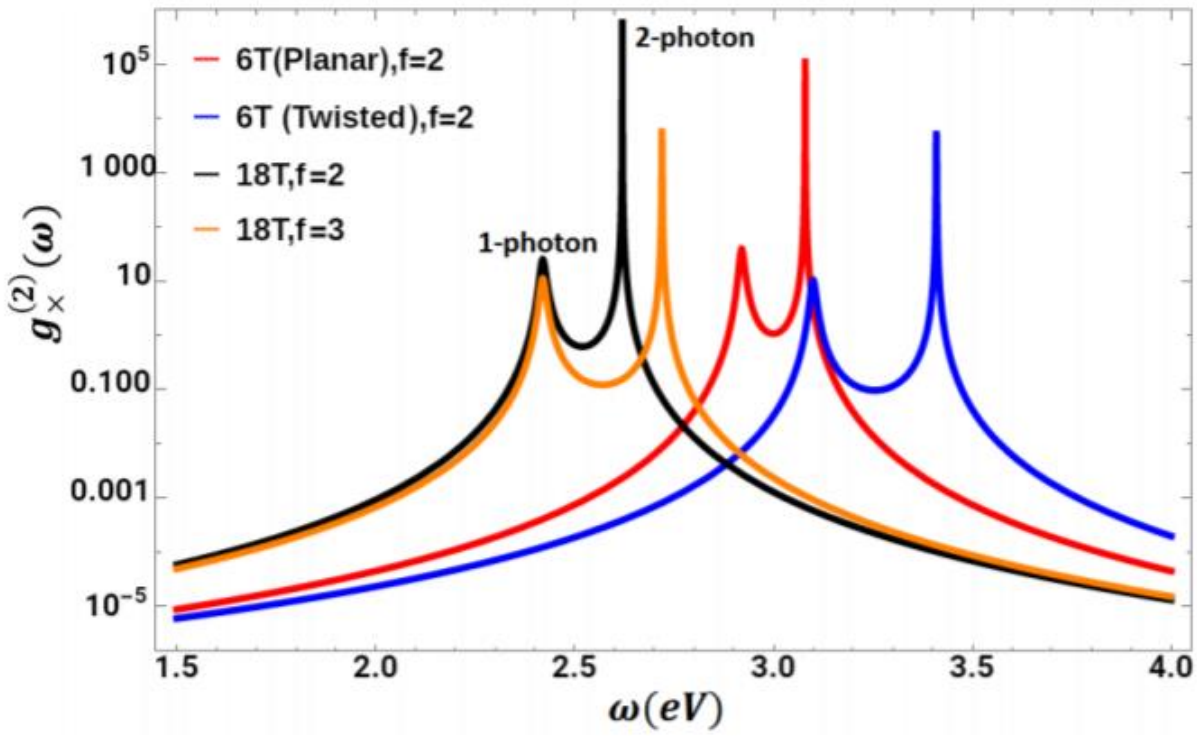

Figure 4.10. Second order frequency correlation function $g_x^{(2)}(\omega)$ in the emission process. In these set of calculations, we used the values in Table 4.1 and 4.3 in the main text for the excitation energies (ω_α, ω_β). For planar 6T, twisted 6T and 18T (f = 2 and 3) γ_α = 0.001, 0.0057, 0.0011, 0.012 MHz, and γ_β = 1.6, 1.8, 1.9, 1.9 MHz respectively.

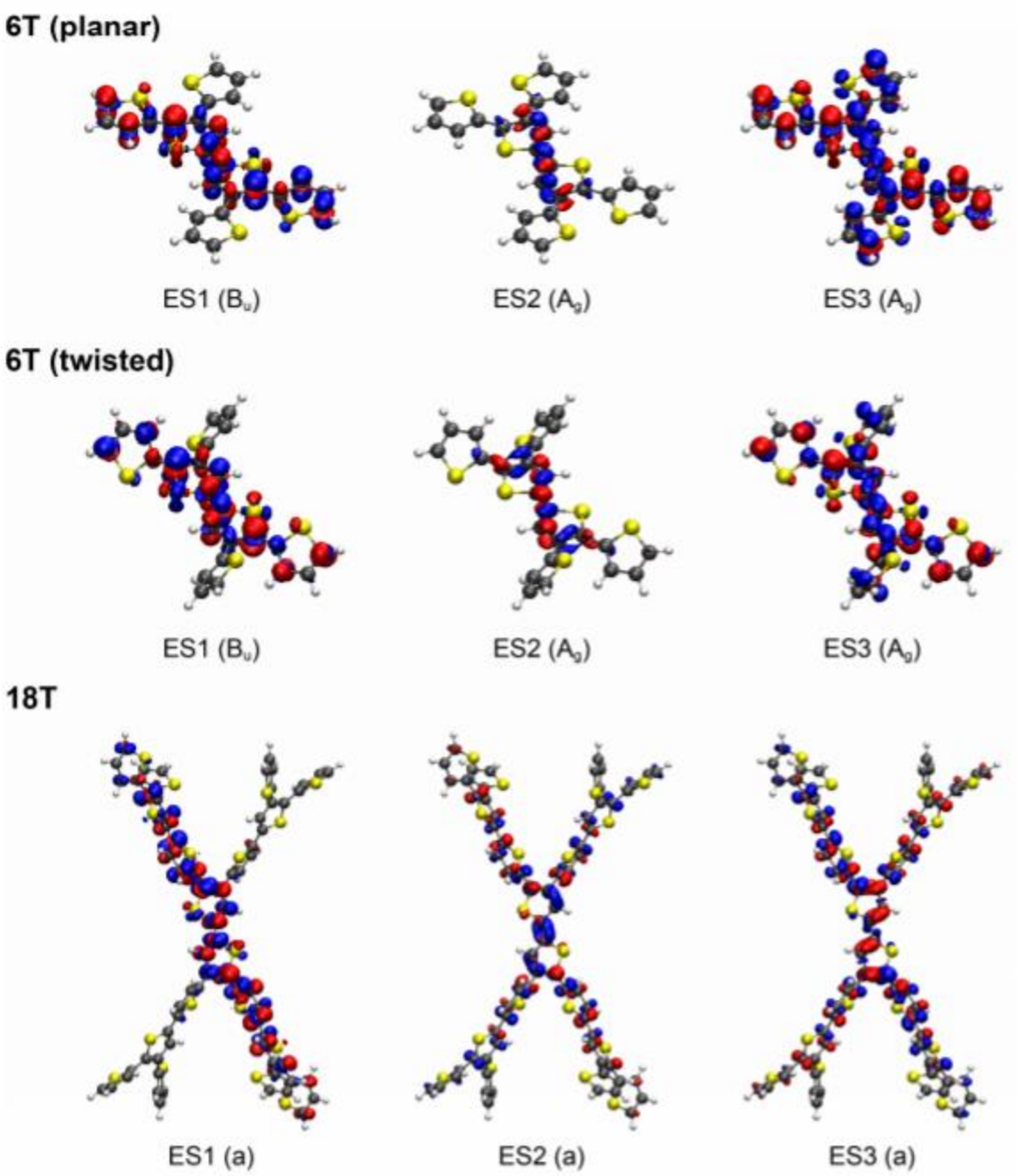

Figure 4.11. Transition density plots for planar 6T (top), twisted 6T (middle), and 18T (bottom) of three lowest singlet transitions calculated using LR-TDDFT.

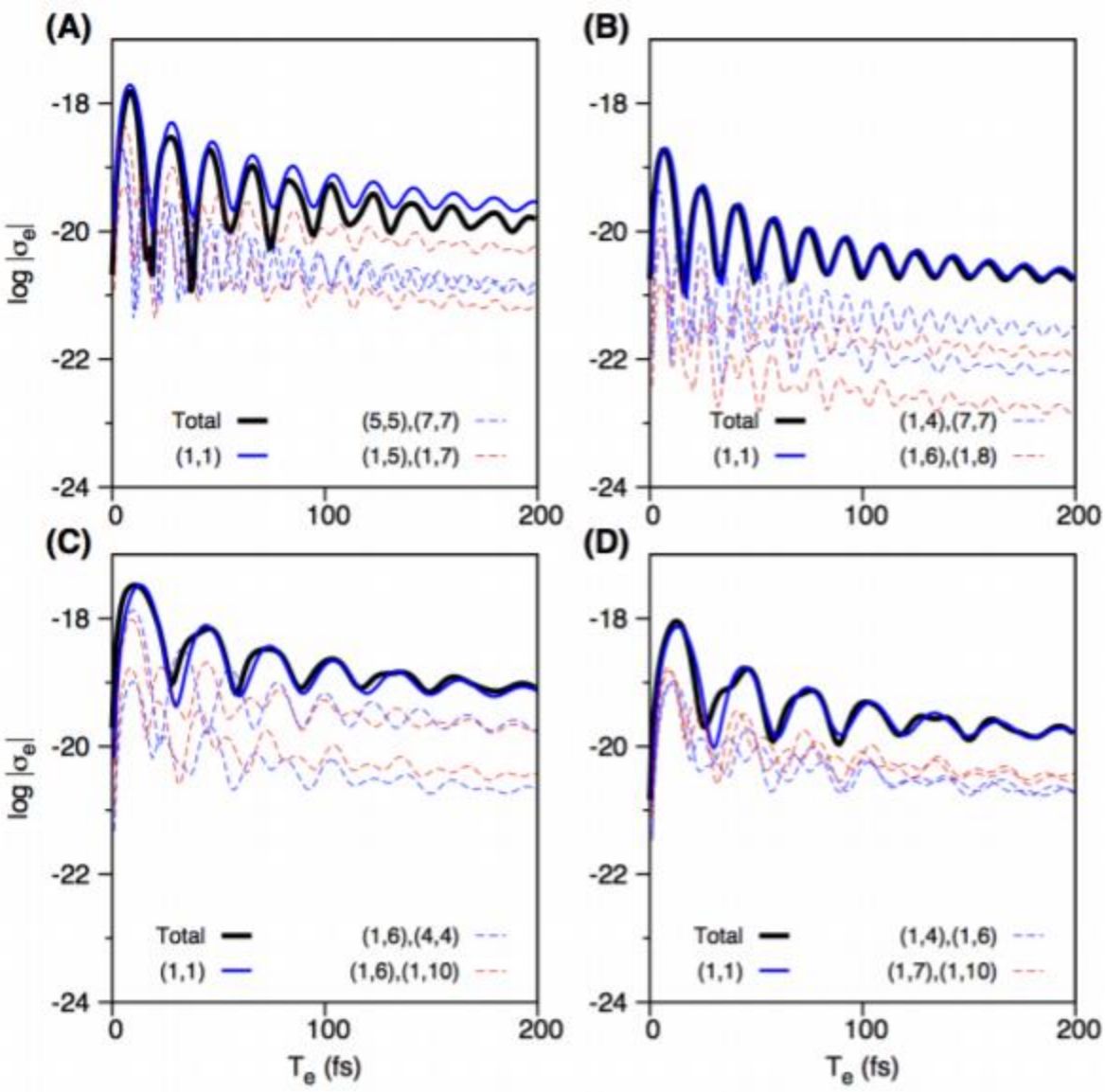

Figure 4.12. ETPA cross section plots at ωp = 3.1 eV and κ_j = 0.1 eV for (A) planar 6T (f = ES2), (B) twisted 6T (f = ES2) and (C) 18T (f = ES2), and (D) 18T (f = ES3). Bold black curve: total σ_e, bold blue curve: major σ_e^{jk}, blue dashed curve: minor positive σ_e^{jk}, and red dashed curve: absolute value of minor negative σ_e^{jk}. The unit of σ_e is cm^2 and the y-value is plotted in a log scale of σ_e.

References

1. Scully, M.; Zubairy, M. S. *Quantum optics*; Cambridge University Press, Cambridge, UK, 1997.
2. Avanaki, K. N.; Schatz, G. C. Entangled photon resonance energy transfer in arbitrary media. *J. Phys. Chem. Lett.* **2019**, *10*, 3181–3188.

CHAPTER 5

Modern Anesthetic Ethers Demonstrate Quantum Interactions with Entangled Photons

The work in this chapter was published as the journal article:

Burdick, R. K.; Villabona-Monsalve, J. P.; Mashour, G. A.; Goodson, T., Modern Anesthetic Ethers Demonstrate Quantum Interactions with Entangled Photons. *Scientific Reports* **2019,** *9* (1), 11351.

Modifications have been made for the style and content of this dissertation. References and supporting information for the manuscript are included in this chapter.

In this chapter, I performed the experimental measurements of the UV-vis spectra, linear fluorescence spectra, entangled photon transmission measurements, and classical TPA measurements of the ethers and standards. I also performed the electronic structure calculations that estimated the energies of the ethers' excited states. I provided the analysis and discussion of the implications of the halogenated anesthetic ethers being sensitive to the entangled but not the classical photons, and diethyl ether not being sensitive to either type of photons.

5.1 Abstract

Despite decades of research, the mechanism of anesthetic-induced unconsciousness remains incompletely understood, with some advocating for a quantum mechanical basis. Despite associations between general anesthesia and changes in physical properties such as electron spin, there has been no empirical demonstration that general anesthetics are capable of functional quantum interactions. In this work, we studied the linear and non-linear optical properties of the halogenated ethers sevoflurane (SEVO) and isoflurane (ISO), using UV-Vis spectroscopy, time dependent-density functional theory (TD-DFT) calculations, classical two-photon spectroscopy, and entangled two-photon spectroscopy. We show that both of these halogenated ethers interact with pairs of 800 nm entangled photons while neither interact with 800 nm classical photons. By contrast, nonhalogenated diethyl ether does not interact with entangled photons. This is the first

experimental evidence that halogenated anesthetics can directly undergo quantum interaction mechanisms, offering a new approach to understanding their physicochemical properties.

5.2 Introduction

Inhalational anesthetics were first used more than 170 years ago, when simple aliphatic ethers, such as diethyl ether, were commonly used to induce unconsciousness. Most inhalational anesthetics in clinical use today are halogenated ethers, such as sevoflurane (SEVO) and isoflurane (ISO), which can be considered derivatives of the anesthetic diethyl ether. To date, a description of the mechanism of anesthetic-induced unconsciousness has been approached from the perspective of classical chemistry interactions between anesthetics and neuronal compounds on the macroscopic level.[1] This approach has shown how anesthetics can target particular proteins and protein-based compounds to manipulate the conformation of these compounds found in neurochemical synapses, leading to changes in the chemical potential of the surrounding environment. However, other studies have suggested that anesthetics may undergo a quantum interaction mechanism to induce unconsciousness,[2-5] but—unlike the foundational empirical studies identifying binding between anesthetics and protein targets—it is unclear if general anesthetics can interact directly with quantum systems, including those involving long-distance entanglement. In order for a quantum interaction mechanism to be possible, two initial conditions would have to be met: 1) the anesthetic molecules must have the ability to target particles much smaller than the macroscopic compounds previously studied, as only atomic and subatomic particles will strongly adhere to the unique behaviors of quantum mechanics; and 2) the interactions cannot be explained using classical mechanics. Two previous studies have shown how quantum properties may play a role in anesthetic-induced unconsciousness. Turin et al.[6] reported electron spin changes in fruit flies that occurred after they were given anesthetics and Li et al.[7] reported that xenon isotopes without nuclear spin were more potent anesthetics than isotopes with nuclear spin. Although both of these studies indirectly suggest that quantum mechanics might relate to the mechanism of general anesthesia, neither study investigated whether anesthetics could directly interact with a quantum system.

Previous physical, pharmacological, and neuroscientific studies have not been able to describe completely the mechanism of anesthetic action for SEVO and ISO. Despite studies of SEVO's and ISO's NIR/IR optical properties[8-17] as well as ground state chemical structures and

properties,[10,18-29] very little is known about their linear and nonlinear optical properties in the visible and UV light range and their excited state electronic properties. Although the optical properties of anesthetics have not been studied in an attempt to understand their ability to change neuronal functioning and induce unconsciousness, spectroscopy experiments have been completed on neurons to produce action potentials using only light. Hirase et al.[30] used high intensity pulsed IR light to trigger action potentials in pyramidal neurons. Although this experiment with high energy laser light damaged the cells, Wells *et al*.[31] performed a similar experiment using IR light with much lower incident laser power and triggered action potentials in neurons *in vivo*, attributed to a photothermal effect[32], without damaging the cells. The low light intensity required to trigger the action potentials shows the high sensitivity of neurons to light. In addition to these experimental light sources, biophotons, i.e. light emitted by cells during specific metabolic processes,[33] have been identified in neural tissue and hypothesized as auxiliary carriers in neuronal information transfer.[34-38] Thus, the study of photons is justified in the context of neural function and anesthetic-induced disruption of information processing

In this study we investigated the direct interaction between anesthetics and a quantum system using entangled two-photon spectroscopy. This spectroscopy technique utilizes pairs of photons whose quantum states are strongly correlated such that they must be treated as one body (i.e., they are entangled). The interaction mechanisms of a molecule with entangled photons vs classical photons are different, as shown in previous work by Lee et al[39]. Therefore, both interaction processes must be investigated for a complete understanding of the optical properties of the molecule. Using 800 nm photons in a classical two-photon spectroscopy experiment, neither SEVO nor ISO interacted with the classical photons despite using very high light intensity (i.e. large number of photons) in our experiment. However, SEVO and ISO did interact with the 800 nm entangled photons at extremely low light intensity. By contrast, diethyl ether (a nonhalogenated ether used for reference) did not, showing a unique and unexpected sensitivity to a quantum correlated system in association with halogenation.

5.3 Methods

5.3.1 Computational methods

Ground state and first excited state electronic structure calculations were completed using GAMESS.[40] Optimization of ground state geometries and calculation of molecular

orbitals were completed with DFT using the B3LYP functional and 6-311+G(2d,p) basis set. A previous study confirmed the accuracy of this functional and basis set for SEVO and another halogenated ether, halothane.[27] We compared our optimized geometries, ground state dipole moments, and molecular orbitals with previous studies to confirm the accuracy of our calculations.[18,20-22,27,41] Images of molecular orbitals in the supporting information were created using wxMacMolPlt.[42] Electronic properties of the first excited state, including the excitation energy, transition dipole moment, oscillator strength, and TPA cross-section, were completed with TD-DFT using the same functional and basis set.

5.3.2 Materials

Sevoflurane ($C_4H_3F_7O$) and isoflurane ($C_3H_2ClF_5O$) were obtained commercially and used without further purification methods. No impurities were found in their respective mass spectra (See supporting information). HPLC grade methanol (≥ 99.9 %) and diethyl ether (≥ 99.9 %) were obtained from Sigma-Aldrich and used as received.

5.3.3 Steady-state spectroscopy

UV-Vis absorption spectra (190 – 900 nm) were measured on an Agilent 8432 UV−visible spectrometer. Fluorescence spectra were collected on a Varian Cary Eclipse fluorimeter. 1.0 cm pathlength quartz cuvettes were used for all measurements.

5.3.4 Classical two-photon excited fluorescence (TPEF)

The two-photon excited fluorescence technique[43,44] was used for the classical two-photon experiments. Our experimental setup has been described elsewhere.[45,46] In brief, the pure liquid (or a liquid solution of the compound of interest) contained in a 1 cm path length quartz cuvette is excited with the output beam of a Ti:Sapphire femtosecond pulsed laser (KMLabs, 800 nm, Δt ~30 fs) with a 80 MHz repetition rate. The fluorescence emission was collected at 90° angle to the excitation beam. Fluorescence emission at a selected wavelength was detected using a monochromator (ORIEL, Cornerstone 130) and a photomultiplier tube (Hamamatsu). The power of the 800 nm excitation beam was changed by using a variable neutral density filter.

5.3.5 Entangled two-photon spectroscopy

The entangled two-photon spectroscopy technique has been previously described.[39,47,48,45] A sketch of the experimental setup used in this work is presented in Figure 5.1. Orthogonally polarized entangled photon pairs were generated by the spontaneous parametric down-conversion (SPDC) process. A 0.5 mm BBO (β-Barium Borate) crystal (type II) is pumped with the second harmonic generation (SHG) beam, 400 nm, of a Ti:Sapphire pulsed laser emitting ~70 fs pulses (MaiTai, Spectra Physics). Entangled photon intensity is varied by changing the pump power on the SPDC crystal with a variable neutral density filter. Transmitted entangled photons are focused onto an avalanche photodiode (SPCM-AQR13, Perkin Helmer). Fig. 5.1 shows the complete set-up, previously shown by Harpham et al.[48]

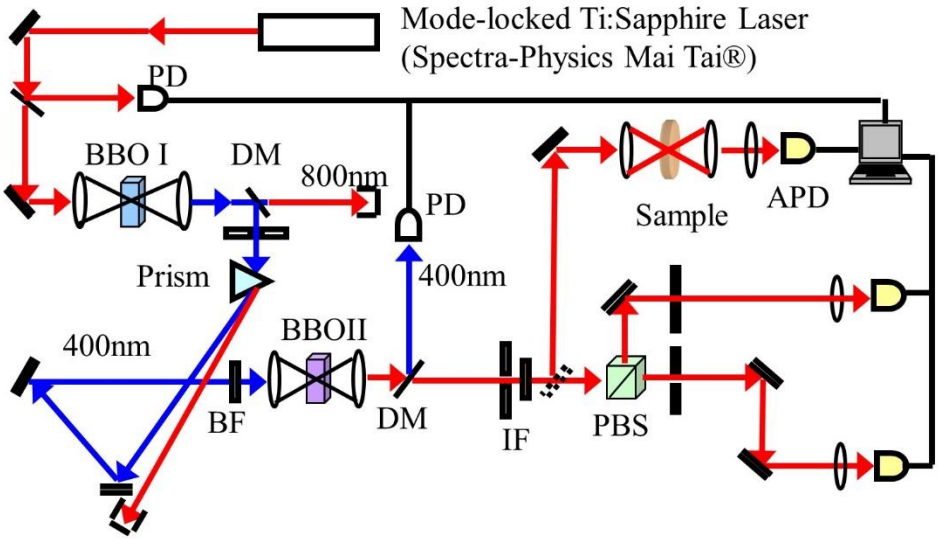

Figure 5.1. Experimental setup used for entangled two-photon spectroscopy.

5.4 Results

5.4.1 Linear optical properties

Previous studies of steady-state UV absorption of SEVO and ISO were completed in the gas phase.[49,50] It was stated that SEVO did not have any absorption above 200 nm, and no absorption spectrum was shown.[49] ISO had an UV absorption onset at 215 nm and continued to increase down to 200 nm,[49] with another report showing the UV absorption continuing to increase down to 120 nm.[50] To the best of our knowledge, the UV absorption spectra for SEVO and ISO in Fig. 5.2 are the first reported absorption spectra for ISO in the liquid phase and for

SEVO in any phase. The absorption spectrum for diethyl ether, an aliphatic ether with a similar structure as SEVO and ISO, is shown for comparison. Fig. 5.2 also shows the emission spectra of SEVO and ISO when excited at their respective λ_{max} (while 190 nm may not be the true λ_{max} of liquid SEVO, it was the lowest wavelength available from our spectrophotometer and thus treated as λ_{max} for emission experiments). The emission spectrum for diethyl ether, excited at 210 nm, is also shown for comparison.

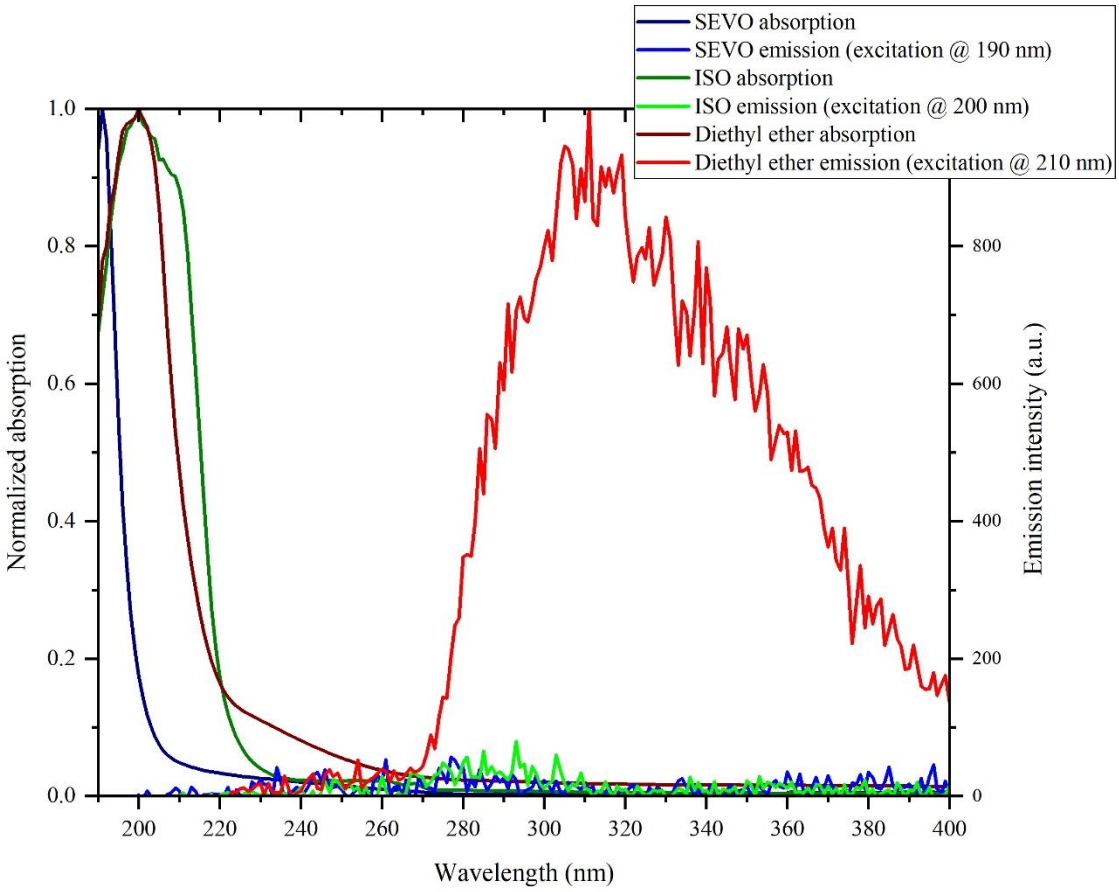

Figure 5.2. UV absorption and emission spectra of sevoflurane, isoflurane and diethyl ether in liquid phase.

The absorption spectrum for ISO peaks at 200 nm, the same as diethyl ether, while the absorption spectrum of SEVO is blue-shifted and continues to increase down to 190 nm without peaking. No absorption was shown for either compound above 270 nm. Previous studies have shown that fluorinated ethers have an UV absorption that is blue-shifted relative to aliphatic ethers[51,52], as we see when comparing SEVO to diethyl ether in Fig. 5.2. However, the fluorinated ether ISO, which also contains a chlorine atom, is not blue-shifted from diethyl ether at all. Although diethyl ether shows broad emission from ~270 nm to beyond 400 nm,

peaking around 310 nm (which corresponds well with a previous study that reported an emission peak around 306 nm[53]), neither SEVO nor ISO show any emission above background noise.

5.4.2 Ground and first excited state electronic properties

Ground and first excited state electronic structure calculations were completed for SEVO and ISO to explain the linear optical properties in Fig. 5.2. In order to understand the effect that the halogens in SEVO and ISO have on the molecular orbitals and energy levels, calculations were also completed for aliphatic ethers that have the same structure as the halogenated ethers but with all halogens replaced with hydrogens. The aliphatic parent ether of SEVO is methyl isopropyl ether and that of ISO is ethyl methyl ether. The results of the TD-DFT calculations for the ground-state-to-excited-state transitions in all four molecules are summarized in Table 5.1. Results for diethyl ether are also shown to compare with the experimental linear optical properties obtained in Fig. 5.2.

Table 5.1. TD-DFT/B3LYP/6-311+G(2d,p) calculations for SEVO, ISO, their aliphatic parent ethers (methyl isopropyl ether and ethyl methyl ether, respectively), and diethyl ether.

Compound	$S_0 \rightarrow S_1$ excitation energy (eV / nm)	HOMO-LUMO gap (eV)	$S_0 \rightarrow S_1$ transition dipole moment (D)	$S_0 \rightarrow S_1$ oscillator strength	Permanent dipole moment (D)
methyl isopropyl ether	6.307 / 196.6	7.185	0.6318	0.0096	1.2974
SEVO	8.339 / 148.7	9.290	0.6905	0.0151	2.2638
ethyl methyl ether	6.368 / 194.7	7.313	0.9523	0.0219	1.2461
ISO	6.923 / 179.1	8.324	0.2374	0.0015	1.8675
diethyl ether	6.343 / 195.5	7.268	0.8621	0.0179	1.1498

Similar to the observed blue-shift for SEVO (compared to diethyl ether) in the UV absorption spectra in Fig. 5.2, the TD-DFT results in Table 5.1 also show a blue-shift for SEVO in the first excitation energy, corresponding to the ground state (S_0) to first excited state (S_1) transition, compared to its aliphatic parent ether, methyl isopropyl ether. A similar blue-shift is observed in ISO compared to its aliphatic parent ether, ethyl methyl ether, though the shift (+0.555 eV) is not as large as compared to SEVO's blue-shift (+2.032 eV). This correlates well with our UV absorption spectra in Fig. 5.2, where SEVO has a large blue-shift compared to

the aliphatic ether while ISO has little to no blue-shift. This difference between SEVO and ISO is most likely due to the different characteristics of their HOMOs, shown in Fig. 5.3. The HOMO for SEVO is located predominantly on the oxygen lone pairs, while that of ISO is located predominantly on the chlorine lone pairs.

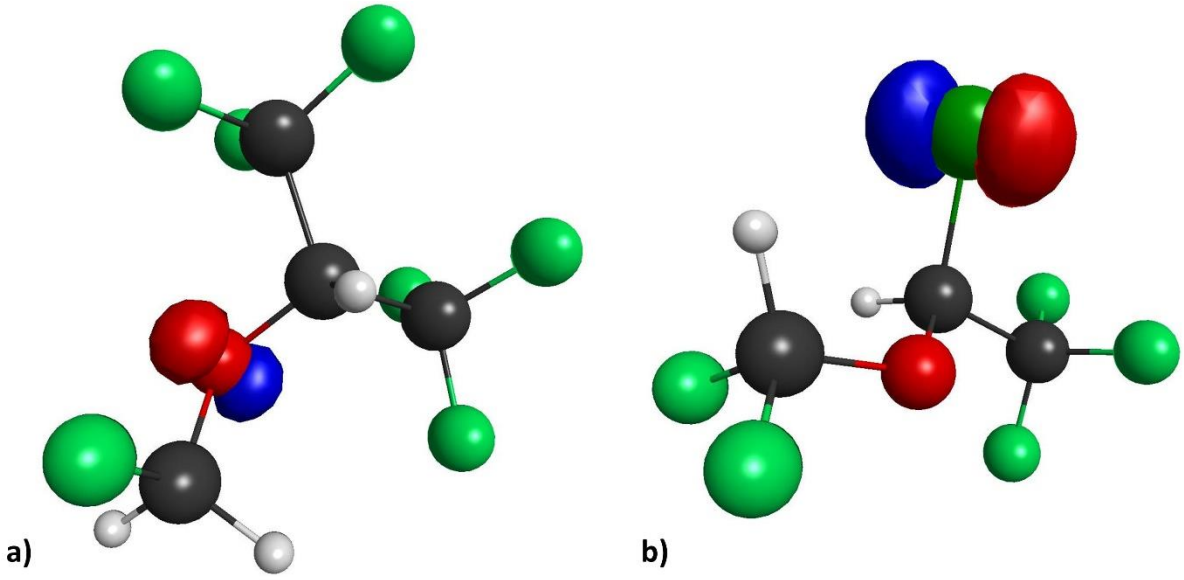

Figure 5.3. HOMO for **a)** SEVO, and **b)** ISO. Isosurface values were chosen such that only the most predominant location of each orbital is shown in order to identify the character of the HOMO.

The excitation wavelength for SEVO in Table 5.1 (148.7 nm) shows why λ_{max} is not seen in the UV absorption spectrum in Fig. 5.2, since the calculated energy to the first excited state in SEVO requires a wavelength beyond the limits of our spectrophotometer. The wavelength of the first excitation energy in Table 5.1 for diethyl ether (195.5 nm) corresponds very well with the peak in the absorption spectrum for diethyl ether in Fig. 5.2 (200 nm), thus confirming the accuracy of our electronic structure calculations. The calculated permanent dipole moments are also very close to literature values for diethyl ether,[41] SEVO,[18,20,21,27] and ISO.[22] Additional electronic structure calculation results for molecular orbitals are provided in supporting information.

5.4.3 Nonlinear optical properties

Since the absorption spectra in Fig. 5.2 and the theoretical calculations in Table 5.1 show that the first excited electronic state for both SEVO and ISO is below 200 nm, neither

compound was expected to have a two-photon interaction with 800 nm photons through nonlinear optical processes. The classical two-photon interaction properties of pure SEVO and pure ISO were tested by measuring the two-photon excited fluorescence (TPEF) using 800 nm incident light. The results are shown in the inset of Fig. 5.4, using Coumarin 153 as a standard.

The entangled two-photon interaction properties of pure SEVO and pure ISO were studied next, also using 800 nm incident light. The results are shown in Fig. 5.4, using ZnTPP as a standard. In our entangled two-photon experiments, the transmission of the entangled photons through a blank (solvent) is compared with the transmission through the sample (SEVO and ISO). Any difference between the transmission intensities is due to an interaction between the sample and entangled photons.

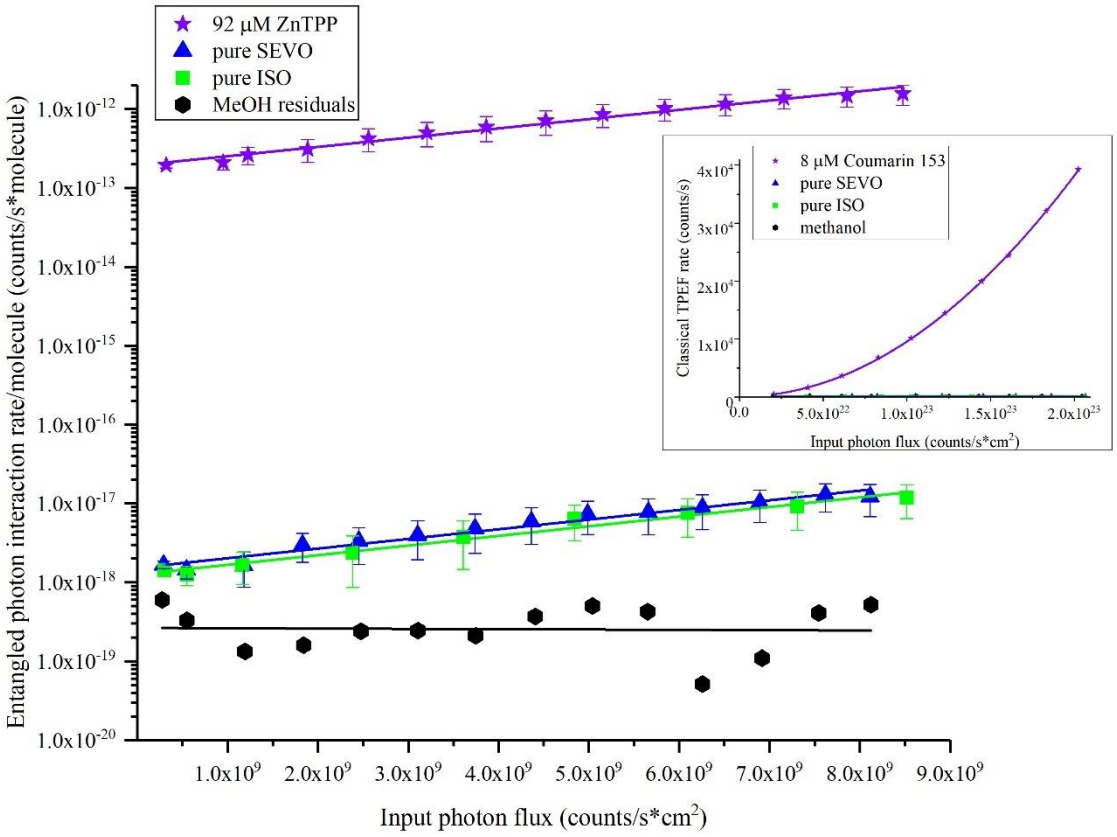

Figure 5.4. Entangled photon interaction rate per molecule vs input photon rate for sevoflurane and isoflurane, with ZnTPP used as a standard. Classical two-photon results for sevoflurane and Coumarin 153 as a standard are shown in the inset. Error bars were calculated first for the sample and solvent transmission scans separately using the percent standard deviation of 50 single photon count measurements for toluene (a non-interacting solvent) at 4 different incident laser powers. This error was then propagated to calculate the interaction signal error bars.

As expected for the classical two-photon experiment, seen in the inset of Fig. 5.4, neither SEVO nor ISO interacted with the 800 nm light. Coumarin 153, used as a standard, showed the expected quadratic dependence of TPEF on the input photon flux, validating our experimental method. Surprisingly, the entangled two-photon experiment did show interaction with the 800 nm entangled photons for the SEVO and ISO solutions, seen in Fig. 5.4. The log scale of the y-axis in Fig. 5.4 (entangled photon interaction rate per molecule) shows that SEVO and ISO yielded entangled two-photon interaction signals that are 5 and 6 orders of magnitude smaller than that of the standard, ZnTPP, respectively. The difference in signal intensity between the anesthetics and ZnTPP is expected since the molecules undergo different interaction mechanisms, shown in Fig. 5.5.

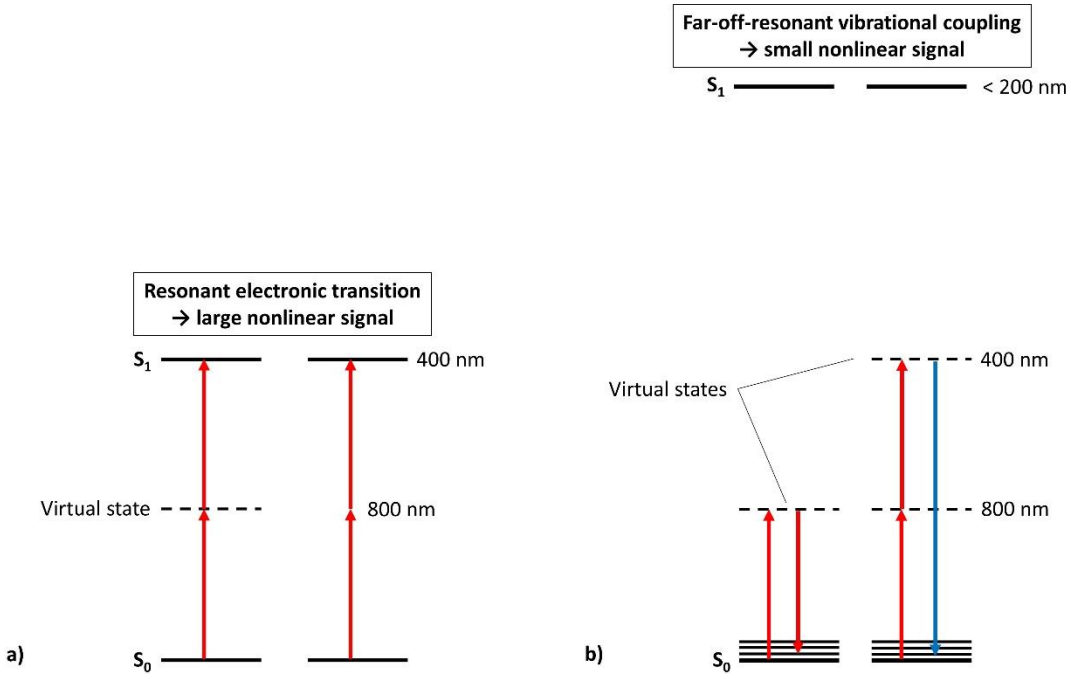

Figure 5.5. Comparison of interaction mechanisms using entangled photons: **a)** absorption transitions resonant with excited electronic states, seen in ZnTPP; **b)** far-off-resonant interactions yielding no electronic excitation, seen in SEVO and ISO.

For chromophores that can absorb light at 400 nm, like ZnTPP, the two 800 nm photons are resonant with a real, excited electronic state in the molecule, seen in Fig. 5.5a. When the incoming entangled photons are resonant with a real eigenstate, the molecule can interact with the photons through two pathways (as explained in previous work[47,48]): 1) the virtual state pathway, where the light can create a coupling with an intermediate virtual state, and the

molecule will absorb the two photons in a two-step transition through that virtual state; 2) the permanent dipole pathway, where the light can create a coupling between the permanent dipoles of the ground and excited electronic state, and the molecule will absorb the two photons simultaneously. The probability of the virtual state pathway is inversely proportional to the detuning energy of the virtual state, i.e. the difference in energy between the virtual state and the real eigenstates in the molecule. Since this detuning energy is usually quite large (~12,500 cm^{-1}), the virtual state pathway has a low probability; but the higher probability of the permanent dipole pathway leads to a large optical signal, as seen in many chromophores studied previously[39,45,47,49,50], including ZnTPP.

For SEVO and ISO, the 800 nm entangled photons are far-off-resonance with the first excited electronic state, shown in Fig. 5.5b. Because the energy difference between the photons' combined energy and the first electronic excited state is ~25,000 cm^{-1}, a two-photon absorption mechanism, like that seen in ZnTPP, is impossible. Fig. 5.5b shows two other possible ways that SEVO and ISO may interact with the entangled photons. The first photon must create a coupling with a virtual state. The second photon can then induce a stimulated one-photon scattering back to the ground state, or it can create a coupling with a second virtual state and induce a two-photon scattering. As explained above, these virtual state couplings are very weak because the detuning energy with real eigenstates is very small, particularly in SEVO and ISO which will have detuning energies twice as large as that for ZnTPP. These large detuning energies make either of the mechanisms in Fig. 5.5b have a very low probability, so any optical signal seen through these mechanisms will be extremely small. As expected, the entangled two-photon interaction signal for SEVO and ISO are 5 and 6 orders of magnitude smaller than the signal from ZnTPP, respectively.

In order for SEVO and ISO to have a nonlinear interaction with the entangled photons as described in Fig. 5.5b, the ethers must have vibrational modes that are active to these nonlinear interactions. To confirm this, we analyzed the neat liquids with Raman spectroscopy, particularly in the low frequency shift "fingerprint" region, with spectra shown in Fig. 5.6.

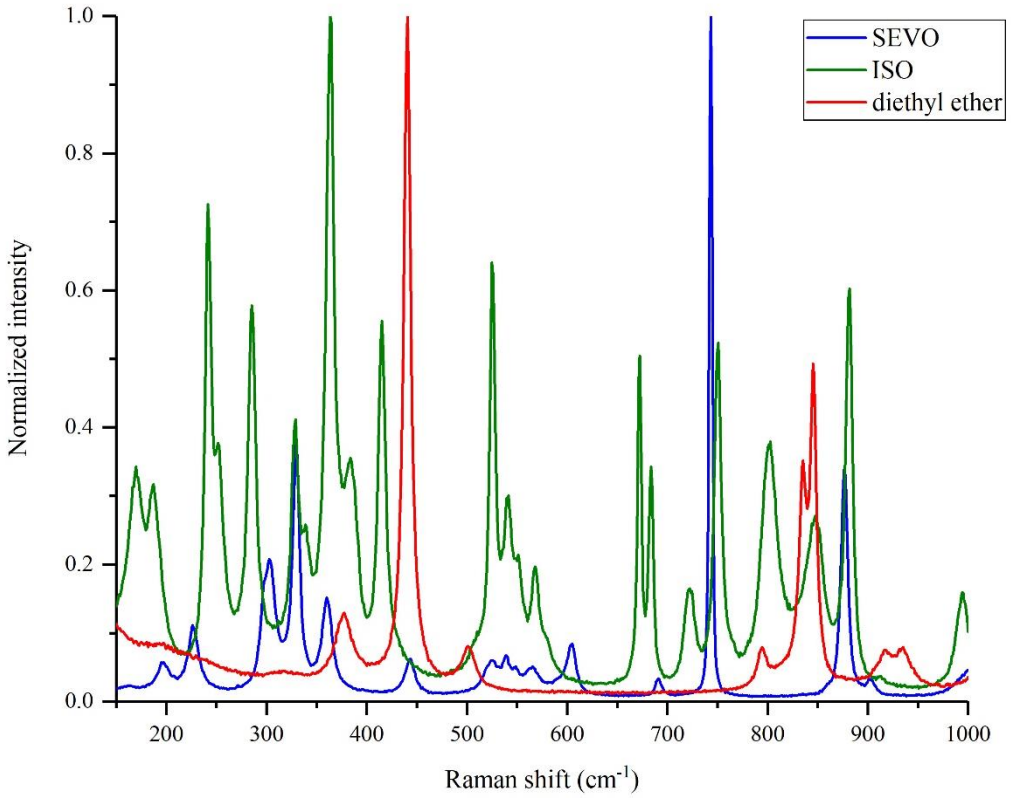

Figure 5.6. Raman spectra of SEVO, ISO, and diethyl ether with excitation of 785 nm.

Both SEVO and ISO have many Raman-active modes in the low frequency shift region, unlike diethyl ether shown for comparison. Another experimental study[15] has previously shown SEVO and ISO to have active modes in coherent anti-Stokes Raman scattering (CARS), another nonlinear interaction mechanism. While our Raman study and the CARS study[15] used classical photons, it has already been shown theoretically that entangled photons can be used to induce Raman and other nonlinear interactions.[56,57] Additionally, it has already been shown experimentally by Upton et al.[47] that the use of entangled photons for nonlinear interactions can offer an enhancement in the signal compared to using classical photons. Our experimental results show a similar result: since the entangled photon experiment shows an interaction signal while the classical photon experiment does not show a signal, SEVO and ISO gain an enhancement in their interaction with the use of entangled photons, suggesting that the two anesthetics have a preference for interacting with the quantum system of photons as opposed to the classical system of photons.

Because the experiment is extremely sensitive and can measure very small signals, it is important to ensure that the signal we measure is from SEVO and ISO, not any impurity that may be in the sample. Both neat SEVO and neat ISO were analyzed using mass spectrometry. The mass spectra, shown in the supporting information, were compared with literature spectra[58,59] and show no signs of impurities. (Note, an additional peak at 39.9 m/z in Fig. 5.13 for ISO is attributed to Ar gas leaking into the instrument during analysis.) We can rule out any possibility of an impurity interacting with the entangled photons.

Given how sensitive the entangled two-photon experiment is to the small signals from SEVO and ISO, it must also be emphasized that this interaction signal seen in SEVO and ISO is not common and cannot be found in just any organic compound. Other organic solvents, such as methanol and toluene, show no signal in this experimental set-up. We also compared the halogenated ethers with another ether that is nonhalogenated, diethyl ether, which showed no signal. The ability to interact with entangled photons through a far-off-resonance transition is a property that is unique to SEVO and ISO and not found in any other organic compounds studied to date.

5.5 DISCUSSION

Although previous studies on the mechanism of action of anesthetics have focused on anesthetics' ability to interact with macromolecules such as lipid bilayers and proteins, our results show that individual anesthetic molecules can interact with photons. Even more significant is that the halogenated ethers studied here selectively interacted with a quantum system, entangled photons, as opposed to the classical system of photons. This distinction is important because the interaction mechanisms with classical vs entangled photons are different. In both two-photon interactions, the molecule interacting with the photons can take different pathways to go from its initial state to its final state. In classical two-photon interactions, the pathways cannot be controlled, due to the Fourier uncertainty relationship between frequency and time.[60] However, in entangled two-photon interactions, specific pathways can be selected because the entangled photons are not limited by the Fourier uncertainty principle.[60] In other words, during the interaction event with two entangled photons, the molecule and the photons become correlated such that the specific interaction pathway in the molecule is strongly correlated with the quantum state of the photons.[60] In order for a molecule to interact with entangled photons, it must be able to interact

with the strongly correlated photons such that it enters into a correlation with them and thus affects the state of the photons; in this case, the molecule affects the photons by interacting with them instead of allowing them to transmit through the medium. Fig. 5.4 clearly shows that the anesthetics have the ability to interact with the strongly correlated 800 nm entangled photons in our experiment. This is the first empirical evidence that certain anesthetic molecules can directly interact with particles through a quantum mechanism. In addition, diethyl ether, a structurally similar ether, does not interact with the 800 nm entangled photons (transmission plots provided in the supporting information). Thus, SEVO and ISO have a unique property that diethyl ether does not have. Although not explored in this work, this property may be related to the specific actions of SEVO and ISO vs diethyl ether. We have only investigated the interaction the ethers have with one wavelength of entangled photons, 800 nm. It is not known whether the ethers studied here can or cannot interact with entangled photons of other wavelengths, and this would be an interesting direction for further study.

This result does not prove any mechanism of anesthetic-induced unconsciousness but it serves as a first proof-of-principle demonstration that anesthetic molecules meet the initial conditions we have outlined to be necessary for a quantum interaction mechanism that may induce unconsciousness. This result motivates further studies on the possible quantum interactions that anesthetic molecules may have in the brain and the atomic or subatomic particles they may be targeting, such as their interaction with the dynamic electronic states of proteins known to be targeted by general anesthetics.[61]

Methodologic strengths of this study include a well-defined experimental model that can differentiate quantum vs. non-quantum interactions as well as the use of both halogenated and non-halogenated ethers. Methodologic limitations include the purely *in vitro* experiments, the high concentration of the anesthetics used, the fact that the anesthetic was in liquid rather than gaseous phase, and the lack of spectral resolution. These limitations make it impossible to determine if there is any neurobiological or clinical relevance associated with the resultant data. Furthermore, the data do not suggest that general anesthesia has an exclusively quantum basis because diethyl ether is an effective anesthetic but demonstrated no quantum interactions. However, we have not conducted a systematic study of all possible quantum interactions with photons, including interaction with other entangled photon wavelengths, or other physical substrates such as microtubules, which have been posited to mediate quantum effects of general anesthetics.[2,5]

Further studies should explore other quantum systems as well as more neurobiologically relevant models.

In conclusion, this is (to our knowledge) the first experimental study to rigorously assess the ability of a general anesthetic to interact with subatomic particles with quantum vs. classical features. The finding that halogenation confers the ability of an ether to engage in quantum mechanical processes advances our understanding of these critically important drugs and motivates further investigation regarding non-classical mechanisms of action.

References

1. Covarrubias, M., Barber, Annika F., Carnevale, V., Treptow, W. & Eckenhoff, Roderic G. Mechanistic insights into the modulation of voltage-gated ion channels by inhalational anesthetics. *Biophys. J.* **2015**, *109*, 2003-2011.
2. Craddock, T. J. A. *et al.* Anesthetic alterations of collective terahertz oscillations in tubulin correlate with clinical potency: Implications for anesthetic action and post-operative cognitive dysfunction. *Sci. Rep.* **2017**, *7*, 9877.
3. Hameroff, S. R. The entwined mysteries of anesthesia and consciousnessis there a common underlying mechanism? *Anesthesiology* **2006**, *105*, 400-412.
4. Hameroff, S. R. Anesthetic action and "quantum consciousness"a match made in olive oil. *Anesthesiology* **2018**, *129*, 228-231.
5. Craddock, T. J. A., Stuart, R. H., Ahmed, T. A., Mariusz, K. & Jack, A. T. Anesthetics act in quantum channels in brain microtubules to prevent consciousness. *Curr. Top. Med. Chem.* **2015**, *15*, 523-533.
6. Turin, L., Skoulakis, E. M. C. & Horsfield, A. P. Electron spin changes during general anesthesia in Drosophila. *Proc. Natl. Acad. Sci.* **2014**, *111*, E3524.
7. Li, N. *et al.* Nuclear spin attenuates the anesthetic potency of xenon isotopes in miceimplications for the mechanisms of anesthesia and consciousness. *Anesthesiology* **2018**, *129*, 271-277
8. Allison, J. M., Birch, K. P. & Crowder, J. G. Precise determination of refractometric parameters for anesthetic agent vapors. *Appl. Opt.* **1994**, *33*, 2459-2464.
9. Cieślik-Boczula, K. & Rospenk, M. Interaction of anesthetic molecules with α-helix and polyproline ii extended helix of long-chain poly-l-lysine. *Spectrochim. Acta A* **2018**, *189*, 436-442
10. Dom, J. J. J. *et al.* On the weakly c–h···π hydrogen bonded complexes of sevoflurane and benzene. *PCCP* **2011**, *13*, 14142-14152.
11. Kuć, M., Cieślik-Boczula, K. & Rospenk, M. Influence of inhalation anesthetics on the chain-melting phase transition of dppc liposomes. Near-infrared spectroscopy studies supported by pca analysis. *Vib. Spectrosc* **2016**, *85*, 55-61.
12. Kuć, M., Cieślik-Boczula, K. & Rospenk, M. Anesthetic-dependent changes in the chain-melting phase transition of dppg liposomes studied using near-infrared spectroscopy supported by pca. *Spectrochim. Acta A* **2017**, *186*, 37-43.
13. Kuć, M., Cieślik-Boczula, K. & Rospenk, M. Nir studies of cholesterol-dependent structural modification of the model lipid bilayer doped with inhalation anesthetics. *J. Mol. Struct.* **2018**, *1162*, 17-25.
14. Ren, H., Li, X., Qu, Y. & Li, F. Theoretical investigation on h abstraction reaction mechanisms and rate constants of sevoflurane with the oh radical. *Chem. Phys. Lett.* **2018**, *692*, 345-352.
15. Nagashima, Y., Suzuki, T., Terada, S., Tsuji, S. & Misawa, K. In vivo molecular labeling of halogenated volatile anesthetics via intrinsic molecular vibrations using nonlinear raman spectroscopy. *J. Chem. Phys.* **2011**, *134*, 024525.

16. Sulbaek Andersen, M. P., Nielsen, O. J., Karpichev, B., Wallington, T. J. & Sander, S. P. Atmospheric chemistry of isoflurane, desflurane, and sevoflurane: Kinetics and mechanisms of reactions with chlorine atoms and oh radicals and global warming potentials. *J. Phys. Chem. A* **2012**, *116*, 5806-5820.
17. Wu, R.-J. *et al.* New sensing technology for detection of the common inhalational anesthetic agent sevoflurane using conducting polypyrrole films. *Sensors Actuators B: Chem.* **2007**, *126*, 387-393.
18. Arcario, M. J., Mayne, C. G. & Tajkhorshid, E. Atomistic models of general anesthetics for use in in silico biological studies. *J. Phys. Chem. B* **2014**, *118*, 12075-12086.
19. Floate, S. & Hahn, C. E. W. Electrochemical reduction of the anaesthetic agent sevoflurane (fluoromethyl 2,2,2-trifluoro-1-[trifluoromethyl] ethyl ether) in the presence of oxygen and nitrous oxide. *Sensors Actuators B: Chem.* **2004**, *99*, 236-252.
20. Freitas, M. P., Bühl, M., O'Hagan, D., Cormanich, R. A. & Tormena, C. F. Stereoelectronic interactions and the one-bond c–f coupling constant in sevoflurane. *J. Phys. Chem. A* **2012**, *116*, 1677-1682.
21. Lesarri, A., Vega-Toribio, A., Suenram, R. D., Brugh, D. J. & Grabow, J.-U. The conformational landscape of the volatile anesthetic sevoflurane. *PCCP* **2010**, *12*, 9624-9631.
22. Lesarri, A. *et al.* Structural evidence of anomeric effects in the anesthetic isoflurane. *PCCP* **2011**, *13*, 6610-6618.
23. Mehdipour, A. R., Hemmateenejad, B. & Miri, R. Qsar studies on the anesthetic action of some polyhalogenated ethers. *Chem. Biol. Drug Des.* **2007**, *69*, 362-368.
24. Ren, H., Yang, X., Li, X., Liu, Y. & Wei, X. The hydrogen abstraction reaction mechanism and rate constants from 200k to 2000k between sevoflurane and chlorine atom: A theoretical investigation. *Chem. Phys. Lett.* **2014**, *605-606*, 28-34.
25. Sang, P., Zou, J.-W., Yu, Y.-L. & Huang, M.-L. Predicting minimum alveolar concentration (mac) of anesthetic agents by statistical modeling methods and theoretical descriptors derived from electrostatic potentials on molecular surface. *Chemometrics Intellig. Lab. Syst.* **2012**, *112*, 8-16.
26. Sear, J. W. What makes a molecule an anaesthetic? Studies on the mechanisms of anaesthesia using a physicochemical approach. *Br. J. Anaesth.* **2009**, *103*, 50-60.
27. Tang, P., Zubryzcki, I. & Xu, Y. Ab initio calculation of structures and properties of halogenated general anesthetics: Halothane and sevoflurane. *J. Comput. Chem.* **2001**, *22*, 436-444.
28. Trogdon, G., Murray, J. S., Concha, M. C. & Politzer, P. Molecular surface electrostatic potentials and anesthetic activity. *J. Mol. Model.* **2007**, *13*, 313-318.
29. Wang, T., Smith, D. & Španěl, P. Selected ion flow tube studies of the reactions of h3o+, no+ and o2+ with the anaesthetic gases halothane, isoflurane and sevoflurane. *Rapid Commun. Mass Spectrom.* **2002**, *16*, 1860-1870.
30. Hirase, H., Nikolenko, V., Goldberg, J. H. & Yuste, R. Multiphoton stimulation of neurons. *J. Neurobiol.* **2002**, *51*, 237-247.
31. Wells, J. *et al.* Optical stimulation of neural tissue in vivo. *Opt. Lett.* **2005**, *30*, 504-506.
32. Wells, J. *et al.* Biophysical mechanisms of transient optical stimulation of peripheral nerve. *Biophys. J.* **2007**, *93*, 2567-2580.
33. Chang, J. J. F., J.; Popp, F. A. *Biophotons*. (Springer Netherlands, 1998).
34. Sun, Y., Wang, C. & Dai, J. Biophotons as neural communication signals demonstrated by in situ biophoton autography. *Photochem. Photobiol. Sci.* **2010**, *9*, 315-322.

35. Tang, R. & Dai, J. Spatiotemporal imaging of glutamate-induced biophotonic activities and transmission in neural circuits. *PLOS ONE* **2014**, *9*, e85643.
36. Fels, D. Cellular communication through light. *PLOS ONE* **2009**, *4*, e5086.
37. Kumar, S., Boone, K., Tuszyński, J., Barclay, P. & Simon, C. Possible existence of optical communication channels in the brain. *Sci. Rep.* **2016**, *6*, 36508.
38. Simon, C. Are there optical communication channels in the brain. *Front. Biosci.* **2018**, *23*, 1407-1421.
39. Lee, D. I., Goodson, T. Entangled photon absorption in an organic porphyrin dendrimer. *J. Phys. Chem. B* **2006**, *110*, 25582-25585.
40. Schmidt, M. W. *et al.* General atomic and molecular electronic structure system. *J. Comput. Chem.* **1993**, *14*, 1347-1363.
41. Hayashi, M. & Kuwada, K. The microwave spectrum, the rs structure and the dipole moment of the tt isomer of diethyl ether. *Bull. Chem. Soc. Jpn.* **1974**, *47*, 3006-3009.
42. Bode, B. M. & Gordon, M. S. Macmolplt: A graphical user interface for gamess. *J. Mol. Graphics Modell.* **1998**, *16*, 133-138.
43. Xu, C. & Webb, W. W. Measurement of two-photon excitation cross sections of molecular fluorophores with data from 690 to 1050 nm. *J. Opt. Soc. Am. B* **1996**, *13*, 481-491.
44. Makarov, N. S., Drobizhev, M. & Rebane, A. Two-photon absorption standards in the 550–1600 nm excitation wavelength range. *Opt. Express* **2008**, *16*, 4029-4047.
45. Guzman, A. R., Harpham, M. R., Süzer, O. z. n., Haley, M. M. & Goodson, T. G. Spatial control of entangled two-photon absorption with organic chromophores. *J. Am. Chem. Soc.* **2010**, *132*, 7840-7841.
46. Madu, I. K. *et al.* Heteroatom and side chain effects on the optical and photophysical properties: Ultrafast and nonlinear spectroscopy of new naphtho[1,2-b:5,6-b′]difuran donor polymers. *J. Phys. Chem. C* **2018**, *122*, 17049-17066.
47. Upton, L. *et al.* Optically excited entangled states in organic molecules illuminate the dark. *J. Phys. Chem. Lett.* **2013**, *4*, 2046-2052.
48. Burdick, R. K. *et al.* Predicting and controlling entangled two-photon absorption in diatomic molecules. *J. Phys. Chem. A* **2018**, *122*, 8198-8212.
49. Harpham, M. R., Süzer, O. z. n., Ma, C.-Q., Bäuerle, P. & Goodson, T. Thiophene dendrimers as entangled photon sensor materials. *J. Am. Chem. Soc.* **2009**, *131*, 973-979.
50. Villabona-Monsalve, J. P., Calderón-Losada, O., Nuñez Portela, M. & Valencia, A. Entangled two photon absorption cross section on the 808 nm region for the common dyes zinc tetraphenylporphyrin and rhodamine b. *J. Phys. Chem. A* **2017**, *121*, 7869-7875.
51. Langbein, T. *et al.* Volatile anaesthetics and the atmosphere: Atmospheric lifetimes and atmospheric effects of halothane, enflurane, isoflurane, desflurane and sevoflurane. *Br. J. Anaesth.* **1999**, *82*, 66-73.
52. Lewis, B. R., Berzins, L. & Carver, J. H. Vacuum uv absorption cross sections for enflurane and isoflurane. *Appl. Opt.* **1986** *25*, 2647-2648.
53. Good, D. A., Li, Y. & Francisco, J. S. Location of the first excited states of fluorinated ethers, e143a (ch3ocf3), e134 (chf2ochf2), and e125 (chf2ocf3). *Chem. Phys. Lett.* **1999**, *313*, 267-270.
54. Orkin, V. L., Villenave, E., Huie, R. E. & Kurylo, M. J. Atmospheric lifetimes and global warming potentials of hydrofluoroethers: Reactivity toward oh, uv spectra, and ir absorption cross sections. *J. Phys. Chem. A* **1999**, *103*, 9770-9779.

55. Song, C.-y., Li, R.-q., Ge, L.-x. & Liu, Y. Study on the fluorescence characteristic and mechanism of ether-water solution. *Spectroscopy and Spectral Analysis* **2007**, *27*, 534-538.
56. Roslyak, O., Marx, C. A. & Mukamel, S. Nonlinear spectroscopy with entangled photons: Manipulating quantum pathways of matter. *Phys. Rev. A* **2009**, *79*, 033832.
57. Lanzagorta, M. Entangled-photons raman spectroscopy. *Proc. SPIE* **2012**, *8382*, 838207.
58. Bouche, M.-P. L. A. *et al.* Quantitative determination of vapor-phase compound a in sevoflurane anesthesia using gas chromatography–mass spectrometry. *Clin. Chem.* **2001**, *47*, 281.
59. Deng, X.-s. & Simpson, V. J. Determination of volatile anesthetics isoflurane and enflurane in mouse brain tissues using gas chromatography-mass spectrometry. *J. Pharmacol. Toxicol. Methods* **49**, 131-136.
60. Schlawin, F., Dorfman, K. E. & Mukamel, S. Entangled two-photon absorption spectroscopy. *Acc. Chem. Res.* **51**, 2207-2214, 10.1021/acs.accounts.8b00173 (2018).
61. Woll, K. A. *et al.* Photoaffinity ligand for the inhalational anesthetic sevoflurane allows mechanistic insight into potassium channel modulation. *ACS Chem. Biol.* **12**, 1353-1362.

5.6 Supporting Information

Fig. 5.7-5.11 show the HOMO and LUMO of methyl isopropyl ether, SEVO, ethyl methyl ether, ISO, and diethyl ether, respectively. Isosurface values were chosen such that only the most predominant location of each orbital is shown in order to identify the character of each orbital. The orbitals for SEVO in Fig. 5.8 show a $n_O \rightarrow \sigma_{C\text{-}H}^*$ HOMO-LUMO transition, and the orbitals for ISO in Fig. 5.11 show a $n_{Cl} \rightarrow \sigma_{C\text{-}Cl}^*$ HOMO-LUMO transition, both of which match previously reported orbital characteristics for SEVO[3,4] and ISO[5], respectively. While the orbitals for SEVO and ISO have been reported before, we show our results here as further confirmation of the accuracy of our electronic structure calculations.

Fig. 5.12-5.13 show the mass spectra of the SEVO and ISO, respectively, used in our experiments. Mass spectra were obtained through electron ionization using a Micromass AutoSpec Ultima magnetic sector mass spectrometer.

Because the laser power in the entangled two-photon spectroscopy set-up can fluctuate in a short period of time, each time a new solution is to be tested, a fresh solvent transmission scan must be completed before the transmission scan of the new solution. This method ensures the highest accuracy when comparing a solution's transmission line to a solvent's transmission line to determine whether or not the solution is interacting with entangled photons. When completing these two scan back-to-back, the random fluctuations of the laser's power should be minimized, as opposed to comparing a solution's transmission lines to a solvent transmission line taken hours earlier. Each of the transmission lines for the solutions tested in Fig. 5.14-5.17 are compared with the solvent transmission line acquired immediately before the solution was tested. The pure liquids SEVO and ISO were tested, with each solution's transmission lines (and solvent transmission lines of pure methanol) shown in Fig. 5.14 for SEVO and Fig. 5.15 for ISO. The same experiment and analysis were completed for diethyl ether and methanol, shown in Fig. 5.16. Zinc tetraphenylporphyrin (ZnTPP) in toluene was used as a standard to validate our experiment and analysis, shown in Fig. 5.17.

Fig. 5.17 shows a difference between the transmission lines for ZnTPP and toluene, which is expected since this compound has previously been reported to interact with entangled photons[6,7], thus validating our experiment and analysis. Fig. 5.16 shows that the transmission lines for diethyl ether and methanol lie within each other's error bars. Therefore, interaction is not occurring in diethyl ether, and the difference in the transmission lines is due to random fluctuations of the laser.

However, SEVO in Fig. 5.13 and ISO in Fig. 5.14 have transmission lines outside of the error bars of their respective solvent transmission lines. Therefore, these two samples are interacting with entangled photons.

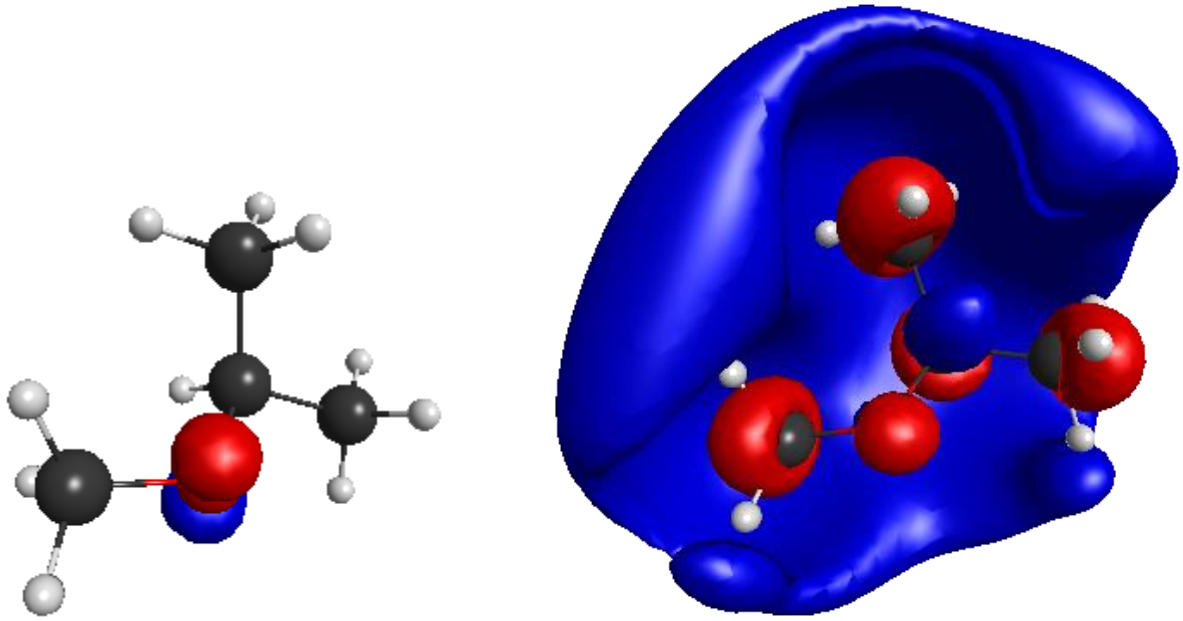

Figure 5.7. HOMO (left) and LUMO (right) of the ground state (S_0) of methyl isopropyl ether.

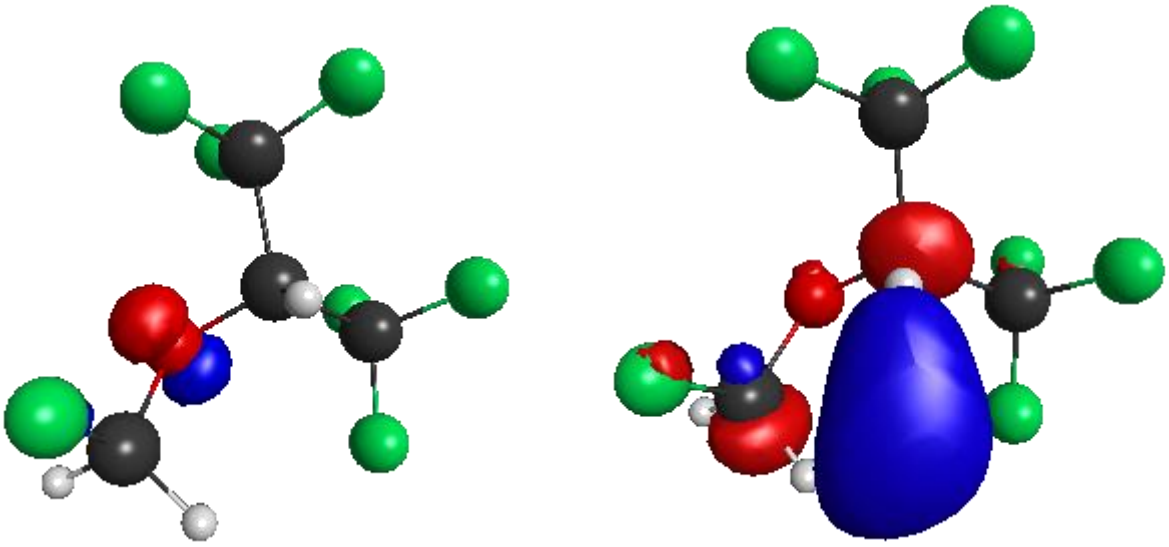

Figure 5.8. HOMO (left) and LUMO (right) of the ground state (S_0) of SEVO.

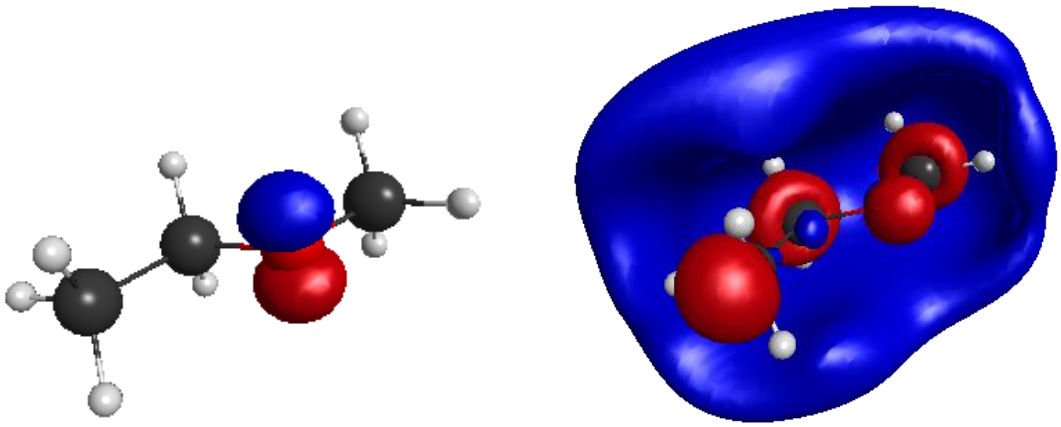

Figure 5.9. HOMO (left) and LUMO (right) of the ground state (S_0) of ethyl methyl ether.

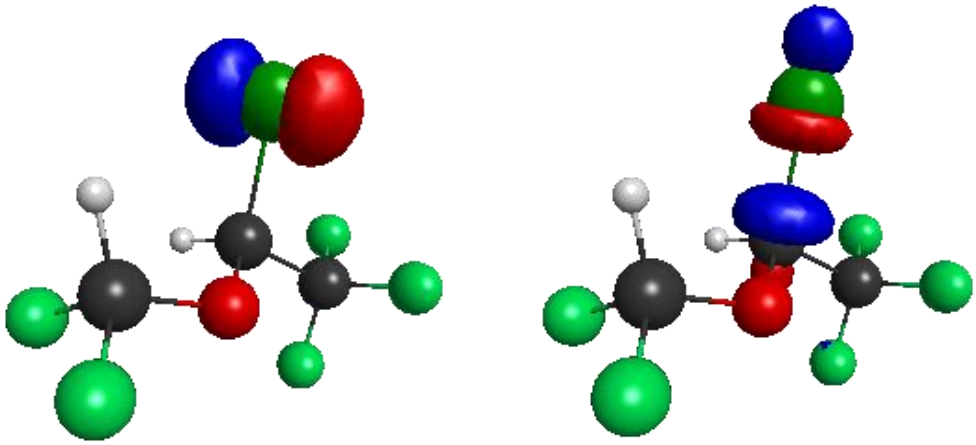

Figure 5.10. HOMO (left) and LUMO (right) of the ground state (S_0) of ISO.

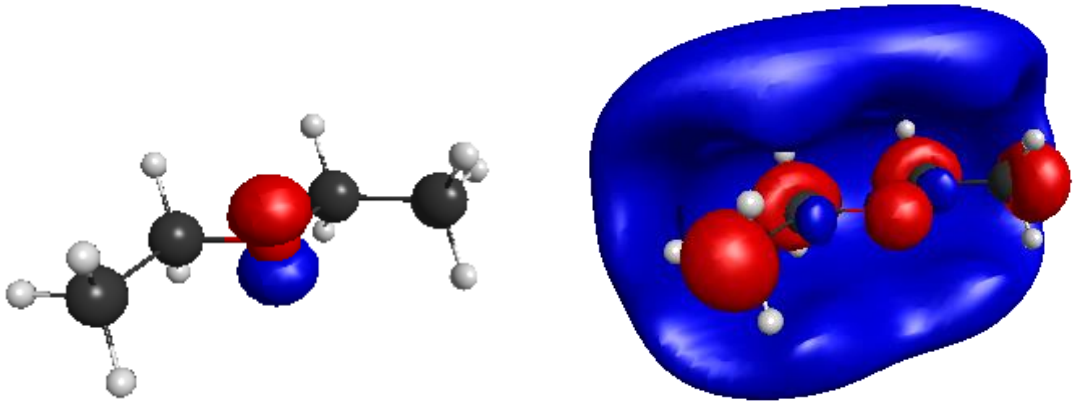

Figure 5.11. HOMO (left) and LUMO (right) of the ground state (S_0) of diethyl ether.

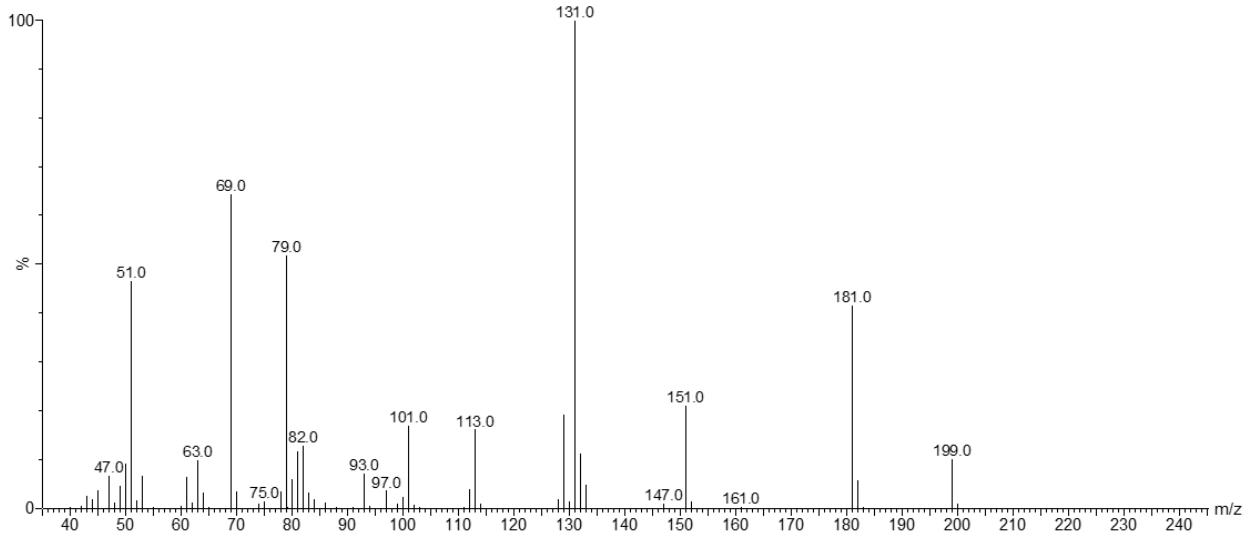

Figure 5.12. Mass spectrum of SEVO.

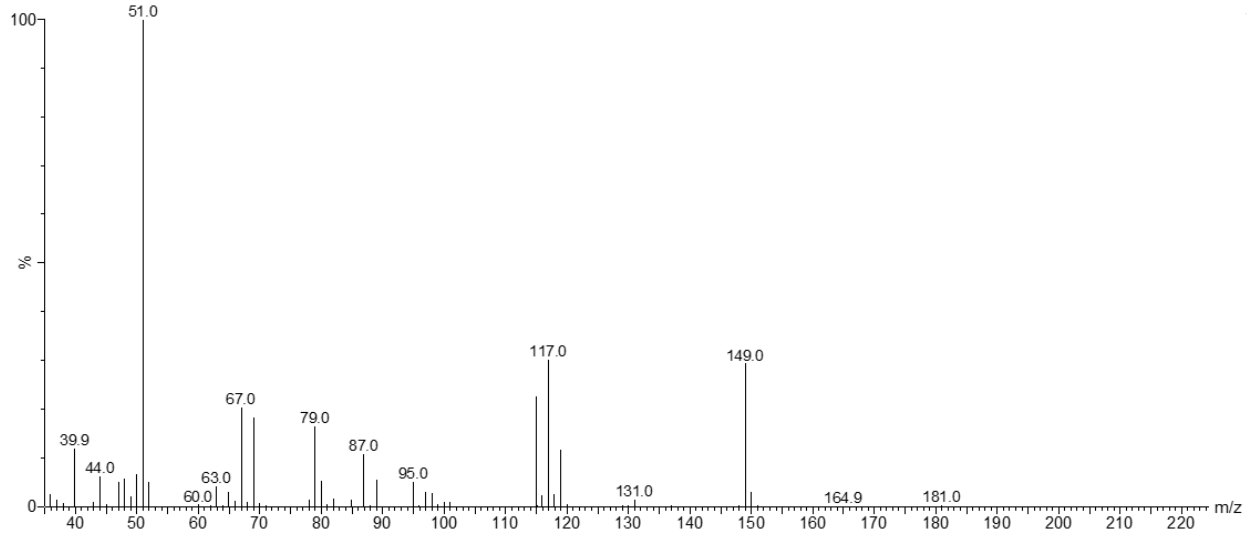

Figure 5.13. Mass spectrum of ISO.

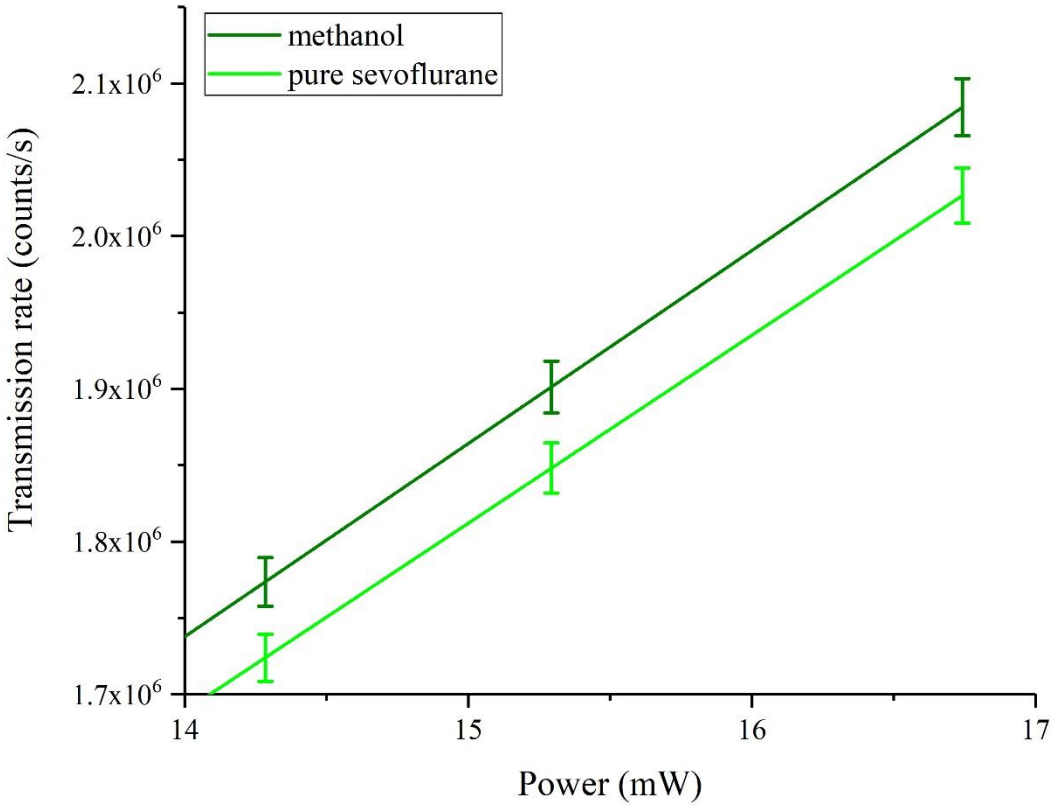

Figure 5.14. Transmission rate as a function of incident laser power for pure SEVO, compared to methanol.

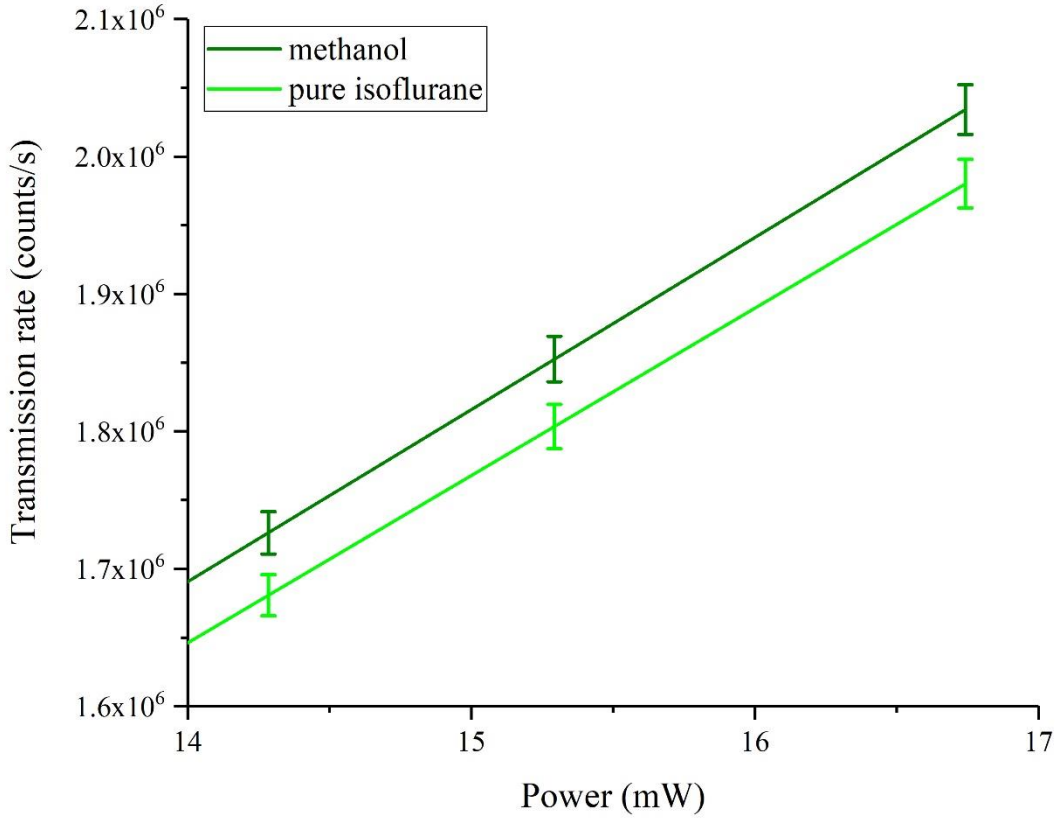

Figure 5.15. Transmission rate as a function of incident laser power for solutions of ISO, compared to methanol.

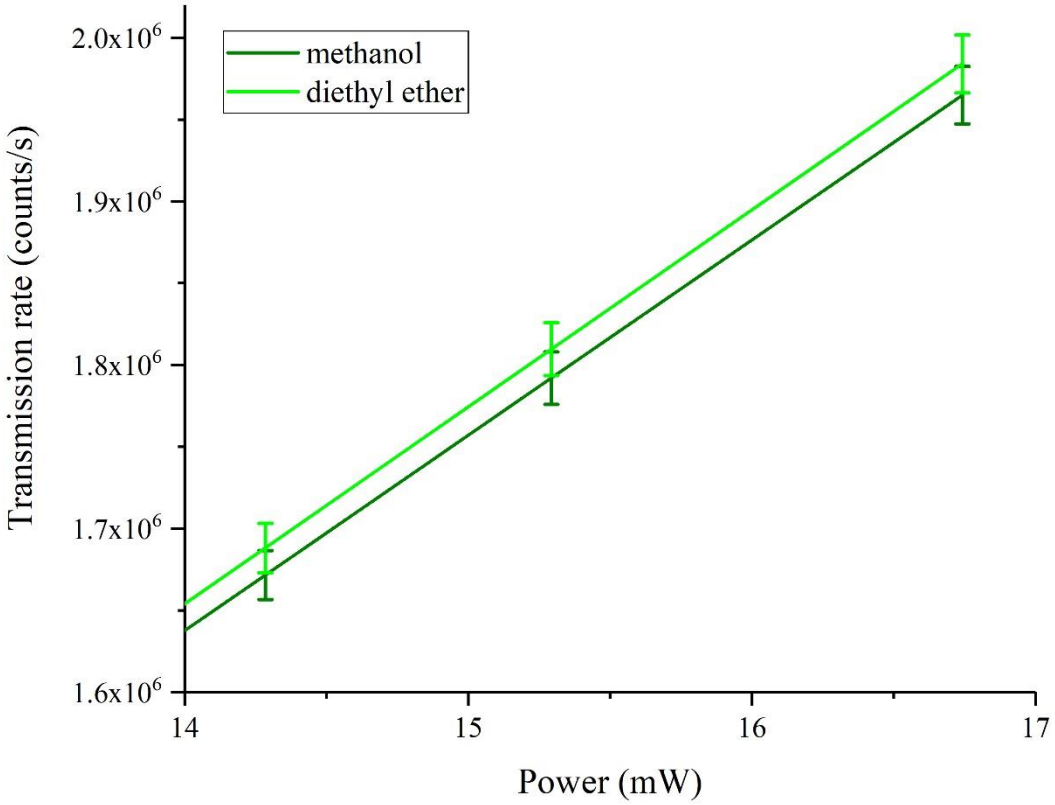

Figure 5.16. Transmission rate as a function of incident laser power for diethyl ether, compared to methanol.

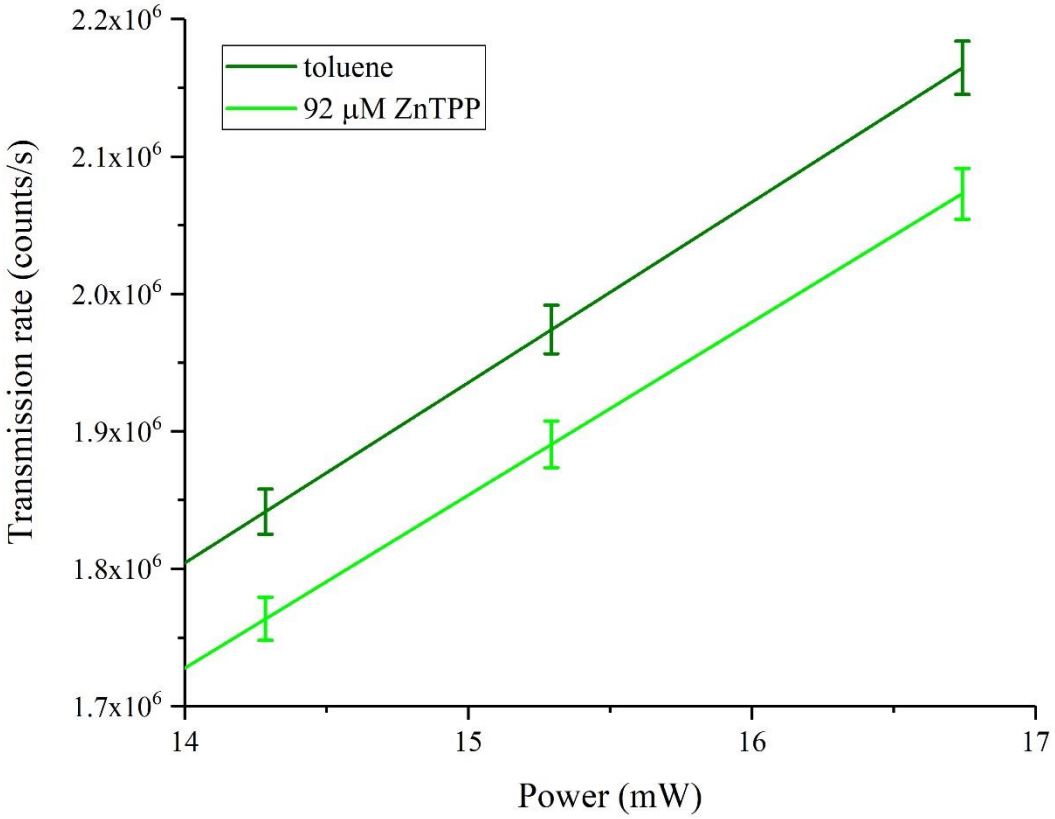

Figure 5.17. Transmission rate as a function of incident laser power for ZnTPP in toluene, compared to toluene.

References

1. Bouche, M.-P. L. A. *et al.* Quantitative determination of vapor-phase compound a in sevoflurane anesthesia using gas chromatography–mass spectrometry. *Clin. Chem.* **2001**, *47*, 281.
2. Deng, X.-s. & Simpson, V. J. Determination of volatile anesthetics isoflurane and enflurane in mouse brain tissues using gas chromatography-mass spectrometry. *J. Pharmacol. Toxicol. Methods* **2004**, *49*, 131-136.
3. Freitas, M. P., Bühl, M., O'Hagan, D., Cormanich, R. A. & Tormena, C. F. Stereoelectronic interactions and the one-bond c–f coupling constant in sevoflurane. *J. Phys. Chem. A* **2012**, *116*, 1677-1682.
4. Tang, P., Zubryzcki, I. & Xu, Y. Ab initio calculation of structures and properties of halogenated general anesthetics: Halothane and sevoflurane. *J. Comput. Chem.* **2001**, *22*, 436-444.
5. Lesarri, A. *et al.* Structural evidence of anomeric effects in the anesthetic isoflurane. *PCCP* **2011**, *13*, 6610-6618.
6. Villabona-Monsalve, J. P., Calderón-Losada, O., Nuñez Portela, M. & Valencia, A. Entangled two photon absorption cross section on the 808 nm region for the common dyes zinc tetraphenylporphyrin and rhodamine b. *J. Phys. Chem. A* **2017**, *121*, 7869-7875.
7. Upton, L. *et al.* Optically excited entangled states in organic molecules illuminate the dark. *J. Phys. Chem. Lett.* **2013**, *4*, 2046-2052.

CHAPTER 6

Measurements of Entangled Two-Photon Absorption in Organic Molecules with CW Pumped Type-I Spontaneous Parametric Down-Conversion

The work in this chapter was published as the journal article:

Villabona-Monsalve, J. P.; Burdick, R. K.; Goodson, T. "Measurements of Entangled Two-Photon Absorption in Organic Molecules with CW-Pumped Type-I Spontaneous Parametric Down-Conversion." *The Journal of Physical Chemistry C* **2020,** *124* (44), 24526-24532.

Modifications have been made for the style and content of this dissertation. References and supporting information for the manuscript are included in this chapter.

In this chapter, I built the ETPA experimental setup with CW pumping of Type-I SPDC. I measured the ETPA cross-sections of each molecule studied. I measured the SPDC joint frequency spectra and calculated the Schmidt decomposition to quantify the degree of frequency entanglement. I calculated the estimated losses due to linear optical processes. I provided the analysis of tuning the Schmidt modes to control photochemical reactions.

6.1 Abstract

Entangled photons exhibit strong nonclassical frequency and time correlations simultaneously, which allow them to excite and extract information about molecules in new ways compared to classical spectroscopy. In this report, we demonstrate the accessibility of entangled two-photon absorption (ETPA) as an analytical technique using CW-pumped Type-I degenerate spontaneous parametric down-conversion. We made improvements to lower the noise, error, and limit of detection of the ETPA experiment. We prove and quantify frequency entanglement from the experimentally measured joint frequency spectrum by using the Schmidt decomposition. As evidence of the ETPA process, we found a clear linear dependence of the ETPA and ETPA-induced fluorescence rates with the entangled input photon rate for all the studied chromophores. This ETPA experiment can be used to analyze a wide variety of chromophores of chemical and

biological significance and shows the potential for ETPA-induced fluorescence detection capabilities. As an application of our work, we show one may control the population of specific excited states in molecules with the use of a spatial light modulator in the setup.

6.2 Introduction

Entangled photons (EP) can interact with and extract information from atoms or molecules in unique ways compared to classical spectroscopy techniques, reviewed in detail by Dorfman *et al.*[1] The power of EP spectroscopy lies in the fact that EP are not restricted to the uncertainty principle, allowing them to achieve high-frequency and high-time resolution simultaneously.[2] Classical light sources can only produce one of these at a time. Entangled two-photon absorption (ETPA) is at the forefront of new spectroscopic techniques for studying the electronic states of molecules. It can selectively excite electronic states in atoms[3] or molecules[4] and requires orders of magnitude less input flux compared to classical two-photon absorption (cTPA)[5] because it scales linearly with the input intensity.[6] ETPA offers a negligible risk of damaging photosensitive samples–which is often a problem when performing non-linear spectroscopy with intense classical laser sources–, phototoxicity reduction, and potential in bio-imaging applications.[2, 7-12] ETPA is highly attractive as an analytical technique to a wide range of researchers in the physical sciences.

The most common method to produce EP for ETPA is spontaneous parametric down-conversion (SPDC). Here, we demonstrate the performance of an ETPA experiment using EP generated by CW-pumped Type-I degenerate SPDC. ETPA is measured in a variety of chromophores of chemical and biological significance, demonstrating the applicable range of ETPA. Previous experiments suffered from the error being on the same order of magnitude as the ETPA signal.[13, 14] While qualitative measurements to compare the trends of ETPA cross-sections in molecules were possible, the low signal-to-noise ratio (SNR) prevented ETPA from being a robust, quantitatively reliable analytical technique. In this work, we have made significant improvements to the ETPA experiment that offers lower noise, error, and limit of detection (LOD). We show how all other possible light-matter interactions are negligible compared to the ETPA signal.

For the SPDC source characterization, we prove and quantify frequency-entanglement from the experimental joint frequency spectrum (JFS) using the Schmidt decomposition (SD).[15, 16]

The SD allows to reformulate the JFS as a linear combination (LC) of many frequency modes, also called Schmidt modes. The Schmidt coefficients, $\{\lambda_n\}$, which are the weights of each Schmidt mode, define the JFS that is produced. We propose a method for achieving control with EP by controlling the values of $\{\lambda_n\}$ to tune the JFS, allowing one to control the excited state (ES) populations in molecules. This method would be advantageous for controlling photochemical reactions and excited state populations.

We use Type-I SPDC in particular because it produces a broader frequency spectrum of EP than Type-II SPDC,[17, 18] providing more flexibility for tuning the JFS for controlling ES populations. Additionally, Type-I SPDC produces more photon pairs than Type-II SPDC.[18, 19] Previously, ETPA using CW-pumped Type-I SPDC was studied with the collinear phase-matching condition where the EP are spatially overlapped.[11] Here, we focus on the non-collinear phase-matching condition since it allows for more effective spatial separation of the photons when measuring the JFS. For comparison purposes, collinear ETPA measurements are provided in the SI.

ETPA using ultrafast lasers to pump SPDC is expensive and requires significant space on the optical table. Instead, CW-pumped SPDC significantly reduces the size, weight, and cost of ETPA experiments, suggesting the potential for portability. Additionally, our CW-pumped ETPA experiment is easier to operate and maintain, offering an accessible route for measuring higher-order light-matter interactions by researchers who are not experts in ultrafast spectroscopy.

6.3 Methods

6.3.1 ETPA and JFS experimental setup

The experimental setup is presented in Fig. 6.1. It consists of two black boxes. In the first box, EP are generated by using non-collinear Type-I degenerate SPDC from a BBO crystal pumped using 405 nm focused light (f = 5 cm) from a CW diode laser. A variable neutral density filter mounted on a motorized and computer-controlled stage allows us to change the pump power for the SPDC process. Our source produces EP at a rate of 1.4×10^5 photons/s per mW of pump power. EP are collimated after the BBO crystal with a plano-convex lens (f = 5 cm) and separated from the pump beam by using a combination of a dichroic mirror and a bandpass filter (λ_c = 810 nm, $\Delta\lambda$= 30, or 80 nm). In the second black box, EP are focused into

the sample with a plano-convex lens and collimated with another lens after the sample (both f = 5 cm). After collimation, transmitted EP are focused on an avalanche photodiode (APD) by using a plano-convex lens (f = 2.5 cm). To obtain the ETPA rate, the EP transmission through a cuvette of pure solvent is measured first. Then the solvent is replaced with a dilute chromophore solution, and the EP transmission is measured again. A loss in the entangled photon transmission is due to ETPA.

For non-collinear Type-I SPDC photons, the photons form a ring centered around the pump beam axis. Because entangled pairs must conserve momentum with the pump, each photon is located on the ring 180° from its entangled partner. By aligning the center of the ring onto the edge of a mirrored knife-edge prism, EP on opposite sides of the ring are reflected in opposite directions. For JFS measurements, the spatially separated EP are sent through monochromators and focused (f = 2.5 cm) onto separated APDs. Coincidence counts are measured with a coincidence counter with a 10 ns time window.

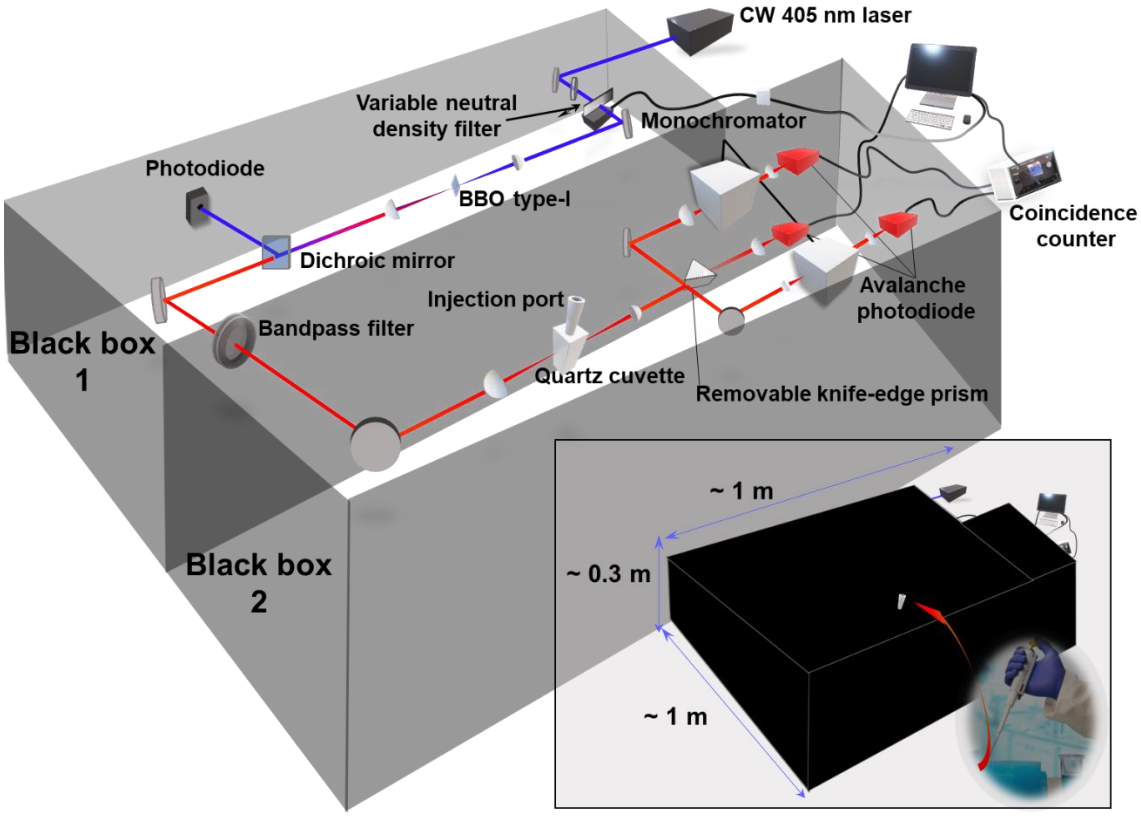

Figure 6.1. Entangled photon spectroscopy optical setup for completing ETPA and JFS measurements.

6.3.2 Proof of frequency-entanglement in Type-I SPDC

Before the ETPA experiments, it is necessary to characterize the entanglement between the photons. For Type-II SPDC, it is common to characterize the polarization entanglement by measuring the visibility of the polarization Bell state. For Type-I SPDC, which we use here, the frequency-entanglement can be characterized by measuring the JFS and performing the Schmidt decomposition (SD). SPDC follows energy conservation and momentum conservation, expressed as: $\omega_p = \omega_s + \omega_i$ and $\vec{k}_p = \vec{k}_s + \vec{k}_i$, the so-called phase-matching conditions, where ω and $\vec{k}$ correspond to energy (frequency) and wave vectors for the pump, signal, and idler (*p, s,* and *i*) photons. The possible energy (or wave vector) combinations are determined by the solutions to the Helmholtz equation, such as the Hermite-Gaussian modes (H-GM). The LC of these Schmidt modes with their respective weights (Schmidt coefficients, $\{\lambda_n\}$) gives the joint frequency amplitude of the EP. The JFS, which is the modulus squared of the joint amplitude, has the physical interpretation that if the signal photon is measured to have frequency X, then the idler photon has a distribution Y of possible frequencies, with the bandwidth of the distribution determined by the bandwidth of the pump.

To quantify the frequency-entanglement, the SD can decompose the measured joint frequency amplitude into the H-GM and calculate their weights.[15, 16] This decomposition is the continuous function formulation of the matrix singular value decomposition (SVD). The degree of entanglement (DOE) is more accurately determined by the effective number of occupied Schmidt modes, often called the Schmidt number, *K*:[16]

$$K = (\sum_n \lambda_n^2)^{-1} \tag{6.1}$$

where λ_n is the Schmidt coefficient for the nth mode. Entanglement is also sometimes quantified with the entanglement entropy, *E*:[16]

$$E = -\sum_n \lambda_n log_2 \lambda_n \tag{6.2}$$

As shown previously[16], if two photons are not entangled, $K = 1$ and $E = 0$. If two photons are entangled, $K > 1$ and $E > 0$, and both parameters increase as the DOE increases. Previous works have quantified frequency-entanglement in SPDC based on theoretical simulations.[20-22] However, few reports have experimentally measured and calculated the SD, *K*, and *E* for the

JFS of SPDC.[23-26] The details about how to measure the JFS and fit it with a model that provides a more precise SD are presented in the supporting information.

6.4 Results

6.4.1 Proof of and Quantifying Entanglement

For our Type-I degenerate, CW-pumped SPDC source passing through an 810 nm centered, FWHM = 30 or 80 nm bandpass (BP) filter, the values of K and E for non-collinear phase-matching obtained from experimental spectra are reported in Table 6.1. Also shown in Table 6.1 is the experimentally measured Fedorov ratio, R, which has been used to try to simplify the measurement of the DOE.[20, 27, 28] R is calculated as the width of the single-photon SPDC spectrum divided by the width of the coincidence count SPDC spectrum. Previous works have suggested that R should closely approximate K,[20, 27, 28] so we compare the two parameters in Table 6.1.

Table 6.1. Schmidt number, K, Fedorov ratio, R, and entanglement entropy, E, for non-collinear phase-matching of Type-I degenerate, CW-pumped SPDC from a BBO crystal.

Parameter	810-30 nm BP filter	810-80 nm BP filter
K	5.11 ± 0.11	12.62 ± 0.30
R	7.65	14.03
E	2.63 ± 0.03	3.90 ± 0.03

The results in Table 6.1, $K > 1$, and $E > 0$, prove that our SPDC photons are frequency entangled. Comparing the DOE for the two different frequency bandwidths, the number of effectively occupied Schmidt modes (K) more than doubles when increasing the bandwidth from 30 to 80 nm. Using different width bandpass filters thus provides a simple way to tailor the DOE for the desired application. We expect the unfiltered SPDC to have even more frequency-entanglement, but since the SPDC spectrum is broader than the APDs detection range, direct measurement of K and E of the unfiltered SPDC is not possible with our current experimental setup.

As seen in Table 6.1, R overestimates K for both frequency bandwidths. While the collection of data and calculation is quicker for R than for K, the results may significantly differ in the CW-pumping regime. It is particularly troublesome that R overestimates K because $R >$

1 does not guarantee that $K > 1$, i.e., $R > 1$, does not definitively proof frequency-entanglement for CW-pumped SPDC.

6.4.2 ETPA with Type-I degenerate, CW-pumped SPDC

Having proven frequency-entanglement between our Type-I SPDC photons, we then demonstrate the linear ETPA rate at very low input entangled photon rates, a well-known hallmark of ETPA.[4, 6] ETPA was measured in a variety of molecules of chemical and biological importance, shown in Fig. 6.2**.**

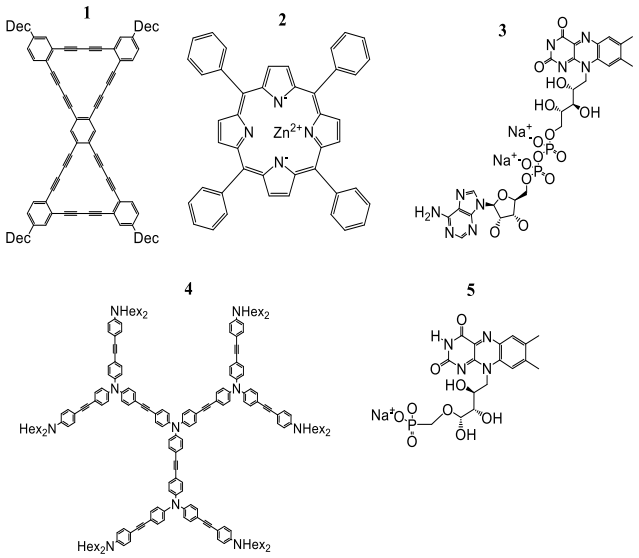

Figure 6.2. Chemical structures of the molecular systems studied in this work: bowtie (*bis*-[18]annulene) (**1**), zinc tetraphenyl porphyrin (ZnTPP) (**2**), flavin adenine dinucleotide (FAD) (**3**), OM82C dendrimer (**4**),[29] flavin mononucleotide (FMN) (**5**).

In our experiment, the CW pump power for Type-I SPDC ranges from 7 mW to 70 mW, producing $1x10^6$ photons/s to $1x10^7$ photons/s, respectively. In comparison, our Type-II SPDC source used in previous work[4] required 100 mW to produce $1x10^7$ photons/s, showing that Type-I SPDC is more efficient at producing EP. This is expected from theory as well if one uses the equations derived by Schneeloch *et al*.[30] to calculate the EP pair rate for Type-I and Type-II SPDC.

For ETPA, the total TPA absorption rate, R_{TPA}, is defined by:[7]

$$R_{TPA} = \sigma_e \Phi + \delta_r \Phi^2 \tag{6.3}$$

where σ_e is the ETPA cross-section, δ_r is the classical or "random" TPA cross-section, and Φ is the input photon flux. At low Φ, the linear term in (eq. 6.3), which is ETPA, dominates the total TPA rate. In our experiments, we use small input photon fluxes so that only ETPA, *i.e.*, the linear term, contributes to the measured signal. Results for the ETPA rate using non-collinear phase-matched Type-I degenerate, CW-pumped SPDC are shown in Fig. 6.3. The slope of each linear fit represents the percentage of input EP that is absorbed by the sample. Using this slope, the path length of the cuvette (l), and the concentration (c) of the sample, σ_e (in cm^2/molecule) is calculated by the equation[9]:

$$\sigma_e = \frac{slope}{c \times l \times N_A} \tag{6.4}$$

where N_A is Avogadro's number. The ETPA cross-section for each chromophore is shown in Table 6.2.

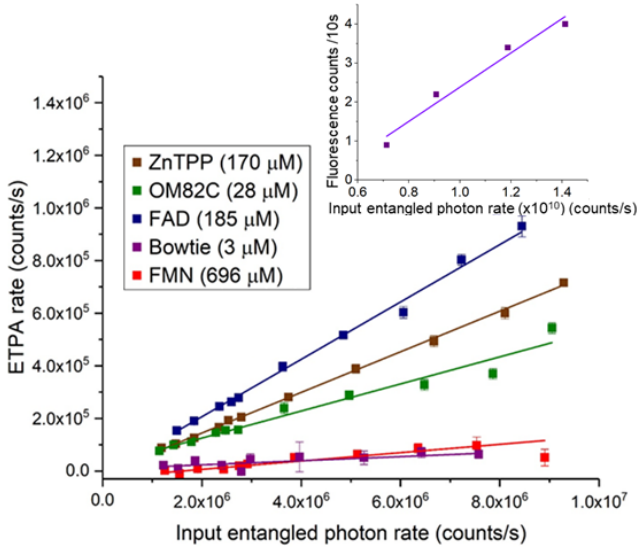

Figure 6.3. ETPA as a function of input entangled photon rate for organic chromophores using non-collinear Type-I degenerate, CW-pumped SPDC. Error bars are the propagated error of the sample's and the solvent's standard deviation of 5 transmission rate measurements. Inset: ETPA-induced fluorescence for collinear Type-I CW-pumped SPDC EP excitation.

Table 6.2. ETPA cross-section, σ_e, at 405 nm pump wavelength using non-collinear Type-I degenerate, CW-pumped SPDC.

Sample	σ_e **(x10^{-19} cm^2/molecule)**
Bowtie (*bis*-[18]annulene)	45.0 ± 5.8
OM82C dendrimer	30.8 ± 0.6
FAD	9.79 ± 0.09
ZnTPP	7.54 ± 0.10
FMN	0.38 ± 0.02

The ETPA as a function of the EP input rate shows the expected linear dependence dominance at low photon rates (eq. 6.3) and fits well to calculate σ_e (eq. 6.4). The σ_e values presented in Table 6.2 are within one order of magnitude reported previously.[8, 9, 11, 12] As might be anticipated on a first rough approximation,[5] bowtie and the OM82C dendrimer present the largest σ_e given its large cTPA cross-section at 800 nm (150 GM and 370 GM respectively)[8, 9] and correspondingly FMN has the smallest σ_e given its smallest (1.6 GM) cTPA cross-section.[12]

ETPA cross-sections with collinear Type-I SPDC EP were smaller than the non-collinear case, except for ZnTPP (Fig. 6.9 in the SI). When measuring ETPA-induced fluorescence, the fluorescence collection efficiency (FCE) of our experiment is ~0.4%, calculated by using the 405 nm CW beam to excite the sample, measuring the resulting fluorescence, and comparing the measured fluorescence count rate to the expected fluorescence count rate for a one-photon excitation of the sample. To compensate for the very small efficiency, we maximized the entangled photon input rate by sending the entire spectrum of entangled photons into the sample (no BP filter). Additionally, we used collinear phase-matching for fluorescence excitation since collinear Type-I SPDC has a broader bandwidth than non-collinear,[18] which increases the photon flux.[31] Because the APDs saturate around 10^7 photons/s, the entangled photon rate was estimated using an absorptive filter to range between 10^9-10^{10} photons/s. With this high entangled photon flux, we measured ETPA-induced fluorescence in bowtie (inset of Fig. 6.3).

6.5 Discussion

In our experiment, the input EP rate is on the order of 10^6 photons/s when the CW pump power ranges from 7-70 mW. The ETPA rate is calculated by measuring the difference in

entangled photon transmission through pure solvent and the chromophore solution. The difference in transmission between two trials of pure solvent is used as a reference "blank" and is subtracted from the chromophore's loss in transmission. We measured transmission losses on the order of 10^4-10^5 photons/s, which equals a percent loss of 1-10 % of the input photon rate. To ensure that the chromophore's loss in transmission is due to ETPA and not any other process, we have carefully analyzed any potential losses (shown in Table 6.3), and mechanical movements experienced during the experiment that can alter beam alignment. See the supporting information for details.

Table 6.3. Summary of losses in entangled photon transmission due to various processes. □ = 810 nm for all the processes.

Mechanism	**Percent loss (%)**
ETPA	1-10
OPA	< 0.1
Rayleigh scattering (chromophore)	$< 10^{-8}$
Resonant hyper-Rayleigh scattering (chromophore)	$< 10^{-10}$
cTPA	10^{-15}
Rayleigh scattering (solvent)	10^{-6}
Noise/baseline/LOD	0.1
Error	0.1

By making chromophore solutions with a concentration < 1000 μM, ETPA signals can reach 10% of the input photon rate, allowing signal-to-noise (SNR) and signal-to-error ratios on the order of 100. We measured this for the FAD solution in Fig. 6.3, which had an ETPA signal of 10.9 % and noise/error of ~0.1%. With this SNR of 10-100, the analysis summarized in Table 6.3 shows that loss in transmission from OPA, cTPA, chromophore or solvent scattering, or mechanical movement is within the noise of the experiment and does not contribute to the ETPA signal. Concentration values in this range enable us to perform ETPA experiments without potential artifacts in the signal due to scattering. Aggregation effects have been previously analyzed for ETPA in mM concentration Rhodamine B and ZnTPP samples.[11] We keep all of our concentrations in the μM range to avoid aggregation effects. Therefore, the chromophore's 1-10 % loss in transmission can only be caused by ETPA. In other ETPA experiments, the noise level and ETPA signal can both be on the order of 1 % of the input entangled photon rate, resulting in

SNR on the order of ~1.[14] Such a result would require more complex techniques to isolate the ETPA signal from background noise.

With the measures we took to reduce the noise, the SNR is now limited by the electronic noise of the detectors/counter and fluctuation of the pump laser power. Since the noise level and error of our experiment is 0.1 % of the input photon rate, this also represents the LOD of our experiment. Using a chromophore solution with a $\leq$ 1 mM concentration, we determine the smallest measurable σ_e in our experiment to be ~2x10^{-21} cm^2/molecule. This cross-section limit is a factor of 10x improvement compared to previous ETPA using either Type-I or Type-II SPDC.[11, 13]

Due to the very small FCE, only bowtie was able to yield a measurable ETPA-induced fluorescence signal because it was the only molecule tested here that had both a relatively large ETPA cross-section (~10^{-18} cm^2/molecule) and a reasonably large quantum yield (0.45). To the best of our knowledge, this is the first ETPA-induced fluorescence in an organic chromophore using Type-I SPDC, and the first ETPA-induced fluorescence in an organic chromophore using SPDC pumped by a CW laser. Future design of a unit with higher FCE could greatly increase ETPA-induced fluorescence measurements. Previous ETPA-fluorescence results for different organic chromophores (bowtie among them) were obtained with fs-pumped Type-II SPDC.[9, 10, 13] Recently, the fluorescence emission from fluorescein and the laser dye DCM by exciting with squeezed light has been reported.[32] However, squeezed light preparation by four-wave mixing requires a more complex array than entangled photons generation by CW-pumped Type-I SPDC.

The $\{\lambda_n\}$ measured for our EP create one specific LC of the Schmidt frequency modes. This LC of modes forms the joint spectrum (shown in the supporting information). If one were to change the values of $\{\lambda_n\}$, a different LC of modes, and therefore different JFS, would be produced. The JFS can thus be tailored to have control over the transition pathway and ES populations of any sample. Frequency shaped EP have shown theoretically to shape the fluorescence spectrum of molecular aggregates, which have potential applications in quantum spectroscopy and the control of photoreaction pathways with EP of biological systems.[33]

As a model, consider two TPA pathways, each populating a different final ES, that can be very close in energy and interfere with each other when exciting a sample (Fig. 6.4a). In one pathway, there are strong transition dipole moments from the ground state, $|g\rangle$, to an intermediate

ES, $|e_1\rangle$, and from $|e_1\rangle$, to the final ES, $|f_1\rangle$. In the second pathway, the intermediate state, $|e_2\rangle$, and final ES, $|f_2\rangle$, are strongly coupled, but the transition $|g\rangle \rightarrow |e_2\rangle$ is very weak. As a result, when exciting the sample via cTPA, $|g\rangle$ is largely coupled to $|e_1\rangle$ and not $|e_2\rangle$, creating population on $|f_1\rangle$ after absorbing the second photon.

By tuning the JFS so that the photon pair will be more resonant with the $|g\rangle \rightarrow |e_2\rangle \rightarrow |f_2\rangle$ pathway, $|f_2\rangle$ can be populated instead of $|f_1\rangle$. Controlling $\{\lambda_n\}$ in this manner would be advantageous for many applications, including being able to measure spectroscopic properties of ESs that are difficult to excite with classical light or that are energy degenerate but with different electronic configurations, achieving a new way to control chemical reactions. While tuning a laser may provide the necessary frequency resolution to excite only $|f_2\rangle$ (e.g., a ns pulse or CW light), $|e_2\rangle$ may be coupled to $|e_1\rangle$ by some ultrafast (fs time-scale) non-radiative decay channel. Therefore, to achieve control over the ES populations, simultaneous high-frequency- and high-time-resolution is required, which a classical laser cannot achieve. EP inherently have a fs entanglement time, allowing them to have high-frequency- and high-time-resolution simultaneously.

To change $\{\lambda_n\}$, it has been shown that the spatial profile of the pump, tuned with a spatial light modulator (SLM), is mapped onto the JFS of the EP.[34] We then propose that the SLM can be incorporated into a feedback loop in our Type-I ETPA experiment. By measuring the JFS after some of the EP have been absorbed by a sample, one can identify which frequency pairs resulted in the most absorption, revealing the locations of intermediate-to-final state ETPA pathways. Using the SLM, the JFS can be changed to remove frequency pair probability from one pathway ($|g\rangle \rightarrow |e_1\rangle \rightarrow |f_1\rangle$) and increase frequency pair probability at another pathway ($|g\rangle \rightarrow |e_2\rangle \rightarrow |f_2\rangle$). This loop leads to precise control over which ES is populated.

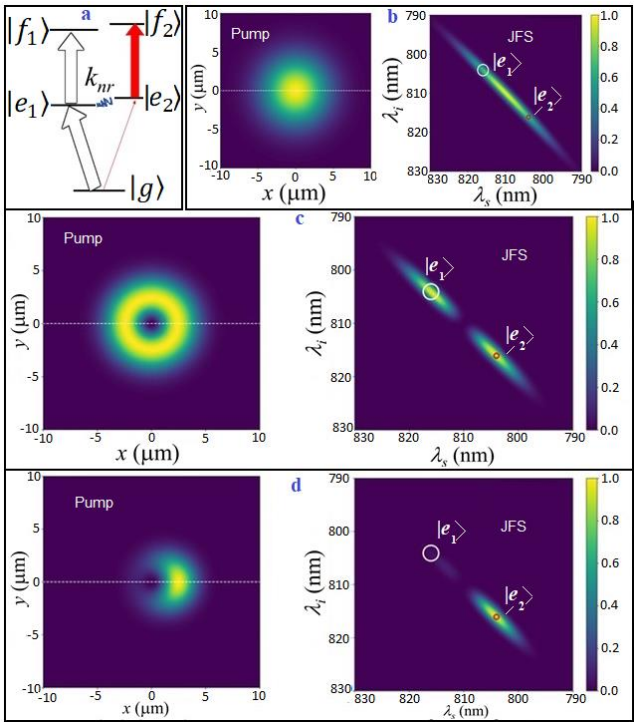

Figure 6.4. **a)** Energy level diagram with interfering ESs. The intermediate states, $|e_1\rangle$ and $|e_2\rangle$, can be coupled with an ultrafast non-radiative decay (k_{nr}) process. The thickness of each arrow represents the strength of the transition dipole moment between the connected states. Spatial distribution for the pump (left panels) and corresponding JFS (right panels) for *b)* Gaussian, *c)* symmetric Laguerre-Gauss, and *d)* asymmetric Laguerre-Gauss pump beam. The dotted lines show the plane on which EP have the JFS shown. Circles on the JFS indicate intermediate-to-final state pathways that will interact selectively with the entangled beam (*a*) for *c)* and *d)* cases.

Fig. 6.4b-d shows examples of how different pump spatial profiles produce different JFS of the EP. Fig. 6.4b shows the trivial case of a Gaussian pump, creating a very broad JFS that overlaps with both pathways in the molecule. Here, the most intense part of the JFS does not overlap with either pathway in the molecule, making ETPA very inefficient. Fig. 6.4c shows a Laguerre-Gauss (LG) beam, which produces a JFS that is most intense at the frequency pairs that overlap with the pathways in the molecule. This JFS would yield a much more efficient ETPA than that in Fig. 6.4b. In Fig. 6.4d, an asymmetric LG beam is produced so that in the JFS, there is only SPDC intensity at the weaker pathway (leading to $|f_2\rangle$) and no intensity at the stronger pathway that keeps dominating the ETPA excitation (leading to $|f_1\rangle$). With this JFS, $|f_2\rangle$ can be populated instead of $|f_1\rangle$. It is important to note that for an asymmetric pump, entangled photon pairs in different planes will have different JFS due to the asymmetry. The dotted lines in Fig. 6.4 show the plane from which EP have the JFS shown.

Fig. 6.5 shows the corresponding $\{\lambda_n\}$ for each JFS presented in Fig. 6.4, highlighting that by changing the pump spatial profile, the SD of the JFS has changed.

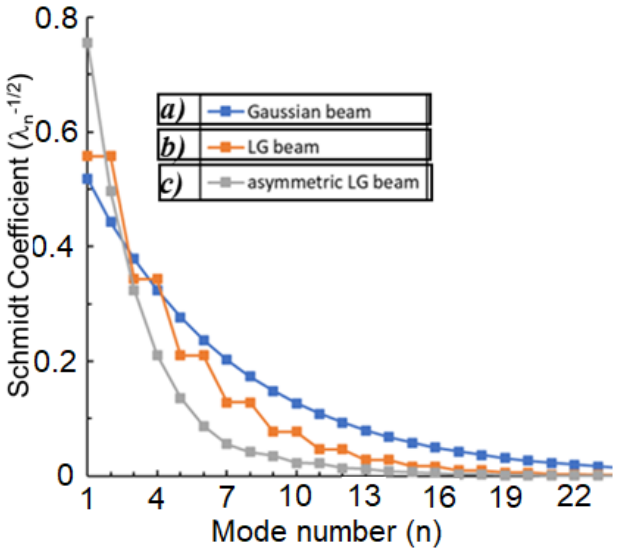

Figure 6.5. Contribution for each Schmidt mode for the considered spatial distributions of the pump beam and corresponding JFS presented in Fig. 6.4b-d. The lines for each curve are to guide the eye.

Previous work has shown that the final state population, p_f, is directly related to $\{\lambda_n\}$ of the EP:[35]

$$p_f(t) = \sum_{n=1}^{\infty} \lambda_n^2 \qquad (6.5)$$

Fig. 6.5 shows that the different pump beams directly impact $\{\lambda_n\}$ of the EP they each produce. Therefore, each pump beam creates a unique final state population in the molecule. For molecular systems with a high density of ESs, simple manipulation of the pump with an SLM provides a new level of control over the ES population in ETPA experiments.

6.6 Conclusions

Spectroscopy experiments with EP have previously been performed mainly in the framework of quantum optics studies. While there have been several proposals for using EP in physical chemistry applications, experiments with EP had yet to achieve the quantitative accuracy and reliability needed for such studies. By using a CW-pumped Type-I SPDC experimental setup, we have created an entangled photon experiment that significantly improves the accuracy of ETPA measurements in chromophore solutions. We have ruled out all other sources of photon-matter

interactions that may contribute to the noise of the ETPA signal, and we determined the LOD of our ETPA technique is 0.1% of the input photon rate. Our experiment is quantitatively robust, and previous quantum optics or ultrafast spectroscopy experience is not required to operate it. By detecting the ETPA-induced fluorescence signal for a bowtie solution and observing the linear dependence with the entangled photon flux, we demonstrated the use of CW-pumped Type-I SPDC for ETPA-induced fluorescence. Additionally, we have illustrated how one can achieve ES population control through ETPA by manipulating the EP frequency correlations, for instance, with a spatial light modulator. The presented experimental array paves the way for the future realization of difficult spectroscopic tasks that classical techniques cannot handle. For instance, with Type-I non-collinear SPDC one can conveniently create an on-demand JFS that might allow distinguishing between different interference pathways which leads to final states close in energy for a given molecular system.

References

1. Dorfman, K. E.; Schlawin, F.; Mukamel, S., Nonlinear optical signals and spectroscopy with quantum light. *Rev. Mod. Phys.* **2016,** *88* (4), 045008.
2. Schlawin, F.; Dorfman, K. E.; Mukamel, S., Entangled Two-Photon Absorption Spectroscopy. *Accounts of Chemical Research* **2018,** *51* (9), 2207-2214.
3. Georgiades, N. P.; Polzik, E. S.; Edamatsu, K.; Kimble, H. J.; Parkins, A. S., Nonclassical Excitation for Atoms in a Squeezed Vacuum. *Phys. Rev. Lett.* **1995,** *75* (19), 3426-3429.
4. Lee, D.-I.; Goodson, T., Entangled Photon Absorption in an Organic Porphyrin Dendrimer. *J. Phys. Chem. B* **2006,** *110* (51), 25582-25585.
5. Harpham, M. R.; Süzer, Ö.; Ma, C.-Q.; Bäuerle, P.; Goodson, T., Thiophene Dendrimers as Entangled Photon Sensor Materials. *J. Am. Chem. Soc.* **2009,** *131* (3), 973-979.
6. Javanainen, J.; Gould, P. L., Linear intensity dependence of a two-photon transition rate. *Phys. Rev. A* **1990,** *41* (9), 5088-5091.
7. Fei, H.-B.; Jost, B. M.; Popescu, S.; Saleh, B. E. A.; Teich, M. C., Entanglement-Induced Two-Photon Transparency. *Phys. Rev. Lett.* **1997,** *78* (9), 1679-1682.
8. Guzman, A. R.; Harpham, M. R.; Süzer, Ö.; Haley, M. M.; Goodson, T. G., Spatial Control of Entangled Two-Photon Absorption with Organic Chromophores. *J. Am. Chem. Soc.* **2010,** *132* (23), 7840-7841.
9. Upton, L.; Harpham, M.; Suzer, O.; Richter, M.; Mukamel, S.; Goodson, T., Optically Excited Entangled States in Organic Molecules Illuminate the Dark. *J. Phys. Chem. Lett* **2013,** *4* (12), 2046-2052.
10. Varnavski, O.; Pinsky, B.; Goodson, T., Entangled Photon Excited Fluorescence in Organic Materials: An Ultrafast Coincidence Detector. *J. Phys. Chem. Lett* **2017,** *8* (2), 388-393.
11. Villabona-Monsalve, J. P.; Calderón-Losada, O.; Nuñez Portela, M.; Valencia, A., Entangled Two Photon Absorption Cross Section on the 808 nm Region for the Common Dyes Zinc Tetraphenylporphyrin and Rhodamine B. *J. Phys. Chem. A* **2017,** *121* (41), 7869-7875.
12. Villabona-Monsalve, J. P.; Varnavski, O.; Palfey, B. A.; Goodson, T., Two-Photon Excitation of Flavins and Flavoproteins with Classical and Quantum Light. *J. Am. Chem. Soc.* **2018,** *140* (44), 14562-14566.
13. Eshun, A.; Cai, Z.; Awies, M.; Yu, L.; Goodson, T., Investigations of Thienoacene Molecules for Classical and Entangled Two-Photon Absorption. *The Journal of Physical Chemistry A* **2018,** *122* (41), 8167-8182.
14. Mikhaylov, A.; Parzuchowski, K.; Mazurek, M.; Lum, D.; Gerrits, T.; Camp, C.; Stevens, M.; Jimenez, R., *A comprehensive experimental system for measuring molecular two-photon absorption using an ultrafast entangled photon pair excitation source*. SPIE: 2020; Vol. 11295.
15. Ekert, A.; Knight, P. L., Entangled quantum systems and the Schmidt decomposition. *Am. J. Phys.* **1995,** *63* (5), 415-423.
16. Fedorov, M. V.; Miklin, N. I., Schmidt modes and entanglement. *Contemporary Physics* **2014,** *55* (2), 94-109.

17. Kim, Y.-H., Measurement of one-photon and two-photon wave packets in spontaneous parametric downconversion. *J. Opt. Soc. Am. B* **2003,** *20* (9), 1959-1966.
18. Baek, S.-Y.; Kim, Y.-H., Spectral properties of entangled photon pairs generated via frequency-degenerate type-I spontaneous parametric down-conversion. *Phys. Rev. A* **2008,** *77* (4), 043807.
19. Dayan, B.; Pe'er, A.; Friesem, A. A.; Silberberg, Y., Nonlinear Interactions with an Ultrahigh Flux of Broadband Entangled Photons. *Phys. Rev. Lett.* **2005,** *94* (4), 043602.
20. Brida, G.; Caricato, V.; Fedorov, M. V.; Genovese, M.; Gramegna, M.; Kulik, S. P., Characterization of spectral entanglement of spontaneous parametric-down conversion biphotons in femtosecond pulsed regime. *EPL (Europhysics Letters)* **2009,** *87* (6), 64003.
21. Avenhaus, M.; Chekhova, M. V.; Krivitsky, L. A.; Leuchs, G.; Silberhorn, C., Experimental verification of high spectral entanglement for pulsed waveguided spontaneous parametric down-conversion. *Phys. Rev. A* **2009,** *79* (4), 043836.
22. U'Ren, A. B.; Banaszek, K.; Walmsley, I. A., Photon engineering for quantum information processing. *Quantum Info. Comput.* **2003,** *3* (7), 480-502.
23. Chen, J.; Pearlman, A. J.; Ling, A.; Fan, J.; Migdall, A., A versatile waveguide source of photon pairs for chip-scale quantum information processing. *Opt. Express* **2009,** *17* (8), 6727-6740.
24. Cordier, M.; Orieux, A.; Debord, B.; Gérome, F.; Gorse, A.; Chafer, M.; Diamanti, E.; Delaye, P.; Benabid, F.; Zaquine, I., Active engineering of four-wave mixing spectral correlations in multiband hollow-core fibers. *Opt. Express* **2019,** *27* (7), 9803-9814.
25. Eckstein, A.; Boucher, G.; Lemaître, A.; Filloux, P.; Favero, I.; Leo, G.; Sipe, J. E.; Liscidini, M.; Ducci, S., High-resolution spectral characterization of two photon states via classical measurements. *Laser & Photonics Reviews* **2014,** *8* (5), L76-L80.
26. Harder, G.; Ansari, V.; Brecht, B.; Dirmeier, T.; Marquardt, C.; Silberhorn, C., An optimized photon pair source for quantum circuits. *Opt. Express* **2013,** *21* (12), 13975-13985.
27. Fedorov, M. V.; Efremov, M. A.; Kazakov, A. E.; Chan, K. W.; Law, C. K.; Eberly, J. H., Packet narrowing and quantum entanglement in photoionization and photodissociation. *Phys. Rev. A* **2004,** *69* (5), 052117.
28. Mikhailova, Y. M.; Volkov, P. A.; Fedorov, M. V., Biphoton wave packets in parametric down-conversion: Spectral and temporal structure and degree of entanglement. *Phys. Rev. A* **2008,** *78* (6), 062327.
29. Varnavski, O.; Yan, X.; Mongin, O.; Blanchard-Desce, M.; Goodson, T., Strongly Interacting Organic Conjugated Dendrimers with Enhanced Two-Photon Absorption. *The Journal of Physical Chemistry C* **2007,** *111* (1), 149-162.
30. Schneeloch, J.; Knarr, S. H.; Bogorin, D. F.; Levangie, M. L.; Tison, C. C.; Frank, R.; Howland, G. A.; Fanto, M. L.; Alsing, P. M., Introduction to the absolute brightness and number statistics in spontaneous parametric down-conversion. *Journal of Optics* **2019,** *21* (4), 043501.
31. Hendrych, M.; Shi, X.; Valencia, A.; Torres, J. P., Broadening the bandwidth of entangled photons: A step towards the generation of extremely short biphotons. *Phys. Rev. A* **2009,** *79* (2), 023817.
32. Li, T.; Li, F.; Altuzarra, C.; Classen, A.; Agarwal, G. S., Squeezed light induced two-photon absorption fluorescence of fluorescein biomarkers. *Applied Physics Letters* **2020,** *116* (25), 254001.

33. Schlawin, F.; Dorfman, K. E.; Fingerhut, B. P.; Mukamel, S., Manipulation of two-photon-induced fluorescence spectra of chromophore aggregates with entangled photons: A simulation study. *Phys. Rev. A* **2012,** *86* (2), 023851.
34. Valencia, A.; Ceré, A.; Shi, X.; Molina-Terriza, G.; Torres, J. P., Shaping the Waveform of Entangled Photons. *Phys. Rev. Lett.* **2007,** *99* (24), 243601.
35. Schlawin, F.; Buchleitner, A., Theory of coherent control with quantum light. *New Journal of Physics* **2017,** *19* (1), 013009.

6.7 Supporting Information

6.7.1 Absorption Spectra

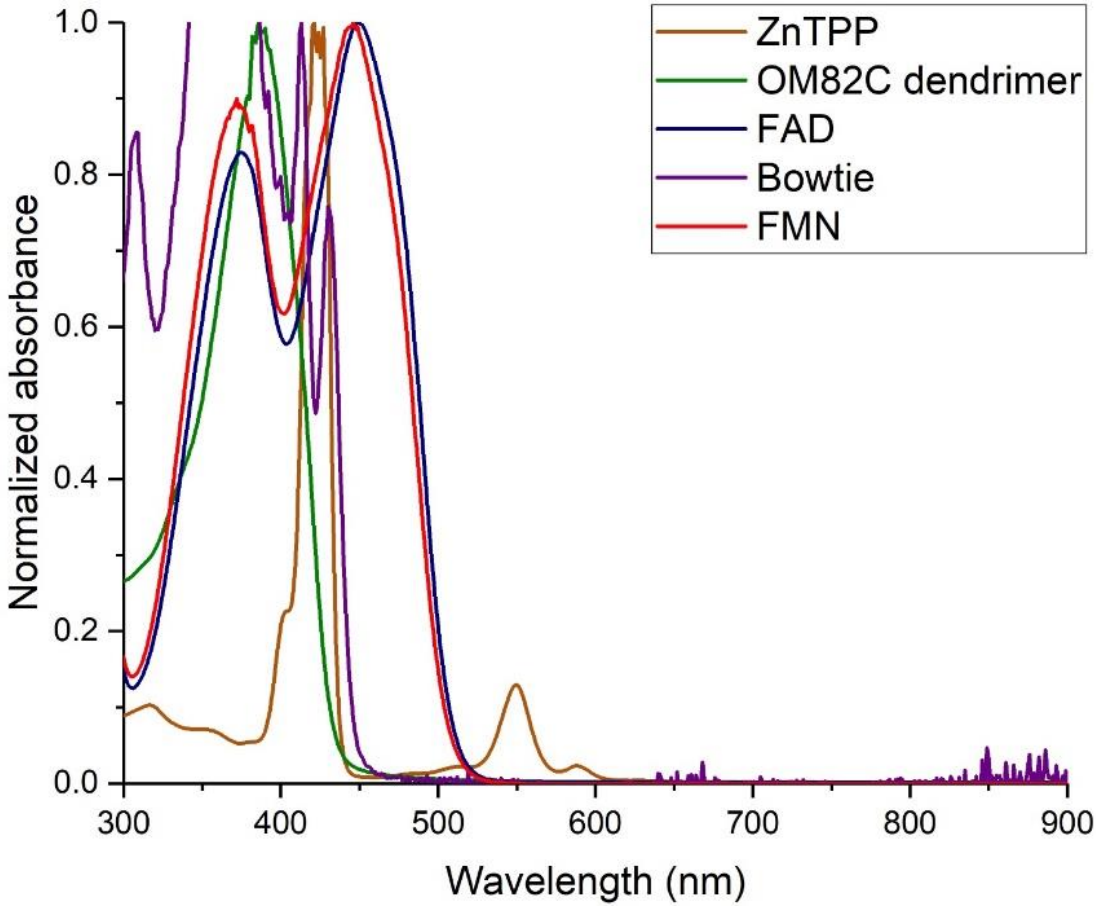

Figure 6.6. Absorption spectra of all molecules studied in this work.

6.7.2 Joint frequency spectrum and Schmidt decomposition

To calculate K and E of the SPDC photons in our experiment, the joint photon frequency spectrum must be measured, and then the Schmidt decomposition performed on this spectrum. First, the entangled photons are passed through a bandpass (BP) filter centered at the degenerate wavelength (810 nm) so that only wavelengths within the APD's detection range are collected. The photons are then separated from each other in space. For non-collinear phase-matching, the entangled photons can easily be separated from each other with a mirrored knife-edge prism. Once separated, each photon is sent through its monochromator and focused onto its APD. The joint frequency spectrum is measured by performing a series of scans as follows: one monochromator (Bob's) for the signal photon is set at a given wavelength (e.g.

840 nm). Then the other monochromator (Alice's) for the idler photon is scanned across the wavelength range of the bandpass filter (775-845 nm in our experiment). Photon counts after the two monochromators are measured in coincidence. The sum of the entangled photons' frequencies must equal the pump photon's frequency: $\omega_A + \omega_B = \omega_p$, or equivalently, $\frac{1}{\lambda_A} + \frac{1}{\lambda_B} = \frac{1}{\lambda_p}$. Additionally, two entangled photons are also strongly correlated in time, so they can only produce a coincidence count with each other. Therefore, if Alice's photon is entangled with Bob's 840 nm photon, coincidence counts should be registered when, and only when, Alice has her monochromator set at 780 nm. The joint frequency spectrum is obtained by scanning one of the monochromators, while the other´s wavelength is kept fixed.

There is a very small chance that two photons that are not entangled happen to arrive at the two APDs within the coincidence window, known as an accidental count. These accidental counts can be subtracted out of the true coincidence count signal. They can be measured by adding a delay to one of the APD's channels to the coincidence counter. This delay (100 ns in our experiment) must be longer than the coincidence window (10 ns in our experiment) so that only the accidental coincidence counts are measured and can then be subtracted from the joint frequency spectrum. The joint frequency spectrum then only contains coincidence counts from entangled photon pairs.

Before applying the Schmidt decomposition to the experimental joint frequency spectrum, we can make the decomposition more precise by fitting the experimental spectrum with an analytical model and applying the decomposition to this analytical model. The model consists of two components: the joint photon intensity (i.e. square of the joint photon amplitude) and the BP filter used in the experiment. It has previously been shown that in the limit of long-pulse-width pumping of SPDC (of which CW pumping is the most extreme limit), the joint photon amplitude of Type I SPDC can be accurately modeled with a double-Gaussian[1]:

$$z = A \cdot exp\left[\begin{matrix} -\frac{1}{2}\left(\frac{x\cdot cos(\theta)+y\cdot sin(\theta)-x_c\cdot cos(\theta)-y_c\cdot sin(\theta)}{\omega_1}\right)^2 \\ -\frac{1}{2}\left(\frac{-x\cdot sin(\theta)+y\cdot cos(\theta)+x_c\cdot sin(\theta)-y_c\cdot cos(\theta)}{\omega_2}\right)^2 \end{matrix}\right] \tag{6.6}$$

where A is the maximum coincidence count probability, x (y) is the frequency of Alice's (Bob's) photon, x_c (y_c) is the central frequency of Alice's (Bob's) one-photon amplitude, ω_1

(ω_2) is the diagonal (anti-diagonal) width of the two-photon amplitude, and θ is the angle of the coincidence count amplitude relative to the x-axis. These parameters are labeled in the example double-Gaussian contour plot in Fig. 6.7.

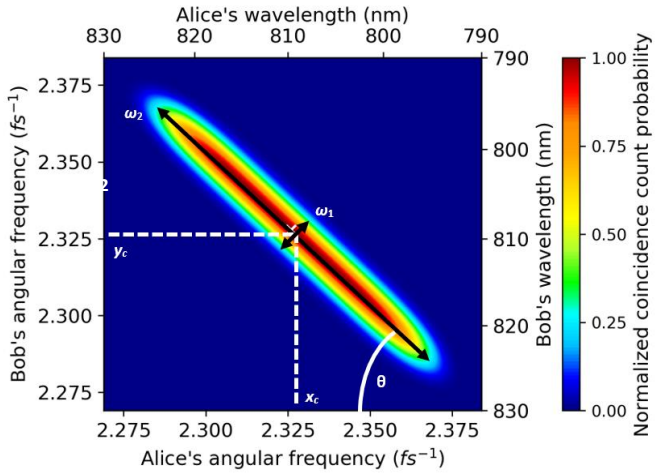

Figure 6.7. Example double-Gaussian showing the parameters to be optimized. Note: when normalized, $A = 1$.

The double-Gaussian model is particularly attractive because the Schmidt modes of a double-Gaussian can be found analytically[1]. Additionally, the double-Gaussian in eq. 6.6 contains only real terms, which is important when one considers that in our experiment with APDs, we measure the joint photon *intensity*, not the joint photon *amplitude*. Therefore, our experimental data must be fit with the square of the double-Gaussian in eq. 6.6, and this can be completed in Matlab. Since all terms are real, we can use the square root of our fit as the absolute value of the joint photon amplitude for the Schmidt decomposition. When calculating K and E, the square of the Schmidt coefficients are used, so the use of the absolute value of the joint amplitude does not affect our calculation of K and E.

To confirm the accuracy of our model, we experimentally measured the joint frequency spectrum of SPDC filtered with a BP filter centered at 810 nm with FWHM = 30 nm (810-30 nm BP filter) and compared this experimental data with the model's calculation of the joint frequency spectrum, where the model is the double-Gaussian spectral amplitude times the 810-30 nm BP filter function. The results are shown in Fig. 6.8. We compared slices of the 2D model to the experimental data at various points of interest: a) when energy is conserved so

that $\omega_A + \omega_B = \omega_p$, b) when Bob's wavelength is constant at the degenerate wavelength, 810 nm, and c) when $\omega_A = \omega_B$. These plots are also shown in Fig. 6.8. All plots and data have been normalized.

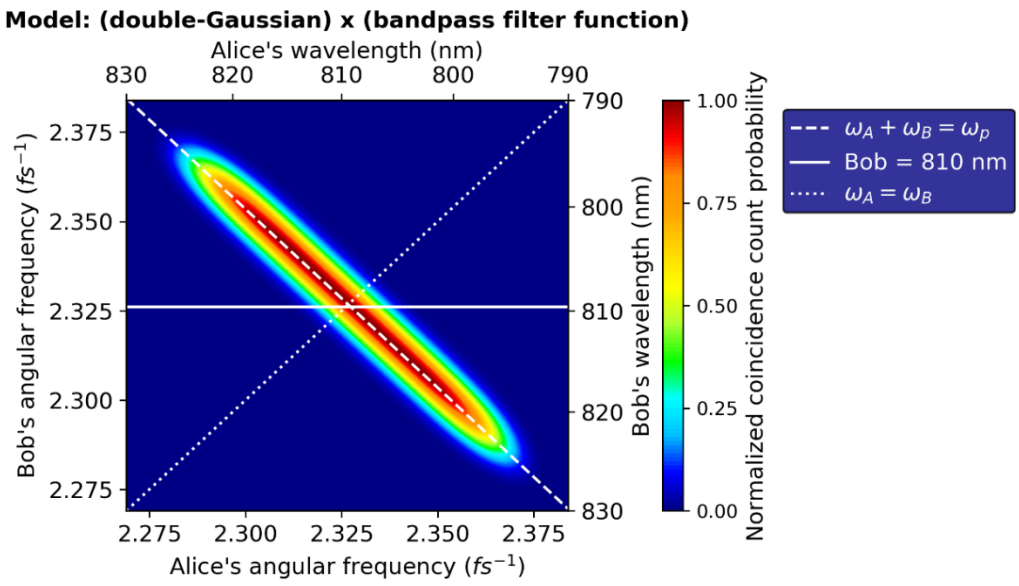

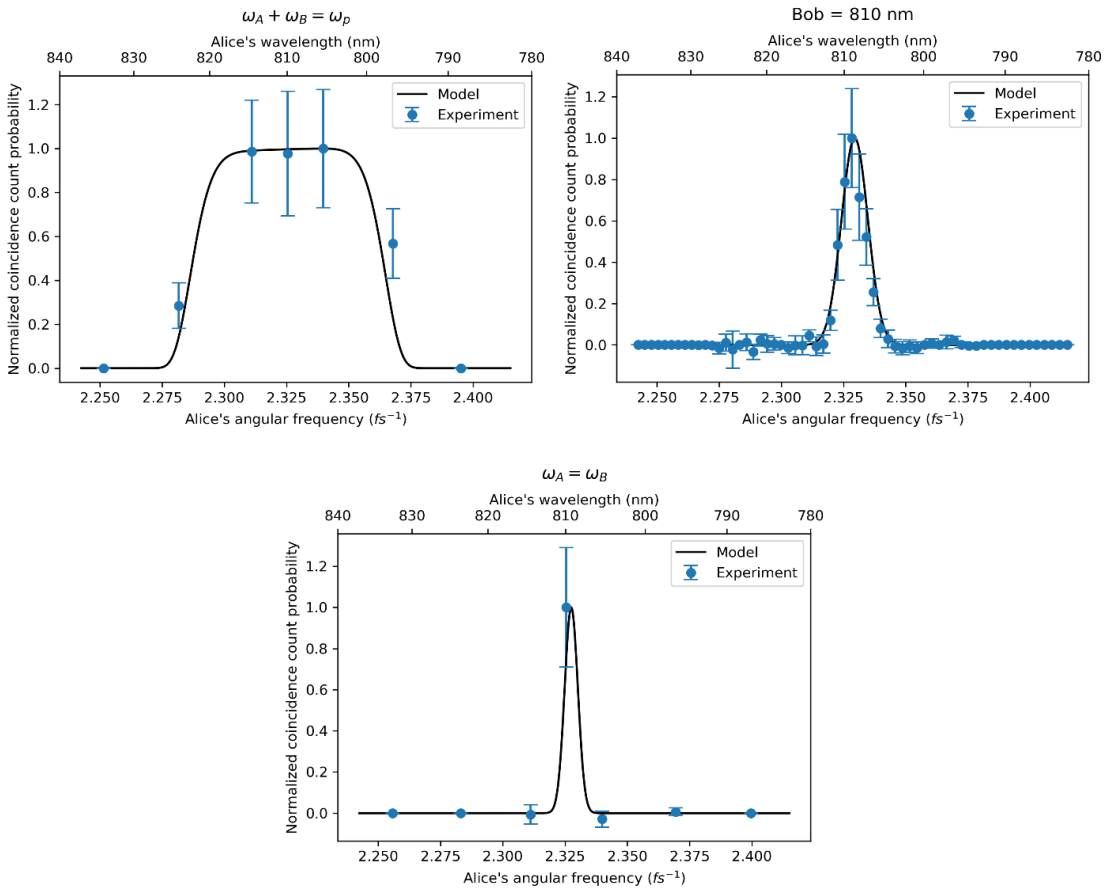

Figure 6.8. Model of non-collinear Type-I degenerate, CW-pumped SPDC filtered by an 810-30 nm BP filter. Shown is the full 2D model as well as slices used to compare with experimental data.

The plots in Fig. 6.8 confirms that our fitted model of the filtered SPDC joint frequency spectrum accurately compares to experimental data. Therefore, to quantify the degree of frequency entanglement of our filtered SPDC photons, the Schmidt decomposition is performed on this fitted model of the joint frequency spectrum. Since the Schmidt decomposition is a continuous function reformulation of the matrix formulated singular value decomposition (SVD), we can discretize our continuous function model into a matrix. The SVD can then be performed on the matrix form of our fitted model using the SVD function from a linear algebra programming package, such as NumPy or Matlab. With the calculated Schmidt coefficients, we then determine *K* and *E*, as shown in the manuscript.

6.7.3 ETPA signal details

Error bars are calculated as the propagated error from the standard deviation of 5 measurements. For a reference "blank," we measure the entangled photon transmission through two different pure solvent trials. The difference in their transmission is the baseline of the experiment, and we subtract that baseline from the measured ETPA signal. When removing the solvent from the cuvette and adding either the chromophore solution or second solvent sample, the black box containing the cuvette always remains closed. An injection port connecting the lid of the box to the cuvette allows for easy removal and addition of liquid from the cuvette. By not opening the box during experiments, the entangled photon alignment on the APD remains as steady as possible, which helps to lower the noise level and limit of detection of the experiment.

6.7.4 Analysis of potential signals interfering with the ETPA signal

The probability of OPA at the entangled photon wavelength (810 ± 15 nm) is very small since none of the chromophores have excited states near the entangled photon wavelength. Any small loss due to OPA can be estimated using the UV-vis absorbance at 810 ± 15 nm. Since there are no excited states at those wavelengths (Fig. 6.6), we can use the limit of detection of the spectrophotometer as an upper-bound for OPA: absorbance = ~0.0005, which equates to a 0.1 % loss in transmission. For an input of 10^6 photons/s, this loss equates to, at most, 10^3 photons/s, 1-2 orders of magnitude smaller than the chromophore's loss in transmission in our ETPA experiment. Classical TPA cross-sections of chromophores are typically around ~10^{-47} cm^4/s/molecule or smaller, which could only result in an extremely small loss in transmission of 10^{-11} photons/s.

Previous ETPA experiments have used chromophore concentrations as high as 110 mM without noticeable scattering from the chromophore.[2] To be cautious with avoiding scattering, we use solutions no more concentrated than 1 mM, where the chromophore-to-solvent molecule ratio is at most ~1:10^4. Scattering detected from such a diluted solution comes mainly from the solvent, and the solvent scattering is typically around 1-2 orders of magnitude larger than the chromophore's scattering in dilute solutions.[3] Anyway, scattering from the solvent is accounted for in the pure solvent transmission scan and is subtracted out of the ETPA signal. Nonetheless, we can estimate the intensity of scattering from both the chromophore and solvent

to definitively rule out the possibility of scattering contributing to our measured signal. For the chromophores, the most probable sources of scattering could come from non-resonant Rayleigh scattering at 810 nm or resonant hyper-Rayleigh scattering of the entangled photon pair at the two-photon energy, 405 nm. It has been shown that for chromophores with molar extinction coefficients of ~10^5 M^{-1} cm^{-1} (which is typical for chromophores, if not smaller), the intensity of resonance Rayleigh scattering is only $4x10^{-6}$ of the one-photon absorption at the same wavelength.[4] The intensity of non-resonant Rayleigh scattering would be an additional 1-2 orders of magnitude smaller than the resonance Rayleigh scattering.[3] Using our estimate of OPA at 810 ± 15 nm, the non-resonant Rayleigh scattering of the chromophore would at most be 10^{-4} photons/s. To estimate resonant hyper-Rayleigh scattering, we first estimate the non-resonant hyper-Rayleigh scattering intensity, which is 3-4 orders of magnitude smaller than non-resonant Rayleigh scattering.[5] Resonant hyper-Rayleigh scattering can have an enhancement over the non-resonant scattering by about a factor of 5.[6] Therefore, at most, the loss in transmission from resonant hyper-Rayleigh scattering would be 10^{-6} photons/s. Raman or hyper-Raman scattering would have even smaller intensities.

For the solvent, the scattering cross-section for an organic solvent is on the order of 10^{-26} cm^2/molecule.[7] We calculate the number of solvent molecules within the beam path using its density and estimate that the solvent would only scatter 10^{-2} photons/s. As expected, the solvent would scatter more than the chromophore by 2 orders of magnitude,[3] but the solvent scattering is still several orders of magnitude smaller than ETPA.

To reduce the mechanical movement of the equipment during the experiment, we use an injection port attached to the cuvette that opens at the lid of the black box containing all the optics and detectors. We can remove and refill liquid in the cuvette without opening the black box or disturbing the equipment inside it. In this way, all sources of mechanical movement in the setup are significantly reduced.

The noise level, or baseline, of our ETPA experiment, is measured by comparing the entangled photon transmission for two different pure solvent trials. The process of removing the first solvent trial from the cuvette and replacing it with the second solvent trial in the cuvette perfectly mimics the process of adding a chromophore solution to the cuvette. This process accounts for any remaining movement to the equipment caused by inserting the pipette into

the injection port. It also accounts for fluctuations in the average pump laser power over time, which would change the input entangled photon rate. For entangled photon input rates on the order of 10^6 photons/s, the noise level is around 10^3 counts/s, which corresponds to 0.1 % of the input rate.

The error in the ETPA signal is measured by taking multiple measurements (in our experiment, 5) at each input rate. The standard deviations of the measured transmitted count rates for the solvent reference and the chromophore solution are propagated to calculate error bars. This error accounts for fluctuations in the input entangled photon rate, caused primarily by power fluctuations of the CW pump laser, and accounts for the electronic noise of the APDs and counter. For entangled photon input rates on the order of 10^6 photons/s, the typical error is around 10^3 counts/s, the same as the 0.1 % noise level. These results were summarized in Table 6.3 in the main manuscript.

6.7.5 ETPA with Collinear Type-I CW-Pumped SPDC

Results for the ETPA rate using collinear phase-matched Type-I degenerate, CW-pumped SPDC are shown in Fig. 6.9.

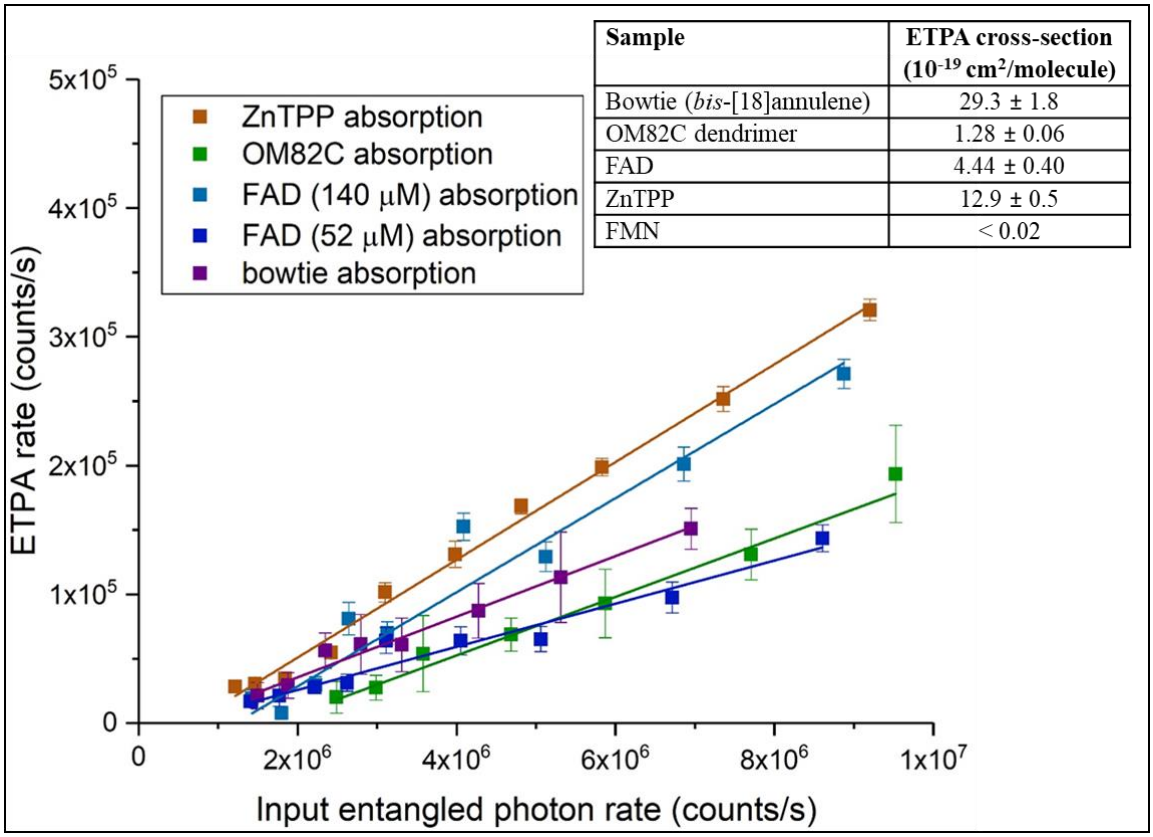

Sample	ETPA cross-section (10^{-19} cm^2/molecule)
Bowtie (*bis*-[18]annulene)	29.3 ± 1.8
OM82C dendrimer	1.28 ± 0.06
FAD	4.44 ± 0.40
ZnTPP	12.9 ± 0.5
FMN	< 0.02

Figure 6.9. ETPA results obtained with type-I collinear SPDC entangled photons excitation.

6.7.6 Fluorescence ETPA experiments

For fluorescence ETPA experiments, the entangled photons were focused by using a plano-convex lens, *fl* = 2.5 cm. A previously designed fluorescence collection unit (Ref. [8] and references therein), l_{cut} = 450 and 650 nm long and short pass filters, and a photomultiplier tube with a single photon counting module were used to isolate and detect the ETPA induced fluorescence signal.

6.7.7 Control on the population of a final state through the frequency joint spectrum

The probability on a three-level system to be in a final state *f*, driven by entangled two-photon excitation from the ground state (*g*) and using intermediate states (*e*), as a function of time, obtained perturbatively is[9]:

$$\langle \hat{p}_f(t) \rangle_\psi = \langle \hat{T}_{fg}^{\dagger}(t) \hat{T}_{fg}(t) \rangle \qquad (6.8)$$

The transition amplitude corresponds to:

$$\hat{T}_{fg}(t) = \int d\omega_1 \int d\omega_2 \, T_t(\omega_1, \omega_2)\hat{E}_2(\omega_2)\hat{E}_1(\omega_1) \tag{6.9}$$

$$T_t(\omega_1, \omega_2) = \left(\frac{E_0}{\hbar}\right)^2 \sum_e \left(\frac{\mu_{ge}}{\omega_1 - \omega_e + i\gamma_e} + \frac{\mu_{ge}}{\omega_2 - \omega_e + i\gamma_e}\right)\left(\frac{\mu_{ef}}{\omega_1 + \omega_2 - \omega_f + i\gamma_f} e^{-i(\omega_1+\omega_2)t}\right) \tag{6.10}$$

$\hat{T}_{fg}(t)$ is expressed in terms of the transition dipole moments (μ_{ge} and μ_{ef}) and subscripts 1 and 2 represent signal and/or idler photon. ω_e and ω_f correspond to the energy of the intermediate and final states; and γ_x ($x = e, f$) is the state linewidth.

As can be seen from eq. 6.8–6.10, the population of a particular final excited state can be adjusted precisely by tuning the frequency correlations of the entangled pair.[9,10] The frequency correlation can be controlled by shaping the spatial distribution of the pump beam. It was demonstrated that the optimal T_f function can be represented in a Schmidt decomposition of the matter response function as[9]

$$T_t(\omega_1, \omega_2) = \sum_k r_k \psi_k^*(\omega_1)\, \phi_k^*(\omega_2) \tag{6.11}$$

ψ_k and ϕ_k functions form an orthonormal basis set, with r_k chosen to be real and positive numbers. This orthonormal set is also a way to represent the ideal joint spectrum of the entangled photon pairs inducing with maximum probability the ETPA transition from an initial to final states through selectively excited intermediate states.

References

1. Fedorov, M. V.; Mikhailova, Y. M.; Volkov, P. A. Gaussian Modelling and Schmidt Modes of SPDC Biphoton States. *J. Phys. B: At. Mol. Opt. Phys.* **2009**, *42*, 175503.
2. Villabona-Monsalve, J. P.; Calderón-Losada, O.; Nuñez Portela, M.; Valencia, A. Entangled Two Photon Absorption Cross Section on the 808 nm Region for the Common Dyes Zinc Tetraphenylporphyrin and Rhodamine B. *J. Phys. Chem. A* **2017**, *121*, 7869-7875.
3. Anglister, J.; Steinberg, I. Z. Depolarized Rayleigh Light Scattering in Absorption Bands Measured in Lycopene Solution. *Chem. Phys. Lett.* **1979**, *65*, 50-54.
4. Anglister, J.; Steinberg, I. Z. Resonance Rayleigh Scattering of Cyanine Dyes in Solution. *J. Chem. Phys.* **1983**, *78*, 5358-5368.
5. Xu, C.; Shear, J. B.; Webb, W. W. Hyper-Rayleigh and Hyper-Raman Scattering Background of Liquid Water in Two-Photon Excited Fluorescence Detection. *Anal. Chem.* **1997**, *69*, 1285-1287.
6. Wang, C.-K.; Macak, P.; Luo, Y.; Ågren, H. Effects of Π Centers and Symmetry on Two-Photon Absorption Cross Sections of Organic Chromophores. *J. Chem. Phys.* **2001**, *114*, 9813-9820.
7. Schomacker, K. T.; Delaney, J. K.; Champion, P. M. Measurements of the Absolute Raman Cross-Sections of Benzene. *J. Chem. Phys.* **1986**, *85*, 4240-4247.
8. Varnavski, O.; Pinsky, B.; Goodson, T. Entangled Photon Excited Fluorescence in Organic Materials: An Ultrafast Coincidence Detector. *J. Phys. Chem. Lett.* **2017**, *8*, 388-393.
9. Schlawin, F.; Buchleitner, A. Theory of Coherent Control with Quantum Light. *New J. Phys.* **2017**, *19*, 013009.
10. Roslyak, O.; Marx, C. A.; Mukamel, S. Nonlinear Spectroscopy with Entangled Photons: Manipulating Quantum Pathways of Matter. *Phys. Rev. A* **2009**, *79*, 033832.

CHAPTER 7

Enhancing Entangled Two-Photon Absorption for Picosecond Quantum Spectroscopy

The work in this chapter is part of a manuscript in preparation for publication:

Burdick, R. K.; Schatz, G. C.; Goodson III, T. "Enhancing Entangled Two-Photon Absorption for Picosecond Quantum Spectroscopy."

Modifications have been made for the style and content of this dissertation. References and supporting information for the manuscript are included in this chapter.

In this chapter, I conceived of using the SPDC frequency bandwidth to control the entanglement area, A_e, expanding on previous literature that showed the connection between A_e and the SPDC crystal length. I measured the Type-I and Type-II ETPA cross-sections vs SPDC frequency bandwidth. I proposed the A_e expressions for Type-I and Type-II SPDC and performed the fitting of the expressions with the experimental cross-sections. I provided the analysis and discussion for using longer T_e SPDC to control photochemical reactions and study ps excited state dynamics.

7.1 Abstract

Entangled two-photon absorption (ETPA) is known to create photoinduced transitions with extremely low light intensity, reducing the risk of phototoxicity in sensitive samples compared to classical two-photon absorption. Previous theoretical works have predicted the ETPA cross-section, σ_e, to vary inversely with the product of entanglement time (T_e) and the entanglement area (A_e), i.e. $\sigma_e \sim 1/A_eT_e$. The decreasing σ_e with increasing T_e has limited ETPA to fs-scale T_e, while ETPA applications for ps-scale spectroscopy have been unexplored. However, we show that spectral-spatial coupling, which reduces A_e as the SPDC bandwidth (σ_f) decreases, plays a significant role in determining σ_e when $T_e \gtrsim 100$ fs. For Type-I ETPA, σ_e increases as σ_f decreases down to 0.1 ps^{-1}. For Type-II SPDC, the influence of spectral filtering on A_e cancels the effect on T_e, resulting in a constant σ_e for a wide range of σ_f. We illustrate these results by experimentally measuring σ_e for zinc tetraphenylporphyrin at several σ_f values. With a theoretical analysis of the

data, the maximum Type-I σ_e would occur at σ_f = 0.1 ps^{-1}, or T_e = 10 ps. At this maximum, σ_e is 1 order of magnitude larger than fs-scale σ_e and 3 orders of magnitude larger than what previous predictions of ps-scale σ_e would be. By utilizing the spectral-spatial coupling of the entangled photons, narrowband Type-I ETPA provides a new opportunity to increase the efficiency of measuring nonlinear optical signals and to control photochemical reactions requiring ps temporal precision.

7.2 Introduction

Entangled two-photon absorption (ETPA) was shown to be measurable in atoms[1, 2] and organic chromophores[3] using extremely low light intensity more than a decade ago. The well-known linear absorption rate for ETPA vs photon flux significantly enhances the ETPA rate compared to classical two-photon absorption (TPA) rate at these low light intensities.[4, 5] To date, ETPA has only been performed in the fs-scale of the fourth-order temporal correlation, or entanglement time, T_e. ETPA with ps T_e would be beneficial for probing chemical processes such as isomerization,[6, 7] proton transfer,[8, 9] water solvation,[10, 11] and ligand binding/unbinding.[12, 13] However, previous reports on ETPA suggest that ETPA would not be measurable practically with ps-scale T_e because the ETPA cross-section, σ_e, was predicted to decrease with increasing T_e.[14-18] Other parameters of SPDC, such as the fourth-order transverse spatial correlation, or entanglement area, A_e, may be used to counteract the effect of increasing T_e.

With spontaneous parametric down-conversion (SPDC) as the entangled photon source, the ETPA cross-section with a Gaussian frequency filter has been derived previously as:[19, 20]

$$\sigma_e = \frac{\sqrt{2}\omega_s^0\omega_i^0}{\hbar^2\varepsilon_0^2c^2A_eT_e}\frac{k_f}{\left(\varepsilon_f-\varepsilon_g-\omega_s^0-\omega_i^0\right)^2+\left(\frac{k_f}{2}\right)^2}\left|\sum_j \mu_{fj}\mu_{jg}T_eF\left[\left(\Delta_j - ik_j/2\right)T_e\right]\right|^2 \qquad (7.1)$$

Here, ε_g, ε_j, ε_f are the energies of the molecule's ground, intermediate, and final states, respectively; μ_{jg} and μ_{fj} are the transition dipole moments (TDMs) from the ground-to-intermediate and intermediate-to-final states, respectively; $\omega^0{}_{s/i}$ are the central frequencies of the signal/idler entangled photons, respectively; $\Delta_j = \varepsilon_j - \varepsilon_g - \omega^0{}_s$ is the detuning energy; F is the plasma dispersion function. We assume a monochromatic pump. The molecule's excited states are Lorentzian broadened with linewidths k_j and k_f for the intermediate and final states, respectively. Previous work showed that the lifetime of the final ETPA excited state can be calculated using the spontaneous radiative lifetime for two-photon emission.[17]

While eq. 7.1 provides the exact σ_e dependence on T_e, a simpler probabilistic model is used to describe σ_e when the T_e dependence of the modulus squared term is negligible ($T_e \gtrsim 500$ fs):[14]

$$\sigma_e = \frac{\delta_r}{2A_eT_e} \tag{7.2}$$

Here δ_r is the classical TPA cross-section. In previous theoretical[14-17] and experimental[3, 21, 22] reports, it was assumed that T_e can be changed while A_e remains constant. From eq. 7.2, if A_e is constant, σ_e decreases as T_e increases. However, there exists a coupling between the spectral and spatial properties of the entangled photon wavefunction (see supporting information).[14] To change T_e, the bandwidth of the photons from SPDC must change, which should also change A_e. While this spectral-spatial coupling has been discussed in the literature before,[23, 24] how the coupling affects the ETPA cross-section has not been considered nor explored experimentally.

7.3 Results and Discussion

Here we consider the effect of a spectral filter, with bandwidth σ_f, that is applied to the SPDC photons after they emerge from the SPDC process. Full details of our experimental setup have been reported previously[25] and can be found in the SI. In Fig. 7.1a, the experimental σ_e for Type-I and Type-II filtered SPDC are plotted as a function of σ_f ranging from 0.9-40 ps^{-1}. In our passive filtering technique, where SPDC photons are produced in a crystal and filtered after their generation, the input photon rate for ETPA decreases with decreasing σ_f. We found that we can choose σ_f as small as 0.9 ps^{-1} before the input rate was too small to measure an ETPA signal. Due to the limited wavelength detection range of APDs, we could not obtain σ_e at $\sigma_f > 40$ ps^{-1}. The smooth curves in this figure are the results of an analytical theory that we describe below.

Given that eq. 7.1-7.2 show that σ_e varies inversely with T_e, it is of interest to convert Fig. 7.1a to show dependence on T_e. Standard filter theories can be used to show that T_e varies inversely with σ_f,[26-28] so experimentally, T_e increases when filtering the SPDC with different bandwidth filters or a monochromator. Since σ_f was always smaller than the initial SPDC bandwidth emitted by the crystal (σ_L), T_e was calculated in Fig. 7.1b from σ_f, taking dispersion into account using the standard relation for the pulse width in a dispersive medium:[29]

$$T_e = \frac{1}{\sigma_f}\sqrt{1+\left(4ln2\frac{GDD}{\left(\frac{1}{\sigma_f}\right)^2}\right)^2} \tag{7.3}$$

GDD in this expression is the group delay dispersion for the optical elements in our experiment.

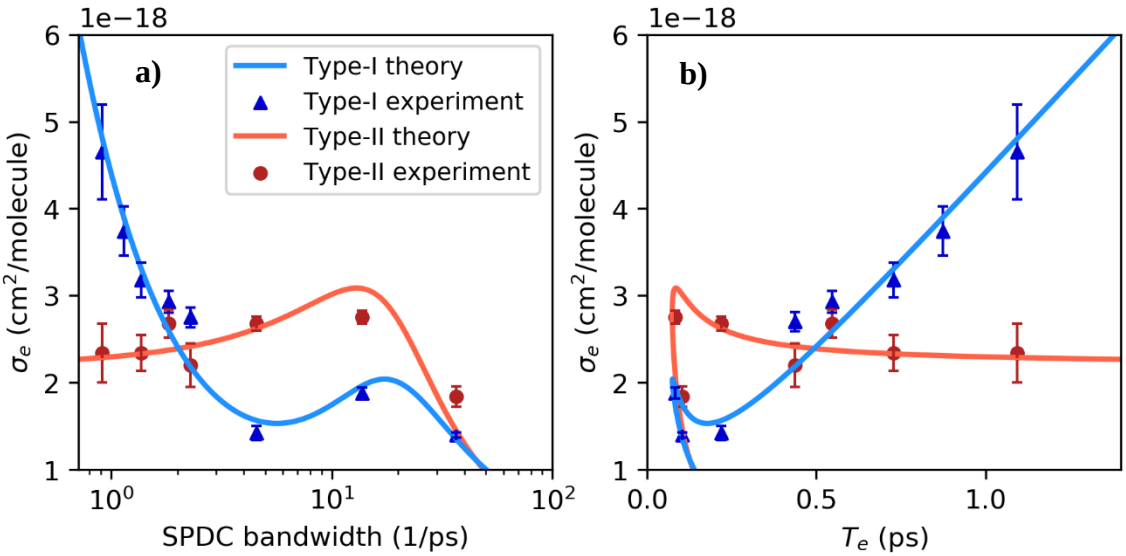

Figure 7.1. a) Experimental and theoretical Type-I and Type-II ETPA cross-sections, σ_e, vs σ_f for a ~20 μM solution of zinc tetraphenylporphyrin (ZnTPP). **b)** Same as **(a)** with the x-axis converted to T_e.

The experimental data in Fig. 7.1 shows that for Type-I SPDC at small σ_f, σ_e increases as σ_f decreases (T_e increases). For Type-II SPDC at long T_e, σ_e is constant as σ_f decreases. Not only do the two SPDC Types differ from each other in their cross-section trends, they are also incompatible with the constant A_e prediction that σ_e should decrease as σ_f decreases. We note that the GDD term in eq. 7.3 leads to two branches in the curves in Fig. 7.1b: an upper branch corresponding to small σ_f in which T_e is determined by $T_e=1/\sigma_f$, and a lower branch corresponding to large σ_f where the GDD dominates, and T_e is proportional to σ_f. Fig. 7.1 shows that both branches are involved in the data fit. However, we are only concerned with the small σ_f branch. Even with eq. 7.3 factored in, the variation of σ_e with σ_f is still not explained by the assumption of a constant A_e. We then take into account the spectral-spatial coupling and how changing σ_f would change A_e. The solid curves in Fig. 7.1 are the theoretical model in eq. 7.1 including the spectral-spatial coupling, which is explained below.

The origin of A_e is the uncertainty in the SPDC emission angles from the crystal source, as determined by the polar and azimuthal entanglement angles, θ^e and φ^e, respectively.[30, 31] Because each frequency within the SPDC frequency superposition experiences a different refractive index inside the crystal, each frequency propagates at a different angle. Therefore, uncertainty in the frequency causes an uncertainty in the propagation angle and ultimately the spatial position.

Decreasing the frequency uncertainty (σ_f), is then expected to decrease A_e, which should increase σ_e. However, decreasing σ_f also increases T_e, which should decrease σ_e. From the experimental data in Fig. 7.1a, for Type-II SPDC, these competing effects cancel each other, leaving σ_e constant for small σ_f. For Type-I SPDC, the decreasing A_e outweighs the increasing T_e, resulting in a net increase in σ_e.

The work in ref. [32] showed that the entanglement angle θ^e, and thus A_e, is dependent on the length, L, of the SPDC crystal. As the crystal length increases, θ^e decreases linearly. This is expected from the reasoning above since as the length of the SPDC crystal increases, the frequency bandwidth decreases (eq. 1.28-1.29 in Chapter 1). This linear relationship between L and θ^e is true for Type-I and Type-II SPDC. In our experiment, the Type-I A_e is expected to have a quadratic dependence on the frequency bandwidth because the frequency bandwidth is quadratically dependent on L (eq. 1.28). A quadratic relationship between L and the bandwidth, and a linear relationship between L and the entanglement angle/area, results in a quadratic relationship between the bandwidth and A_e. Since this previous work did not directly correlate the frequency bandwidth to A_e, we propose the following relationships between A_e and the SPDC frequency bandwidth (for small σ_f) for Type-I and Type-II (see supporting information for more details):

$$\text{Type-I: } A_e = \left(\frac{\alpha}{\sigma_f^2} + \frac{\beta}{\sigma_L^2}\right)^{-1} + A_d \propto \left(\alpha T_{e,f}^2 + \beta T_{e,L}^2\right)^{-1} + A_d \tag{7.4}$$

$$\text{Type-II: } A_e = \left(\frac{\gamma}{\sigma_f} + \frac{\zeta}{\sigma_L}\right)^{-1} + A_d \propto \left(\gamma T_{e,f} + \zeta T_{e,L}\right)^{-1} + A_d \tag{7.5}$$

σ_L is the bandwidth of the SPDC that is emitted from the crystal before filtering, which is controlled by the length, L, and represents the upper limit for σ_f in our experiment. $T_{e,L}$ is the corresponding entanglement time. The term A_d recognizes that there is a lower bound to the area A_e that is determined by diffraction. The coefficients α, β, γ, and ζ are solved for by fitting with the experimental data in Fig. 7.1. Substituting eq. 7.4-7.5 into eq. 7.2 provides new probabilistic models (to highest order in T_e) for Type-I and Type-II ETPA, respectively:

$$\text{Type-I: } \sigma_e \propto \delta_r T_{e,f} \tag{7.6}$$

$$\text{Type-II: } \sigma_e \propto \delta_r \tag{7.7}$$

Eq. 7.6-7.7 predict the σ_e vs T_e trends (for small σ_f) that we see with the experimental data in Fig. 7.1b for both SPDC Types. To confirm the validity of eq. 7.6-7.7, we substitute the equations into eq. 7.1 and fit the resulting equations with our experimental data to determine the coefficient values and extract A_e. See supporting information for calculation parameters. The models are accurate

until σ_f decreases to the point where A_e reaches A_d, as determined by eq. 7.4-7.5, which we calculate below to occur around T_e = 10 ps.

The resulting fits for Type-I and Type-II are shown in Fig. 7.1 as the solid curves, and they agree reasonably well with the experimental data. The trends for $\sigma_f < 5$ ps^{-1} are the same if a sinc SPDC spectrum is considered for the theoretical equation (see supporting information). For $\sigma_f >$ 10 ps^{-1}, dispersion significantly increases T_e and decreases σ_e, which is shown in Fig. 7.1b as the bottom branch that decreases with increasing T_e. For σ_f in the range 0.9-40 ps^{-1}, the Type-I A_e ranges 1.95x10^{-7}-7.39x10^{-6} cm^2, and the Type-II A_e ranges 4.12x10^{-7}-6.91x10^{-6} cm^2. These ranges are within an order of magnitude of the assumption of A_e = 1x10^{-6} cm^2 in previous theoretical works for fs-scale T_e.[14, 16, 17]

Inclusion of the A_d parameter in eq. 7.4-7.5 assumes that there is a diffraction limit to A_e. In the supporting information, we provide estimates of σ_e where this limit has been assumed to be $(\lambda/2)^2$=1.6x10^{-9} cm^2. Fig. 7.2 shows how the Type-I ETPA cross-section changes as the SPDC bandwidth is decreased until A_e reaches the diffraction limit. For comparison, the same theoretical model (eq. 7.1) but using a constant A_e is shown.

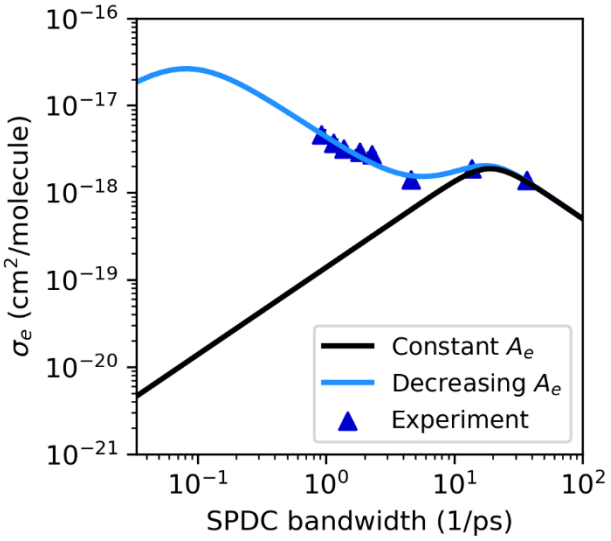

Figure 7.2. Comparison of the Type-I ETPA experimental data for ZnTPP with theoretical model (eq. 7.1) for constant A_e (black) and decreasing A_e (blue).

In Fig. 7.2, at the smallest experimental bandwidth (~1 ps^{-1}), the model with a constant A_e is more than an order of magnitude smaller than the experimental value. For the decreasing A_e, the maximum occurs at σ_f = 0.1 ps^{-1} (T_e = 10 ps), and here σ_e is ~3x10^{-17} cm^2, which is over 3 orders of magnitude larger than what the constant A_e predicts (~1x10^{-20} cm^2).

Comparison of ETPA with one-photon absorption (OPA) at the intermediate state has previously been explored.[20, 33, 34] In this report, we considered a molecular system where the intermediate states are far off-resonance with the single photon energies, such that OPA at the intermediate states is negligible. The final-state OPA cross-section of ZnTPP at 405 nm is ~2×10^{-16} cm^2/molecule.[35] At the maximum, σ_e is within an order of magnitude of the final-state OPA cross-section, rather than 2 orders of magnitude smaller in the tens of ps^{-1} range where ETPA experiments are performed today.[43-45]

It is clear from the data in Fig. 7.2 that the ETPA cross-section increases with decreasing SPDC frequency bandwidth due to A_e decreasing. As A_e decreases, the spatial location of the entangled photons becomes known to the molecule with greater certainty, i.e. the entangled photons become more localized. Since it is important for any TPA transition that the two absorbed photons overlap with the same molecule in the solution, having the entangled photons become more localized increases the probability that they will overlap with the same molecule, thus enhancing the molecule's ability to absorb them. It is important to note that A_e is different, and in fact smaller, than the total spatial distribution of the SPDC beam, i.e. the SPDC ring(s). For classical TPA, the location of the two absorbed photons has an uncertainty of the entire spatial distribution of the laser beam. For ETPA, the uncertainty (A_e) is smaller than the entire spatial distribution and can be tuned separately from the entire spatial distribution. ETPA thus has a unique control knob for tuning the cross-section that classical TPA does not have.

With this unique control knob, ETPA may be used to measure the size of molecules or chemical structures by measuring how the ETPA cross-section changes with A_e. Of course the cross-section should increase with decreasing A_e, but the rate of the cross-section's increase may be dependent upon the size of the molecule or structure. Thus, by measuring the exact rate that the cross-section changes with A_e may be used to measure the size of chromophores, different generations of dendrimers, quantum dots, proteins, or cell organelles.

While the ETPA cross-section increases from 1 to 10 ps, the photon pair rate decreases as the SPDC is passively filtered more and more. The increasing cross-section and decreasing input SPDC rate can leave the ETPA signal unchanged. To fully take advantage of the increased ETPA cross-section, the SPDC rate cannot be drastically reduced through filtering. The SPDC pair rate through the monochromator in this work was 0.114 pairs/s/mW per GHz of SPDC bandwidth. This rate resulted in ~1×10^4 pairs/s at T_e = 1.1 ps, and upon further filtering, the pair rate was too small

to measure an ETPA signal. This establishes the current minimum count rate needed to measure an ETPA signal at $1x10^4$ pairs/s. Filtering the SPDC to a 0.1 ps^{-1} bandwidth would only leave ~$1x10^3$ pairs/s, an order of magnitude too small to measure the ETPA signal. We propose using one of the following techniques to measure ETPA at the cross-section maximum: cavity-enhanced SPDC or periodically poled SPDC. We outline both of these techniques in the following section.

7.4 Proposed Techniques for ETPA Cross-Section Maxima Measurements

Usually when more narrowband SPDC photons are needed, an active filtering technique called *cavity-enhanced SPDC* (CE-SPDC) is used.[36-42] In this technique, the SPDC crystal is placed inside of an optical cavity. Common arrangements for the cavity include Fabre-Perot and bowtie. The pump beam is sent into the cavity to pass through the crystal where SPDC is produced. The length of the cavity is fine-tuned using piezo-electric elements on one of the mounted cavity mirrors. The piezo element locks the cavity length to be resonant with at least one of the SPDC photon fields. Because one (or both) of the SPDC fields is resonant with the cavity, the frequency of the emitted SPDC must be resonant with a cavity mode. This requirement essentially adds another condition to the SPDC phase-matching conditions. The SPDC is still created inside the SPDC crystal, which has a sinc frequency distribution, but the entire sinc distribution is not resonant with a cavity mode. The frequency spectrum of the SPDC is therefore the product of the cavity modes times the sinc distribution from the SPDC crystal. The spectrum resembles a frequency comb with a sinc envelope. This is shown in Fig. 7.3.

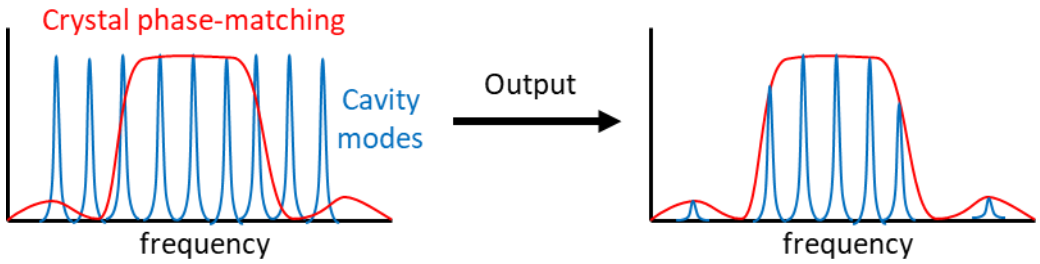

Figure 7.3. Frequency spectrum of cavity-enhanced SPDC.

The width of the cavity modes in Fig. 7.3 is determined by the length of the optical cavity and its finesse, which is a measure of how long the photons stay inside the cavity before exiting. Longer cavities and higher finesse keep the SPDC photons inside the cavity longer and have

stricter bounds on the frequencies resonant with the cavity, which narrows the cavity modes. The width of the cavity modes, $\Delta\nu_{cav}$, is calculated as:[36]

$$\Delta\nu_{cav} = \frac{c}{F\tilde{n}L_{rt}} \approx \frac{\alpha_{rt}c}{2\pi\tilde{n}L_{rt}} \tag{7.8}$$

F is the cavity finesse, which is approximated as $2\pi/\alpha_{rt}$ for the second equality, and α_{rt} is the power loss from the cavity during one round trip. The finesse is mostly determined by the reflectivity of the input and output couplers of the cavity. L_{rt} is the length of the cavity for one round trip, and $\tilde{n}$ is the average refractive index inside the cavity. For CE-SPDC, T_e is inversely proportional to the cavity mode linewidth.

While the maximum ETPA cross-section in Fig. 7.2 occurs around T_e = 10 ps, any T_e within the range of 2.5-75 ps would yield a cross-section on the order of 10^{-17} cm^2/molecule, which is within an order of magnitude of the OPA cross-section and an order of magnitude larger than the cross-sections with T_e < 250 fs where ETPA is commonly performed today. A cavity mode linewidth on the order of 10 ps is relatively large for a cavity, so a low finesse and short cavity length would be needed. Assuming a power loss of 90 % per round trip from an input mirror reflectivity of 99 % and an output coupler with 10 % reflectivity, the finesse would be ~7. For a short path length SPDC crystal such as a 0.5 mm BBO, $\tilde{n} \approx 1$. A Fabre-Perot cavity would need a mirror separation of 8.5 mm to then achieve a mode linewidth of 14 GHz, or T_e = 70 ps.

CE-SPDC has the advantage that the number of photons created is enhanced compared to free-space SPDC. The SPDC frequencies resonant with the cavity create a standing wave and constructively interfere to increase their intensity. Therefore, even though free-space SPDC and CE-SPDC can be passively filtered to the same bandwidth, the CE-SPDC would have more photons at that same bandwidth. The cavity can be resonant with just the signal photon (singly-resonant oscillator, or SRO) or both the signal and idler photons (doubly-resonant oscillator, or DRO). DRO provides a higher enhancement in the photon rate per mode since both photons will experience constructive interference. Degenerate SPDC, as is needed for the proposed experiment, will naturally be doubly-resonant since both photons have the same central frequency. The enhancement in the pairs/s of SPDC bandwidth for DRO SPDC compared to free-space SPDC is a factor of the finesse squared. In the free-space Type-I SPDC setup used in this work, filtering the SPDC to 14 GHz would leave an SPDC rate of 1.6x10^2 pairs/s. The DRO finesse of 7 gives an x49 enhancement in the count rate, yielding 7.8x10^3 pairs/s in each cavity mode. However, many modes of the cavity are excited as long as they are within the phase-matching bandwidth of the

SPDC crystal. The frequency spacing between the modes, known as the *free spectral range*, $\Delta\nu_{fsr}$, is given by:

$$\Delta\nu_{fsr} = \Delta\nu_{cav}F \tag{7.9}$$

The free spectral range for this case would be 98 GHz. Filtering the CE-SPDC output with a simple 10 nm bandwidth bandpass filter leaves ~47 modes, resulting in a total SPDC pair rate of $3.7\text{x}10^5$ pairs/s. Using a broader bandpass filter can increase the pair rate more. While this method of creating ps T_e is possible, such a short cavity would be challenging to stabilize. Additionally, achieving T_e = 70 ps is already pushing the technique to its constraints. To achieve T_e = 10 ps, the cavity length would have to be 1 mm. Configuring such an extremely short cavity to keep the SPDC crystal aligned inside and keep the cavity length stabilized would be very difficult.

Another method for creating ps T_e SPDC with a higher pair rate is using periodically poled (pp) SPDC. In this technique, longer crystals ($L \geq 10$ mm) made from materials with higher nonlinear susceptibilities compared to BBO, commonly potassium titanyl phosphate (KTP) or lithium niobate (LN), are used to generate SPDC.[43-45] The longer crystals and higher nonlinearities can greatly increase the generated SPDC rate. However, these materials do not have the proper refractive indices to phase-match the SPDC. If a pump beam were to enter a crystal of these materials without periodic poling, some SPDC could be generated at the front of the crystal, but as the signal and idler fields become out of phase with the pump field due to the lack of phase-matching, destructive interference destroys the SPDC fields. As the pump field continues propagating through the crystal, signal and idler fields can be generated again once they are back in phase with the pump, but this cycle of destructive interference will occur again once the fields are out of phase. To obtain any SPDC at all, the crystal would have to be cut to a very precise length on a μm scale. Such a short crystal would provide very few photons/s, not to mention it would be technically challenging to make and very fragile.

To counteract the lack of phase-matching in the materials, the crystals can have the direction of their nonlinearity flipped at periodic lengths along the crystal. This length, called the *poling period*, Λ, is chosen so that when the pump field becomes out of phase with the signal and idler fields, the flipped nonlinearity will allow SPDC to be generated from these out of phase fields. When the fields are in phase again, the nonlinearity flips back, and so on throughout the whole crystal. The generated signal and idler fields throughout the crystal can then constructively

interfere to yield a large photon rate exiting the crystal. This process is known as *quasi-phase-matching*. The phase-mismatch for quasi-phase-matching is given as:[46]

$$\Delta\vec{k} = \vec{k}_p - \vec{k}_s - \vec{k}_i - \frac{2\pi}{\Lambda} \tag{7.10}$$

The longer crystals and higher nonlinearity of ppKTP and ppLN allow for much more efficient SPDC generation compared to thin BBO crystals. For a 30 mm ppKTP crystal, Type-0 SPDC can be generated at a rate of 352 pairs/s/mW per GHz of SPDC bandwidth.[43] The Type-0 SPDC from this crystal will naturally have a bandwidth of ~30 nm, but filtering it with a monochromator or volume bragg grating to a bandwidth of 14 GHz would yield $4.9\text{x}10^5$ pairs/s of T_e = 70 ps SPDC at 100 mW of pump power. Additionally, unlike the CE-SPDC, the ppSPDC pair rate increases with increasing bandwidth. To achieve the maximum ETPA cross-section at T_e = 10 ps, a 100 GHz bandwidth is needed. For 100 mW of pump power of the ppKTP, a pair rate of $3.5\text{x}10^6$ pair/s is obtained. This pair rate is larger than the free-space BBO with T_e = 100 fs pair rate but with a much smaller SPDC bandwidth to achieve the smallest possible A_e. This pair rate is plenty to excite a molecule and measure its ETPA signal. All of the pair rates for each SPDC source at various T_e values are summarized in Table 7.1.

Table 7.1 Pairs/s rates at various T_e for 3 SPDC sources: free-space BBO, cavity-enhanced BBO, and free-space ppKTP.

SPDC source	**Pairs/s at T_e = 100 fs**	**Pairs/s at T_e = 10 ps**	**Pairs/s at T_e = 70 ps**
Free-space BBO	$1.1\text{x}10^5$	$1.1\text{x}10^3$	$1.6\text{x}10^2$
Cavity-enhanced BBO	-	-	$\geq 3.7\text{x}10^5$
Free-space ppKTP	$3.5\text{x}10^8$	$3.5\text{x}10^6$	$4.9\text{x}10^5$

For the purposes of the proposed experiment of measuring ETPA with T_e = 10 ps degenerate Type-I/Type-0 SPDC, the best method is to use free-space ppSPDC with passive filtering with a monochromator or volume bragg grating to the necessary bandwidth. The much higher pair rates of ppSPDC compared to SPDC from a thin BBO crystal compensates for the passive filtering removing many photons. It is still an open question whether other molecules may have maximum cross-sections at other T_e values. If so, particularly if the maxima are at T_e > 10 ps, the CE-SPDC technique would become the more favorable technique since the pair rate from CE-

SPDC increases with increasing T_e, compared to the decreasing pair rate with increasing T_e from free-space ppSPDC.

7.5 Conclusion

With ps-scale T_e entangled photons easily achievable, the maximum σ_e in Fig. 7.2 can be reached today. A_e at this maximum σ_e is more than 3 orders of magnitude smaller than A_e at the fs-scale T_e (see supporting information). This much smaller A_e would improve the spatial resolution of ETPA microscopy by more than 3 orders of magnitude, while also yielding brighter images due to the enhanced σ_e.[22] This enhancement would also provide chemists the ability to measure nonlinear optical signals, which are notoriously much weaker than linear signals, with the same absorption efficiency as linear OPA. Chemists could then more easily identify, for example, molecules with efficient charge transfer for solar cells or OLEDs.

Most interestingly, ETPA at ps-scale T_e provides a new opportunity to control chemical reactions that require intermediate conversion processes with fs-ps times, such as an isomerization, proton transfer, or intersystem crossing to a triplet state. A primary example is the photochemical reactivity of T_n triplet states in green fluorescence proteins (GFPs).[47, 48] With ps T_e ETPA, the first photon would excite the GFP to the S_1 state, allow the population to cross to the T_1 state, and then the second photon would excite the GFP to the T_n state. Entangled photons are particularly unique in that they can provide high frequency resolution simultaneously with the required temporal resolution.[49] Classical ps laser pulses are Fourier limited, so they would lack frequency resolution in this photochemical reaction. Since excited states become closer in energy as the energy increases, maintaining high frequency resolution with the temporal resolution is crucial for control over the photochemical reaction.

References

1. Dayan, B.; Pe'er, A.; Friesem, A. A.; Silberberg, Y., Two Photon Absorption and Coherent Control with Broadband Down-Converted Light. *Physical Review Letters* **2004,** *93* (2), 023005.
2. Dayan, B.; Pe'er, A.; Friesem, A. A.; Silberberg, Y., Nonlinear Interactions with an Ultrahigh Flux of Broadband Entangled Photons. *Physical Review Letters* **2005,** *94* (4), 043602.
3. Lee, D.-I.; Goodson, T., Entangled Photon Absorption in an Organic Porphyrin Dendrimer. *Journal of Physical Chemistry B* **2006,** *110* (51), 25582-25585.
4. Javanainen, J.; Gould, P. L., Linear intensity dependence of a two-photon transition rate. *Physical Review A* **1990,** *41* (9), 5088-5091.
5. Harpham, M. R.; Süzer, Ö.; Ma, C.-Q.; Bäuerle, P.; Goodson, T., Thiophene Dendrimers as Entangled Photon Sensor Materials. *Journal of the American Chemical Society* **2009,** *131* (3), 973-979.
6. Jung, Y. O.; Lee, J. H.; Kim, J.; Schmidt, M.; Moffat, K.; Šrajer, V.; Ihee, H., Volume-conserving trans–cis isomerization pathways in photoactive yellow protein visualized by picosecond X-ray crystallography. *Nature Chemistry* **2013,** *5* (3), 212-220.
7. Zheng, J.; Kwak, K.; Xie, J.; Fayer, M. D., Ultrafast Carbon-Carbon Single-Bond Rotational Isomerization in Room-Temperature Solution. *Science* **2006,** *313* (5795), 1951.
8. Zhang, Y.; de La Harpe, K.; Beckstead, A. A.; Improta, R.; Kohler, B., UV-Induced Proton Transfer between DNA Strands. *Journal of the American Chemical Society* **2015,** *137* (22), 7059-7062.
9. Stoner-Ma, D.; Jaye, A. A.; Matousek, P.; Towrie, M.; Meech, S. R.; Tonge, P. J., Observation of Excited-State Proton Transfer in Green Fluorescent Protein using Ultrafast Vibrational Spectroscopy. *Journal of the American Chemical Society* **2005,** *127* (9), 2864-2865.
10. Li, T.; Hassanali, A. A.; Kao, Y.-T.; Zhong, D.; Singer, S. J., Hydration Dynamics and Time Scales of Coupled Water−Protein Fluctuations. *Journal of the American Chemical Society* **2007,** *129* (11), 3376-3382.
11. Pham, V.-T.; Penfold, T. J.; van der Veen, R. M.; Lima, F.; El Nahhas, A.; Johnson, S. L.; Beaud, P.; Abela, R.; Bressler, C.; Tavernelli, I.; Milne, C. J.; Chergui, M., Probing the Transition from Hydrophilic to Hydrophobic Solvation with Atomic Scale Resolution. *Journal of the American Chemical Society* **2011,** *133* (32), 12740-12748.
12. Kim, S.; Lim, M., Picosecond Dynamics of Ligand Interconversion in the Primary Docking Site of Heme Proteins. *Journal of the American Chemical Society* **2005,** *127* (16), 5786-5787.
13. Kim, S.; Lim, M., Protein Conformation-Induced Modulation of Ligand Binding Kinetics: A Femtosecond Mid-IR Study of Nitric Oxide Binding Trajectories in Myoglobin. *Journal of the American Chemical Society* **2005,** *127* (25), 8908-8909.

14. Fei, H.-B.; Jost, B. M.; Popescu, S.; Saleh, B. E. A.; Teich, M. C., Entanglement-Induced Two-Photon Transparency. *Physical Review Letters* **1997,** *78* (9), 1679-1682.
15. Saleh, B. E. A.; Jost, B. M.; Fei, H.-B.; Teich, M. C., Entangled-Photon Virtual-State Spectroscopy. *Physical Review Letters* **1998,** *80* (16), 3483-3486.
16. Burdick, R. K.; Varnavski, O.; Molina, A.; Upton, L.; Zimmerman, P.; Goodson, T., Predicting and Controlling Entangled Two-Photon Absorption in Diatomic Molecules. *The Journal of Physical Chemistry A* **2018,** *122* (41), 8198-8212.
17. Kang, G.; Nasiri Avanaki, K.; Mosquera, M. A.; Burdick, R. K.; Villabona-Monsalve, J. P.; Goodson, T.; Schatz, G. C., Efficient Modeling of Organic Chromophores for Entangled Two-Photon Absorption. *Journal of the American Chemical Society* **2020,** *142* (23), 10446-10458.
18. Mukamel, S.; Freyberger, M.; Schleich, W.; Bellini, M.; Zavatta, A.; Leuchs, G.; Silberhorn, C.; Boyd, R. W.; Sánchez-Soto, L. L.; Stefanov, A.; Barbieri, M.; Paterova, A.; Krivitsky, L.; Shwartz, S.; Tamasaku, K.; Dorfman, K.; Schlawin, F.; Sandoghdar, V.; Raymer, M.; Marcus, A.; Varnavski, O.; Goodson, T.; Zhou, Z.-Y.; Shi, B.-S.; Asban, S.; Scully, M.; Agarwal, G.; Peng, T.; Sokolov, A. V.; Zhang, Z.-D.; Zubairy, M. S.; Vartanyants, I. A.; del Valle, E.; Laussy, F., Roadmap on quantum light spectroscopy. *Journal of Physics B: Atomic, Molecular and Optical Physics* **2020,** *53* (7), 072002.
19. de J León-Montiel, R.; Svozilík, J.; Salazar-Serrano, L. J.; Torres, J. P., Role of the spectral shape of quantum correlations in two-photon virtual-state spectroscopy. *New Journal of Physics* **2013,** *15* (5), 053023.
20. Nakanishi, T.; Kobayashi, H.; Sugiyama, K.; Kitano, M., Full Quantum Analysis of Two-Photon Absorption Using Two-Photon Wave Function: Comparison of Two-Photon Absorption with One-Photon Absorption. *Journal of the Physical Society of Japan* **2009,** *78* (10), 104401.
21. Varnavski, O.; Pinsky, B.; Goodson, T., Entangled Photon Excited Fluorescence in Organic Materials: An Ultrafast Coincidence Detector. *Journal of Physical Chemistry Letters* **2017,** *8* (2), 388-393.
22. Varnavski, O.; Goodson, T., Two-Photon Fluorescence Microscopy at Extremely Low Excitation Intensity: The Power of Quantum Correlations. *Journal of the American Chemical Society* **2020,** *142* (30), 12966-12975.
23. Zeilinger, A., Experiment and the foundations of quantum physics. *Reviews of Modern Physics* **1999,** *71* (2), S288-S297.
24. Yin, L.; Li, J.; Zhai, W.; Xia, M.; Hu, Y.; Zheng, X., Analysis of the Spatial Properties of Correlated Photon in Collinear Phase-Matching. *Photonics* **2021,** *8* (1).
25. Villabona-Monsalve, J. P.; Burdick, R. K.; Goodson, T., Measurements of Entangled Two-Photon Absorption in Organic Molecules with CW-Pumped Type-I Spontaneous Parametric Down-Conversion. *The Journal of Physical Chemistry C* **2020,** *124* (44), 24526-24532.
26. Yoon-Ho, K., Measurement of one-photon and two-photon wave packets in spontaneous parametric downconversion. *Journal of the Optical Society of America B* **2003,** *20* (9), 1959-1966.
27. Campos, R. A.; Saleh, B. E. A.; Teich, M. C., Fourth-order interference of joint single-photon wave packets in lossless optical systems. *Physical Review A* **1990,** *42* (7), 4127-4137.
28. Rubin, M. H.; Klyshko, D. N.; Shih, Y. H.; Sergienko, A. V., Theory of two-photon entanglement in type-II optical parametric down-conversion. *Physical Review A* **1994,** *50* (6), 5122-5133.

29. The Effect of Dispersion on Ultrashort Pulses. https://www.newport.com/n/the-effect-of-dispersion-on-ultrashort-pulses (accessed April 19, 2021).
30. Joobeur, A.; Saleh, B. E. A.; Larchuk, T. S.; Teich, M. C., Coherence properties of entangled light beams generated by parametric down-conversion: Theory and experiment. *Physical Review A* **1996,** *53* (6), 4360-4371.
31. Joobeur, A.; Saleh, B. E. A.; Teich, M. C., Spatiotemporal coherence properties of entangled light beams generated by parametric down-conversion. *Physical Review A* **1994,** *50* (4), 3349-3361.
32. Oka, H., Two-photon absorption by spectrally shaped entangled photons. *Physical Review A* **2018,** *97* (3), 033814.
33. Oka, H., Enhanced vibrational-mode-selective two-step excitation using ultrabroadband frequency-entangled photons. *Physical Review A* **2018,** *97* (6), 063859.
34. Dixon, J. M.; Taniguchi, M.; Lindsey, J. S., PhotochemCAD 2: A Refined Program with Accompanying Spectral Databases for Photochemical Calculations¶. *Photochemistry and Photobiology* **2005,** *81* (1), 212-213.
35. Slattery, O.; Ma, L.; Zong, K.; Tang, X., Background and Review of Cavity-Enhanced Spontaneous Parametric Down-Conversion. *Journal of Research of the National Institute of Standards and Technology* **2019,** *124*, 1-18.
36. Tomoyuki, H., Quantum key distribution with mode-locked two-photon states. *2015 Conference on Lasers and Electro-Optics Pacific Rim* **2015**, 27P_41.
37. Fekete, J.; Rieländer, D.; Cristiani, M.; de Riedmatten, H., Ultranarrow-Band Photon-Pair Source Compatible with Solid State Quantum Memories and Telecommunication Networks. *Physical Review Letters* **2013,** *110* (22), 220502.
38. Kuklewicz, C. E.; Wong, F. N. C.; Shapiro, J. H., Time-Bin-Modulated Biphotons from Cavity-Enhanced Down-Conversion. *Physical Review Letters* **2006,** *97* (22), 223601.
39. Ou, Z. Y.; Lu, Y. J., Cavity Enhanced Spontaneous Parametric Down-Conversion for the Prolongation of Correlation Time between Conjugate Photons. *Physical Review Letters* **1999,** *83* (13), 2556-2559.
40. Polzik, J. S. N.-N. a. B. M. N. a. H. T. a. A. I. V. a. E. S., High purity bright single photon source. *Optics Express* **2007,** *15* (13), 7940-7949.
41. Bao, X.-H.; Qian, Y.; Yang, J.; Zhang, H.; Chen, Z.-B.; Yang, T.; Pan, J.-W., Generation of Narrow-Band Polarization-Entangled Photon Pairs for Atomic Quantum Memories. *Physical Review Letters* **2008,** *101* (19), 190501.
42. Liu, J.; Liu, J.; Yu, P.; Zhang, G., Sub-megahertz narrow-band photon pairs at 606 nm for solid-state quantum memories. *APL Photonics* **2020,** *5* (6), 066105.
43. Byrdin, M.; Duan, C.; Bourgeois, D.; Brettel, K., A Long-Lived Triplet State Is the Entrance Gateway to Oxidative Photochemistry in Green Fluorescent Proteins. *Journal of the American Chemical Society* **2018,** *140* (8), 2897-2905.
44. Mohr, M. A.; Kobitski, A. Y.; Sabater, L. R.; Nienhaus, K.; Obara, C. J.; Lippincott-Schwartz, J.; Nienhaus, G. U.; Pantazis, P., Rational Engineering of Photoconvertible Fluorescent Proteins for Dual-Color Fluorescence Nanoscopy Enabled by a Triplet-State Mechanism of Primed Conversion. *Angewandte Chemie International Edition* **2017,** *56* (38), 11628-11633.
45. Schlawin, F.; Dorfman, K. E.; Mukamel, S., Entangled Two-Photon Absorption Spectroscopy. *Accounts of Chemical Research* **2018,** *51* (9), 2207-2214.

7.6 Supporting Information

7.6.1 Origin and Derivation of Entanglement Area

When the location of the signal photon in the transverse plane is measured, the transverse location of the idler photon is also known to within an uncertainty determined by the entanglement area, A_e.[50] The origin of A_e is an uncertainty in the emission angles of the idler photon from the SPDC crystal, shown in Fig. 7.4.[30, 31]

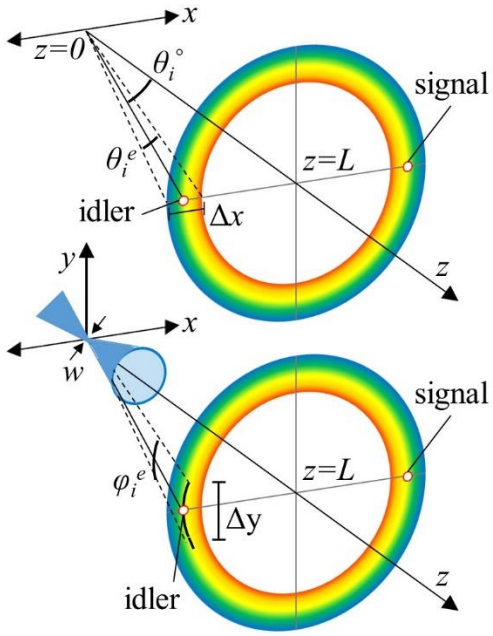

Fig. 7.4. Emission angles and their uncertainties of Type-I SPDC from a crystal with length L along the pump beam propagation axis (z-axis).

The idler photon is emitted in the x-z plane at the central polar angle θ_i° with an uncertainty, or polar entanglement angle, θ_i^e. The polar entanglement angle creates uncertainty of the photon location in the x-z plane, Δx. The uncertainty in the y-direction, Δy, comes from the azimuthal entanglement angle, φ_i^e. This angle originates from the divergence angle of the focused pump beam with waist w. A_e is defined by the product of uncertainties Δx and Δy.[50]

While the azimuthal entanglement angle is easily seen from the pump divergence angle, where Δy is proportional to $1/w$, the polar entanglement angle has a more complicated origin. When SPDC photons are created inside of the crystal, they are in a superposition of frequencies, which originates from the phase mismatch of the pump and SPDC photons' wave vectors along the z-axis, Δk_z. It is well known that expanding Δk_z as a Taylor series results in the approximation:[26]

$$\Delta k_z \approx -\nu D - \frac{\nu^2}{2} D'' \tag{7.8}$$

Here, ν is the detuning frequency from the central frequency of the SPDC photons, D is the difference in inverse group velocity of the signal and idler, and D'' is the group velocity dispersion (GVD) of the photons. Higher order terms in ν are negligible. For Type-II SPDC (and non-degenerate Type-I/-0 SPDC), the signal and idler have different group velocities, so D is non-zero, and the second-order term is negligible. For degenerate Type-I/-0 SPDC (which we will refer to as "Type-I" from here for brevity), the signal and idler have the same group velocity, so D vanishes and only the second-order term is left. Thus, the phase mismatch for Type-II SPDC depends linearly on the SPDC frequency, while the phase mismatch for Type-I SPDC depends quadratically on the SPDC frequency.

For Type-II SPDC, each frequency of the idler photon travels at a different polar angle inside the crystal due to the different refractive indices. Thus, the frequencies are spread out in space when they exit the crystal. Because the idler has an uncertainty in its frequency (the bandwidth of its frequency superposition), the photon also has an uncertainty in its polar emission angle, i.e. the polar entanglement angle. Decreasing the frequency uncertainty also reduces the polar entanglement angle linearly. For Type-I SPDC, each frequency of the idler is dispersed inside the crystal due to GVD. The GVD, which is second-order dispersion, then determines the uncertainty in the polar emission angle. Reducing the frequency uncertainty thus decreases the polar entanglement angle quadratically.

One way to change the polar entanglement angle is by changing the crystal length, L, which was shown in a paper from Joobeur et. al.[30] They showed that by increasing L, the polar entanglement angle decreases, which would decrease A_e. Increasing L has the effect of decreasing the SPDC bandwidth, and so decreasing the bandwidth should also decrease the polar entanglement angle and A_e.[26] In our experiments, we keep L constant and decrease the SPDC bandwidth with frequency bandpass filters and a monochromator. For Type-I SPDC, since the frequency uncertainty is dependent on second-order dispersion, the uncertainty should be related to the filter or monochromator's bandwidth (σ_f) squared. The relationship between A_e and the bandwidth can be represented simply (taking the Δy contribution to be independent of σ_f) as:

$$A_e \propto \theta_i^e \propto \alpha \sigma_f^2 + A_d \tag{7.9}$$

α is a coefficient to be solved for by fitting experimental results, and here we include a constant parameter A_d in this formula to account for the fact that A_e cannot be smaller (at least for classical light) than the diffraction limited area. As mentioned in the main manuscript, A_d should be a number on the order of $(\lambda/2)^2=1.6\text{x}10^{-9}\text{cm}^2$.

While eq. 7.9 shows that A_e decreases as σ_f decreases, it also suggests that A_e would increase as long as σ_f continues to increase. This latter point, however, is not physically realistic since the SPDC has an initial bandwidth determined by the SPDC crystal length before the photons are filtered further downstream. The SPDC bandwidth, and thus A_e, cannot be bigger than that initially formed in the SPDC crystal. We can account for this upper limit with the following phenomenological modification to eq. 7.9:

$$A_e \propto \theta_i^e \propto \left(\frac{\alpha}{\sigma_f^2}+\frac{\beta}{\sigma_L^2}\right)^{-1} + A_d \tag{7.10}$$

σ_L is the SPDC bandwidth defined by the crystal with length L, and it has a coefficient β to be solved for. Eq. 7.10 is a simple way to represent that when $\sigma_f << \sigma_L$, the second term is negligible, and A_e is determined by the filter but subject to a diffraction limit. When $\sigma_f >> \sigma_L$, the first term is negligible, and A_e is determined by the SPDC crystal. Eq. 7.10 was used in eq. 7.1 to fit with the Type-I experimental data in Fig. 7.1. The coefficients α and β were the fitting parameters. With the coefficients, A_e was calculated with eq. 7.10, and the upper and lower bounds in our experiment are reported in the main text.

For Type-II SPDC, the frequency uncertainty is determined by first-order dispersion, and thus is related to the SPDC bandwidth linearly. Following along the same lines as eq. 7.9-7.10 for Type-I, but keeping A_e proportional to the frequency bandwidth linearly, a similar expression for A_e when using Type-II SPDC can be used:

$$A_e \propto \theta_i^e \propto \left(\frac{\gamma}{\sigma_f}+\frac{\zeta}{\sigma_L}\right)^{-1} + A_d \tag{7.11}$$

γ and ζ are the coefficients, which were calculated by using eq. 7.11 in eq. 7.1 and fitting with the Type-II experimental data in Fig. 7.1 of the main text. The upper and lower A_e are reported in the main text.

Using the fitted parameters for eq. 7.11, the range of A_e from its minimum to maximum value for both SPDC Types are plotted in Fig. 7.5.

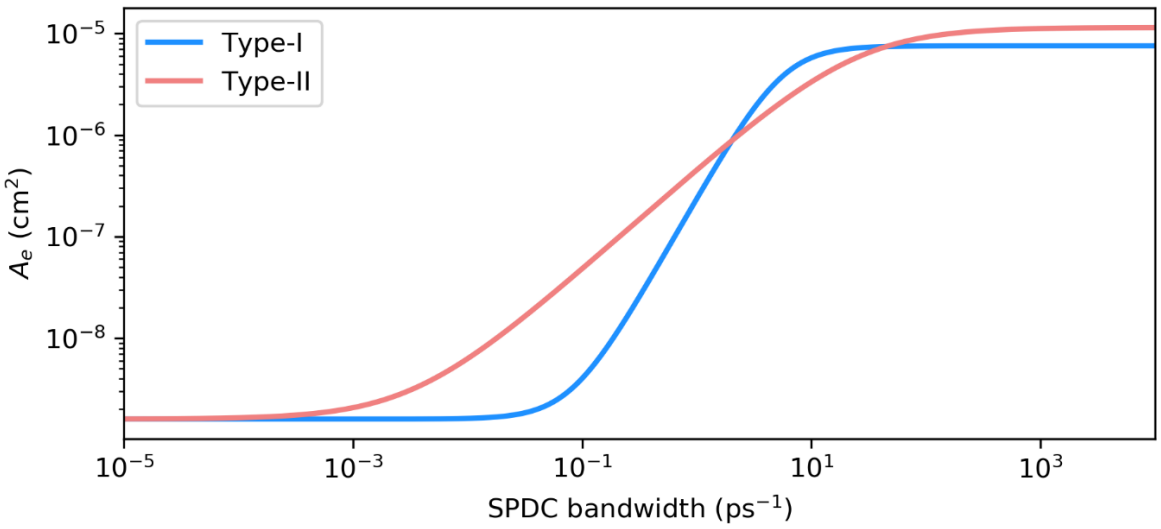

Figure 7.5. A_e vs the SPDC bandwidth for Type-I and Type-II SPDC.

7.6.2 ETPA Cross-Section vs T_e for Sinc and Gaussian Function SPDC Spectra with and without Dispersion

The ETPA cross-section vs T_e was calculated using eq. 7.1 from the main text for three cases: increasing A_e with increasing σ_f using eq. 7.10 (7.11) for Type-I (Type-II) SPDC, constant A_e that has been assumed historically, and decreasing A_e for comparison. In the calculation, we use the model of a strong TPA chromophore.[51] We consider the Q band in ZnTPP at 550 nm as the most dominant intermediate state due to its smallest detuning energy.[52] Calculating the linewidth of intermediate excited states in molecules can be very challenging, so using an upper limit of k_j = 0.1 eV for organic chromophores in solution is reasonable and standard practice.[53] The TDM product in eq. 1 was estimated to be 16.1 D^2 using the classical TPA cross-section of ZnTPP and the classical TPA cross-section equation.[16, 54] These parameters were used for the calculations in Fig. 7.1-7.2 and Fig. 7.6-7.7. In Fig. 7.6, a Gaussian SPDC spectrum was used, and both the cases with and without dispersion were used to calculate T_e (eq. 7.3) are shown. The sinc spectra (Fig. 7.7) yield the well-known oscillations when T_e < ~500 fs,[14] but the overall trend as T_e increases is the same regardless of the SPDC spectral function. Two important features of Figs. 7.6 and 7.7 are: (1) For the results that include dispersion, there are two branches to the cross-sections (the upper branch corresponding to small σ_f and the lower branch for high σ_f) when plotted as a function of T_e for both Type-I and Type-II, with the two branches coming together at T_e slightly below 100 fs;

(2) For the upper branch, the Type-I cross-section increases linearly with increasing $1/\sigma_f$ as σ_f goes toward 0.1 ps^{-1}, where A_e is limited by the diffraction area A_d. At this bandwidth, the Type-I cross-section reaches a maximum, and the Type-II cross-section plateaus before decreasing.

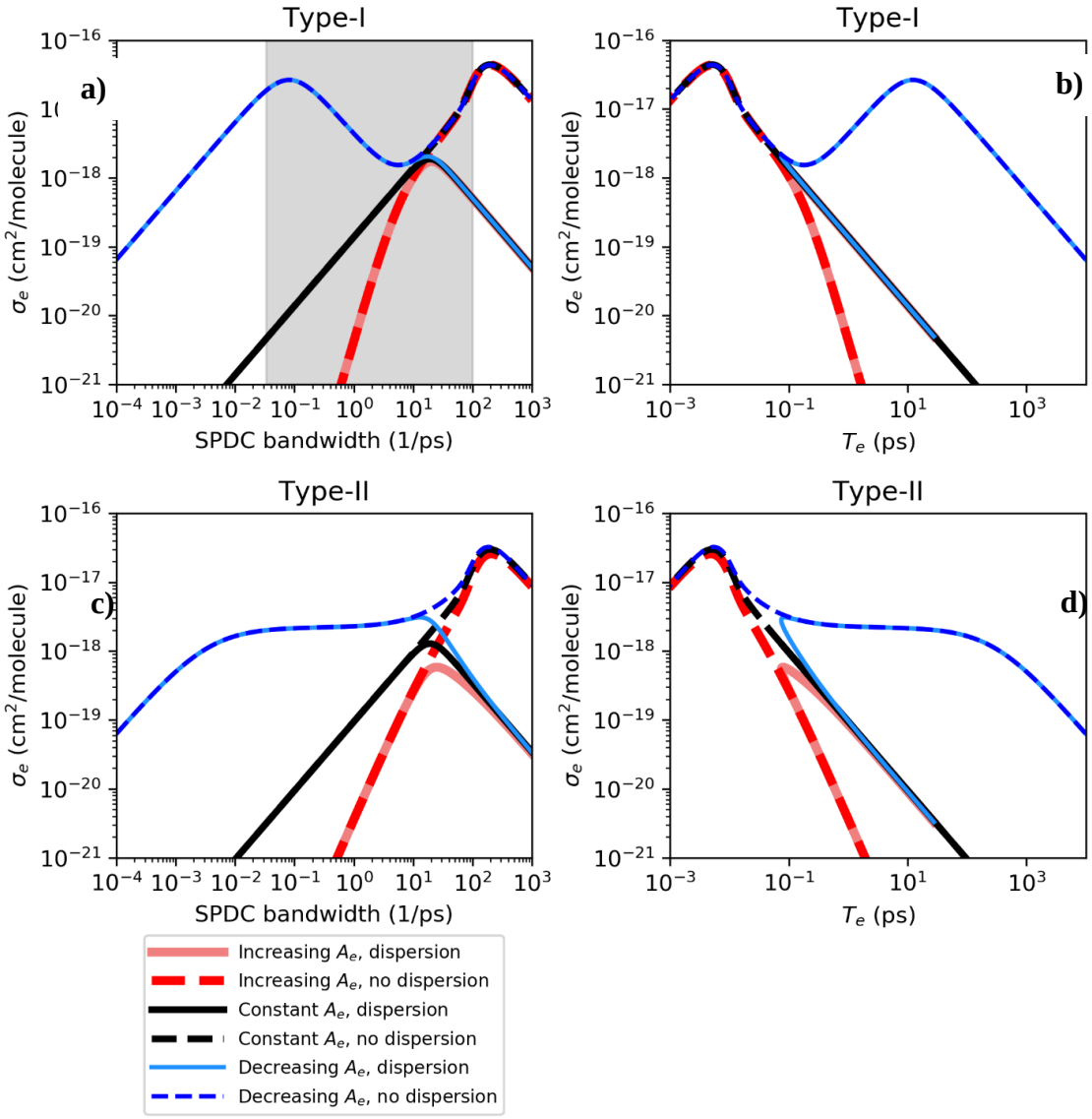

Figure 7.6. a) Type-I ETPA cross-section, σ_e, vs σ_f using Gaussian SPDC spectra for increasing A_e (red), constant A_e (black), and decreasing A_e (blue) with (solid) and without (dotted) dispersion. The shaded region is the bandwidth range that is shown in Fig. 7.2; **b)** Same as **(a)** but with the x-axis converted to T_e; **c)** Type-II σ_e vs σ_f using Gaussian SPDC spectra for increasing A_e (red), constant A_e (black), and decreasing A_e (blue) with (solid) and without (dotted) dispersion. **d)** Same as **(c)** but with the x-axis converted to T_e; The same parameters from Fig. 1 of the main text are used here.

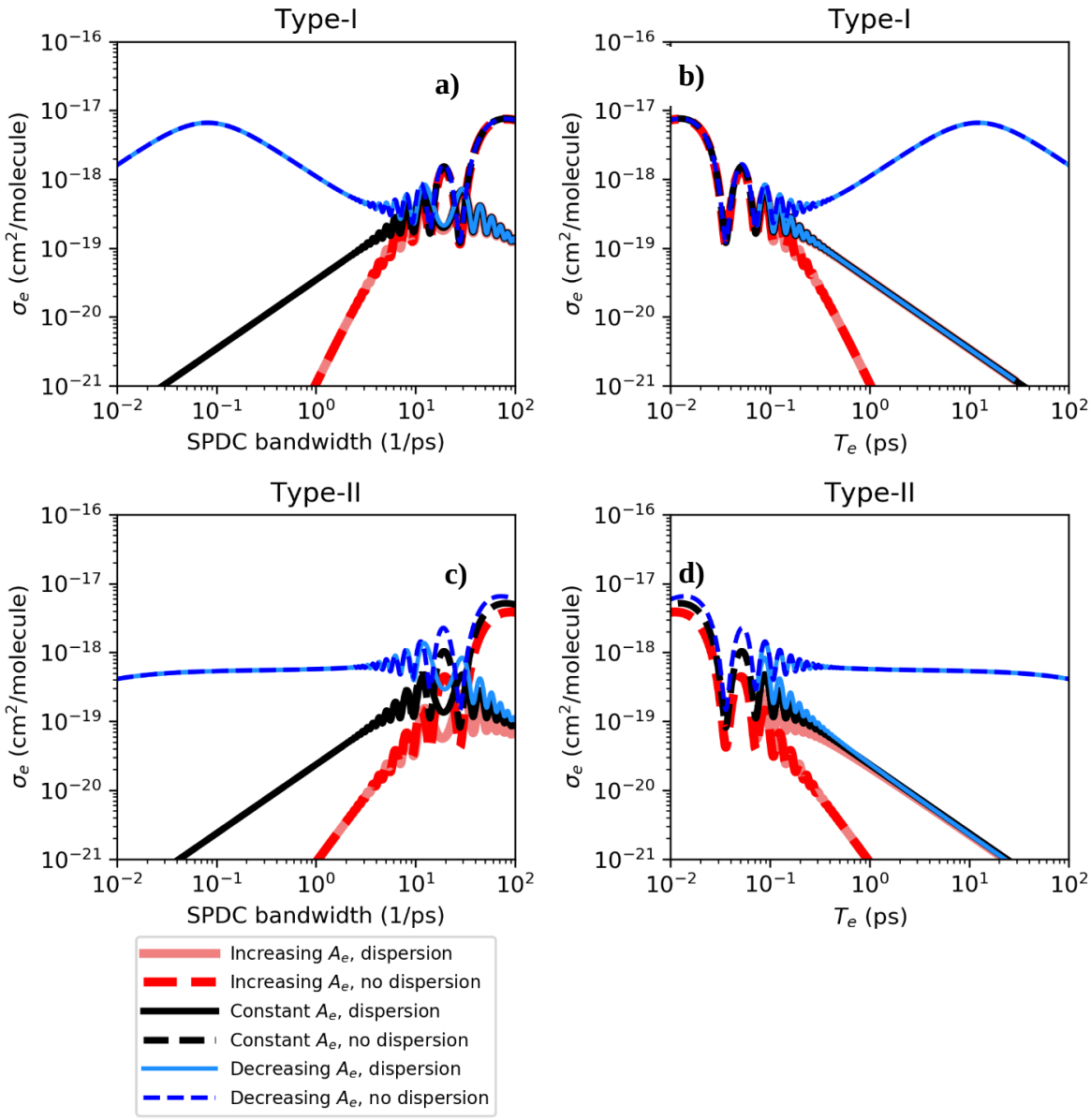

Figure 7.7. a) Type-I ETPA cross-section, σ_e, vs σ_f using sinc SPDC spectra for increasing A_e (red), constant A_e (black), and decreasing A_e (blue) with (solid) and without (dotted) dispersion. The shaded region is the bandwidth range that is shown in Fig. 7.2; **b)** Same as **(a)** but with the x-axis converted to T_e; **c)** Type-II σ_e vs σ_f using sinc SPDC spectra for increasing A_e (red), constant A_e (black), and decreasing A_e (blue) with (solid) and without (dotted) dispersion. **d)** Same as **(c)** but with the x-axis converted to T_e; The same parameters from Fig. 1 of the main text are used here.

7.6.3 Experimental Details

Our experimental setup uses a 405 nm CW laser with maximum SPDC pump power of ~150 mW. The pump beam is focused into a Type-I or Type-II SPDC crystal cut for

degenerate, non-collinear phase-matching. After removing the residual pump beam with a dichroic mirror and longpass filters, the SPDC is sent through one of several bandpass filters with different bandwidths (10, 30, and 80 nm) or a monochromator with variable bandwidth (2, 2.5, 3, 4, and 5 nm) to alter the SPDC spectral bandwidth. After filtering, the SPDC is focused into a cuvette, and the transmitted entangled pairs are separated with a knife-edge mirrored prism. Coincidence counts were measured with single-photon detecting APDs with a 5 ns coincidence window. The difference in the transmitted coincidence counts for the cuvette filled with pure solvent vs the sample solution (~20 μM zinc tetraphenylporphyrin, ZnTPP, in toluene) gives the ETPA rate. Calculation of the ETPA cross-section from this rate was completed as reported in previous works:[25, 54]

$$\sigma_e = \frac{m}{lcN_A} \tag{7.12}$$

m is the slope of the linear fit for ETPA rate vs input rate, l is the cuvette length, c is the concentration, and N_A is Avogradro's number. The plots of ETPA rate in ZnTPP vs input rate are given in Fig. 7.8-7.9. Since reducing the SPDC bandwidth also reduces the input rate in a passive filtering scheme used here, the input rates were normalized for each bandwidth for easy comparison of the slopes. The y-axis was normalized so that the slope for each bandwidth is the same as what it was before normalization.

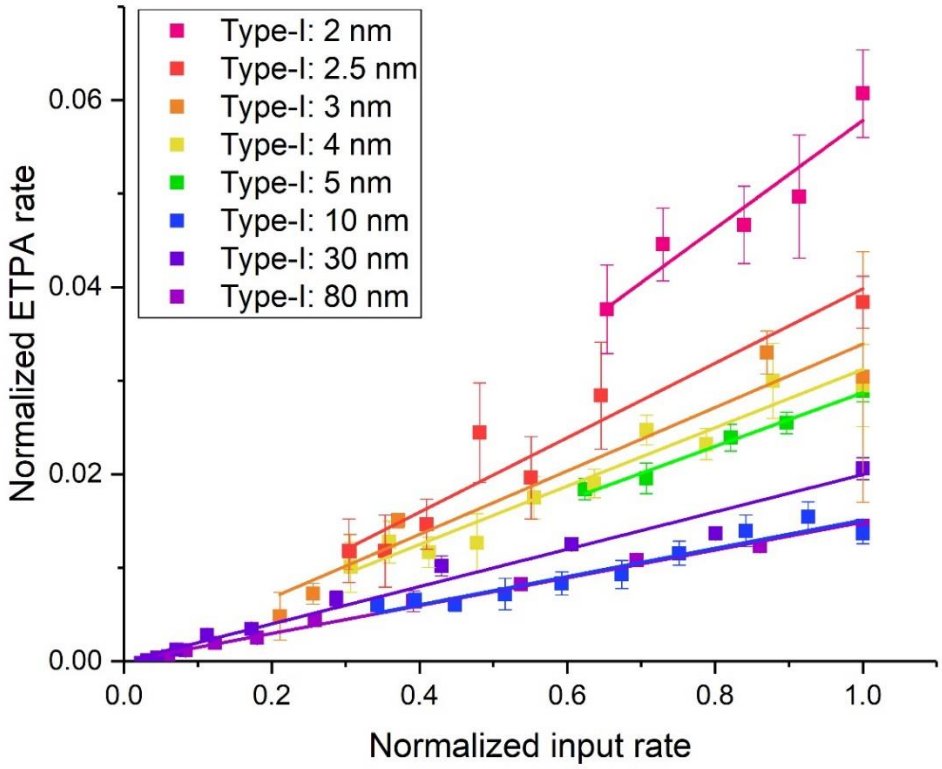

Figure 7.8. Type-I ETPA rate in ZnTPP vs input rate for all SPDC bandwidths.

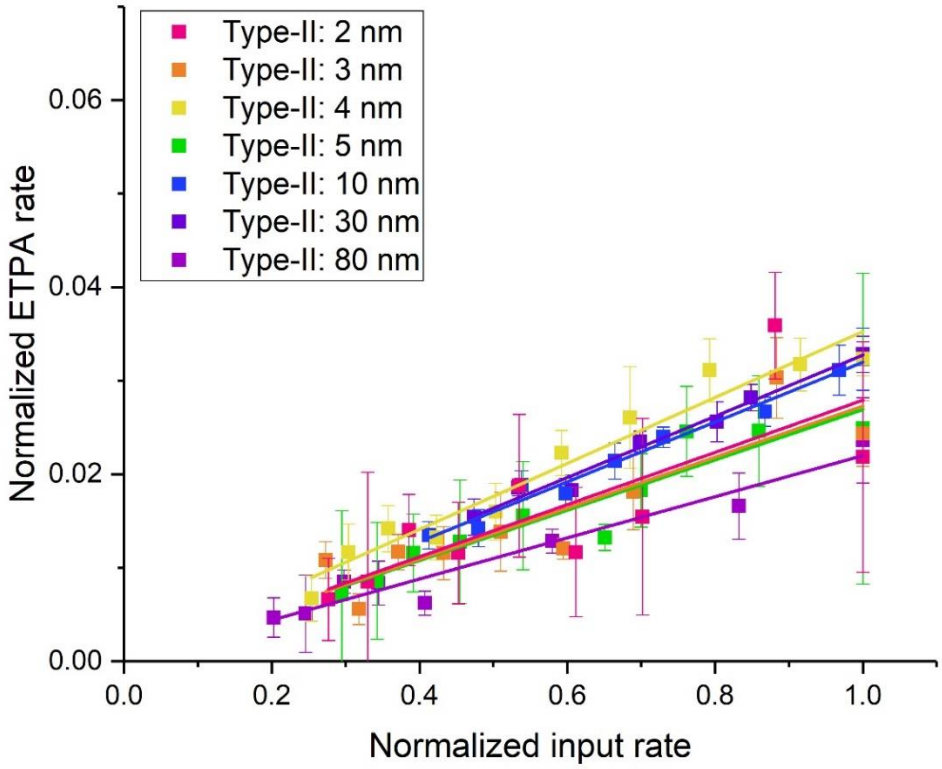

Figure 7.9. Type-II ETPA rate in ZnTPP vs input rate for all SPDC bandwidths.

The dependence of the SPDC attenuation percentage (slope of ETPA rate vs input rate) on the SPDC bandwidth, or T_e, shows that the SPDC attenuation is due to ETPA and not other linear optical processes, such as one-photon absorption or scattering. These other optical processes would not depend on T_e. Additionally, the different ETPA cross-section dependences vs σ_f (or T_e) for Type-I vs Type-II SPDC also show that the measured signal is not due to other optical processes since for a one-photon process, Type-I and Type-II SPDC only differ in the polarizations of the photons. The molecule being in solution would rotationally average out any polarization dependence of a one-photon optical process. Thus, if a one-photon process were attenuating the SPDC, the Type-I and Type-II SPDC would have yielded the same ETPA cross-section with no dependence on σ_f or T_e. This is clearly not the case in our measurements.

7.6.4 ETPA cross-section measurements in flavin adenine dinucleotide

To ensure that the ETPA cross-section vs σ_f trends we measured in ZnTPP for Type-I and Type-II SPDC are indicative of the SPDC properties and not something unique to ZnTPP, we performed similar measurements in another molecule that has been studied with ETPA: flavin adenine dinucleotide (FAD).[25, 55] Fig. 7.10-7.11 shows the normalized ETPA rate vs input rate plots for the cross-sections for FAD. We obtained the same cross-section trends for Type-I and Type-II ETPA with FAD, shown in Fig. 7.12, validating our proposed theory that changing σ_f is also changing A_e, independent of the chromophore.

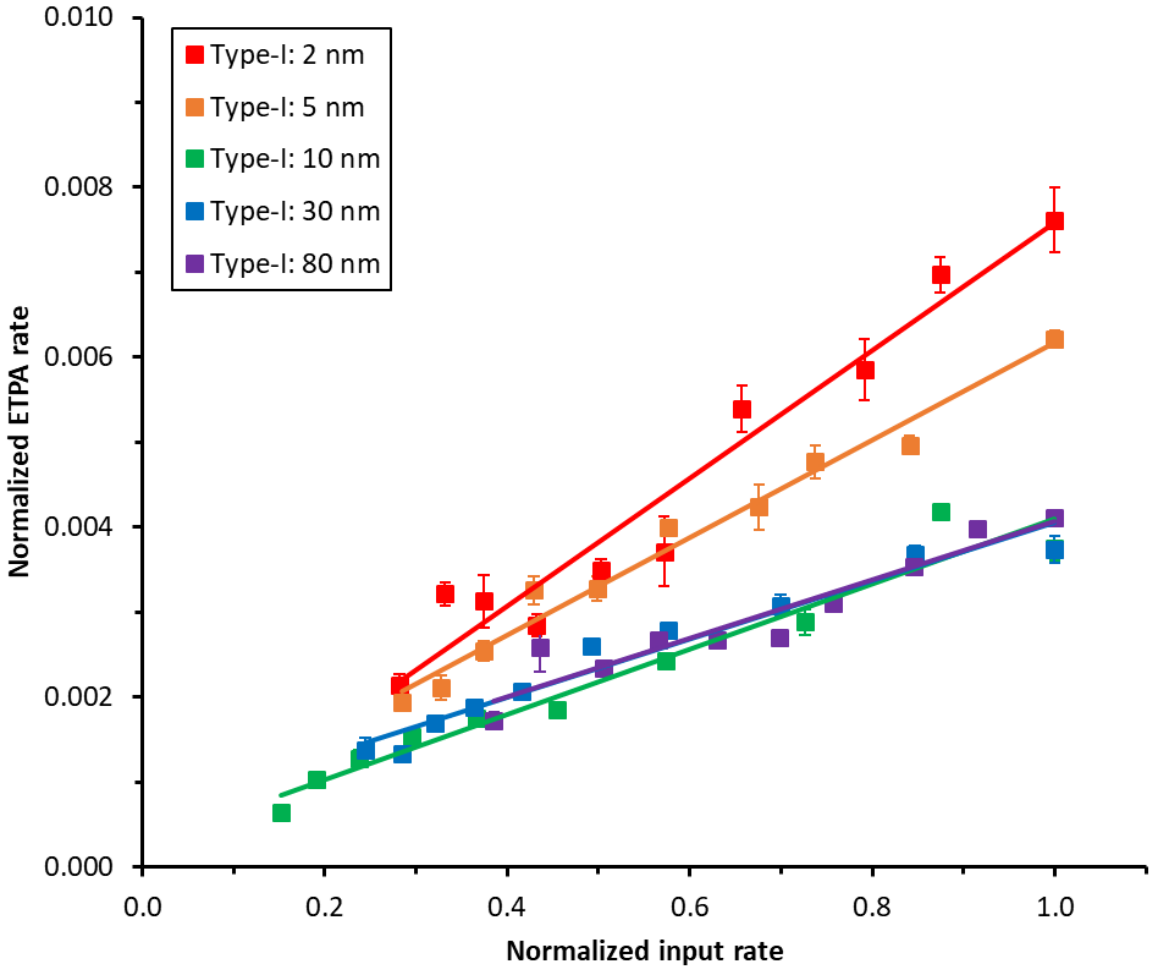

Figure 7.10. Type-I ETPA rate vs input rate in FAD for all SPDC bandwidths.

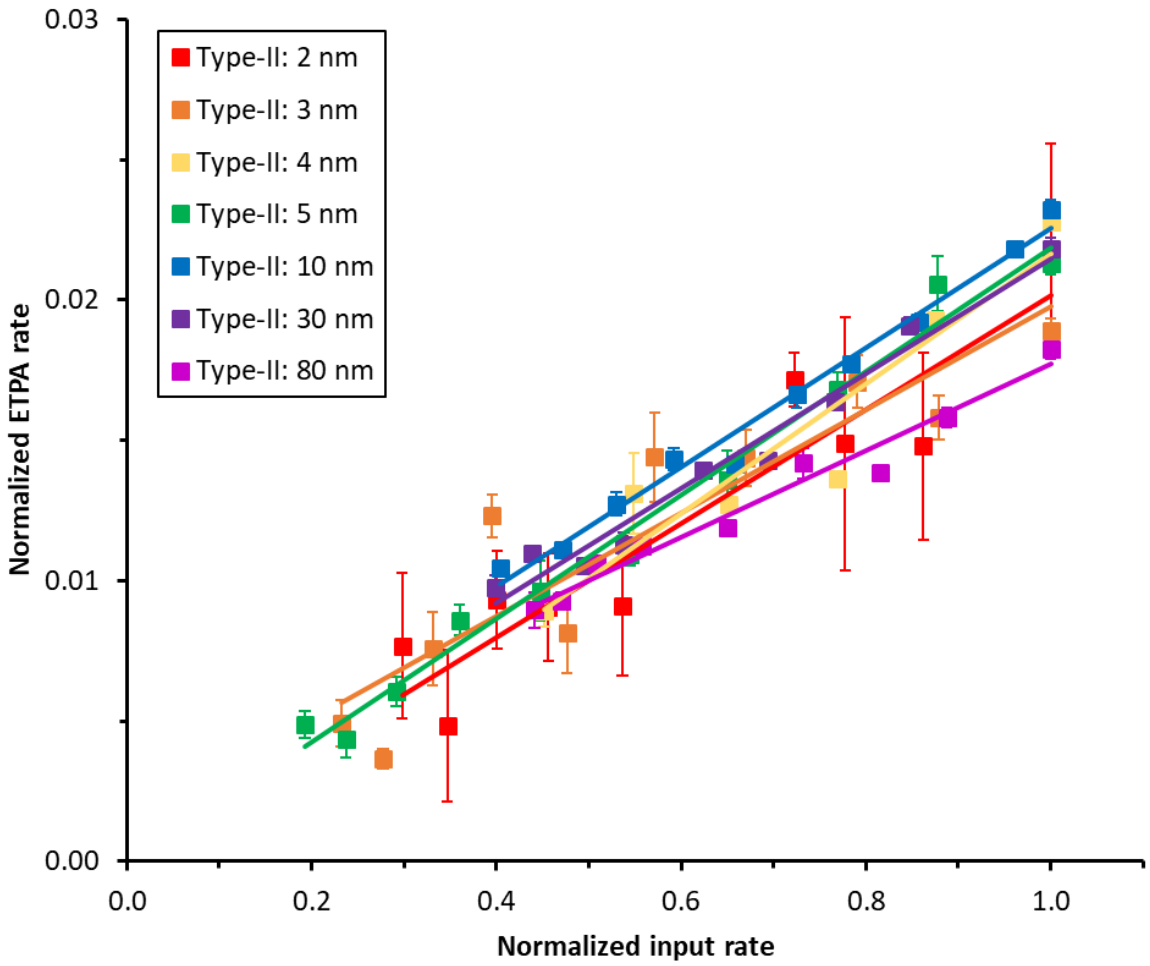

Figure 7.11. Type-II ETPA rate vs input rate in FAD for all SPDC bandwidths.

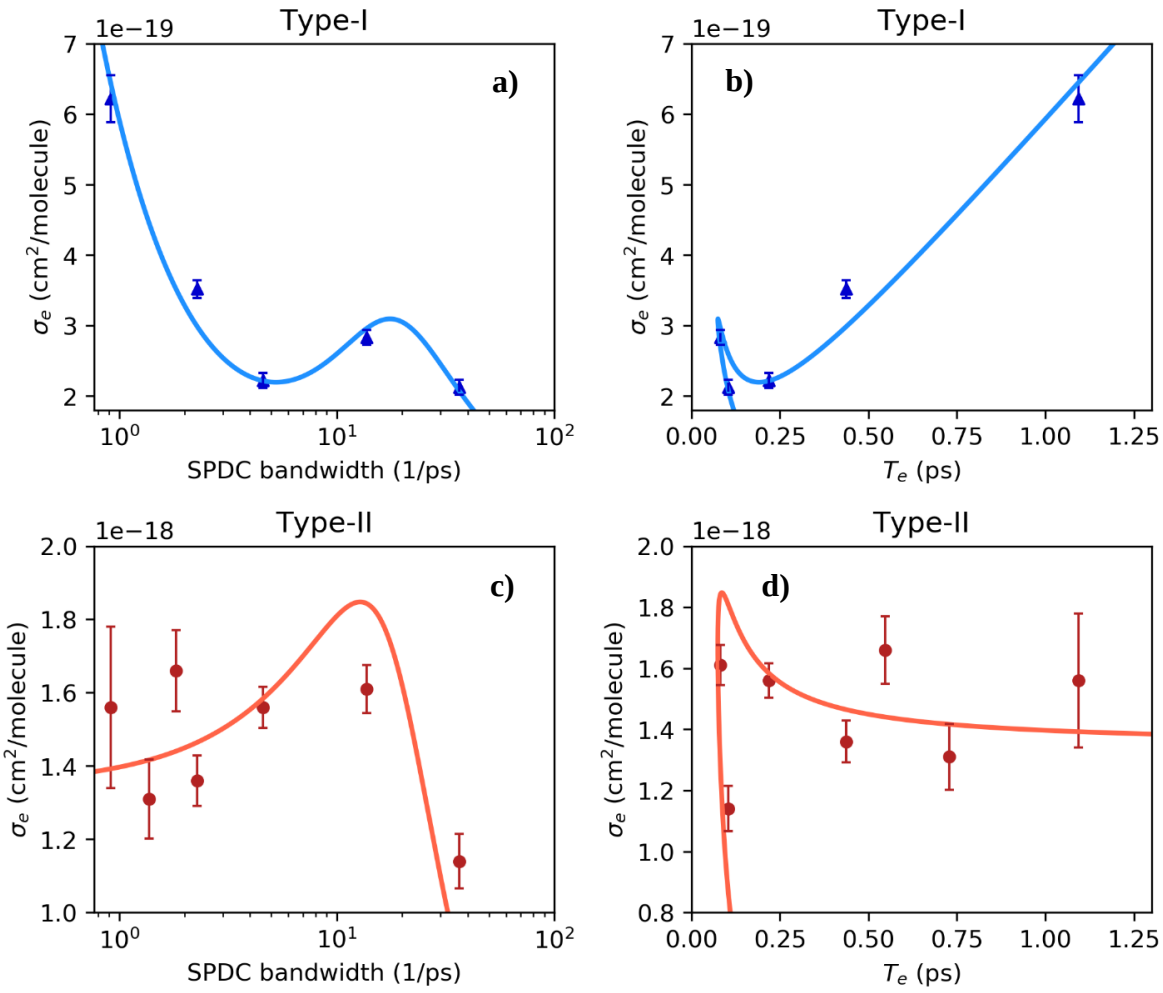

Figure 7.12. a) Experimental (points) and theoretical (solid curve) Type-I ETPA cross-sections, σ_e, vs σ_f for FAD, with dispersion applied. **b)** Same as **(a)** but with the x-axis converted to T_e. **c)** Experimental (points) and theoretical (solid curve) Type-II σ_e vs σ_f for FAD, with dispersion applied. **d)** Same as **(c)** but with the x-axis converted to T_e.

7.6.5 Pitfalls When Using Low Entangled Photon Rates

When measuring the ETPA cross-section using passively filtered SPDC, the input entangled photon rate decreases as the frequency spectrum is narrowed. When using low entangled photon rates (< 10^5 pairs/s), great care must be taken to ensure accurate measurements of the ETPA signal. These troubleshooting steps are important during any ETPA experiment if the ETPA signal is not consistent with previous measurements. These steps are especially important as the input SPDC rate decreases due to frequency filtering.

First, the pump power at the crystal needs to remain as stable as possible, both during the measurement at each pump power and when repeating each pump power step for the solvent and sample power scans. Changes in the pump power will hurt the accuracy of the subtraction method for quantifying the ETPA signal above the solvent baseline. The ETPA signal will be underestimated if the pump power increases during the sample scan or overestimated if the pump power decreases during the sample scan. To ensure the most stable pump power, the laser should be warmed up for approximately 2 hours before beginning ETPA measurements. Monitoring the voltage signal from the reference photodiode can help determine when the pump power is stable. Additionally, the power before and after each attenuation filter before the SPDC crystal should be measured for a few minutes to ensure the transmission through each filter is stable. If the transmission is unstable, the filter should be slightly moved so that the laser beam passes through a new spot, cleaned to remove dust, or both. It is also worth cleaning dust from all optics elements in the beam path, though the filters are the most important.

In addition to having a stable pump power, the alignment of the SPDC on the APD must remain steady for consistent readings of the count rate. All optics must be securely tightened to their mounts, mounts to their posts and bases, and bases to the optical table. The cuvette should not be touched or removed between solvent and sample scans. If the black box containing the cuvette must remain covered to prevent room light from hitting the APD, then an injection port that passes through the black box lid should be attached to the cuvette. The solvent can be removed with a pipette gently placed through the injection port, and the sample can be placed into the cuvette with a pipette. Measurement of the ETPA baseline (difference in count rate for two successive solvent scans) can be used to monitor the stability of the measured SPDC rate. The baseline should have a slope of no more than ~0.1 % of the SPDC rate, and the y-axis should also be no higher than ~0.1 %.

7.6.6 Effects of Vibrational Relaxation and of Molecular Motion

Vibrational relaxation could also cause the modulus squared term to decrease as T_e increases if eq. 7.1 included the vibrational wave function of the molecule. However, assuming that the vibrational states have an exponential decay like the electronic states, the modulus squared term would have a Lorentzian function dependent on the vibrational lifetime. The tails

of a Lorenztian decrease slower than the plasma dispersion function which defines the electronic state relaxation in eq. 7.1, so the vibrational lifetime would not cause the light-matter coupling to decrease any faster than it is already decreasing from the electronic lifetime. As a result, the trend of the ETPA cross-section vs T_e should hardly be affected by vibrations. This same reasoning applies to the rotational movement of the molecule.

References

1. Dayan, B.; Pe'er, A.; Friesem, A. A.; Silberberg, Y., Two Photon Absorption and Coherent Control with Broadband Down-Converted Light. *Physical Review Letters* **2004,** *93* (2), 023005.
2. Dayan, B.; Pe'er, A.; Friesem, A. A.; Silberberg, Y., Nonlinear Interactions with an Ultrahigh Flux of Broadband Entangled Photons. *Physical Review Letters* **2005,** *94* (4), 043602.
3. Lee, D.-I.; Goodson, T., Entangled Photon Absorption in an Organic Porphyrin Dendrimer. *Journal of Physical Chemistry B* **2006,** *110* (51), 25582-25585.
4. Javanainen, J.; Gould, P. L., Linear intensity dependence of a two-photon transition rate. *Physical Review A* **1990,** *41* (9), 5088-5091.
5. Harpham, M. R.; Süzer, Ö.; Ma, C.-Q.; Bäuerle, P.; Goodson, T., Thiophene Dendrimers as Entangled Photon Sensor Materials. *Journal of the American Chemical Society* **2009,** *131* (3), 973-979.
6. Jung, Y. O.; Lee, J. H.; Kim, J.; Schmidt, M.; Moffat, K.; Šrajer, V.; Ihee, H., Volume-conserving trans–cis isomerization pathways in photoactive yellow protein visualized by picosecond X-ray crystallography. *Nature Chemistry* **2013,** *5* (3), 212-220.
7. Zheng, J.; Kwak, K.; Xie, J.; Fayer, M. D., Ultrafast Carbon-Carbon Single-Bond Rotational Isomerization in Room-Temperature Solution. *Science* **2006,** *313* (5795), 1951.
8. Zhang, Y.; de La Harpe, K.; Beckstead, A. A.; Improta, R.; Kohler, B., UV-Induced Proton Transfer between DNA Strands. *Journal of the American Chemical Society* **2015,** *137* (22), 7059-7062.
9. Stoner-Ma, D.; Jaye, A. A.; Matousek, P.; Towrie, M.; Meech, S. R.; Tonge, P. J., Observation of Excited-State Proton Transfer in Green Fluorescent Protein using Ultrafast Vibrational Spectroscopy. *Journal of the American Chemical Society* **2005,** *127* (9), 2864-2865.
10. Li, T.; Hassanali, A. A.; Kao, Y.-T.; Zhong, D.; Singer, S. J., Hydration Dynamics and Time Scales of Coupled Water−Protein Fluctuations. *Journal of the American Chemical Society* **2007,** *129* (11), 3376-3382.
11. Pham, V.-T.; Penfold, T. J.; van der Veen, R. M.; Lima, F.; El Nahhas, A.; Johnson, S. L.; Beaud, P.; Abela, R.; Bressler, C.; Tavernelli, I.; Milne, C. J.; Chergui, M., Probing the Transition from Hydrophilic to Hydrophobic Solvation with Atomic Scale Resolution. *Journal of the American Chemical Society* **2011,** *133* (32), 12740-12748.
12. Kim, S.; Lim, M., Picosecond Dynamics of Ligand Interconversion in the Primary Docking Site of Heme Proteins. *Journal of the American Chemical Society* **2005,** *127* (16), 5786-5787.
13. Kim, S.; Lim, M., Protein Conformation-Induced Modulation of Ligand Binding Kinetics: A Femtosecond Mid-IR Study of Nitric Oxide Binding Trajectories in Myoglobin. *Journal of the American Chemical Society* **2005,** *127* (25), 8908-8909.

14. Fei, H.-B.; Jost, B. M.; Popescu, S.; Saleh, B. E. A.; Teich, M. C., Entanglement-Induced Two-Photon Transparency. *Physical Review Letters* **1997,** *78* (9), 1679-1682.
15. Saleh, B. E. A.; Jost, B. M.; Fei, H.-B.; Teich, M. C., Entangled-Photon Virtual-State Spectroscopy. *Physical Review Letters* **1998,** *80* (16), 3483-3486.
16. Burdick, R. K.; Varnavski, O.; Molina, A.; Upton, L.; Zimmerman, P.; Goodson, T., Predicting and Controlling Entangled Two-Photon Absorption in Diatomic Molecules. *The Journal of Physical Chemistry A* **2018,** *122* (41), 8198-8212.
17. Kang, G.; Nasiri Avanaki, K.; Mosquera, M. A.; Burdick, R. K.; Villabona-Monsalve, J. P.; Goodson, T.; Schatz, G. C., Efficient Modeling of Organic Chromophores for Entangled Two-Photon Absorption. *Journal of the American Chemical Society* **2020,** *142* (23), 10446-10458.
18. Mukamel, S.; Freyberger, M.; Schleich, W.; Bellini, M.; Zavatta, A.; Leuchs, G.; Silberhorn, C.; Boyd, R. W.; Sánchez-Soto, L. L.; Stefanov, A.; Barbieri, M.; Paterova, A.; Krivitsky, L.; Shwartz, S.; Tamasaku, K.; Dorfman, K.; Schlawin, F.; Sandoghdar, V.; Raymer, M.; Marcus, A.; Varnavski, O.; Goodson, T.; Zhou, Z.-Y.; Shi, B.-S.; Asban, S.; Scully, M.; Agarwal, G.; Peng, T.; Sokolov, A. V.; Zhang, Z.-D.; Zubairy, M. S.; Vartanyants, I. A.; del Valle, E.; Laussy, F., Roadmap on quantum light spectroscopy. *Journal of Physics B: Atomic, Molecular and Optical Physics* **2020,** *53* (7), 072002.
19. de J León-Montiel, R.; Svozilík, J.; Salazar-Serrano, L. J.; Torres, J. P., Role of the spectral shape of quantum correlations in two-photon virtual-state spectroscopy. *New Journal of Physics* **2013,** *15* (5), 053023.
20. Nakanishi, T.; Kobayashi, H.; Sugiyama, K.; Kitano, M., Full Quantum Analysis of Two-Photon Absorption Using Two-Photon Wave Function: Comparison of Two-Photon Absorption with One-Photon Absorption. *Journal of the Physical Society of Japan* **2009,** *78* (10), 104401.
21. Varnavski, O.; Pinsky, B.; Goodson, T., Entangled Photon Excited Fluorescence in Organic Materials: An Ultrafast Coincidence Detector. *Journal of Physical Chemistry Letters* **2017,** *8* (2), 388-393.
22. Varnavski, O.; Goodson, T., Two-Photon Fluorescence Microscopy at Extremely Low Excitation Intensity: The Power of Quantum Correlations. *Journal of the American Chemical Society* **2020,** *142* (30), 12966-12975.
23. Zeilinger, A., Experiment and the foundations of quantum physics. *Reviews of Modern Physics* **1999,** *71* (2), S288-S297.
24. Yin, L.; Li, J.; Zhai, W.; Xia, M.; Hu, Y.; Zheng, X., Analysis of the Spatial Properties of Correlated Photon in Collinear Phase-Matching. *Photonics* **2021,** *8* (1).
25. Villabona-Monsalve, J. P.; Burdick, R. K.; Goodson, T., Measurements of Entangled Two-Photon Absorption in Organic Molecules with CW-Pumped Type-I Spontaneous Parametric Down-Conversion. *The Journal of Physical Chemistry C* **2020,** *124* (44), 24526-24532.
26. Yoon-Ho, K., Measurement of one-photon and two-photon wave packets in spontaneous parametric downconversion. *Journal of the Optical Society of America B* **2003,** *20* (9), 1959-1966.
27. Campos, R. A.; Saleh, B. E. A.; Teich, M. C., Fourth-order interference of joint single-photon wave packets in lossless optical systems. *Physical Review A* **1990,** *42* (7), 4127-4137.
28. Rubin, M. H.; Klyshko, D. N.; Shih, Y. H.; Sergienko, A. V., Theory of two-photon entanglement in type-II optical parametric down-conversion. *Physical Review A* **1994,** *50* (6), 5122-5133.

29. The Effect of Dispersion on Ultrashort Pulses. https://www.newport.com/n/the-effect-of-dispersion-on-ultrashort-pulses (accessed April 19, 2021).
30. Joobeur, A.; Saleh, B. E. A.; Larchuk, T. S.; Teich, M. C., Coherence properties of entangled light beams generated by parametric down-conversion: Theory and experiment. *Physical Review A* **1996,** *53* (6), 4360-4371.
31. Joobeur, A.; Saleh, B. E. A.; Teich, M. C., Spatiotemporal coherence properties of entangled light beams generated by parametric down-conversion. *Physical Review A* **1994,** *50* (4), 3349-3361.
32. Joobeur, A.; Saleh, B. E. A.; Larchuk, T. S.; Teich, M. C., Coherence properties of entangled light beams generated by parametric down-conversion: Theory and experiment. *Physical Review A* **1996,** *53* (6), 4360.
33. Oka, H., Two-photon absorption by spectrally shaped entangled photons. *Physical Review A* **2018,** *97* (3), 033814.
34. Oka, H., Enhanced vibrational-mode-selective two-step excitation using ultrabroadband frequency-entangled photons. *Physical Review A* **2018,** *97* (6), 063859.
35. Dixon, J. M.; Taniguchi, M.; Lindsey, J. S., PhotochemCAD 2: A Refined Program with Accompanying Spectral Databases for Photochemical Calculations¶. *Photochemistry and Photobiology* **2005,** *81* (1), 212-213.
36. Slattery, O.; Ma, L.; Zong, K.; Tang, X., Background and review of cavity-enhanced spontaneous parametric down-conversion. *Journal of Research of the National Institute of Standards and Technology* **2019,** *124*, 1-18.
37. Tomoyuki, H., Quantum key distribution with mode-locked two-photon states. *2015 Conference on Lasers and Electro-Optics Pacific Rim* **2015**, 27P_41.
38. Fekete, J.; Rieländer, D.; Cristiani, M.; de Riedmatten, H., Ultranarrow-Band Photon-Pair Source Compatible with Solid State Quantum Memories and Telecommunication Networks. *Physical Review Letters* **2013,** *110* (22), 220502.
39. Kuklewicz, C. E.; Wong, F. N. C.; Shapiro, J. H., Time-Bin-Modulated Biphotons from Cavity-Enhanced Down-Conversion. *Physical Review Letters* **2006,** *97* (22), 223601.
40. Ou, Z. Y.; Lu, Y. J., Cavity Enhanced Spontaneous Parametric Down-Conversion for the Prolongation of Correlation Time between Conjugate Photons. *Physical Review Letters* **1999,** *83* (13), 2556-2559.
41. Polzik, J. S. N.-N. a. B. M. N. a. H. T. a. A. I. V. a. E. S., High purity bright single photon source. *Optics Express* **2007,** *15* (13), 7940-7949.
42. Bao, X.-H.; Qian, Y.; Yang, J.; Zhang, H.; Chen, Z.-B.; Yang, T.; Pan, J.-W., Generation of Narrow-Band Polarization-Entangled Photon Pairs for Atomic Quantum Memories. *Physical Review Letters* **2008,** *101* (19), 190501.
43. Jabir, M. V.; Samanta, G. K., Robust, high brightness, degenerate entangled photon source at room temperature. *Scientific Reports* **2017,** *7* (1), 12613.
44. Kuklewicz, C. E.; Fiorentino, M.; Messin, G.; Wong, F. N. C.; Shapiro, J. H., High-flux source of polarization-entangled photons from a periodically poled ${\mathrm{KTiOPO}}_{4}$ parametric down-converter. *Physical Review A* **2004,** *69* (1), 013807.
45. Fiorentino, M.; Spillane, S. M.; Beausoleil, R. G.; Roberts, T. D.; Battle, P.; Munro, M. W., Spontaneous parametric down-conversion in periodically poled KTP waveguides and bulk crystals. *Optics Express* **2007,** *15* (12), 7479-7488.

46. Peeters, W. H.; van Exter, M. P., Optical characterization of periodically-poled KTiOPO4. *Optics Express* **2008,** *16* (10), 7344-7360.
47. Byrdin, M.; Duan, C.; Bourgeois, D.; Brettel, K., A Long-Lived Triplet State Is the Entrance Gateway to Oxidative Photochemistry in Green Fluorescent Proteins. *Journal of the American Chemical Society* **2018,** *140* (8), 2897-2905.
48. Mohr, M. A.; Kobitski, A. Y.; Sabater, L. R.; Nienhaus, K.; Obara, C. J.; Lippincott-Schwartz, J.; Nienhaus, G. U.; Pantazis, P., Rational Engineering of Photoconvertible Fluorescent Proteins for Dual-Color Fluorescence Nanoscopy Enabled by a Triplet-State Mechanism of Primed Conversion. *Angewandte Chemie International Edition* **2017,** *56* (38), 11628-11633.
49. Schlawin, F.; Dorfman, K. E.; Mukamel, S., Entangled Two-Photon Absorption Spectroscopy. *Accounts of Chemical Research* **2018,** *51* (9), 2207-2214.
50. Peřina, J.; Saleh, B. E. A.; Teich, M. C., Multiphoton absorption cross section and virtual-state spectroscopy for the entangled n-photon state. *Physical Review A* **1998,** *57* (5), 3972-3986.
51. Lahankar, S. A.; West, R.; Varnavski, O.; Xie, X.; Goodson, T.; Sukhomlinova, L.; Twieg, R., Electronic interactions in a branched chromophore investigated by nonlinear optical and time-resolved spectroscopy. *The Journal of Chemical Physics* **2003,** *120* (1), 337-344.
52. Barnett, G. H.; Hudson, M. F.; Smith, K. M., Concerning meso-tetraphenylporphyrin purification. *Journal of the Chemical Society, Perkin Transactions 1* **1975,** (14), 1401-1403.
53. Kang, G.; Nasiri Avanaki, K.; Mosquera, M. A.; Burdick, R. K.; Villabona-Monsalve, J. P.; Goodson Iii, T.; Schatz, G. C., Efficient modeling of organic chromophores for entangled two-photon absorption. *Journal of the American Chemical Society* **2020**.
54. Upton, L.; Harpham, M.; Suzer, O.; Richter, M.; Mukamel, S.; Goodson, T., Optically Excited Entangled States in Organic Molecules Illuminate the Dark. *Journal of Physical Chemistry Letters* **2013,** *4* (12), 2046-2052.
55. Villabona-Monsalve, J. P.; Varnavski, O.; Palfey, B. A.; Goodson, T. I., Two-Photon Excitation of Flavins and Flavoproteins with Classical and Quantum Light. *J. Am. Chem. Soc.* **2018,** *140* (44), 14562-14566.

Chapter 8
Overall Summary and Future Directions

8.1 Overall Summary

As spectroscopic techniques develop, chemists are continuously seeking new ways to probe their molecules. Some wish to understand how certain molecules interact with their environment, such as chromophore-protein interactions, protein solvation, and media effects on chromophores' nonlinear properties.[1-3] Others seek to optimize the performance of newly synthesized molecules, such as for light harvesting and energy storage.[4-7] Regardless of the specific applications that chemists are studying, the heart of the matter lies in how the excited states in molecules interact with other quantum states and how these interactions develop in time. It is only after a molecule has been excited to a higher energy state that interesting chemistry happens. The goal of all spectroscopy, be it classical- or quantum-based, is to obtain snapshots of what happens inside of a molecule once it has been excited. With this spectroscopic information, chemists hope to form a picture of how the structure of a molecule influences how it evolves dynamically. This structure-function relationship is what allows chemists to then design new molecules that can replicate processes in nature, such as photosynthesis,[8] or optimize the performance of synthetic systems, such as OLEDs.[9]

Chemical research using light as a probing device began as early as 1859 when Gustav Kirchhoff theorized that the dark Fraunhofer lines seen in the sun's light spectrum where do to the molecules of the sun absorbing those specific wavelengths of light.[10] Research later took a major leap forward with the invention of the laser in 1960 by Theodore Maiman.[11] Since then, classical spectroscopy has developed numerous experimental setups and methods to extract information about a molecule's excited states, dynamics, and interactions. As important and helpful as classical spectroscopy has been, it has inherent limitations that can provide issues to chemists. Most notably, the frequency and time resolutions limit each other, where as one increases, the other must decrease.[12] As a result, the more knowledge chemists gain about the energy of a state, the less they know about how that state evolves in time, and vice versa. Additionally, classical states of light

are limited in their potential interactions with the states of a molecule. Quantum states can interfere with other states in ways that classical states cannot, allowing quantum states of light to probe molecules in new ways that are not possible with classical states of light.[13, 14]

The goal of quantum sensing within the multidisciplinary field of quantum information science (QIS) is to use quantum states of light to probe these interactions with molecules that classical spectroscopic techniques simply cannot do.[15] One of the hottest approaches to do quantum spectroscopy is with entangled photon pairs produced by spontaneous parametric down-conversion (SPDC).[14] SPDC is the nonlinear optical process where a higher frequency pump field loses one photon, and the energy from it is transferred to two new photons, referred to as signal and idler.[16, 17] The signal and idler are quantum-correlated, meaning that the correlations between them cannot be explained using classical mechanics. Though the two photons can exist in two different points in space, they can only be described as a single quantum object. The properties of the photons as a pair are well-defined, but the properties of either photon individually have complex superpositions. Measurement of the properties of one photon, including its frequency, momentum, position, and polarization, causes a change in the quantum state of the other photon that was not interacted with. It is also true that if both photons were to interact with an object, the two interaction events would be correlated with each other. This is where the interest and application of entangled photon spectroscopy for chemistry research lies.

In classical spectroscopy techniques, a molecule can have two (or more) interactions with a light field to induce excitation or particular excited state dynamics. In particular relevance to this work, classical two-photon absorption (TPA) is the process where a molecule absorbs two photons to be excited to a higher energy state.[18] While the two absorption events must occur very quickly together before the short-lived virtual intermediate state decays, the events are not correlated with each other. Rather, the molecule absorbs one photon and then absorbs another photon at random, hence classical TPA also being known as random TPA. With entangled two-photon absorption (ETPA), when the molecule absorbs one photon, the second absorbed photon is a specific photon within the light field, with a specific arrival time, frequency state, position, polarization, etc. as determined by the first absorbed photon. Therefore, the dynamics of the two absorption events are correlated, leading to unique signatures and interferences between the absorption events and the molecule's excited states.[19, 20]

The earliest research on ETPA focused on the advantage of the ETPA rate scaling linearly with the input photon intensity.[20, 21] This scaling is a unique feature of ETPA since, classically, two-photon interactions scale quadratically with input intensity. Since entangled photon pairs are actually just one quantum object, the ETPA rate scales linearly with the intensity of these quantum objects.[22] The benefit of the linear scaling allows ETPA signals to be measured using extremely lower input intensities compared to classical TPA. Experimental work showed this difference being 10 orders of magnitude.[23] The extremely low input intensities for ETPA allow for two-photon transitions in molecules to be excited and probed without risk of damaging the molecule, which can often happen with the high intensity pulsed lasers needed for classical TPA.[24]

While the linear ETPA rate is very advantageous for chemists, this property of the entangled photons does not provide new quantum signals that yield new information about molecules that classical spectroscopy cannot reveal. An important work from the Teich group at Boston University theorized a new form of spectroscopy, called virtual-state spectroscopy (VSS), that does yield new information about a molecule that classical spectroscopy cannot replicate.[25] VSS utilizes the correlation of the two absorption events in ETPA to reveal a unique quantum interference pattern that arises from changing the temporal correlation, or entanglement time, T_e, of the entangled photons. As T_e is increased, the ETPA cross-section oscillates, changing by orders of magnitude at its maxima and minima. This oscillation also occurs when changing the time delay between the entangled photons after their generation. This oscillation is an interference between the two absorption events of the ETPA transition, and only occurs because the photons are temporally correlated. The oscillation usually has a beating pattern as well, due to interference between the different intermediate states that can be used for the ETPA transition. The Fourier transform of this non-monotonic pattern then yields the frequency spectrum of the excited states in the molecule that contribute to the ETPA transition. Assuming none of the states are near resonance with either of the entangled photons, these states are being probed without actually being excited by the photons. This means that even states with small oscillator strength that cannot be directly excited by light can now be discovered and probed using ETPA.

VSS was one of the earliest examples of new molecular spectroscopic information that can only be obtained from entangled photon spectroscopy. Since its initial proposal, experiments have shown the oscillations of the ETPA cross-section when changing the time delay between the two entangled photons.[21, 26, 27] VSS has thus become an exciting experiment to realize in its full

potential. Theoretical research has continued suggesting improved ways to complete VSS, such as with a temperature-controlled SPDC source.[28] While all of these developments over the past couple of decades has made great strides toward making quantum spectroscopy a useful tool for chemists, the prior work has focused heavily on the unique physics of the entangled photons. But for VSS to be useful to chemists, it must be known how the molecule under study affects the measured signal. In other words, each molecule should have a unique oscillation pattern that is dependent upon the excited state properties of the molecule. Only by knowing the signatures that the molecule leaves on the oscillation pattern can new molecules with unknown excited state properties can be probed with VSS. The work in this dissertation begins at this point. When it comes to interactions between entangled photon pairs and molecules, what does the molecule bring to the table?

In addition to understanding the role that molecules play during ETPA excitation, this work also aims to show how ETPA provides an opportunity to make studies of excited state interactions much simpler and more accessible compared to the classical spectroscopy techniques used today. While classical nonlinear spectroscopy provides useful information about molecules, completing these experiments requires specialized knowledge and experience in using the necessary equipment and collecting the data. Most chemists are not able to complete these experiments themselves, as opposed to measuring the linear absorption spectrum with a UV-vis spectrophotometer, which any chemist should know how and have the means to do. However, development of simpler ways to generate and measure entangled photons makes ETPA a much more accessible way to measure excited state interactions, *a la* a kind of "ETPA spectrophotometer." Such a device would allow any chemist to measure nonlinear properties of molecules with the push of a button.

Chapter 1 set the context for the work in this dissertation. My interests are in making the unique physics of quantum entangled photon interactions with molecules more interesting, useful, and accessible to chemists. While the application of this work lies in chemistry, there are several important physical concepts needed to understand what makes the entangled photons so special compared to classical light. The background information needed as a foundation for this work is also highlighted in chapter 1. The experimental and theoretical methods used in completing this work has outlined in detail in chapter 2. The information provided includes what the experiments

look like, how they work, how data is collected from them, and what useful molecular information is gained from them.

I began my graduate studies working on a theoretical investigation of how different dipole pathways between the ground and final state affect the ETPA oscillation pattern vs T_e.[29] As mentioned, while previous work on these oscillation patterns focused on how the unique physics of entangled photons causes the oscillations, it was largely unknown how the properties of the molecule can affect the oscillations. In the prior works, only the energy of different excited states in the molecule was considered, which showed that the frequency of the oscillations was determined by the detuning energy between the excited states and first absorbed entangled photon. While the energies of excited states are certainly important, another crucial aspect of excited state interactions in chemistry applications is the strength of transition dipole moments (TDMs). The TDMs determine how strongly states can interact and transfer energy between each other. When looking at a TPA transition, whether classical or entangled, the first photon can create a coupling between the ground and virtual state, which is represented as a superposition of many non-resonant intermediate excited states in the molecule, and the second photon would then create a coupling between the virtual and final state. The strength of these couplings is determined by the TDMs between the states involved. This is known as the virtual-state pathway. However, the photons can also use the permanent dipole moment (PDM) of the ground or final state, if it is non-zero. Then the first utilize the PDM and the TDM directly between the ground and final state. This is known as the permanent dipole pathway. I was curious about how these different pathways interfere with each other during ETPA and how this interference affects the oscillation pattern. With calculations of molecular parameters from multi-reference configuration interaction (MRCI) from the Zimmerman group in the University of Michigan Chemistry department, I calculated the ETPA cross-sections for four diatomic molecules with varying permanent dipole strength: HF, strong PDM; OH, intermediate PDM; NO, weak PDM; N_2, no PDM. The results showed that N_2 has a significantly higher enhancement in ETPA cross-section due to constructive interference between the virtual-state pathways. The other molecules, whose transitions were dominated by the permanent dipole pathway, had a much smaller enhancement above a classical approximation. Additionally, the oscillations for N_2 had a much longer period between its minima, so-called entanglement-induced transparencies. This longer period provides easier resolution between the maxima and minima, allowing for the development of ETPA-based sensors that can turn the signal

on and off by changing the entangled photon delay or T_e, without having to change the molecule, its environment, or frequency of the light. These results indicate that the ETPA oscillation pattern, and ETPA in general, is very sensitive to the dipole moments of the molecule. The dipole strength of the excited states ultimately determines the pathway the entangled photons are most likely to take to excite the molecule. This suggests that VSS may also be able to identify the pathway of nonlinear transitions in molecular be probing how the ETPA pathways interfere with each other.

In my ETPA experiments, I use organic chromophores as my molecular systems. While it would have been interesting to study such chromophores with the MRCI calculations and ETPA cross-sections, these molecules are too large for MRCI to calculate their excited state energies and TDMs in a reasonable amount of time. However, recent development of second-linear response time-dependent perturbation theory (SLR TD-DFT) has allowed these molecular parameters to be calculated in large organic chromophores on reasonable time scales.[30, 31] SLR TD-DFT then allowed for a natural extension of the work in Chapter 3. Chapter 4 presented work on the ETPA oscillation pattern of organic chromophores, the calculations for which were completed by the Schatz group in the Northwestern University chemistry department.[32] In addition to studying the oscillation pattern for two organic dendrimers, another molecular parameter was explored to see how it contributes to ETPA: the excited state lineshape. The lineshape determines what the excited state population will look like upon excitation, which will influence how the state evolved dynamically. For future ETPA experiments that probe how the excited state evolves after ETPA excitation, knowledge of the initial lineshape will be crucial. As expected, the ETPA cross-sections showed oscillations vs T_e. The magnitude of the calculated cross-sections agreed remarkably well with the experimental values, to within a factor of 1.3 for both dendrimers studied. With regards to the lineshape, the ETPA lineshape was shown to be orders of magnitude narrower compared to classical TPA excitation. The narrower lineshape is due to the large uncertainty of the arrival time of the photon pair as a whole, making the absorption and relaxation times have large uncertainty. Previous studies on the ETPA cross-section have assumed the ETPA lineshape would be the same as in classical TPA. However, this work showed that only when the newly derived narrow ETPA lineshape is used do the calculations match the experimental cross-sections. This new insight into how the lineshape affects ETPA is useful for future studies that wish to study the dynamics of excited states after ETPA excitation.

Chapter 5 shifted gears to the experimental work of this dissertation. In this chapter, a molecular system not previously probed with entangled photons was studied, that of halogenated ether anesthetics.[33] Anesthetics have been used for decades to temporarily induce unconsciousness in surgical patients. However, the mechanism of action remains almost completely unknown. Attempts to explain the mechanism using classical biology, chemistry, and physics concepts have not been completely successful. In recent years, researchers have hypothesized that the mechanism may be explained with quantum mechanics. While ideas have been proposed,[34] no experiment has demonstrated whether anesthetic molecules even have the ability to target quantum particles and interact through a quantum mechanism. This proof-of-principle is essential before any theories about the mechanism of anesthetic action can be proposed. The goal of this project was to complete the proof-of-principle experiment: can some anesthetics interact with quantum particles (in this case, entangled photons)? The transmission of entangled photon pairs through two halogenated ether anesthetics, sevoflurane (SEVO) and isoflurane (ISO), were measured. Despite linear absorption spectra and quantum chemical calculations showing no electronic states near the one- or two-photon resonance of the entangled pair, the transmission rate was attenuated. Conversely, classical light at the same wavelength showed no interaction, even with much stronger intensities than the entangled photon pair. For comparison, the non-halogenated diethyl ether, a much weaker anesthetic, did not show interaction with either the classical or entangled photons. Both SEVO and ISO showed very strong Raman scattering activity, which suggests that the ethers were able to scatter the entangled photons. The exact scattering mechanism is still unclear. However, what is clear is that the ethers were sensitive only to the entangled photons. This work encourages further studies into the interaction between anesthetics and entangled photons, providing future studies of anesthetic action a valuable new tool in entangled photons.

Chapter 5 showed an exciting new application for entangled photon spectroscopy in molecular biological. However, the experimental setup used a fs pulsed laser with frequency doubling before even creating the SPDC. While experienced spectroscopists are easily capable of operating such a setup, most chemists will not be looking to do this experiment themselves in their labs. However, it is well-known that a CW diode laser can pump SPDC with no worse efficiency than a pulsed laser. The SPDC generation rate seems to be determined more by the average pump power, not instantaneous pump power of an ultrafast laser pulse like other nonlinear processes. I was then interested in implementing ETPA in a smaller, simpler, and more cost effective

experimental setup, one that could resemble an "ETPA spectrometer" that any chemist would be able to use daily in their own labs.[35] This ETPA experimental setup used a CW diode laser already at 405 nm (no frequency doubling required) to pump Type-I SPDC in a BBO crystal. The entangled photons were passed through a cuvette and focused onto an APD for singles detection. ETPA was measured in a variety of molecules ranging in size and structure. While the experimental setup itself was certainly simpler than the previously used pulsed laser setup, the ETPA data showed another advantage for chemists. The noise of the experiment was improved by an order of magnitude compared to the pulsed laser experiments, and the SNR of the experiment was 10-100 times better than the pulsed laser experiments. This improvement in the SNR, as well as the lower detection limit from the lowered noise, makes ETPA a quantitatively robust analytical technique for chemists. Additionally, since singles detection was used, it was important to ensure that the measured attenuation was due to ETPA and not a linear one-photon interaction. Calculations of one-photon absorption (OPA) and various scattering mechanisms showed that ETPA is orders of magnitude more likely to occur. This provides confidence in using singles detection for the experiment, which is simpler than using coincidence detection. Finally, this work outlined the process of quantifying frequency entanglement of the SPDC source, which is an essential step to prove entanglement between the photons. By measuring the joint frequency spectrum and completing the Schmidt decomposition, the frequency entanglement was proven and quantified. The Schmidt decomposition also revealed a new potential for controlling excited state populations with ETPA. By tuning the spatial profile of the pump beam, the entangled frequency states can be manipulated to selectively excite certain energy states and not excite others. This would be a useful application for controlling photochemical reactions. Chemists would be able to use the ETPA spectrometer not only to measure ETPA cross-sections but also as a tool for completing photochemical reactions, particularly reactions that classical light sources cannot catalyze.

The final work in this dissertation, found in Chapter 7, explored an oversight from previous theory on ETPA.[36] Previous work showed that the ETPA cross-section is inversely proportional to T_e as well as the entanglement area, A_e, which is the spatial uncertainty of one photon given the location of the other photon.[19] A_e was assumed to remain constant in an experiment, even if T_e changes. Thus, when T_e is increased, the ETPA cross-section was expected to decrease. However, the literature has shown that the origin of both T_e and A_e is the frequency spectrum of the SPDC, caused by dispersion within the SPDC crystal.[37] Thus, since changing the frequency bandwidth is

required to change T_e, A_e would also have to change when T_e changes. As a result, the ETPA cross-section may not simply decrease as T_e increases. If so, A_e would be a previously neglected control knob to control ETPA cross-sections. Historically, T_e has remained in the timescale of a few hundred fs and no more, since increasing T_e was expected to decrease the cross-section. To measure ETPA at much longer T_e, such as the ps scale, was not thought possible. However, if A_e can be systematically decreased to compensate for the increasing T_e, ETPA could still be measurable at longer T_e. This would open new avenues of ETPA spectroscopy for chemists, allowing them to study longer time scale dynamics, such as the ps dynamics of isomerizations, solvation, ligand binding/unbinding, and proton transfer.[38-45] Some multistep photochemical transitions also require time delays between light interactions, such as in green fluorescent proteins that need time to transfer energy from an excited singlet to a triplet state before being further excited.[46, 47] In this work, the ETPA cross-section for degenerate Type-I SPDC was shown to actually increase as T_e increased from ~250 fs to 1.1 ps. T_e was increased by decreasing the SPDC frequency bandwidth with filters and a monochromator. A theoretical model presented in this work shows that as the frequency bandwidth decreases, A_e must also decrease due to the coupling between the frequency and spatial position of the SPDC photons. This coupling arises from dispersion in the crystal, which is second-order for degenerate Type-I SPDC, causing A_e to decrease quadratically with the frequency bandwidth. The quadratic decrease in A_e compensates the linear increase in T_e, resulting in a net linear increase in the ETPA cross-section until A_e reaches the diffraction limit around T_e = 10 ps. The cross-section at this maximum is an order of magnitude larger than the low fs T_e cross-section, 4 orders of magnitude more than previous predictions of ps T_e cross-sections, and within an order of magnitude of the OPA cross-section. Type-II SPDC, on the other hand, plateaued as T_e increased. For Type-II SPDC, the dispersion in the SPDC crystal is first-order, so A_e only decreases linearly with the frequency bandwidth. This effect cancels the linear increase in T_e, leaving the cross-section constant until A_e reaches the diffraction limit. This work shows that not only is ETPA at ps T_e measurable, it is actually stronger than fs T_e. And ps T_e is achievable today using one of two methods: cavity-enhanced SPDC, which produces more narrowband SPDC by placing the crystal inside of an optical cavity,[48] or filtering of periodically poled SPDC, which produces orders of magnitude more SPDC photons than thin BBO crystals so that enough photons still remove after filtering.[49]

8.2 Future Directions

The experimental and theoretical results obtained throughout this dissertation have shown avenues for future work that further develops ETPA as a useful technique for chemistry research. As more is learned about the unique ways that molecules interact with entangled photons, as well as enhancing measurements of ETPA to yield both larger signals and larger SNRs, the interest among chemists will only continue to grow. The work on the effect that TDMs and PDMs have on ETPA transitions suggests ways that ETPA cross-section can be enhanced with rational design of chromophores. To maximize the constructive interference of ETPA pathways, the virtual-state pathways should be made more favorable and the permanent dipole pathways less favorable with proper design of the chromophore's structure. One approach is to make molecules more symmetric in an effort to reduce the strength of PDMs, as was seen with the symmetric diatomic molecule N_2. It is interesting to note that throughout this work, zinc tetraphenylporphoryin (ZnTPP) has shown to be particularly sensitive to ETPA, yielding some of the largest cross-sections among the chromophores studied. ZnTPP is a symmetric molecule, which should help it have a very small PDM and allow its virtual-state pathways to be stronger for ETPA transitions. It would be interesting to study then how other symmetric chromophores respond to ETPA, compared to asymmetric chromophores with similar functional groups. Another approach to encourage stronger virtual-state pathways could be to increase the conjugation length of chromophores. Increased conjugation should lower the excited state energies,[50] making their detuning energies with the first absorbed photon smaller and making the virtual-state pathways stronger compared to the permanent dipole pathways. Measurements of the ETPA cross-section on increasing conjugation length would be interesting to explore.

With the new understanding of the ETPA lineshape, this is another molecular parameter that can be tuned to enhance ETPA cross-sections. The lineshape was shown to be affected by the temporal properties of the entangled photons upon their creation. The results suggest that narrower pump beams increase the excited state life time since the time at which the pair as a whole was absorbed is less well defined. Work completed in this dissertation used pulsed and CW pump lasers to complete ETPA. Though the measured cross-sections were not exactly the same, they were still on the same order of magnitude. The frequency bandwidths of the pulsed and CW lasers were also on the same order of magnitude. For this reason, it would be interested to see how using a much more narrowband pump laser would affect the measured ETPA cross-section. CW lasers today can

have linewidths as narrow as a few MHz, compared to the hundreds of GHz bandwidth CW laser used here. This extremely more narrow pump laser may be able to enhance the ETPA cross-section by significantly narrowing the excited state linewidth.

The work on the entangled photon interaction with the anesthetics revealed an interesting potential for entangled photon spectroscopy: entangled photon scattering. While ETPA provides excitation and information of electronic excited states, entangled photon scattering may provide unique information about the vibrational state of molecules. Advantages for using entangled photon pairs in a variety of scattering mechanisms can be explored. Spontaneous Raman scattering with one of the entangled photons would allow the other photon to remain outside the sample and be measured to probe the interaction that occurs between its partner and the sample, a form of remote sensing. Stimulated Raman can be induced with the second photon, with the broad frequency bandwidth of the entangled photon able to probe a wide range of vibrational state and the narrow summed frequency of the photons still yielding high frequency resolution. Two-photon scattering, or hyper-Raman, may be enhanced in an analogous way to TPA being enhanced using entangled pairs. The effect of T_e and/or entangled photon time delay on the ETPA cross-section would be interesting to explore as well. The interference between the two interactions may produce oscillations similar to ETPA, allowing for a vibrational state form of VSS.

One of the most exciting potentials for chemistry-based ETPA applications is the control of photochemical reactions. Since chemical reactions are triggered from certain molecular states, high precision of the photoexcited state can be required from some reactions.[51] Prior work has shown how the simultaneous frequency and time resolution of entangled photons can populate excited states that require an ultrafast-decaying intermediate.[52] Classical spectroscopy does not provide the simultaneous high frequency and time resolution needed for this experiment. Another method stemming from this work to control photochemical reactions is by manipulation of the entangled photons frequency states. Photon pairs can be created at the specific frequency pairs that can excite the desired state, while frequency pairs that would excite undesirable states would be suppressed. The random nature of classical TPA would not allow the suppression of the undesirable states to happen since the frequency state of one photon is not affect by the other. Control of the entangled photon frequency states is rather simple using a spatial light modulator to tune the spatial profile of the pump beam.[53] Another method for controlling photochemical reactions is through ETPA with longer T_e. While some photochemical reactions may have

ultrafast-decaying intermediates, others have intermediate processes that must be allowed to occur before the second photon interaction. An example is that of the singlet-to-triplet charge transfer in GFP in between the first and second photoexcitation.[46, 47] ETPA with ps T_e would allow these intermediate processes to occur before the second excitation.

Finally, applications for studying ps-scale dynamics with ETPA have been explored since ETPA was previously assumed to be too weak with ps T_e. ps dynamics are important in many molecular and biological systems, including isomerizations, solvation, ligand binding/unbinding, and proton transfer.[38-45] Time-delayed experiments with ps T_e would allow for higher spectral resolution than similar experiments using classical fs or ps pulses since narrowband CW lasers can be used to pump the ps T_e SPDC. Knowing that ETPA can be measured into the ps range allows for full implementation of a transient absorption-like experiment using entangled photons. In fact, pulsed lasers would not even be required to obtain transient absorption measurements since even CW lasers can generate temporally-resolved entangled photons. Future developments of "ETPA spectrometers" can include time-resolved nonlinear spectroscopy measurements simply at the push of a button.

References

1. Ihalainen, J. A.; Gustavsson, E.; Schroeder, L.; Donnini, S.; Lehtivuori, H.; Isaksson, L.; Thöing, C.; Modi, V.; Berntsson, O.; Stucki-Buchli, B.; Liukkonen, A.; Häkkänen, H.; Kalenius, E.; Westenhoff, S.; Kottke, T., Chromophore–Protein Interplay during the Phytochrome Photocycle Revealed by Step-Scan FTIR Spectroscopy. *Journal of the American Chemical Society* **2018,** *140* (39), 12396-12404.
2. Zagorec-Marks, W.; Foreman, M. M.; Verlet, J. R. R.; Weber, J. M., Probing the Microsolvation Environment of the Green Fluorescent Protein Chromophore In Vacuo. *The Journal of Physical Chemistry Letters* **2020,** *11* (5), 1940-1946.
3. Lou, A. J. T.; Righetto, S.; Barger, C.; Zuccaccia, C.; Cariati, E.; Macchioni, A.; Marks, T. J., Unprecedented Large Hyperpolarizability of Twisted Chromophores in Polar Media. *Journal of the American Chemical Society* **2018,** *140* (28), 8746-8755.
4. Chen, D.; Wang, J.-H.; Chou, T.-F.; Zhao, B.; El-Sayed, M. A.; Liu, M., Unraveling the Nature of Anomalously Fast Energy Storage in T-Nb2O5. *Journal of the American Chemical Society* **2017,** *139* (20), 7071-7081.
5. Hu, B.; DeBruler, C.; Rhodes, Z.; Liu, T. L., Long-Cycling Aqueous Organic Redox Flow Battery (AORFB) toward Sustainable and Safe Energy Storage. *Journal of the American Chemical Society* **2017,** *139* (3), 1207-1214.
6. Li, Y.; Dong, Y.; Cheng, L.; Qin, C.; Nian, H.; Zhang, H.; Yu, Y.; Cao, L., Aggregation-Induced Emission and Light-Harvesting Function of Tetraphenylethene-Based Tetracationic Dicyclophane. *Journal of the American Chemical Society* **2019,** *141* (21), 8412-8415.
7. Segatta, F.; Cupellini, L.; Jurinovich, S.; Mukamel, S.; Dapor, M.; Taioli, S.; Garavelli, M.; Mennucci, B., A Quantum Chemical Interpretation of Two-Dimensional Electronic Spectroscopy of Light-Harvesting Complexes. *Journal of the American Chemical Society* **2017,** *139* (22), 7558-7567.
8. Eberhart, M. S.; Bowers, L. M. R.; Shan, B.; Troian-Gautier, L.; Brennaman, M. K.; Papanikolas, J. M.; Meyer, T. J., Completing a Charge Transport Chain for Artificial Photosynthesis. *Journal of the American Chemical Society* **2018,** *140* (31), 9823-9826.
9. Lai, P.-N.; Brysacz, C. H.; Alam, M. K.; Ayoub, N. A.; Gray, T. G.; Bao, J.; Teets, T. S., Highly Efficient Red-Emitting Bis-Cyclometalated Iridium Complexes. *Journal of the American Chemical Society* **2018,** *140* (32), 10198-10207.
10. Thomas, N. C., The early history of spectroscopy. *Journal of Chemical Education* **1991,** *68* (8), 631.
11. Maiman, T. H., Stimulated Optical Radiation in Ruby. *Nature* **1960,** *187* (4736), 493-494.
12. Heisenberg, W., Über den anschaulichen Inhalt der quantentheoretischen Kinematik und Mechanik. *Zeitschrift für Physik* **1927,** *43* (3), 172-198.
13. Dorfman, K. E.; Schlawin, F.; Mukamel, S., Nonlinear optical signals and spectroscopy with quantum light. *Reviews of Modern Physics* **2016,** *88* (4), 045008.
14. Mukamel, S.; Freyberger, M.; Schleich, W.; Bellini, M.; Zavatta, A.; Leuchs, G.; Silberhorn, C.; Boyd, R. W.; Sánchez-Soto, L. L.; Stefanov, A.; Barbieri, M.; Paterova, A.; Krivitsky, L.; Shwartz, S.; Tamasaku, K.; Dorfman, K.; Schlawin, F.; Sandoghdar,

V.; Raymer, M.; Marcus, A.; Varnavski, O.; Goodson, T.; Zhou, Z.-Y.; Shi, B.-S.; Asban, S.; Scully, M.; Agarwal, G.; Peng, T.; Sokolov, A. V.; Zhang, Z.-D.; Zubairy, M. S.; Vartanyants, I. A.; del Valle, E.; Laussy, F., Roadmap on quantum light spectroscopy. *Journal of Physics B: Atomic, Molecular and Optical Physics* **2020,** *53* (7), 072002.
15. Degen, C. L.; Reinhard, F.; Cappellaro, P., Quantum sensing. *Reviews of Modern Physics* **2017,** *89* (3), 035002.
16. Klyshko, D. N.; Penin, A. N.; Polkovnikov, B. F., Parametric Luminescence and Light Scattering by Polaritons. *Soviet Journal of Experimental and Theoretical Physics Letters* **1970,** *11*, 5.
17. Burnham, D. C.; Weinberg, D. L., Observation of Simultaneity in Parametric Production of Optical Photon Pairs. *Physical Review Letters* **1970,** *25* (2), 84-87.
18. Göppert-Mayer, M., Über Elementarakte mit zwei Quantensprüngen. *Annalen der Physik* **1931,** *401* (3), 273-294.
19. Fei, H.-B.; Jost, B. M.; Popescu, S.; Saleh, B. E. A.; Teich, M. C., Entanglement-Induced Two-Photon Transparency. *Physical Review Letters* **1997,** *78* (9), 1679-1682.
20. Javanainen, J.; Gould, P. L., Linear intensity dependence of a two-photon transition rate. *Physical Review A* **1990,** *41* (9), 5088-5091.
21. Lee, D.-I.; Goodson, T., Entangled Photon Absorption in an Organic Porphyrin Dendrimer. *Journal of Physical Chemistry B* **2006,** *110* (51), 25582-25585.
22. Hong, C. K.; Mandel, L., Theory of parametric frequency down conversion of light. *Physical Review A* **1985,** *31* (4), 2409-2418.
23. Harpham, M. R.; Süzer, Ö.; Ma, C.-Q.; Bäuerle, P.; Goodson, T., Thiophene Dendrimers as Entangled Photon Sensor Materials. *Journal of the American Chemical Society* **2009,** *131* (3), 973-979.
24. Hopt, A.; Neher, E., Highly nonlinear photodamage in two-photon fluorescence microscopy. *Biophysical journal* **2001,** *80* (4), 2029-2036.
25. Saleh, B. E. A.; Jost, B. M.; Fei, H.-B.; Teich, M. C., Entangled-Photon Virtual-State Spectroscopy. *Physical Review Letters* **1998,** *80* (16), 3483-3486.
26. Varnavski, O.; Pinsky, B.; Goodson, T., Entangled Photon Excited Fluorescence in Organic Materials: An Ultrafast Coincidence Detector. *Journal of Physical Chemistry Letters* **2017,** *8* (2), 388-393.
27. Varnavski, O.; Goodson, T., Two-Photon Fluorescence Microscopy at Extremely Low Excitation Intensity: The Power of Quantum Correlations. *Journal of the American Chemical Society* **2020,** *142* (30), 12966-12975.
28. León-Montiel, R. d. J.; Svozilík, J.; Torres, J. P.; U'Ren, A. B., Temperature-Controlled Entangled-Photon Absorption Spectroscopy. *Physical Review Letters* **2019,** *123* (2), 023601.
29. Burdick, R. K.; Varnavski, O.; Molina, A.; Upton, L.; Zimmerman, P.; Goodson, T., Predicting and Controlling Entangled Two-Photon Absorption in Diatomic Molecules. *The Journal of Physical Chemistry A* **2018,** *122* (41), 8198-8212.
30. Mosquera, M. A.; Chen, L. X.; Ratner, M. A.; Schatz, G. C., Sequential double excitations from linear-response time-dependent density functional theory. *J. Chem. Phys.* **2016,** *144* (20), 204105.
31. Mosquera, M. A.; Jackson, N. E.; Fauvell, T. J.; Kelley, M. S.; Chen, L. X.; Schatz, G. C.; Ratner, M. A., Exciton Absorption Spectra by Linear Response Methods: Application to Conjugated Polymers. *J. Am. Chem. Soc.* **2017,** *139* (10), 3728-3735.

32. Kang, G.; Nasiri Avanaki, K.; Mosquera, M. A.; Burdick, R. K.; Villabona-Monsalve, J. P.; Goodson, T.; Schatz, G. C., Efficient Modeling of Organic Chromophores for Entangled Two-Photon Absorption. *Journal of the American Chemical Society* **2020,** *142* (23), 10446-10458.
33. Burdick, R. K.; Villabona-Monsalve, J. P.; Mashour, G. A.; Goodson, T., Modern Anesthetic Ethers Demonstrate Quantum Interactions with Entangled Photons. *Scientific Reports* **2019,** *9* (1), 11351.
34. Adams, B.; Petruccione, F., Quantum effects in the brain: A review. *AVS Quantum Science* **2020,** *2* (2), 022901.
35. Villabona-Monsalve, J. P.; Burdick, R. K.; Goodson, T., Measurements of Entangled Two-Photon Absorption in Organic Molecules with CW-Pumped Type-I Spontaneous Parametric Down-Conversion. *The Journal of Physical Chemistry C* **2020,** *124* (44), 24526-24532.
36. Burdick, R. K.; Goodson III, T., Enhancing Entangled Two-Photon Absorption for Picosecond Quantum Spectroscopy. **2021,** *Manuscript in preparation*.
37. Joobeur, A.; Saleh, B. E. A.; Larchuk, T. S.; Teich, M. C., Coherence properties of entangled light beams generated by parametric down-conversion: Theory and experiment. *Physical Review A* **1996,** *53* (6), 4360-4371.
38. Jung, Y. O.; Lee, J. H.; Kim, J.; Schmidt, M.; Moffat, K.; Šrajer, V.; Ihee, H., Volume-conserving trans–cis isomerization pathways in photoactive yellow protein visualized by picosecond X-ray crystallography. *Nature Chemistry* **2013,** *5* (3), 212-220.
39. Zheng, J.; Kwak, K.; Xie, J.; Fayer, M. D., Ultrafast Carbon-Carbon Single-Bond Rotational Isomerization in Room-Temperature Solution. *Science* **2006,** *313* (5795), 1951.
40. Zhang, Y.; de La Harpe, K.; Beckstead, A. A.; Improta, R.; Kohler, B., UV-Induced Proton Transfer between DNA Strands. *Journal of the American Chemical Society* **2015,** *137* (22), 7059-7062.
41. Stoner-Ma, D.; Jaye, A. A.; Matousek, P.; Towrie, M.; Meech, S. R.; Tonge, P. J., Observation of Excited-State Proton Transfer in Green Fluorescent Protein using Ultrafast Vibrational Spectroscopy. *Journal of the American Chemical Society* **2005,** *127* (9), 2864-2865.
42. Li, T.; Hassanali, A. A.; Kao, Y.-T.; Zhong, D.; Singer, S. J., Hydration Dynamics and Time Scales of Coupled Water−Protein Fluctuations. *Journal of the American Chemical Society* **2007,** *129* (11), 3376-3382.
43. Pham, V.-T.; Penfold, T. J.; van der Veen, R. M.; Lima, F.; El Nahhas, A.; Johnson, S. L.; Beaud, P.; Abela, R.; Bressler, C.; Tavernelli, I.; Milne, C. J.; Chergui, M., Probing the Transition from Hydrophilic to Hydrophobic Solvation with Atomic Scale Resolution. *Journal of the American Chemical Society* **2011,** *133* (32), 12740-12748.
44. Kim, S.; Lim, M., Picosecond Dynamics of Ligand Interconversion in the Primary Docking Site of Heme Proteins. *Journal of the American Chemical Society* **2005,** *127* (16), 5786-5787.
45. Kim, S.; Lim, M., Protein Conformation-Induced Modulation of Ligand Binding Kinetics: A Femtosecond Mid-IR Study of Nitric Oxide Binding Trajectories in Myoglobin. *Journal of the American Chemical Society* **2005,** *127* (25), 8908-8909.
46. Byrdin, M.; Duan, C.; Bourgeois, D.; Brettel, K., A Long-Lived Triplet State Is the Entrance Gateway to Oxidative Photochemistry in Green Fluorescent Proteins. *Journal of the American Chemical Society* **2018,** *140* (8), 2897-2905.

47. Mohr, M. A.; Kobitski, A. Y.; Sabater, L. R.; Nienhaus, K.; Obara, C. J.; Lippincott-Schwartz, J.; Nienhaus, G. U.; Pantazis, P., Rational Engineering of Photoconvertible Fluorescent Proteins for Dual-Color Fluorescence Nanoscopy Enabled by a Triplet-State Mechanism of Primed Conversion. *Angewandte Chemie International Edition* **2017,** *56* (38), 11628-11633.
48. Slattery, O.; Ma, L.; Zong, K.; Tang, X., Background and review of cavity-enhanced spontaneous parametric down-conversion. *Journal of Research of the National Institute of Standards and Technology* **2019,** *124*, 1-18.
49. Tanzilli, S.; De Riedmatten, H.; Tittel, W.; Zbinden, H.; Baldi, P.; De Micheli, M.; Ostrowsky, D. B.; Gisin, N., Highly efficient photon-pair source using periodically poled lithium niobate waveguide. *Electron. Lett.* **2001,** *37* (1), 26-28.
50. Meier, H.; Stalmach, U.; Kolshorn, H., Effective conjugation length and UV/vis spectra of oligomers. *Acta Polymerica* **1997,** *48* (9), 379-384.
51. Schlawin, F.; Dorfman, K. E.; Fingerhut, B. P.; Mukamel, S., Suppression of population transport and control of exciton distributions by entangled photons. *Nature Communications* **2013,** *4* (1), 1782.
52. Schlawin, F.; Dorfman, K. E.; Mukamel, S., Entangled Two-Photon Absorption Spectroscopy. *Accounts of Chemical Research* **2018,** *51* (9), 2207-2214.
53. Valencia, A.; Ceré, A.; Shi, X.; Molina-Terriza, G.; Torres, J. P., Shaping the waveform of entangled photons. *Physical review letters* **2007,** *99* (24), 243601.